



ESCOLA
TÉCNICA
SUPERIOR DE INGENIERÍA INDUSTRIAL

Universidad Politécnica de Madrid

Escuela Técnica Superior de Ingeniería Industrial
Universidad Politécnica de Madrid

Avenida de la Ilustración, 3. 28040 Madrid

Tel. (+34) 91 339 00 00

www.etsiiind.upm.es

www.etsiiind.upm.es/ingles/

INSTITUTO

DE TESIS DOCTORAL

TESIS DOCTORAL

SOFT ROBOTICS: APPLICATIONS, DESIGN AND CONTROL

Silvia Terrile

TESIS DOCTORAL
PARA LA OBTENCIÓN DEL
TÍTULO DE DOCTOR

DICIEMBRE 2021

Silvia Terrile

DIRECTOR DE LA TESIS DOCTORAL:

Antonio Barrientos Cruz





UNIVERSIDAD POLITÉCNICA DE MADRID
ESCUELA TÉCNICA SUPERIOR DE INGENIEROS INDUSTRIALES
CENTRO DE AUTOMÁTICA Y ROBÓTICA
CAR-CSIC UPM

**SOFT ROBOTICS: APPLICATIONS, DESIGN AND
CONTROL**

A thesis submitted for the degree of
Doctor of Philosophy in Automation and Robotics.

Author:

M.Sc. Silvia TERRILE

Advisor:

PhD. Antonio BARRIENTOS

2021

TRIBUNAL
Universidad Politécnica de Madrid
Escuela Técnica Superior de Ingenieros Industriales

Title:
Soft robotics: applications, design and control

Author:
Silvia Terrile, M.Sc

Advisor:
Antonio Barrientos, PhD

Tribunal nombrado por el Mgfc. Y Excmo. Sr. Rector de la Universidad Politécnica de Madrid el día de de 2021.

Presidente: Claudio Rossi

Secretario: Roemi Emilia Fernández Saavedra

Vocal: José María Sabater Navarro

Vocal: Antonio Giménez Fernández

Vocal: Juan David Hernández Vega

Suplente: Ramón Barber Castaño

Suplente: Francisco Rodríguez Díaz

Calificación de la Tesis:

EL PRESIDENTE

LOS VOCALES

EL SECRETARIO

"The important thing in science is not so much to obtain new facts as to discover new ways of thinking about them."

Sir William Lawrence Bragg

Acknowledgments

La primera persona a la que quiero agradecer es a mi profesor, Antonio Barrientos. Creo que nada es más importante a la hora de realizar un doctorado que tener a un gran supervisor. Y yo desde luego no habría podido tener uno mejor. Así que gracias por haberme dado la posibilidad de emprender un doctorado bajo tu supervisión. Gracias por haber sido un ejemplo y haberme enseñado tanto, no solo desde el punto de vista académico si no también desde el punto de vista humano. Y sobre todo gracias por no haber dejado nunca de creer en mí y haberme apoyado siempre. Sin tu ayuda y tu guía este trabajo nunca habría visto la luz.

La segunda persona a la que más quiero agradecer eres tú Andres. Gracias por las risas y todos los momentos inolvidables que hemos vivido juntos con nuestra hija Kyma. Sin ti no habría sido lo mismo. Eres para mi un amigo y un ejemplo y sin tu apoyo hoy no estaría aquí. Y ahora yo tengo una casa en Bruselas y tú una en Madrid, o en cualquier otro lugar del mundo nos lleve la vida.

Gracias a todos los que compartieron ese mismo camino del doctorado conmigo. Gracias a Mario, Juanje, Jorge y Pablo. Gracias por todo vuestro cariño, apoyo y ayuda. Gracias por las risas y todos los momentos pasados juntos. Todos y cada uno habéis sido un ejemplo y yo, única chica del grupo, siempre he sentido que podía contar con vosotros. De cada uno he aprendido mucho y ha sido un honor y un placer compartir parte de este camino con vosotros. Gracias también a Jaime, Carlos, Rosa, Ángel por toda su disponibilidad y ayuda.

Chrystian, nos hemos conocido porque yo pensé que era muy buena idea construir una medusa de silicona y hoy eres un gran investigador (aunque, en lugar de las medusas de silicona, has preferido los perros de metal). Gracias por todos los momentos y las charlas que hemos compartido. Y gracias por haberme hecho conocer gente tan linda como Miguel, Paul, Guido y Manuel. Gracias a todos vosotros por haberme apoyado tanto en estos últimos meses, por haberme hecho sentir parte del grupo y por vuestra disponibilidad y cariño, sois personas muy especiales.

Gracias también a mis estudiantes de TFG y TFM que conmigo han desarrollados los prototipos presentados en este trabajo: Cecilia, Miguel A., Miguel M., Alejandro, Andrea, Matilde, Jesús, Carlos, Jaime, Manuel.

Gracias a los más de 600 alumnos que he tenido a lo largo de estos 5 años, desde los niños de infantil hasta los más mayores: todos me habéis enseñado algo. Gracias a los niños que me han desafiado clase tras clase, vosotros me habéis hecho una profe mejor. Gracias a los niños que me han recibido con abrazos y dibujos, a los que más se han esforzado y que con mucho orgullo me han enseñado sus robots y videojuegos, vosotros habéis hecho que siempre mereciera la pena. Y gracias a todas aquellas niñas que se han sentido inspirada por mí y que han decidido ser científicas en un futuro.

Gracias a mis alumnos de informática, porque ya jubilados os habéis esforzado para aprender algo que os resulta totalmente ajeno. Muchos de vosotros habéis sido ejemplos de superación, ya que después de enfermedades o vidas complicadas, aún teníais las ganas de aprender.

Pero entre todos, quiero especialmente agradecer a mis alumnos de italiano. Con ellos he compartido nacimientos y lutos, momentos alegres, risas y momentos más complicados, porqué así es la vida. Ellos no lo saben, pero muchas veces han mejorado increíblemente mi día porque siempre han sido mucho más que alumnos. Así que, gracias a Alex, Alicia, Amalia, Fernando, Juan Antonio, María Jesús, María Victoria y mi abuelita española María Ángeles, y a todos los demás, pero sois tantos que me es imposible nombrarlos a todos. Gracias por todo el cariño que siempre me habéis demostrado.

Ser profe ha sido todo un desafío, y aunque yo os puedo haber ensañado a programar un coche, a adjuntar un archivo en el correo electrónico o a mejorar vuestro nivel de italiano, vosotros me habéis enseñado mucho más.

Grazie a Barbara Mazzolai per avermi permesso di realizzare un periodo del mio dottorato con il suo gruppo di ricerca all'IIT. Grazie per la sua disponibilità e gentilezza. Lei è per me un esempio ed è stato un onore conoscerla. Grazie a Emanuela del Dottore, che mi ha accolto all'IIT e mi ha introdotto nel mondo delle piante robotiche bio-inspirate. Grazie per tutto quello che mi hai insegnato, non avrei potuto avere un supervisore migliore. Grazie anche a Alessio, Stefano, Marilena e Giulia e a tutte le altre persone che ho conosciuto all'IIT per la loro gentilezza, disponibilità, simpatia e soprattutto per avermi insegnato moltissime cose.

Gracias a los amigos que siempre han estado y que siempre estarán porque a pesar de la lejanía nuestro vínculo sigue igual de fuerte. Así que gracias a Ambra, mi hermana no de sangre, pero si de corazón, por estar siempre allí y por todos los momentos que hemos compartido y compartiremos. Y gracias a Marco por ser, desde que nos conocemos, un gran amigo y apoyo.

Y gracias a Andres S., por haberme siempre apoyado a lo largo de la carrera, del master y cuando decidí hacer un doctorado. También es gracias a ti si hoy estoy aquí. Gracias por haber creído en mí siempre.

Gracias a todos los amigos que he conocido en Madrid y que se han transformado en una nueva familia, gracias a Bea, Edu, Jorge, Ignacio, Pame, Julia y Jorge y Ally por todos los momentos que hemos compartido y que seguiremos compartiendo. Gracias por haber estado allí por mí. De todos vosotros he aprendido mucho y me siento muy afortunada de tenerlos en mi vida. Y, sobre todo, muchas gracias a Javi, entre los amigos más especiales que me ha regalado Madrid. Gracias por todas tus enseñanzas, tu cariño, apoyo, por todas las charlas, meriendas y momentos que hemos compartido.

Gracias a mis padres porque sin ellos nunca habría llegado hasta aquí. Gracias a mi padre por haber sido un gran ejemplo durante toda mi vida de esfuerzo, trabajo y por su gran sabiduría. Gracias a mi mamá por haberme enseñado que la felicidad está en las pequeñas cosas. Y gracias a ambos por haberme dejado libre de tomar mi camino. Gracias a Caterina, mi hermana de sangre, por siempre estar allí, y gracias a mi cuñado William, que en muchas ocasiones me ha ayudado y aconsejado: habéis sido un apoyo precioso.

Y, por último, gracias a Rafa, la persona que más ha sufrido conmigo durante este camino, pero que siempre ha creído en mí y siempre me ha animado. Gracias por haber traído a mi vida tantas risas y alegría y a Michigan y Richi, dos gatos adorables que nunca me han dejado sola durante las largas horas delante del ordenador.

Abstract

This work studies soft robots in their different applications fields. Soft robotics is a relatively new field of robotics characterized above all by the use of soft materials that allow obtaining more flexible robots that adapt better to their environment and interact more safely with people. Despite having many advantages, their flexibility and softness make them much more complicated to model and control than conventional robots. This work begins by offering an updated state of the art on soft robots, proposing a definition and dividing them into four large groups: bio-inspired, manipulators, grippers, and wearable. The different prototypes realized are presented for each group, showing the design and control used in each case. In some cases, the use of more conventional actuators as motors is compared with others better adapted to soft prototypes such as SMA (Shape Memory Alloy). The use of the SMA is an added challenge in the already complicated world of soft robotics due to its difficult control.

Concerning bio-inspired robots, the developments of a starfish and a jellyfish actuated with SMA and a preliminary study on plants are presented. Concerning manipulative robots, two prototypes are presented, both continuous and soft, but actuated in one case with motors and the other with SMA springs. Regarding the grippers, the comparison of four different soft gripper solutions is presented, being able to see the advantages and defects of each one and have chosen, in this case, pneumatic actuators and motors. Finally, different prototypes are developed concerning wearable devices divided into haptic devices and exoskeletons. In all cases, these are gloves whose purpose is to rehabilitate the hand. Therefore, the main objective is to propose prototypes that are light and adapt better to the hand, and consequently, SMA has been used to actuate them. These devices have also been integrated into virtual reality environments in some cases.

In summary, different designs, actuators, manufacturing systems, modeling, and controls have been analyzed in soft robotics, proposing improvements and new designs in different cases.

Resumen

Este trabajo estudia los robots blandos en sus diferentes campos de aplicaciones. La robótica soft es un campo relativamente nuevo de la robótica que es caracterizado sobre todo por el uso de materiales blandos que permiten obtener robots más flexibles, que se adaptan mejor a su entorno y que interactúan de forma más segura con las personas. A pesar de presentar muchas ventajas, su propia flexibilidad y capacidad de deformarse antes de esfuerzos externos hacen que su modelado y control sea considerablemente más complejo que en el caso de los robots convencionales. Este trabajo empieza ofreciendo un actualizado estado del arte sobre los robots blandos, proponiendo una definición de los mismos y subdividiéndolos en cuatro grandes grupos: bio-inspirados, manipuladores, grippers, y wearable. Para cada uno de estos grupos se presentan los diferentes prototipos realizados, presentando el diseño y el control empleados en cada ocasión. En algunos casos se compara el uso de actuadores más convencionales como motores, con otros que se adaptan mejor a los prototipos blandos como las SMA (Shape Memory Alloy). El uso de las SMA supone un reto añadido en el ya complejo mundo de la robótica blanda por su complicado control.

Con respecto a los robots bio-inspirados se presentan los desarrollos de una estrella de mar y de una medusa actuados con SMA y un estudio preliminar sobre plantas robóticas. Con respecto a los robots manipuladores se presentan dos prototipos, ambos continuos y blandos, pero actuados en un caso con motores y en el otro con muelles de SMA. Con respecto a las garras se presenta la comparación de cuatro diferentes soluciones de garras blandas, analizando las ventajas y defectos de cada una y habiendo elegido en este caso actuadores neumáticos y motores. Por último, con respecto a los dispositivos vestibles se presenta el desarrollo de diferentes prototipos que se pueden dividir en dos categorías: los dispositivos hapticos y los exoesqueletos. En todos los casos se trata de guantes cuyo fin es la rehabilitación de la mano. Por ende, el objetivo principal es proponer prototipos que sean ligeros y se adapten mejor a la mano, y en consecuencia para actuarlos se ha empleado SMA. En algunos casos estos dispositivos han sido también integrados en entornos de realidad virtual.

En resumen, se han analizado diferentes diseños, actuadores, sistemas de fabricación, métodos de modelado y controles en el ámbito de la robótica blanda, proponiendo mejoras y nuevos diseños en los diferentes casos.

Contents

Acknowledgments.....	i
Abstract.....	iii
Resumen.....	iv
Contents.....	v
List of Figures.....	vii
List of Tables.....	xiv
Acronyms	xv
1. Introduction	1
1.1 Background and motivation	2
1.2 Objectives	4
1.3 Organization of this work	5
2. State of the Art.....	6
2.1 What is a soft robot?	7
2.1.1 Definition of Soft Robot	7
2.2. Classification according to applications	9
2.2.1 Bio-Inspired Robots and locomotion	9
2.2.2 The Manipulator Robots.....	9
2.2.3 The Soft Grippers.....	10
2.2.4 Medical and wearable robots.....	10
2.3. Design and manufacture of soft robots	15
2.3.1. Materials	16
2.3.2. Actuators	16
2.3.3. Sensors	20
2.3.4. Electronics.....	21
2.3.5. Power supplies	21
2.3.6. Manufacturing	21
2.4. Design, Modeling, and Control	23
2.4.1 Design.....	23
2.4.2. Modeling and simulation.....	24
2.4.3. Control.....	27
2.5 Conclusions.....	29
3. Shape Memory Alloys actuators	30
3.1 Shape Memory Alloys	31
3.2 Fabrication of SMA springs	37
3.3 Finite Element Analysis of SMA springs.....	40
4. Bio-inspired soft robots	44
4.1 State of the art	45
4.2 Asforb, a bio-inspired soft robotic starfish	47
4.2.1 Choice of movement patterns.....	50
4.2.2 First method: constant pulses	51
4.2.3 Second method: impulses sent to individual limbs.....	53
4.2.4 Results.....	57
4.3 JellyRobcib, a soft jellyfish	59
4.3.1 Design.....	59
4.3.2 Modeling.....	61
4.3.3 Control.....	65
4.3.4 Experiments.....	69

4.3.5 Thermal Maps Generated through Path Tracking	70
4.3.6 Results.....	71
4.3.7. Conclusions	73
4.4 Plant-inspired design for explorative soft robots.....	74
4.5 Discussion.....	77
5. Soft robotics manipulators	78
5.1 State of the art	79
5.2 Kyma, a tendon-driven soft robot.....	83
5.2.1 Design.....	83
5.2.2 Modeling.....	86
5.2.3 Models validation.....	91
5.2.4 Teleoperation	94
5.2.5. Conclusions	103
5.3 Ruān, a continuous soft manipulator	105
5.3.1 Design.....	106
5.3.2 Open-loop control	113
5.3.3 Towards a closed-loop control.....	117
5.3.4 Conclusions	128
6. Soft Grippers	129
6.1 Introduction.....	130
6.2. State of the Art.....	130
6.3 Mechanical Design of Grippers	131
6.3.1. Pneumatic System	131
6.3.2. Electromechanical System	134
6.4. Experiments	136
6.5. Results	139
6.6. Conclusions.....	143
7. Wearable soft robots.....	145
7.1 State of the Art.....	146
7.2 Haptic gloves	151
7.2.1 Force haptic glove	151
7.2.2 Tactile, haptic gloves	163
7.2.2.2 Control.....	167
7.3 Exoskeletons.....	168
7.3.1 Superficial Electromyography Sensors	168
7.3.2 First exoskeleton prototype	170
7.3.3 Second exoskeleton prototype	178
7.4 Virtual Reality for wearable soft robots.....	183
6.4.1 Games.....	184
6.4.2 Experiments.....	186
6.4.2.3 Experiments with tactile, haptic gloves.....	192
6.5 Discussion.....	194
8. Conclusions	195
8.1 Conclusions.....	196
8.2 Contributions	197
8.3 Achievements	197
8.4 Repercussions.....	199
8.5 Future Research Lines.....	199
9. References	200

List of Figures

Figure 1.1 Number of articles related to “soft robotics” or “soft robots” in the last 25 years. Source: Web of Science (Access Date: 03/08/2021).....	2
Figure 1.2 Diagram of the top ten countries for publications in soft robotics and the top 20 research center. In the case of Germany and Canada, there are no research centers in the top 20. In the case of France, it appears at 11th position, and the Centre National de la Recherche Scientifique (CNRS) appears at 13th position in the top 20.....	3
Figure 2.1 Scheme of the classification of robots according to their flexibility and adaptability. From left to right: the Schunk LWA robotic arm [13], MACH I [14], the OctArm [4], a hybrid robot [15], the JellyRobcib [16], the starfish [17], and the tentacle [18].	8
Figure 2.2 Scheme of the main applications of soft robots. Clockwise. Continuous and Soft Manipulators: Octopus Arm [65], OctAir [4], arm with PAM [66]. Medical and wearable: rehabilitation glove [67], endoscope [68], support valves heart [49]. Bio-inspired: Octopus [69], starfish [22], and caterpillar [23]. Grippers: jamming gripper [70], pneumatic gripper [38], soft gripper [71].	11
Figure 2.3 Scheme of the main materials and actuators used in soft robotics.	16
Figure 2.4 Scheme of the modeling strategies for soft robots.	27
Figure 2.5 Scheme of the control strategies for soft robots.	28
Figure 2.6 Scheme of the uses of ML techniques in soft robotics.	28
Figure 3.1 Number of articles related to “shape memory alloys” in the last 32 years. Source: Web of Science (Access Date: 30/11/2021).	31
Figure 3.2 Diagram of the top fifteen countries for publications in SMA (1º China, 2º USA, 3º Japan, 4º Germany, 5º Russia, 6º France, 7º India, 8º Spain, 9º Italy, 10º South Korea, 11º Iran, 12º Canada, 13º England, 14º Poland, 15º Australia)	31
Figure 3.3 Main categories of publications. Source: Web of Science (Access Date: 30/11/2021).	32
Figure 3.4 Crystal structure of martensite (a) and austenite (b).[284]	32
Figure 3.5 Transformation temperatures in shape memory alloys. [286]	33
Figure 3.6 Representation of the thermo-mechanical behavior of an SMA, showing the dependency among temperature, T, stress, σ, and strain, ε, and the related crystal structures.[287]	33
Figure 3.7 Fatigue behavior [291].....	34
Figure 3.8 Comparison of different actuators technologies [291]	35
Figure 3.9 Adapted from [292] The power/weight ratio versus the weight of different actuation technologies.	35
Figure 3.10 One-way shape memory effect in a Nitinol spring.	36
Figure 3.11 Bias spring concept.....	36
Figure 3.12 A load-deflection diagram for the SMA spring and bias spring in the two-way SMA actuator.[295]	37
Figure 3.13 Geometric parameters of SMA spring	38
Figure 3.14 Nitinol wire constrain in a screw with two nuts.....	39
Figure 3.15 Air furnace used.....	39
Figure 3.16 Model of the SMA spring (a) the geometrical model and boundary conditions, (b) finite element model (SOLID185 elements).	42
Figure 3.17 Deformed shape compared with undeformed shape. (a) spring at the initial step 0, (b) deformed spring after step 1, (c) the spring recovers its shape after heating.	42
Figure 3.18 SMA spring analysis. (a) the force applied for each step, (b) thermal conditions applied for each step, (c) total deformation.	43
Figure 4.1 (a) The multigait soft robot [75] (b) The SMSs starfish [110] (c) Starfish with SMA springs [328] and (d) the quadrupedal starfish robot [105]	45

Figure 4.2 (a) Bell-shaped mechanism that generates a contraction. (b) Jellyfish actuated by spring retraction. (c) Jellyfish act pneumatically. (d) Jellyfish capable of performing only vertical movements using a shape-memory alloy (SMA)	46
Figure 4.3 From the starfish to Asforb. (a) Forbes Seastar. (b) Asforb underside. (c) Asforb topside.....	47
Figure 4.4 Mold. (a) CAD model of the mold. (b) the 3D printed mold	48
Figure 4.5 Scheme of the primary electrical circuit	48
Figure 4.6 The electric circuit for the five limbs.....	49
Figure 4.7 The final circuit.....	49
Figure 4.8 Detail of the connection between the SMA and the cable. (a) Topside view. (b) Underside view.....	49
Figure 4.9 Graph of the variation of the contraction speed with the amperage supplied to a 0.3 mm spring.....	50
Figure 4.10 Scheme of the two possible activation modes	50
Figure 4.11 Movement patterns realized by Aforb from Step 1 (a) to Step 5 (f).....	51
Figure 4.12 Drag movement. (a) The two limbs contract and (b) drag the body	51
Figure 4.13 Experiment with constant pulses	52
Figure 4.14 PWM signals send to each limb during a cycle in the case of constant pulses..	53
Figure 4.15 PWM signals send in each step to each limb and their repetition during a cycle	54
Figure 4.16 PWM signals send in each step to each limb during a cycle.....	54
Figure 4.17 Graph Time-Position of two different experiments.	57
Figure 4.18 PWM signals sent to each limb during a cycle in the case of paired pulses	58
Figure 4.19 Graph Time-Position of the experiment realized with paired pulses	58
Figure 4.20 Chrysaora jellyfish movement cycle. (a,b) correspond to the state of relaxation, and (c,d) correspond to the rapid contraction phase.....	59
Figure 4.21 Computer-assisted design (CAD) model implemented in Solidworks: (a) cross-section of the CAD model. (b) Robotic jellyfish implemented inside the test pool. (c) 3D-printed mold. (d) Extended body.....	60
Figure 4.22 (a) Manufacturing of the SMAs. (b) Detailed section of encapsulated lateral SMA	60
Figure 4.23 Simulation of the jellyfish body displacement when the central SMA contraction is applied: (a) before contraction; (b) after the central contraction; (c) after lateral contraction.....	61
Figure 4.24 Responses to parametric modeling to a reference. (a) Contraction of the jellyfish bell. (b) Force produced by the SMA	62
Figure 4.25 Diameter of the jellyfish bell variation comparison.	62
Figure 4.26 Representation of fluid displacement during jellyfish contraction using the Solidworks-Flow Simulation plug-in: (a) vertical displacement—speed (m/s); (b) lateral displacement—speed (m/s); (c) vertical Acceleration (cm/s ²); (d) lateral acceleration.....	63
Figure 4.27 Comparison of the volume ejected, using CFD and the analytical model.	65
Figure 4.28 Experimental assembly of the system for the execution of tests.....	66
Figure 4.29 Interface for control and configuration in MATLAB	66
Figure 4.30 Fuzzy Control loop, two inputs, and three outputs	67
Figure 4.31 The three figures show the jellyfish overlap during the movement along the entire trajectory and the central point of the jellyfish in each moment. Movements developed: (a) vertical displacements; (b) lateral displacements; (c) trajectory composed of several points.	68
Figure 4.32 Experimental kinematic parameters based on vertical displacement. (A) Shows the 3D traveled trajectory; (B) Shows the jellyfish positions along the path; (C) Shows x position; (D) Shows y position; (E) Corresponds to x speed; (F) Shows y speed	69
Figure 4.33 Experimental kinematic parameters based on horizontal displacement. (A) Shows the 3D traveled trajectory; (B) Shows the jellyfish positions along the path; (C)	

Shows x position; (D) Shows y position; (E) Corresponds to x speed and red rectangles are the electrical pulses given; (F) shows y acceleration.	70
Figure 4.34 Thermal maps generated from the thermic measurements with the robotic jellyfish: (a) map with a thermal focus on the upper central part; (b) map with two thermal bulbs in the upper corners.	71
Figure 4.35 (Column A) Comparison of movements and variables of robotic jellyfish developed, compared to jellyfish species: (Column B)[139] <i>Sarsia</i> sp.; (Column C) <i>Proboscidactyla flavigerrata</i> ; (Column D) <i>Mitrocoma cellularia</i>	71
Figure 4.36 Comparison of movements and variables of robotic jellyfish developed.	72
Figure 4.37 Tendril-like soft robot able to climb [340]....	74
Figure 4.38 First design proposal. The black parts represent the functional material, while the green one the inactive structure. In (a), the functional material is perpendicular to the structure, while (b) is inclined 45°.	75
Figure 4.39 Design based on origami. The incomplete cuts represent weakness along which fold the structure.	75
Figure 4.40 Final proposal design.	76
Figure 5.1 Elephant's trunk by Hannan and Walker [238].	79
Figure 5.2 (a) Tendril, made by NASA to perform minimally invasive tasks in space [349]. (b) ET ARM, actuated by artificial muscles [350].	80
Figure 5.3 Robot with 25 DoF for inspection and reparation tasks in wind turbines [352] .	80
Figure 5.4 Air-Octopus, a continuous manipulator robot with multiple sections [30]	81
Figure 5.5 Octarm V, a soft robot inspired in an octopus tentacle [4].....	81
Figure 5.6 Bionic Handling Assistant (BHA) is a pneumatic soft robot with high dexterity made by Festo [31].	82
Figure 5.7 (a) Soft robot inspired in a tentacle [103]. (b) Continuous and soft hyper-redundant robot composed by a braided cover and actuated by SMAs [18].	82
Figure 5.8 (a) Mechanical model of the soft manipulator Kyma, composed by four equispaced modules actuated by tendons. (b) Detail section of one module. Dimensions in centimetres.	83
Figure 5.9 (a) The soft bellow used to realize Kyma's structure. (b) The CAD bellow model used in later simulations and mechanical design.....	84
Figure 5.10 (a) CAD model of the ring connection (b) Detail of the connection between two bellows	84
Figure 5.11 (a) First design of discs (b) The final design of discs	84
Figure 5.12 (a) Custom-designed pulley (b) The assembly between the pulley and the motor (c) Pulleys assembled in Kyma structure	85
Figure 5.13 Different configurations to distribute the cables in a single module. The same color dots represent the movement of a motor and a cable in two directions; the black axis represents independent actuation rotations, and the orange one the combination of all of them.	85
Figure 5.14 The actuation box with the 12 stepper motors divided in two levels	85
Figure 5.15 Framework of Kyma modeling.....	87
Figure 5.16 (a) Full-order deformation mesh with 120000 tetrahedra, infeasible for real-time applications. (b) The heuristic method adapts a model with 1650 elements to match the real robot behavior. (c) The Model Order Reduction decreases the number of state variables of the model to 1886 while retaining its original characteristics	88
Figure 5.17 The multi-model representation in SOFA.....	89
Figure 5.18 Actuation system based on three tendons per section. (a) Not actuated, (b) side view of the left-tendon displacement and (c) multiple-tendon displacement.	90
Figure 5.19 Transmission system based on (a) tendons without guidance and (b) the same system restricted to the robot morphology.....	90
Figure 5.20 Difference between (a) the real robot behavior with physical restrictions, (b) the undesired model without self-collision restrictions, and (c) the simplified collision model based on two different subsets.	90

Figure 5.21 Front and perspective view of the Kyma model interacting with its supporting structure in a zero-gravity environment and with an object.	91
Figure 5.22 Three of a total of twelve infrared-sensitive passive markers used by the motion capture system to obtain the robot pose.....	92
Figure 5.23 Comparison of a single test of the real robot (left) versus the obtained model (right).	92
Figure 5.24 Real robot workspace representation for 100 iterations and validation of the FEM model. The absolute error is compared to the maximum Euclidean distance of the robot from a non-actuated pose.....	93
Figure 5.25 Bilateral scheme for the robot teleoperation.	94
Figure 5.26 Kyma	95
Figure 5.27 Conventional interface.	96
Figure 5.28 Immersive interface.....	96
Figure 5.29 Controller strategy.	97
Figure 5.30 Master-slave.....	97
Figure 5.31 Local gestures strategies.....	98
Figure 5.32 Remote gesture strategies.....	98
Figure 5.33 Voice commands strategy.....	99
Figure 5.34 Hybrid approach of gestures and voice recognition.....	99
Figure 5.35 Results for the human-robot interfaces test. (a) Efficiency in terms of precision and time, (b) situational awareness, (c) subjective visual feedback, and (d) subjective preference	100
Figure 5.36 Results for the interaction-tools test. (a) Efficiency in terms of precision and speed, (b) workload, (c) subjective preference, (d) subjective importance of variables in workload, (e) subjective and objective performance comparison, and (f) previous experience influence in performance	101
Figure 5.37 Previous experience influence efficiency both for the human–robot interfaces and the interaction tools experiments	102
Figure 5.38 Ruǎn.....	105
Figure 5.39 SMA springs disposal	105
Figure 5.40 Motion of range of a segment	106
Figure 5.41 Motion range of three segments.	106
Figure 5.42 Discs.....	107
Figure 5.43 Disc with magnets and stops (a) CAD model (b) Real disc	107
Figure 5.44 Rod and disc structure.....	107
Figure 5.45 The silicone segment	108
Figure 5.46 Power cables connection.	108
Figure 5.47 Springs manufacture	109
Figure 5.48 Tests segment length.....	111
Figure 5.49 (a) controlled bending of the segment b) Appearance of folds at the base of the segment. c) Fully bent segment with folds.....	112
Figure 5.50 Electric circuit.....	112
Figure 5.51 Vision system setup	113
Figure 5.52 Tests	114
Figure 5.53 Folds in the silicon body during actuation.	114
Figure 5.54 Free-end positions.....	115
Figure 5.55 First end segment positions	115
Figure 5.56 User interface.....	116
Figure 5.57 (a) User and (b) development menus.....	117
Figure 5.58 Mappings in constant curvature kinematics [364]	117
Figure 5.59 Kinematic modeling using PCC approach.	118
Figure 5.60 Hypothetical rigid link model of a flexible robot [365]	119
Figure 5.61. Design and kinematic modeling framework for soft robotic systems.....	119
Figure 5.62 Simplified design of the discs.....	120

Figure 5.63 Simplified section of the body	120
Figure 5.64 Tendons inside the body	121
Figure 5.65 Segment simulation with folds	121
Figure 5.66 Desired behavior of tendons.....	122
Figure 5.67 Tendons penetration.....	122
Figure 5.68 On the left boundary condition in simulation. On the right, joints and displacements in the threads.	123
Figure 5.69 Deformation of the soft body of the robot under the action of the threads.	124
Figure 5.70 Paths of deformed nodes.	124
Figure 6.1 Pneumatic system. a) Connection diagram. b) Wiring diagram control. Signals 1, 2, and 3 are the cables the connect to the UR3 for control.....	131
Figure 6.2 First gripper. (a) CAD model, (b) Gripper during the operation, (c) Fingers flexed, (d) and Fingers in extension.....	132
Figure 6.3 Mold for manufacturing silicone fingers: (a) Mold for inner side, (b) Mold for outer side, (c) Male mold, (d) The assembled mold.....	133
Figure 6.4 Second gripper: (a) CAD model of the gripper, (b) Gripper during the operation.	133
Figure 6.5 Wiring diagram of the electromechanical system.	134
Figure 6.6 Third gripper: (a) CAD model of the gripper, (b) Real Gripper.	135
Figure 6.7 Fourth gripper: (a) CAD model of the gripper, (b) Gripper during the operation.	136
Figure 6.8 Test execution: the gripper picks up one of the twelve objects in a predetermined position and place it in the desired location.....	137
Figure 6.9 Selection of objects for experimentation with its identification number. (a) Tennis ball #1, (b) Screen Cleaner #2, (c) Vaseline Container #3, (d) Metallic Container #4, (e) Nut #5, (f) Rock #6, (g) Tomato #7, (h) Egg #8, (i) Glue Stick #9, (l) Dish Sponge #10, (m) Broccoli #11, and (n) Candy Box #12.	137
Figure 6.10 Test execution with Gripper 1 (a,b), Gripper 2 (c,d), Gripper 3 (e,f), Gripper 4 (g,h).	138
Figure 6.11 Summary of test results for the four grippers in the three environments.	141
Figure 6.12 Graphics comparison between (a) Gripper 1 and Gripper 4. As can be seen from the graph, the two grippers generally have similar performances. (b) Gripper 2 and Gripper 3. These are the two grippers with the worst performances, and each one proved to be suitable only for a specific type of object. (c) Graphic comparison between Gripper 1 and Gripper 2 (the two pneumatic grippers). As can be seen from the graph, Gripper 1 works significantly better than Gripper 2. (d) Graphic comparison between Gripper 3 and Gripper 4 (the two mechanic grippers). As can be seen from the graph, Gripper 3 works significantly better than Gripper 4.....	142
Figure 7.1 (a) [407] (b) [408] (c) [409] (d) [411] (e) [412] (f) [414]	147
Figure 7.2 The two principal parts of the haptic glove. (a) Glove made of elastic fabric. (b) 3D printed finger cap (c) Flexible stretch sensors (d) Arduino UNO (e) electronic circuit for SMA control (f) electronic circuit for stretch sensors.	151
Figure 7.3 SMA-spring actuators (a,b) The idea as illustrated in [16] (c) the idea as implemented in our work	152
Figure 7.4 (a) Finger fully stretched (minimum distance between upper joint area). (b) Bent finger (maximum distance between the upper part of the joints).	153
Figure 7.5 Final Haptic Glove.....	154
Figure 7.6 General schematic in LTspice.....	154
Figure 7.7 Code flow diagram in Arduino.	156
Figure 7.8 General setup for the experimental characterization of the SMA spring. (a) Scheme (b,c) Reality.....	156
Figure 7.9 Results of the sensor characterization tests for the Resistance–Weight function elaboration with the equation of the line and correlation coefficient.....	157

Figure 7.10 Weight vs. time graph for a 15 s test, and a demanded weight of (a) 50 g (b) 100 g (c) 150 g (d) 200 g	158
Figure 7.11 Weight vs. time graph for the glove test with a simulated weight of 100 g.....	159
Figure 7.12. Weight vs. time graph for the glove test with a simulated weight of 150 g....	159
Figure 7.13 The three parts of the vibrotactile glove: (a) thimbles, (b) palm, and (c) armband	163
Figure 7.14 Thimble design.....	164
Figure 7.15 Final version of the vibrotactile glove (a) dorsal view and (b) palm view	164
Figure 7.16 Vibrotactile glove electric circuits.....	164
Figure 7.17 The thimble (a) The final version worn by a user (b) Cad model (c) Section view	165
Figure 7.18 Actuation unit.....	166
Figure 7.19 Electric circuit	166
Figure 7.20 Final design of the SMA haptic glove.....	166
Figure 7.21 State diagram of SMA-haptic glove control	167
Figure 7.22 Scheme of the different muscles in the forearm.....	169
Figure 7.23 Correct placement of electrodes [450]	169
Figure 7.24 EMG sensors (a) the one used in the first exoskeleton and (b) the Myoware sensor used in the second prototype	170
Figure 7.25 Hand structure and joints [435]	171
Figure 7.26 (a) Finger kinematics [453] (b) Physiological structure of finger [454].....	171
Figure 7.27 The four-bar linkage structure	172
Figure 7.28 Dynamical simulation of the index finger.....	173
Figure 7.29 Support element S1	174
Figure 7.30 The supports (a) S2 and (b) S3.....	174
Figure 7.31 The tendon connection scheme	175
Figure 7.32 The final prototype (a) CAD model (b) the building model	175
Figure 7.33 The final prototypes with the SMA springs connected (a) top view (b) lateral view	175
Figure 7.34 Integration set-up of the mechanical structure, actuators, and electronic circuit	176
Figure 7.35 (a) EMG sensor placed on forearm volunteer (b) the electrical scheme.....	176
Figure 7.36 EMG signal from the extensor fascicle muscle on a healthy volunteer. Two muscular activations are withdrawn: at 13-17 seconds and 20-24 seconds.....	177
Figure 7.37 Complete set-up of the exoskeleton	178
Figure 7.38 The following design of 4-bar linkage structure	178
Figure 7.39 Detail of the sewn cable (a) dorsal view (b) palm view	179
Figure 7.40 3D printed parts (a)the upper part, (b) the lower part, and (c) the palm part	179
Figure 7.41 Final prototype.....	180
Figure 7.42 Graphic values seen for the user: the signal (in blue), the mean of the signal (in red), the cycle duration of the peak (in green), and the duty cycle (in yellow).	182
Figure 7.43 Framework of virtual reality for wearable soft robots	183
Figure 7.44 Tactile, haptic glove scenarios (a) Box game (b) Donuts game and (c) Keyboard	184
Figure 7.45 The airplane game	185
Figure 7.46 The piano game.....	185
Figure 7.47 Virtual Reality Experiments.....	186
Figure 7.48 Games evaluation	188
Figure 7.49 Comparison between the two games	188
Figure 7.50 Basic exercise with soft exoskeleton (a) Extension of the fingers (b) Gripping task	189
Figure 7.51 Basic exercise with the torus shape	190
Figure 7.52 Soft glove exoskeleton tested with virtual reality	190

Figure 7.53 User's perspective. The screen on the left shows the EMG signal while the screen on the right the VR game.	191
Figure 7.54 General aspects of the experience, as before (1 - Totally disagree, 2 - Strongly agree)	191
Figure 7.55 Experiments with the vibrotactile glove and VR.....	192
Figure 7.56 Comparison between the two haptic devices from the point of view of usability.	193
Figure 7.57 VR game that provides the best haptic sensation	193
Figure 8.1 The different prototypes of soft robots developed. Soft Manipulators: Aeruca Robot [462], Kyma, and Ruān. Wearable soft robots: haptic force glove [406], haptic tactile glove, and exoskeletons. Soft grippers [368] Bio-inspired soft robots: the starfish Asforb, JellyRobcib [16], and soft plant.....	196

List of Tables

Table 2.1 Comparison of the characteristics, capabilities, realization process, and main application of the different groups of robots (Hard robots, Adaptable Robots, Mixed Soft Robots, Soft Robots). Adaptability and safe interaction increase from hard robots to soft ones, while the precision, speed, and loading capacity decrease. Design, modeling, and control are defined as “easy” for hard robots as the problem is well-known. In the case of applications, only real or commercial products are considered applications, not the different prototypes developed. Moreover, only the principal application is cited as the most significant	7
Table 2.2 Summary of bio-inspired soft robots	12
Table 2.3 Summary of manipulators soft robots.....	13
Table 2.4 Summary of soft grippers. The following grippers subdivision is based on that shown in [44] F = force, W = weight, S = speed or gripping time	14
Table 2.5 Summary of medical and wearable soft robots.....	15
Table 2.6 The main actuators in soft robotics. The material (P = Polymers, E = Elastomers, F = Fluids), the advantages, the disadvantages, and some real applications are presented for each actuator. As in Table 2-5, only real applications are taken into account.	19
Table 2.7 Principal 3D printing technology with the operation principle and the advantages and disadvantages.	23
Table 3.1 Nitinol springs’ characteristics.....	41
Table 3.2 Material parameters used for simulation of SMA helical spring.....	41
Table 4.1 Comparison of material properties between Ecoflex 00-30 and Silastic 3483	47
Table 4.2 First attempt to implement the control by impulses sent to individual limbs.....	55
Table 4.3 Second attempt to implement the control by impulses sent to individual limbs ..	55
Table 4.4 Third attempt to implement the control by impulses sent to individual limbs	55
Table 4.5 Fourth attempt to implement the control by impulses sent to individual limbs ..	56
Table 4.6 Last attempt to implement the control by impulses sent to individual limbs	56
Table 4.7. Rules for the fuzzy controller, with two inputs (errors) and tree outputs <i>SMAR – C – L</i>	67
Table 4.8 Variables measured from a data set of experimental tests of Figure 4.29 movements.(No CT = Number of Contractions).....	68
Figure 18 shows a compendium of results (3 tests of the whole dataset from Table 4.9 are shown); the results of the analysis made by MATLAB are shown when establishing a target point (in blue) for all cases, to evaluate the results and obtain the values of accuracy and repeatability.	72
Table 5.1 Main node hierarchy and a bullet list of the principal components to model Kyma in the SOFA environment alongside their descriptions.	87
Table 5.2 Main parameters of Kyma to construct the FEM model and a heuristic adjustment to decrease the computational cost.	88
Table 5.3 Analysis of the model thickness versus the number of FEM elements.	89
Table 5.4 Validation results of the FEM Model for 100 random pose iterations.....	93
Table 5.5 Tendons displacements. Configuration A.	123
Table 5.6 All possible activation combinations	123
Table 5.7 Comparison of the displacement ranges between the second segment of the flexible robot and the simulation.	126
Table 5.8 Total displacement of the free end of the robot.	126
Table 5.9 Comparison of neural network results for the first segment.	126
Table 5.10 Comparison of neural network results for the second segment.	127
Table 6.1 Selection of objects for experimentation. Each object has been assigned a number to facilitate the subsequent display of results (first column). The “Dimensions” column shows the significant dimensions of each object, and the “Weight” column shows the weight	

of the objects used in the experiments. In the last column, “Relevant Aspects,” the aspects that differentiate each object from the others are highlighted.....	138
Table 6.2 Experiments with Gripper 1. On the left, the table with a success rate for every object, in the last column, the average for every object is calculated, and at the end of the table, the average success rate for every environment is determined. On the right, the graphic representation of Table 2 is reported.....	139
Table 6.3 Experiments with Gripper 2. On the left, the table with the success rate for every object, in the last column, the average for every object is calculated, and at the end of the table, the average success rate for every environment is determined. On the right, the graphic representation of Table 3 is reported.....	140
Table 6.4 Experiments with Gripper 3. On the left, the table with the success rate for every object, in the last column, the average for every object is calculated, and at the end of the table, the average success rate for every environment is determined. On the right, the graphic representation of Table 4 is reported.....	140
Table 6.5 Experiments with Gripper 4. On the left, the table with the success rate for every object, in the last column, the average for every object is calculated, and at the end of the table, the average success rate for every environment is determined. On the right, the graphic representation of Table 5 is reported.....	140
Table 7.1 Results of questions about general aspects in a scale of 0 to 10 (where 0 = worst, 10 = best).....	160
Table 7.2 Results of tests.....	161
Table 7.3 Simulation values.....	172
Table 7.4 Dimensions of index finger bars	173
Table 7.5 Dimensions of middle finger bars.....	173
Table 7.6 Score Piano Game.....	186
Table 7.7 Score Airplane Game.....	187
Table 7.8 Results concerning general aspects (1-Low, 10-High)	187

Acronyms

2D/3D/4D	Two/Three/Four Dimensional
2PP	2-photon polymerization
ABS	Acrylonitrile butadiene styrene
AM	Additive Manufacturing
ANN	Artificial Neural Network
AR	Augmented Reality
BHA	Bionic Handling Assistant
CAD	Computer-Aided Design
CAE	Computer-aided engineering
CFD	Computational Fluid Dynamics
CLIP	Continuous Liquid Interface Production
CNN	Convolutional neural network
DEA	Dielectric Elastomer Actuators
DFT	Density Functional Theory
DIW	Direct Ink Writing
DLP	digital light processing
DoF	Degrees of Freedom
EAP	Electroactive Polymers
EMG	Electromyography
ERM	Electro-rheological material
FDM/FFF	Fused Deposition Modeling
FEA	Finite Element Analysis
FEM	Finite Element Method
FF	Feedforward neural network
FFA	Flexible fluidic actuators
HMD	Head-Mounted Display
ICPF	Conductive ionic polymer film
IMU	Inertial Measurement Unit
IPMC	Ionic polymer metal compounds
kNN	k-Nearest Neighbors
LCE	Liquid Crystal Elastomers
LM	Leap Motion
MD	Molecular Dynamics
MIS	Minimally Invasive Surgery
MJ/MJM	Material Injection
ML	Machine Learning
MOR	Model Order Reduction
MRM	Magneto-rheological material
NiTi	Nitinol
ODE	Ordinary Differential Equations
PAM	Pneumatic Artificial Muscle
PBF	Powder Bed Fusion
PCB	Printed circuit board
PCC	Piecewise Constant Curvature
PDMS	Polydimethylsiloxane
PETG	Polyethylene terephthalate glycol
PID	Proportional Integral Derivative
PLA	Polylactic acid
POD	Proper Orthogonal Decomposition
PVC	Polyvinyl Chloride
PWM	Pulse with Modulation

RNN	Recurrent Neural Network
SDM	Shape deposition modeling
SDM	Shape modeling
sEMG	Superficial electromyography
SLA	Stereolithography
SLS	Selective Laser Sintering
SMA	Shape Memory Alloy
SMP	Shape-memory polymers
SMS	Smart Modular Structure
SOFA	Simulation Open Framework Architecture
SVM	Support vector machine
TCT	Task completion time
TPE	Thermoplastic Elastomers
TPU	Thermoplastic polyurethane
UHMwPE	Ultra-High Molecular Weight Polyethylene
VR	Virtual Reality



1. Introduction

*"Sometimes I lie awake at night, and I ask,
"Where have I gone wrong?"
Then a voice says to me,
"This is going to take more than one night."*

Charles M. Schulz

This chapter introduces the present work providing information about the background concepts to understand its context and motivation, followed by the pursued objectives and a brief organization of the rest of the chapters of this thesis.

1.1 Background and motivation

The first uses of modern robots were in factories as industrial robots. These robots are designed to carry out heavy tasks and replace man, often in dangerous environments. They realize tasks quickly, precisely, and efficiently, with a high repeatability rate. However, due to their considerable dimensions and weights, they usually operate within the limits of a cage or other enclosure, being potentially dangerous when interacting with humans. Moreover, they only can work in controlled environments and cannot adapt their shape to the objects they interact with.

Hence, the need for robots capable of interacting with the world around them in a new way to apply robots in other fields and tasks where human contact, adaptability, and safe interactions are the most desired characteristics.

Soft robots owe their name because they are mainly composed of intrinsically flexible and remarkably stretchable soft materials capable of easily adapting their conformation to the environment they interact with. This characteristic allows them to function in less structured environments and be less dangerous for people who use them. It is also one of the main reasons that have allowed soft robotics to be especially interesting in medicine to develop devices that directly interact with patients.

The process that brought the soft robots to their current notoriety was quite gradual, although some prototypes can be found in the late 1990s and early 2000s [1,2]. It will not be until 2008 when the words "soft robot" and "soft robotics" will begin to be used quite widely, seeing in the following years, and especially from 2012, a significant increase in the number of publications related to this term, as can be seen in Figure 1.1. This number will increase due to the new technologies and materials developed in the coming years.

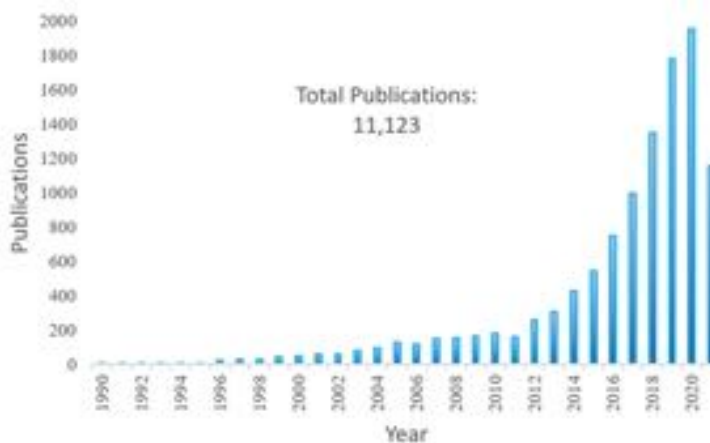


Figure 1.1 Number of articles related to "soft robotics" or "soft robots" in the last 25 years. Source: Web of Science (Access Date: 03/08/2021).

As it is possible to see in Figure 1.2, this research field is considered quite interesting by the principal economies in the world. The diagram shows the top ten countries with their respective research centers. The top ten countries produce more than 90% of soft robotics publications.

In [3], it is possible to find an interesting review about soft robotics' development from the point of view of scientific publications.

The study of soft robots was initially developed mainly inspired by nature. Many animals (especially insects and invertebrates) can realize various movements (swimming, walking, climbing, jumping) and grasp objects with relevant forces, despite not having a bone structure and being composed chiefly of soft tissues. That is why among the prototypes of

soft robots, it is possible to find many examples of bio-inspired robots explored in the following chapter. Other advantages that soft robots tend to have over traditional robots are lightness, simplicity of construction, and low cost. Despite presenting so many benefits, there are still many unsolved problems regarding its control and modeling. The flexibility of the materials that provide so many capacities also represents a challenge in modeling, simulation, and control. On the other hand, it is challenging to imitate nature, and there is still much to study in terms of materials, actuators, and sensors. In this sense, rapid prototyping technologies play a crucial role in their manufacture.

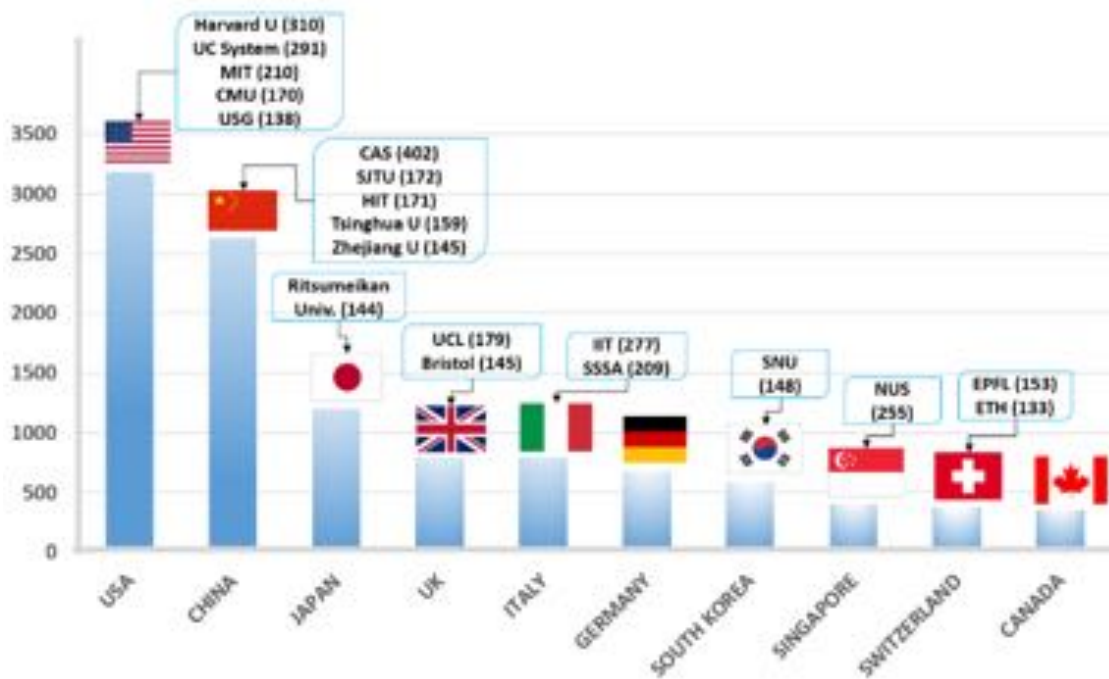


Figure 1.2 Diagram of the top ten countries for publications in soft robotics and the top 20 research center. In the case of Germany and Canada, there are no research centers in the top 20. In the case of France, it appears at 11th position, and the Centre National de la Recherche Scientifique (CNRS) appears at 13th position in the top 20.

This thesis has been developed within this global context, and it is intended to contribute to the development of soft devices that can be applied in real tasks. Nowadays, the majority of them are realized for research purposes and are not fabricated or employed as conventional robots, being relegated to universities and research centers. However, soft robots could become the solution to many tasks that conventional robots cannot realize safely and efficiently in the near future.

1.2 Objectives

The pursued goals in this thesis are organized as follows:

- This work aims to study soft robotics from a generalizable perspective. Thus, a complete state-of-the-art is presented to configure an outlook of the problematics that hinder the development of soft robotics.
- Also, it is essential to precisely define what a soft robot is, so the definition of soft robotics and classifications need to be updated. The following objectives will analyze and propose design solutions, applications, modeling, and control for each group of soft robots identified. The four groups are bio-inspired soft robots, soft manipulators, grippers and, wearable soft robots.
- The principal actuators employed in the prototypes present in this work are actuated with SMA (Shape Memory Alloys) springs. Thus, a complete state of the art is presented to understand the challenges that this type of actuator implies and how they represent an added difficulty in the already complicated world of soft robotics. However, it is considered essential to apply non-conventional actuators to realize soft robots.
- Different prototypes have to be realized to demonstrate the potential of SMA actuators in soft robotics, proposing solutions to their control.
- Previous designs of soft robots have been analyzed to improve them or propose new and more lightweight designs. Materials, sensors, and manufacturing processes aim to realize low-cost prototypes, easy to assemble and reproduce.
- The modeling of soft robotics is approached from different perspectives implemented feasibly modeling strategies.
- Finally, the integration between soft robotics and virtual reality is implemented.

It is essential to highlight that this thesis is very transversal since it is intended to study soft robotics from different points of view and provides contributions to multiple areas of knowledge in this field.

1.3 Organization of this work

This work is structured as follows:

- Chapter 2 presents a complete state-of-the-art soft robotics, providing a definition, a classification, and analyzing the trends and new solutions in their manufacturing. Moreover, the challenges constituted by their design, modeling, and control are presented to comprise better the following problems and solutions proposed.
- Chapter 3 presents a state of the art of the SMA actuators, analyzing their advantages and challenging and motivating their choice to develop the prototypes presented in this work.
- Chapter 4 presents the prototypes of the first group: the bio-inspired soft robots. Here the developments of a starfish and a jellyfish are presented. Also, preliminary work on soft robotics plants is presented.
- Chapter 5 presents the development of two soft manipulators: Kyma and Ruān. Moreover, for each of them, different modeling solutions are proposed.
- Chapter 6 presents the development of four soft grippers. In this case, the aim is to analyze which solution design realizes the most robust and versatile gripper.
- Chapter 7 presents the development of several wearable prototypes divided between haptic devices and exoskeletons. Moreover, the integration of virtual reality with these devices is presented.
- Chapter 8 summarizes the main contributions of the thesis and future research derived from this work.

Chapters 4 to 7 begin with a summarized state of the art about the type of soft robots presented in the corresponding chapter and end with some conclusions about the results obtained. In addition, findings are presented for each prototype shown.



2.State of the Art

*" My definition of an expert in any field
is a person who knows enough about
what's really going on to be scared."*
P.J. Plauger

This chapter presents a complete state of the art of soft robotics. This research field is constantly evolving. A definition is proposed, together with a classification in four main groups. Next, the challenges in materials, actuators, sensors, and electronics are analyzed, and the research lines are presented to understand better how soft robots will evolve in the next future. Finally, all the model and control issues are raised along with the existing solutions.

2.1 What is a soft robot?

In this first section, the meaning of the term “soft robot” will be analyzed, presenting the different definitions that have been developed since it began to be used, and proposing a classification that takes future developments into account. Then the main applications will be presented, dividing them into four groups and providing several prototypes found in the literature.

2.1.1 Definition of Soft Robot

What is a soft robot? If one looks at the published articles that present soft prototypes, it is difficult to answer since it is possible to find from the Octarm [4] to the Meshworm [5]. That is why it is first of all necessary to make a premise: the definition of a soft robot is still under development since the technologies, materials, actuators, and so on that are used to make these robots are being subjected to a great process of innovation, so the definition has to be adapted according to new developments.

Table 2.1 Comparison of the characteristics, capabilities, realization process, and main application of the different groups of robots (Hard robots, Adaptable Robots, Mixed Soft Robots, Soft Robots).
Adaptability and safe interaction increase from hard robots to soft ones, while the precision, speed, and loading capacity decrease. Design, modeling, and control are defined as “easy” for hard robots as the problem is well-known. In the case of applications, only real or commercial products are considered applications, not the different prototypes developed. Moreover, only the principal application is cited as the most significant

	Hard Robots	Adaptable Robots	Mixed Soft Robots	Soft Robots
Characteristics				
DOF, n	$n \leq 6$	$n \geq 12$	$n = \infty$	$n = \infty$
Materials [Pa]	$E = 10^{10} - 10^{11}$	$E = 10^9 - 10^{11}$	$E = 10^4 - 10^{10}$	$E = 10^4 - 10^8$
Flexibility	No	Limited	Infinite	Infinite
Stretchability	No	No	Limited	Near Infinite
Capabilities				
Precision				
Speed				
Loading Capacity				
Adaptability				
Safe interaction				
Realization				
Manufacturing	Traditional Machining	Traditional machining and 3D prototyping	Prototyping 3D and 4D	Prototyping 3D and 4D
Design	Easy	From simple to complex	Complex	Complex
Modeling	Easy	From simple to complex	Complex	Complex
Control	Easy	From simple to complex	Complex	Complex
Cost	High	Medium - High	Medium - Low	Low
Applications				
	Industrials	Manipulation	Medical - Manipulation	Medical

It should also be noted that there are different currents of thought about the aspects taken into account to define a soft robot.

One of the first definitions that can be found of a soft robot is the one presented in [6], according to which robots that present “distributed deformations with theoretically an infinite number of degrees of freedom” can be considered soft. Due to the subsequent development of many bio-inspired prototypes, another definition was proposed in [7,8]. According to this second definition, the word “soft” refers to the robot’s body and therefore divides the materials into soft and not soft according to Young’s Modulus that they present. The range of values used to define soft materials is that of the materials that constitute natural organisms (such as tissues, bones) and present Young’s modulus in the order of $10^4 - 10^9$ Pa. It is the simplest definition to apply and perhaps well suited to define most early bio-inspired prototypes. However, it excludes many others and could be somewhat limited.

Successively in [9], a definition of soft material considering the deformation between the object and its environment was proposed. Hence another definition was presented in [10], which emphasizes stress and the possible damage the robot can exert in its environment. In this case, the environment is part of the definition. According to the authors, an object

could be soft in terms of deformation, but hard for another object with which it comes into contact.

This last definition is quite interesting since many of the robots that are defined as soft still have rigid parts, either in the actuation part or in their internal structure. As will be seen in the following sections, many studies are indeed being carried out to achieve flexible electronics. Moreover, despite having rigid elements, these robots can be considered soft since they can adapt to the environment and interact safely with people.

In this same line of thought, the definition in [11] considers that Young's Modulus is not enough as the only parameter. Its definition (defined for prismatic bars of homogeneous material subject to axial load and small deformations) does not correspond to the usually used soft materials (inhomogeneous, anisotropic, and viscoelastic). Furthermore, it does not consider one of the characteristics of this type of robot: adaptability (or compliance). If this is suitable for the environment in which the robot will have to work, it can be said that it is soft.

This last definition opens a range of possibilities for soft robots since it broadens the definition and allows many types of robots to be included, such as those composed partly of soft materials and parts of more rigid materials to achieve the desired rigidity in this type of structure [12]. However, on the other hand, it includes all those robots that, despite presenting a high degree of adaptability, whether achieved actively or passively, are not made of soft materials.

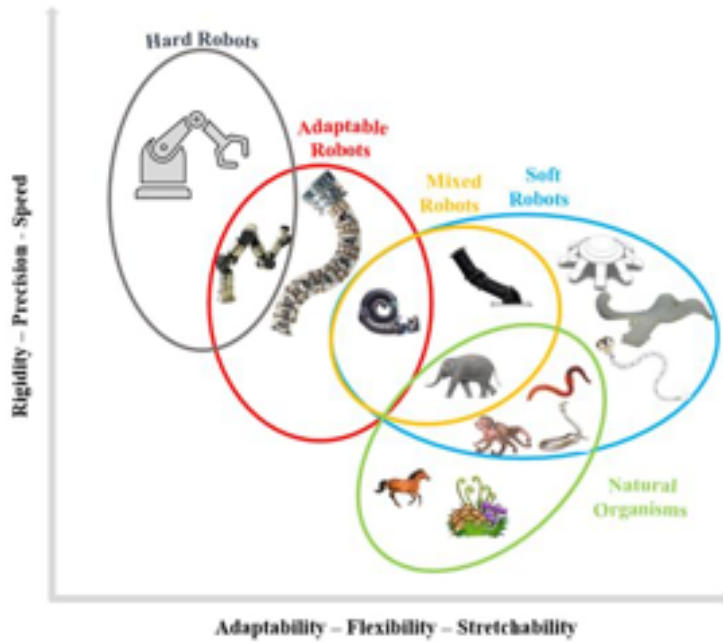


Figure 2.1 Scheme of the classification of robots according to their flexibility and adaptability. From left to right: the Schunk LWA robotic arm [13], MACH I [14], the OctArm [4], a hybrid robot [15], the JellyRobcib [16], the starfish [17], and the tentacle [18].

For this reason, the following definitions are proposed in this article. A robot will be defined as "soft" if made almost entirely of materials with Young's modulus comprised in the ante-specified interval of $10^4\text{-}10^9$ Pa. This characteristic alone ensures that these robots can be deformed (and consequently adapt to the environment) and not harm. A robot will be defined as "mixed soft" if it presents a rigid structure and a soft body. A robot will be defined as "adaptable" if it is a rigid and semi-rigid robot, which can adapt very well to the environment thanks to its configuration and degrees of freedom (as in the case of hyper-redundant robots) [19]. This definition is considered more suitable for future developments

in soft robotics that will employ flexible electronics and new rapid prototyping techniques. As shown in Figure 2.1, mixed robots are halfway between soft robots and adaptable robots, since depending on the rigidity presented, it will be more or less easy to control them. In Table 2.1, these three groups are compared with hard robots, and their characteristics and applications are summarized.

With the improvements in additive manufacturing techniques, integrating rigid and soft materials in the same structure will be improved, the control will likely be more manageable. Consequently, the level of adaptability will be higher and thus the security level. Therefore, adaptability will be a preponderant characteristic of these robots in the future.

2.2. Classification according to applications

Soft robots' classification depends on the definition of soft robots considered since some robots may be excluded. In addition, being a field in full development, many prototypes made do not have any specific application and are simply experiments and testing of materials and actuators. For this reason, four main groups will be considered in this article. Almost all of the prototypes that can be found in the literature can be summarized in these groups. A scheme of this classification is shown in Figure 2.2.

Since state of the art is quite extensive and an article dedicated to each of the following groups would be necessary, only some of the most significant prototypes will be cited, indicating references of papers that treat them more widely for each group.

2.2.1 Bio-Inspired Robots and locomotion

The first group that can be identified is that of bio-inspired robots. This group is probably the most important because it is the study of nature that has driven the development of this new field of robotics since it was the incredible ability of animals to take advantage of their mostly soft structures that caught the attention of researchers. Countless natural organisms have been attempted to reproduce, including earthworms [20], caterpillars [21], tentacles [18], starfish [22], and jellyfish [16]. Thanks to them, rotary locomotion with the GoQBot [23], peristaltic locomotion with the Meshworm [5], underwater locomotion with legs with the PoseiDRONE [24], powered jet swimming [25], have been studied, just to name a few [26].

Something that joins all the previous examples is the fact that the largest invertebrates are found either underwater (octopus, jellyfish) or underground (giant worms), which are environments that support them [27]. That represents a limitation and is also related to the stiffness control problem. However, it is to be expected that in the coming years, better prototypes will be developed thanks to advances in additive manufacturing techniques and efforts to provide these robots with proprioception, that is, the ability to perceive their shape and position in the space, a fundamental notion to be able to interact with the environment [28].

A summary of these robots' current state of the art can be consulted in [29].

2.2.2 The Manipulator Robots

The second group that can be identified is that of continuous robots. Although these robots are markedly bio-inspired by tentacles or trunks, they already constitute a separate group in state-of-the-art [6]. One of the first differences for the first group is that these robots usually have a specific application such as grabbing objects, inspecting inaccessible places, or interacting with humans. In this sense, bio-inspiration is found in the desire to recreate the movement of its natural counterparts.

Not all the prototypes in this group can be considered soft, but they all have great adaptability to the environment thanks to their numerous degrees of freedom (DOF), and thanks to this, they can be considered safe.

Among the most famous prototypes are the Octarm mentioned above [4], an arm made with artificial pneumatic muscles capable of grasping quite large objects such as traffic cones, the Air-Octopus [30], which featured a double pneumatic and tendon actuation, and the Bionic Handling Assistant [31].

These prototypes are focused on adaptability. The successive ones have focused more on using soft materials that are intrinsically adaptable, as in the case of the tentacle [18] or SMA's spring-actuated robotic arm [32].

Thanks to the new materials and actuators used, it has been possible to use this type of robot for medical applications such as endoscopes [33].

Two extensive states of the art on this type of robot can be found in [19,34].

2.2.3 The Soft Grippers

The third group identified is the soft grippers, the most advanced regarding development since many of its prototypes are already being used in the industry. The need for grippers that could not damage the objects they were holding was quite a felt problem in the food and agriculture sector. The soft grippers allow to grasp objects distributing the contact forces and thus avoid leaving marks.

The technologies that allow these grippers to adapt to objects are very varied. The simplest solution is to create the fingers as passive structures formed by several links, actuated with cables and external motors [35,36]. In this case, the gripper is not necessarily soft since its adaptability depends not on the material but the continuous fingers. For this reason, it may not be the best option for handling particularly deformable and delicate objects.

Another possibility is to use passive structures, generally actuated with external motors, made with soft materials that deform when interacting with objects. This solution has proven to be especially valid and used by Festo for its MultiChoice Gripper [37].

Another family of soft grippers used on an industrial level is pneumatic grippers [38]. In this case, the fingers are pneumatic chambers designed so that when they are inflated, they can adapt to the objects. The fingers are generally made of materials such as silicone, which guarantees a lot of flexibility and adaptability.

Other technologies used with very satisfactory results have been electro-adhesion [39] which is especially indicated for the most fragile objects, and which can even be found in combination with pneumatic actuation [40], and jamming [41], which is based on the ability of granular materials to change their rigidity if subjected to vacuum and electroactive polymers [42]. In [43–45], it will be possible to find extensive states of the art of soft grippers.

2.2.4 Medical and wearable robots

The last group that can be identified is medical and wearable robots. It has been decided to join these two groups since the prototypes are designed to interact closely with the human body in both cases. If bio-inspired robots have been the area that initially drove soft robotics, medical robots will drive it in the future. The interest in developing soft robots that can operate, diagnose, administer drugs, perform rehabilitation, be used as prostheses, artificial organs, and organ simulators is enormous [46]. The possibilities seem endless, and it may be witnessing a paradigm shift in healthcare since they provide high safety (they will absorb mechanical loads without passing them on to the patient). Although they still

have a long way to go to be widely used in hospitals, some prototypes are already used for minimally invasive surgeries (MIS) [47]. In particular, soft robots allow the development of better endoscopes since they are intrinsically safe and reduce the possibility of damaging the tissues and organs of patients. In addition, they present higher maneuverability than traditional solutions, a fundamental characteristic in this type of application. In [33], a relatively actualized state of the art on soft endoscopes is presented.

They are already beginning to be used for drug delivery, which is especially useful when the medication needs to reach a remote part of the body, such as the brain, since it would not damage the tissues [48]. However, there are many unresolved issues regarding materials and control.

The most interesting applications are creating artificial organs [49] and body parts for simulations and research [50].

Wearable devices are also attracting significant interest, not only rehabilitation devices such as exoskeletons and prosthetics [51–55], but also haptic devices integrated with virtual reality [56–59]. It is due, among other things, to the lightness and portability that distinguishes these soft devices from those previously developed. These characteristics generate in the user more comfort and less physical fatigue. In addition, they are easier to put on and take off and are safer for users.

In state-of-the-art, it is possible to find numerous articles that collect information, prototypes, challenges of soft medical robotics [51,60–62], and soft wearable prototypes [63,64].

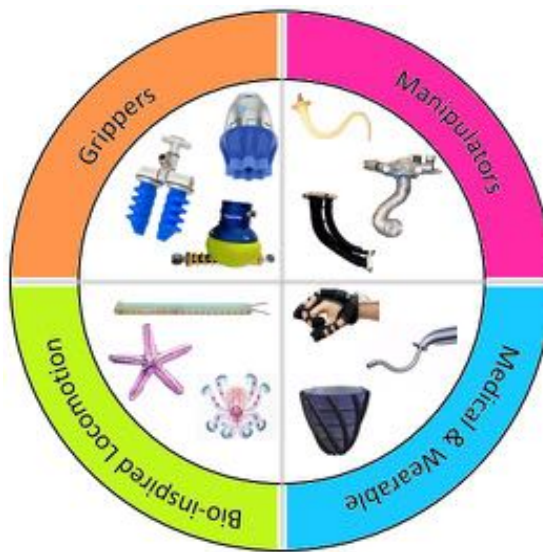


Figure 2.2 Scheme of the main applications of soft robots. Clockwise. Continuous and Soft Manipulators: Octopus Arm [65], OctAir [4], arm with PAM [66]. **Medical and wearable:** rehabilitation glove [67], endoscope [68], support valves heart [49]. **Bio-inspired:** Octopus [69], starfish [22], and caterpillar [23]. **Grippers:** jamming gripper [70], pneumatic gripper [38], soft gripper [71].

In the following tables (Table from 2.2 to Table 2.5), some interesting prototypes are summarized for each category of applications.

Table 2.2 Summary of bio-inspired soft robots

Bio-Inspired - Locomotion							
Environment	Bio-inspiration	Prototypes	Movement	Material	Actuation	Sensor	Application
Underground Soil	Worms 	Meshworm [3]	Rotary Locomotion	Soft braided mesh-tube	NiTi wire	Sliding Resistors	-
		Magworm [72]	Crawling Locomotion	Silicone rubber and rigid magnets	Magnetic	-	Pipeline cleaning, inspection
		Earthworm [73]	Unidirectional crawling	Silicone	Pneumatic	Pneumatic	-
	Caterpillars 	GoQBot [23]	Penitistic Locomotion	2 types of silicone rubber	SMA coils	-	-
		Caterpillar [74]	Unidirectional dipping motion	LCE	LCE (light)	Force	-
	Snake 	Snake [75]	Traveling-Wave Locomotion	TPE	Pneumatic	Pneumatic	Pipeline inspection
		Kinguini snake [76]	Lateral Undulation	Lattice	Pneumatic	-	-
Underwater	Octopus 	Laschi et al [18]	Elongation, shortening and bending	Silicone	Tendon and SMA springs	-	-
		Octopus gripper [77]	Bending and gripping	Silicone	Pneumatic	Pneumatic	Gripping
	Starfish 	PoseDRONE [24]	Crawling, swimming and manipulation	Rubber-like materials	Motor	-	Marine operations
		[78]	Locomotion	Silicone	Pneumatic	-	-
		[79]	Locomotion	PVC + PDMS	SMA wires	-	-
	Jellyfish 	[22]	Locomotion	Silicone	SMA springs	-	-
		KryptofJelly [80]	Jellyfish movement	Silicone	SMA wires	Laser	Underwater exploration
	Fish 	[81]	Jellyfish movement	Hydrogel	Hydrogel	-	Marine environment monitoring
		[82]	Jellyfish movement	Silicone +DEA	DEA	Force	-
	[83]	Swimming	Silicone	Hydrogel	Force	-	-
	[84]	Swimming	Silicone	SMA wires	-	-	-

Table 2.3 Summary of manipulators soft robots

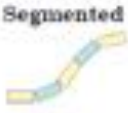
Manipulators						
Body	Prototypes	Segments	Material	Actuation	Sensor	Application
 Segmented	[85]	4	Silicone	Tendon and Pneumatic	Force	-
	[86]	3 +1 (gripper)	Rubber + Fiber	Pneumatic	Pressure	Delicate Grasping in Shallow Water
	[87]	2	Elastomer	Motor	Electromagnetic pose	Minimally Invasive Surgery
	[88]	4	Silicone	SMA coils	Hall	Underwater and space applications
	[89]	3	Silicone	Pneumatic	-	-
	[90]	2	Silicone	Pneumatic	F/T	Minimally Invasive Surgery
	[91]	5	Silicone + Ground coffee	Pneumatic (jamming)	-	-
 Continuum	[92]	1	Elastomer + magnetizable microparticles	Magnetic	-	Medical applications
	[93]	1	Silicone	Tendon-driven	-	-
	[94]	1	Silicone + ferromagnetic elastomer	Tendon-driven + Pneumatic	-	Medical applications
	[95]	1	NTi + McKibben	Pneumatic	Electromagnetic	High-Precision Manipulation
	[96]	1	Elastomer	Twisted and coil	-	Surgical applications
	[97]	1	Elastomer	Pneumatic	Force	Endoscopy

Table 2.4 Summary of soft grippers. The following grippers subdivision is based on that shown in [44] F = force, W = weight, S = speed or gripping time

		Grippers						
Gripping	Type	Prototypes	Structure	Material	Actuation	Sensor	Properties	Applications
By Actuation	Passive Structure	[98]	2 fingers	Silicone	-	-	-	-
		[99]	2 fingers	Elastomer	Motor	Force	F = 530 g	-
		[100]	2 fingers	IPCs	Tendon-driven	-	-	-
		[101]	2 fingers	Rubber + fibers	Pneumatic	Force	W = 45 g	-
		[102]	5 fingers	Silicone	PneuFlex	-	W = 178 g F = 2 N	-
	FEA	[103]	Monolithic	ABS + rubber	DC motor + pneumatic	Pressure, force	W = 1 kg F = 12 N	Grasping of delicate objects
		[104]	3 fingers	PVC + PI + DEA	DEA	-	W = 7.5 g F = 65.6 g	-
		[105]	4 fingers	ICL	IPMC	-	-	Space applications
		[42]	Monolithic	Polymeric	DEA	-	F = 0.7 g	-
		[106]	Monolithic	-	SMA spring	-	F = 4 N	Minimally invasive surgery
By controlled stiffness	SMA	[107]	5 fingers	Silicone	SMA wires	Flexure	W = 282 g F = 412 g	-
		[108]	3 fingers	PDMS	SMA wires	-	-	-
		[41]	Monolithic	Latex + ground coffee	Pneumatic	-	-	Pick-and-place
		[109]	4 fingers	Rubber + rice	Tendons	-	-	Precision grasp
		[110]	Monolithic	Latex + water + glass beads	Pneumatic	-	W = 5N	Deep water operations
	ER/MR fluids	[111]	2 fingers	Polyurethane	MR	Force	S = 460 ms	Pick-and-place of vegetables
		[112]	2 fingers	HNBR	MR	-	S = 200 mm/s F = 50 N	Pick-and-place
		[113]	5 fingers	RTV	MR	-	S = 0.2 s F = 0.1 N	-
		[114]	5 fingers	Multimaterial	SMP	-	-	-
		[115]	3 fingers	Polymer	SMA + SMP	-	F = 5.8 N	Grasping objects with deformable shapes
	Electro adhesion	[116]	2 fingers	PEU	SMP	-	F = 58 g	-
		[39]	Two fingers	Elstomers	DEA	Self-sensing	W = 1.5 g / S = 100 ms F = 82 g	Grasping tasks in the food industry and medical in small transportation drones
		[40]	Monolithic	DEA	EA	Self-sensing	-	Handling of objects including fabrics, bowls, and lenses
		[117]	8 fingers	Polyimide	Motor +	Force	F = 3.5 N	Satellite servicing

				Electro static adhesive	torque	
Gecko adhesion	[118]	Monolithic	Elastomer	gecko adhesive	-	S = 2.5 ms
	[119]	Monolithic	Elastomer	gecko adhesive	-	F = 0.41 N
	[120]	2 fingers	Elastomer	FEA + gecko adhesive	FTIR	W = 48.7 g / F = 50 N

Table 2.5 Summary of medical and wearable soft robots.

Function	Prototypes	Body part	Medical & Wearable			
			Material	Actuation	Sensor	Application
Exoskeleton	RELab tenexo [121]	Hand	Steel strip + 3D printed parts	DC motors	EMG	Grasping assistance in everyday activities
	[122]	Wrist	Mix of soft and rigid material	Motor	IMU & Force	Rehabilitation
	[123]	Knee	Fabric	Pneumatic	-	Planetary Exploration
Prosthetic	[124]	Hand	Elastomer	Pneumatic	Optoelectronic strain sensors	-
	[125]	Finger	TPU	Servo motor	Force	-
Endoscope	STIFF-FLOP [126]	Abdomen	Silicone	Pneumatic	-	Minimally Invasive Surgery
	MINIR II [127]	Intracranial	Silicone	SMA springs	RTD	Neurosurgery
	NeoGuide [128]	Abdomen	Elastomer	Electromechanical	Position	Colonoscopy
Artificial organs	Artificial Heart [49]	Heart	PAM + soft matrix	Pneumatic	Pressure	Support heart functions
	Tongue [129]	Tongue	EcoFlex + PDMS	Pneumatic	Pressure	Simulation
	SoGut [130]	Stomach	Ecoflexpneum	Pneumatic	Pressure	Gastric simulation
Drug	[131]	Body	Permanent magnet	Magnetic	-	Capsule endoscopy
	[132]	Body	Permanent magnet	Magnetic	-	Drug delivery
Haptic	HapWRAP [56]	Arm	Polyethylene	Pneumatic	-	Force feedback
	[57]	Hand	Silicone	Pneumatic	-	Tactile feedback
	FlyJacket [58]	Bust	PLA + foam	Motors	Force, pressure, IMU	Sensation of Flying Like a Drone

2.3. Design and manufacture of soft robots

In this section, the different components that usually compose a robot (materials, actuators, sensors, electronics, and power supplies) will be presented separately. However, these components may not be thoroughly divided in soft robots [72]. Moreover, in the future, it will probably be challenging to determine where the robot's body ends and where its sensors and electronics begin since it is expected that, for example, the sensors can be printed directly on the robot [73].

Finally, 3D prototyping techniques and the new concept of 4D, which is essential to understand and imagine the future of soft robotics, will be analyzed.

2.3.1. Materials

The primary materials used are soft polymers and elastomers such as silicone. As seen in the definition section, Young's modulus is used to compare the different elastomers among them and, in turn, compare them with rigid materials. Some of the most common are polysiloxanes such as Ecoflex (Ecoflex 00-30 or Ecoflex 00-50; Smooth-On Inc.) and poly(dimethylsiloxane) (PDMS) (Sylgard 184, Dow Corning) [74,75], soft polyurethanes [76], polyacrylates, and block copolymer elastomers [77,78].

All these materials are insulating by their nature. However, it is possible to add the ability to conduct electrically or thermally by adding nanoparticles of conductive materials and taking advantage of this new property to control the robots thus made [79,80]. It is also possible to realize composite materials adding layers and creating stimuli-responsive materials [81].

Elastomers are also at the basis of artificial pneumatic muscles (PAM) as they make up the structure, which is then lined with a braided fabric. [82].

Many fluids play an essential role in soft robots so that they can be considered constituent material. Compressed air, water, and aqueous electrolyte solutions are most commonly used.

Another quite popular material is hydrogels, which are semi-solid materials [83–85].

Some novel materials can be found in [86–88]. While in [89], a state of the art of magnetic elastomers applications can be found.

Another significant family of materials includes those used in additive manufacturing, such as FilaFlex [90], NinjaFlex [91], EAA [92], Nylon12 [93], AUD [94], and silicone [95], among others. In [96], it is possible to find an updated state of the art on the materials used in the 3D printing of soft robots.

Finally, it should be mentioned that new biodegradable materials and polymers are being studied. They will be useful both for use in the medical field, where they can be dissolved once their task is finished as in robots that supply drugs [48], both for the environmental problem, with lesser polluting robots [97–99].

Smart materials like electroactive polymers and shape memory alloys will be covered more extensively in the next actuator section. In [100–102], it is possible to find actualized state-of-the-art about materials used to manufacture soft robots.

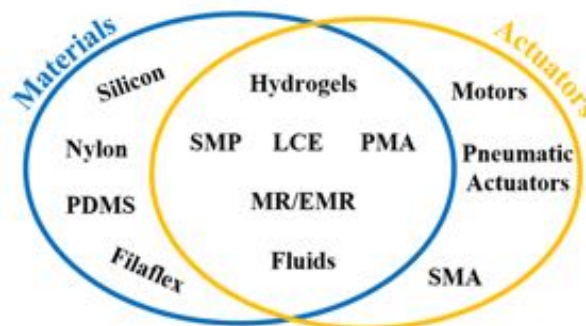


Figure 2.3 Scheme of the main materials and actuators used in soft robotics.

2.3.2. Actuators

The types of actuators used in soft robots vary from the most traditional, such as motors and pneumatic actuation, to intelligent polymers. As mentioned above, there is not always

a clear distinction between what the actuators are and what the robot's body is, as in the Octarm [4], whose structure, made with artificial pneumatic muscles, is at the same time its actuator. This concept is graphically summarized in Figure 2.3. Principals' actuators are outlined in Table 2.6.

Current actuators include motors, shape memory alloys (SMA), shape memory polymers (SMP), dielectric, magnetic, pneumatic, hydraulic elastomers, photosensitive, piezoelectric, and explosives. The advantages and disadvantages and some applications will be presented of the main ones.

Among the prototypes of soft and continuous robots, the most widely used actuator were motors, generally connected to a system of tendons. This type of actuation is the easiest to use because it is well known and is very easy to control. It is not the most suitable for this type of robot since the motors are rigid and can, in some cases, take up much space and be quite heavy. All these characteristics are incompatible with the flexibility and lightness required. Among the prototypes that present a motor and tendon system, we find [103–106].

Other actuators that can be partly assimilated to this actuation concept through tendons are shape memory alloys (SMA). Its operation is based on two principal characteristics: the material's transformations at the level of crystalline structure based on temperature and the ability to memorize a shape, as its name indicates. At room temperature, it is in the martensitic phase and is easily deformable. As the temperature increases, it passes into the austenitic phase, in which Young's modulus increases and the material returns to the shape it has memorized. Although there are many different types of alloys, the most famous is called Nitinol, composed in prevalence by Nickel and Titanium. They are usually used mainly in the form of spring since the range of motion they can realize is greater [107,108], but it is also used in the form of a thread [109] or putting more threads in parallel [110]. Among the advantages that the SMA presents, the lightness, the optimal power/weight ratio, the simplicity of operation, and the low cost stand out, apart from the high resistance to corrosion, the high biocompatibility, and the absence of magnetic behaviors, all characteristics that make it a good candidate for medical prototypes. However, the control is quite complex (due to the thermomechanical behavior of the material), the deformation is usually limited, the operating speed is relatively low (due to the cooling time between cycles), and high currents are needed to reach the temperature at which it is carried out the phase shift.

Another actuator is shape memory polymers (SMP), whose operating principle resembles the SMA. Also, in this case, the material can return to a memorized form when activated, either thermally, chemically, or through light [111,112]. This capacity is not an intrinsic property of the material, as in the case of SMA, but is the result of a polymer functionalization. In this case, the advantages are lightness, low cost, good power/weight ratio, the possibility of manufacturing with 3D printing technologies [113,114], and a more significant deformation than the SMA. They are also biocompatible and sometimes biodegradable [115]. Among the disadvantages, there are also, in this case, the control, the low speed, and the limited force in comparison with other conventional actuators. For all that has been said, also, in this case, this actuator is especially interesting in the medical field [116]. Other types of applications can be seen in [117–119].

In the actuators that can change their shape under electrical, thermal, or light stimulation, liquid crystal elastomers (LCE) combine the flexibility of elastomers with correctly oriented liquid crystals. [120–123] The shape change of LCEs can be programmed during processing by orienting the liquid crystal phase prior to crosslinking. [124]

The last type of actuator capable of changing its shape is hydrogels. They are composed of hydrophilic polymer chains arranged in a network structure and water, the percentage of

which can vary with exposure to thermal, electrical, optical, or chemical stimuli and thus generate a significant contraction. These actuators' main advantages are stretchability, transparency, and biocompatibility [83]. Due to their characteristics, it is easy to understand that they are especially interesting for medical applications [125], mainly to supply drugs [126]. In [127], it is possible to see some applications of hydrogels as actuators.

Others conventional actuators widely used are pneumatic and hydraulic actuators. Among the most famous actuators are pneumatic artificial muscles (PAM) (or McKibben's muscles) that contract when subjected to pressure and loosen at ambient pressure. Among the prototypes developed are rehabilitation devices [128,129] and manipulators [66,130]. In most cases, pneumatic actuators are made to measure through channeled molds in which different elastomers are cured. This technique gives rise to the so-called fluid elastomer actuators (FEA) [131] (comprising the PneuFlex actuators [132], the Pneu-Nets [133], and the FFA, flexible fluidic actuators). The main advantage of this solution is that it is possible to give a specific shape to the actuator, favoring one direction of expansion to the others. The prototypes made are various, such as robots that can grow [134] or bio-inspired ones [75,135]. Many other examples can be seen in [102,136]

Another significant family of actuators is that of electroactive polymers (EAP), which includes dielectric elastomer actuators (DEA) [137,138] and ionic polymer metal compounds (IPMC) [139,140]. These actuators are made up of two electrodes and an elastomer interposed between them. By applying a voltage (generally relatively high), the attractive electrostatic force between the electrodes induces a change in the size or shape of the elastomer. They are very flexible, highly configurable, compact actuators, and have an excellent weight/power ratio. Their main disadvantage is the required high voltages, making them unsuitable for many applications.

The last large group of actuators comprises electro-rheological (ERM) and magneto-rheological (MRM) materials. They are composed of elastomers containing added polarizable (ERM) or ferromagnetic (MRM) particles. These particles can be activated using an electric or magnetic field and consequently deform, stretch and contract the material. The advantages are the ease of control, the wide range of usable materials (since magnetic fields can penetrate many materials), and response speed compared to other actuators such as the SMA. However, it must be taken into account that external magnetic coils are needed, which can be bulky and require much energy, limiting the fields of application. [141,142]. In [143], you can find a state of the art of soft magnetic robots.

Table 2.6 The main actuators in soft robotics. The material (P = Polymers, E = Elastomers, F = Fluids), the advantages, the disadvantages, and some real applications are presented for each actuator. As in Table 2-5, only real applications are taken into account.

Actuator	Types	Material	Advantages	Disadvantages	Cost	Applications
Motors	-	Metals	Control and design	Weight Rigidity	Low	Continuous robots Exoskeletons and prosthetics
SMA	-	Alloys	Lightweight Power / Weight Easy actuation Biocompatibility	Control Low speed High currents	Medium	Continuous robots Medical applications
SMP	-	P	Lightweight Power / Weight Biocompatibility Biodegradability	Control Low speed Limited strength	Medium	Medical robots (endoscopes, prostheses)
FEA	PAM FFA	E	Lightweight, Flexible Speed	High power Compressor	Low	Manipulators Rehabilitation
EAP	DEA IPMC	E	Weight/Power	High voltage	Low	Bio-inspired robots Grippers
ERM/MRM	ER MR	F + E + particles	Simple control Numerous materials Response speed	External magnetic coils	Medium	Grippers Bio-inspired robots
Hydrogels	-	P + water	Stretchability, Transparency, Biocompatibility	Control Low speed Limited strength	High	Drug supply
Photosensitive	Visible light or IR	E, F + gels + nanoparticles	Simple control Biological Materials	High intensity Limited deformation	Medium	Biomedical devices

Finally, a series of actuators that are not widely used but represent novel solutions is worth mentioning. Among them are piezoelectric actuators, photosensitive, and explosives. Piezoelectrics take advantage of the property of some materials to produce a voltage or an electric charge when subjected to mechanical stress or vice versa, to deform if they are subjected to an electric field [144–146]. The photosensitive ones are constituted by elastomers, fluids, or gels and molecules sensitive to light. They can be operated with visible or infrared light [147–150]. It would be a simple action technique in visible light, especially for robots operating outdoors and taking advantage of sunlight. However, they could not carry out a complete operating cycle since they would always be in the activation state. In the case of infrared light, an interesting advantage is its ability to penetrate through biomaterials, which is why it has been used in medical devices [151]. Some robots have used explosive actuators to generate motion through explosive chemical reactions [152–154].

Some more widespread state of the art on methods of action in soft robots can be seen in [155–157].

2.3.3. Sensors

Sensors are essential to feedback and control a robot, and in the case of soft robots, their importance is even greater. Due to its infinite degrees of freedom, modeling is complex and prevents correctly predicting how the robot will act and how it will be affected in terms of position and shape by external loads [28]. The sensors are then the only tool to obtain information about the environment and know the state of deformation of the robot, that is, to provide it with proprioception. There are two main problems with sensors for soft robots: the first is that there cannot be a clear correlation between the number of sensors and the number of DOF as in the case of rigid robots, the second is that the sensors should be flexible and stretchable like the structures to be measured. For these reasons, most of the sensors traditionally used in robotics do not work since they are usually rigid.

Among the sensors used are resistive and piezoresistive sensors. Like the actuators seen above, these sensors base their operating principle on the variations suffered by the material's resistance according to the applied force. Resistive sensors, in general, have a structure made of flexible materials, such as elastomers, which have microchannels in which a conductive liquid is introduced. Polymers and hydrogels with conductive properties can also be used directly [158–160]. While piezoresistive sensors use elastomers to which nanoparticles are added [161–164]. The manufacture of these sensors is relatively simple, as well as their use, they are also insensitive to electromagnetic interference, but their performance and bandwidth are limited. [28]

Capacitive sensors take advantage of the ability of some materials to vary their capacitance as they are deformed. Their operation is usually linear, their response is fast, and they are quite sensitive. However, they need to operate in a clean environment (the measurement is incorrect in the presence of dust or other substances) and where there is no electrostatic charge, which would also affect the measurement [165–167]. This sensor is being used extensively in electronic skin prototypes [168,169].

Optical sensors measure variations in light caused by deformation or stress applied to the body. They are very deformable, and they are not affected by any interference contrary to the capacitive ones. In addition, they need minimal wiring in the area they have to measure. Fiber optics are mainly used to make this type of sensor [170,171] and elastomeric structures with optical components directly integrated during the manufacturing process [172]. Applications include hand prostheses [173] and soft manipulators for surgery [174].

Magnetic sensors detect the variations in a magnetic field by varying the geometry of the soft body in which a Hall effect sensor is located. They are not suitable in all situations where there may be external interference and ferromagnetic objects. However, they are still a valid alternative since they are compact, cheap, and simple [175–177].

Inductive sensors measure inductance variations due to deformation or displacement. They are being used extensively to perform touch sensors [178,179] and measure the deformation of pneumatic actuators [180].

Finally, it should be mentioned that many types of sensors are being developed, such as conductive thermoplastic resistive strain sensors that incorporate conductive particles and also strain-sensitive fibers and fabrics [43].

An updated state of the art on the sensors used in soft robotics can be found in [102].

To develop the sensors necessary to improve the control of this type of robot, the subsequent advances in 3D printing techniques (sensors can be incorporated/embedded in the robots) and the development of flexible electronics (discussed in the next section) will be significant.

2.3.4. Electronics

The electronics that will be part of the soft robots will have to adapt to their shape, being stretchability the most desired characteristic. Two approaches are distinguished to achieve this: a first where ultra-thin metal films are modeled in waves or networks on an elastomeric substrate, and a second where conductive particles are dispersed within an elastomeric matrix [181].

The two techniques are still limited by both maximum strain and efficiency.

Among the most promising materials for this field of research is graphene, thanks to its physical and chemical characteristics and the possibility of using it in various applications, including touch panels, nanogenerators, organic solar cells, actuators, and biosensors [182].

Soft electronics will prove to be a fundamental part of many medical devices, whether monitoring patients [183] or diagnosing diseases [184].

3D printing is in part helping to realize these new circuits, and advances in printing techniques will allow for significant advancements [185].

2.3.5. Power supplies

Like the sensors and actuators, the power supplies will also be based on flexible and stretchable electronics. In [10], a soft energy generator is defined as "a device that generates energy through the deformation of materials in a particular structure."

This issue is quite important since, together with the actuators, it represents the most significant restriction on the potential robot's capabilities (either due to the impossibility of charging with a battery or due to limitations in displacement). In this regard, animals have a significant advantage, and it will be impossible for now to think about bio-inspiration in them since how both plants and animals produce energy is much more complex than the solutions used in the present to feed the robots.

Some examples of energy storage devices that present a certain degree of flexibility can already be found in the literature, for example, solar cells [186], flexible nanogenerators [187–189], supercapacitors [190], flexible batteries [191,192], and even flexible alkaline batteries [193,194].

Still, many of these systems are flexible but not stretchable, preventing the correct functioning of the soft parts they would be coupled.

Another aspect to consider is the weight-power ratio that these devices can present, since many soft robots, despite can require much energy (as in the case of those operated with SMA or DEA), cannot carry much weight because their structure does not allow it. In this case, the best solutions use wireless transmission, photovoltaic or piezoelectric energy [195]. In this sense, piezoelectric generators can transform the repeated movements of robots into energy [189,196].

2.3.6. Manufacturing

New manufacturing techniques are also necessary to make such innovative robots since traditional subtractive manufacturing techniques cannot be applied to the materials usually used. Most of the prototypes have been made with additive manufacturing (AM). In [101], three different roles of this technology are identified in the construction of soft robots: passive, that is AM used only to make the molds of the robots, total AM, when the robot is entirely manufactured with these techniques; and hybrid AM, when the robot is made using different technologies and they are not all AM, as would be the case of shape deposition modeling (SDM).

AM is, by definition, "the process of joining materials to make objects from 3D model data, generally layer upon layer, unlike subtractive manufacturing methodologies, such as traditional machining" [197]. The main advantages it presents are the freedom to make any shape (including complex geometries, without the need for many steps), the minimum amount of waste of materials produced, the low cost, and the speed, all characteristics that make it the perfect technology to test prototypes.

The most used technique is molding, that is, the use of 3D printing to make the molds in which the silicone that will constitute the robot's body will then be poured. This technique allows prototypes to be made cheaply and quickly. The disadvantages mainly affect the silicone, both when pouring it into the mold (due to the possibility of encompassing bubbles that weaken the final structure) and demolding (which can be problematic in the presence of notches, even causing ruptures). This solution also allows inserting more rigid parts into the mold that form part of the robot's body itself [198]. It may be that soon this solution will become less popular compared to direct silicone printing [95].

Moreover, many AM techniques are used to make soft robots directly; a summary of the best known and main advantages and disadvantages are presented in Table 2.7. The best known is undoubtedly the extrusion of material, which comprises FDM / FFF (Fused Deposition Modeling), used to print finger prostheses [199] or pneumatic actuators [200] and DIW (Direct Ink Writing) [201]. Then there is photopolymerization that includes many techniques, from stereolithography (SLA) to 2-photon polymerization (2PP), through Digital Light Processing (DLP) and continuous liquid interface production (CLIP). Examples of these techniques can be seen in [202–204]. The following can be cited the Material Injection (MJ or MJM) used in [205,206] and the Powder Bed Fusion (PBF), better known in this case as Selective Sintering laser (SLS) used in [207]. It can be seen that in the last row of the table, the technique of deposition of shape modeling (SDM) is cited, which is not purely an FA technique since it includes both subtractive and additive processes [208].

Many are the materials that can be used depending on the specific type of FA used, among them DE (Dielectric Elastomers) [209], SMP (Shape Memory Polymers) [113], Hydrogels [210], FE (Fluid Elastomers) [211]. In addition, several prototypes can be found that use the SSC (smart soft composite) technique [212].

A really interesting application is that of printing soft biological robots, which can be of two types: *in vitro* (robots that operate outside the body) [213] or *in vivo* (robots that operate inside an organism) [214].

The manufacturing techniques used in microelectronics that allow making very thin films are also being studied [215–217]. Finally, another interesting concept is decomposing the robots into several parts to join them successively, either through the materials themselves (as silicone, which allows several pieces to be joined together) or by using some glue [218].

The main issues are multi-material printing and inter-material adhesion. The hope is to print structures with rigid parts and less rigid parts (similar to living organisms with a skeleton and soft tissues) to control their movement better.

The following states of the art can be viewed to deepen the state-of-the-art of soft robot manufacturing techniques [12][12,101,219,220].

Finally, a relatively recent concept representing an advance in 3D printing is worth mentioning, that is, 4D printing. This concept applies to all 3D printed objects capable of modifying their structure over time in response to external stimuli such as pressure, temperature, wind, water, and light [221–224].

Table 2.7 Principal 3D printing technology with the operation principle and the advantages and disadvantages.

Technology	Operation Principle	Typologies	Advantages	Disadvantages
Material extrusion	Controlled deposition of a continuous filament of material	FDM	- Variety of materials - Flexibility in design - Reduced costs	- Low surface quality - Low mechanical resistance
		DIW		
Light Curing (VAT)	Polymerization of a photosensitive resin	SLA		
		DLP	- Smooth finish	- Not multi-material.
		CLIP	- Accuracy	- More expensive polymers - Post-processing
Material injection (MJ o MJM)	Photopolymers activated by a UV lamp		- Precision and finish - Multimaterial	- Limited materials
Powder Bed Fusion (PBF)	Sintering a powder	SLS	- Dense and strong parts - Low waste - No need for support	- More expensive process - Rough finish
Shape Deposition Modeling (SDM)	A sequence of additive and subtractive operations		- Complex geometries - Multimaterial	- Many steps - Complicated material bonding

The future lines in the manufacture of soft robots are: (1) the printing of silicone (something already tested but that needs improvements [225]), (2) the printing of sensors directly on the structure to shorten the manufacturing process and improve the perception of these robots [73], (3) the possibility of including different materials in the same AM process [226] and (4) the use of new smart materials [227] or biocompatible elastomers [228].

2.4. Design, Modeling, and Control

This section will analyze the existing solutions for the design, modeling, simulation, and control of soft robots, considering each area's problems.

2.4.1 Design

The design of soft robots today is mainly carried out with programs designed to design rigid robots, and that is why they are not the most appropriate option to carry out the complex inhomogeneous 3D designs that may be necessary to make soft robots [8].

The design of soft robots is a crucial moment of their creation since the designed shape will impact the robot's capabilities when it is built. An important aspect to consider is the rigidity provided to the robot through a correct design (for example, pneumatic actuators).

Rigidity is a central issue when talking about soft robotics since it is proving to be very difficult to reproduce in bio-inspired prototypes, and that plays an important role when it comes to being able to control the robot precisely. If, for example, the robotic arm inspired by an octopus published in [18] is considered, it is seen that, despite having reproduced a tentacle with its characteristics of size, elasticity, adaptability, it does not present even the same strength, nor the same speed. Since it is challenging to reproduce in a robot, the complex system that allows the octopus to tighten and move its tentacles, considering that there is no rigid structure like a skeleton in the octopus, this problem can be solved in part at design time by modifying the geometry, adding ribs, and modulating the thickness of the material [12]. In this way, it is possible to increase the rigidity or decrease the flexibility, where necessary, to obtain the desired movement. These modifications to the drawings are easier to implement in pneumatically actuated robots by changing the shape of the chambers. Other solutions foresee combining different materials, as already mentioned in the section on manufacturing.

A state-of-the-art with many solutions to achieve certain rigidity is presented in [229], as the actuators' arrangement or actuators with variable rigidity (like prototypes based on the jamming principle [230]). However, there are still no guidelines to achieve the expected

result in terms of stiffness. It is quite probable that the first solution to the problem comes from the new rapid prototyping techniques that hope to allow joining materials with different mechanical characteristics and different stiffness in the same structure.

Stiffness is not the only problem in obtaining prototypes from which complex mechanical behaviors can be predicted. Optimization algorithms would be essential to automate the prototype design process [231]. According to the authors, the algorithm should start taking into account the tasks that the robot is desired to perform, divide them into a sequence of basic movements (like stretching, bending, coiling, elongation), and that this information is then used by formulating an inverse design problem that will be solved employing a mathematical algorithm. This algorithm needs three types of information: the robot's objective (mathematical expression of displacements and forces in the time), its design concept (geometry, material, and type of actuation), and the possible constraints regarding mass, size, manufacturing, or stress. All this information is then processed to realize a design. An analysis (kinematics, dynamics, or interactions) is realized, and an optimization method is used to reach the best design. This process is iterative. An example of a robot designed through algorithms can be seen in [232].

These algorithms are essential when soft robots are realized with materials that can significantly change their behavior, only changing their thickness for a few millimeters. In this case, it is more expensive to realize different prototypes, and it is better to simulate the design. It is, for example, the case of materials composed of different layers, some of them stimuli-responsive, in which determine the thickness of each material and the shape it is challenging and can change the material response dramatically.

During the design process, sensors and electronics must also be considered to avoid movement limitations, excessive weight, or an undesired rigidity in some parts. In many bio-inspired robots, electronics are located externally not to add weight to the prototypes. For the same reason, it is complicated to realize autonomous soft robots (robots carrying a battery) due to the battery weight. All these aspects represent a limit in the design, but probably in the next future, it will be easier to integrate all these components.

For all the problems mentioned, "The Soft Robotics Toolkit" [233] was implemented, a set of resources to help researchers develop soft robots.

As can be seen, the design process cannot be entirely separated from the modeling problem, and at any time, the dynamics and kinematics have to be considered, especially when the actuation system coincides with the body of a soft robot.

2.4.2. Modeling and simulation

Once the design is done, the next step consists of modeling and simulating it. As we have said, these two steps are not separated at all. In many cases, the design has to be changed after the modeling and simulation and before the physical realization. This step represents the bridge between the prototype and its control. The principal aim of modeling and simulation is the prediction of robot movement under different conditions. The modeling step is not mandatory, and it is also possible to bypass it, providing the robot with an adequate number of sensors that can measure its exact position at each moment.

Nevertheless, this solution presents some problems. Traditional sensors do not provide all the information required, and their accuracy is not sufficient to describe the pose of this type of robot due to their deformability and DOFs. A high-precision external tracking system could also be a solution, but in this case, it limits the movements only in a controlled environment. For all these reasons modeling soft robots is usually the best choice and is the only one that avoids undesired or dangerous behaviors.

A continuous function can describe a soft robot since its deformation is continuous and its degrees of freedom are theoretically infinite. All this implies that it is complicated to reproduce an exact model of the robot and that it can be done assuming a rigid body hypothesis so that the equations are easier to handle. Many hypotheses are necessary to simplify the problem, and, depending on the prototypes, a different model will be chosen to represent the problem better. In [234], the techniques for modeling soft robots are divided into two main categories: techniques based on the model and those based on the learning (plus a hybrid technique between these two). Almost the same categorization (with different names) is presented in [235]. All these models are primarily studied for continuous soft robots and hyper-redundant robots, so, in the literature, they are specially employed to model this family of soft robots. A scheme of these techniques is shown in Figure 2.4.

The first category or approach is the techniques based on the model. They consist of a user's model that tries to represent the robot accepting different assumptions and presenting different levels of approximation. Some are easier than others, and others can present a higher computational cost since they can be analytical or numerical. The two main subcategories in which model-based techniques can be divided are kinematic models (or geometric models) and dynamic models (or mechanical models).

Kinematic (or geometric) models were the first created when the first hyper-redundant robots started to emerge. As the name indicates, they focus on geometry, especially in the robot's curvature during the operation. In this case, forces are not considered to simplify the problem. The first kinematic model was the so-called "backbone curves" proposed by [236]. It is also known as the non-constant curvature approach and realizes a curve parametrization. This first model was replaced by the model of PCC (Piecewise Constant Curvature) presented by [237]. In this case, the central assumption is that the backbone of the robot can be represented with a piecewise constant curvature. It is possible to calculate the kinematic model through the Denavit-Hartenberg matrix, considering the curvature resulting from three discrete transformations in the plane. It is also possible to use this model in the space with few modifications to the matrix. From the first time in which the accuracy of the model was proved (the Elephant's Trunk [238]), many others started to use this approach for its simplicity [239,240] since, in the case of the soft continuous robot, it is only necessary to assume the continuous body as a finite series of curved elements.

Although these models have been a good option in some cases, they are not realistic since they do not consider gravity, non-conservative forces (friction, resistive forces), or many others materials' properties. Also, the weight of the robot and external loads are not considered. When these variables cannot be neglected, it is necessary to use the second approach, the dynamic one, which adds physical properties to the geometric characteristics.

Probably one of the most important approaches in this second category is the Cosserat-rod model. This theory considers the robot as an infinite number of infinitesimal rigid parts to consider all the mechanical characteristics. Moreover, to use it, three assumptions are required: (1) length much larger than the radius, (2) material incompressibility, and (3) linear elasticity [241]. This method is probably the most realistic since it considers all non-linear effects that affect the curvature, but at the same time, it is more complex than the previous ones because it uses non-linear partial differential equations. [242,243] A simplification of this method uses Euler–Bernoulli beam theory which is equivalent to a shear-free, torsion-free, planar Cosserat rod. [244] Another approach is the spring-mass model that concentrates the robot's mass in discrete points while the actuation is represented by damped springs. It is probably the less used due to its incapacity of reproducing many actuation principles and its inefficiency from a computational point of view. However, it was satisfactorily applied in [245].

These techniques mentioned above can be useful, but they cannot represent the robot's real movements depending on irregularity and nonlinear deformations. For this reason, the most widely used technique currently is that of finite elements (FE), which allows reasonably accurate models, although the computational cost is high and cannot be used in real-time [246]. It is because to represent the robot accurately, a considerable number of elements and nodes are necessary. The model order reduction technique (MOR-Model Order Reduction) [247,248] was proposed to reduce the computational cost. This solution represents a good compromise between the model and the simulation time, which can be real-time. This technique can also be applied for contact forces to realize the control of soft robots in self-collisions. Also, in this case, it allows reducing computational time dramatically [249]. Among the most used software simulators for soft robots, there are Ansys, COMSOL, Abaqus, and SOFA [250].

In some cases, more techniques are merged [251], where FEM combines with PCC.

The second category consists of learning-based models based on machine learning and artificial neural networks (also fuzzy models are used [252]). This approach is quite interesting because it allows to predict the robot's behavior without previous modeling and to use only a database with experimental data. It is the best option when the modeling process is more complicated than real experiments when the environments are significantly complex, and it is impossible to neglect any variable, and when intrinsic nonlinearities are predominant. It is also helpful to solve the inverse kinematics problems as in [253]. Nevertheless, it is not always the best option since it presents a significant limit: the data needed to feed the model change when the operating conditions or the environments change. A significant amount of data is usually necessary to obtain a correct prediction. In this case, it is better to opt for a model-based approach.

It is also worth mentioning the use of differentiable simulation to design and control soft robots. Differentiable simulation is “a powerful family of new techniques that applies gradient-based methods to learning and control of physical systems” [254]. These physical simulators are well-known for hard robot planning and control, but their use is more challenging than soft robots due to their deformability and complex physic laws. One example of this technique applied to a soft robot is shown in [255]. The use of this technique for soft robotics is analyzed, and various examples are provided. [256]

It is not easy to choose the better model technique among as many approaches. A novel solution to facilitate this choice is the use of the softness distribution index (SDI), a dimensionless quantity that for a given soft robot is computed based on the distribution of its structural properties. [257]

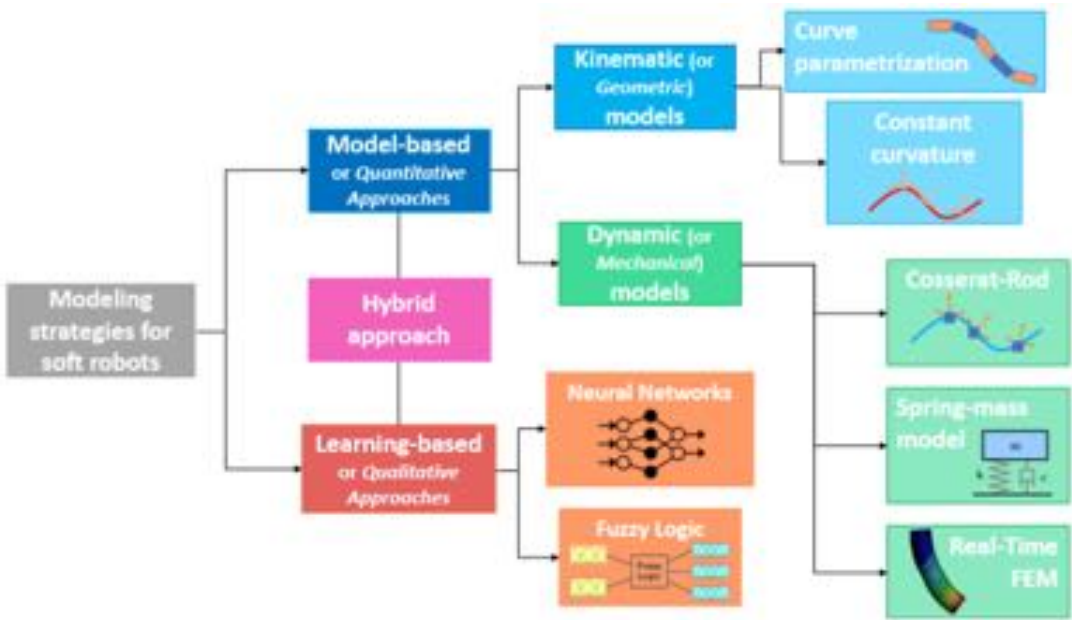


Figure 2.4 Scheme of the modeling strategies for soft robots.

2.4.3. Control

The information obtained through the simulations is finally used to control the robot. Traditional control techniques are not suitable for this type of robotics. It is mainly due to the infinite states of deformation that these robots present, which correspond to their theoretically infinite number of DOFs, which correspond to possible states of the system that are ultimately not all observable and controllable. In addition, the control algorithms must consider the robot's interactions with its environment and how its shape and geometry can change accordingly. Control methods emphasize modeling techniques and can be divided into two main categories: model-based controllers and model-free (or learning-based) controllers, each of which can be static or dynamic [258]. Moreover, it is also important to distinguish between open-loop and closed-loop methods. A scheme of control strategies for soft robots is shown in Figure 2.5.

Open-loop controllers allow studying robot controllability, optimizing the placement of sensors, and simulating the robot [259]. This method has been employed for manipulators [260]. However, open-loop control is not so used due to its limitations as low robustness and unreliability, since without a feedback system is impossible to correct automatically errors resulting from external perturbations. For these reasons, closed-loop controllers are preferred. Depending on the application (and especially on forces and speed), kinematics or dynamics strategies have to be employed. In either case, strategies are also model-based or model-free.

The model-based controllers are based, as their name indicates, on the kinematic and dynamic models seen in the previous section. In most cases, the PCC approach is used, which, as it does not take dynamics into account, is the best option, especially when the actuation is dynamic or hydraulic. In the case of using dynamic models, more precise control can be carried out since multidimensional dynamics are considered, but at the same time, a lot of proprioceptive feedback information is needed. [261,262]

Model-free controllers use Machine Learning (ML) model-based control techniques [263,264]. These techniques have the advantage that it is not necessary to know all the parameters of the configuration space and do not depend on the specific configuration of the robot [258]. In addition, they allow prior knowledge of the system and test the trajectories that the robot will carry out, saving time and energy, although the model can easily become

useless if any condition in its environment changes. Besides, they need a large amount of data to train the algorithm that will perform the control. That is why they are usually integrated with the best modeling technique today, the FEM, to simulate many possible scenarios. In this entire training process, the information provided by the sensors plays a fundamental role, with which it is likely that when they are integrated into the robots, they will be able to restore better proprioceptive feedback. Among the ML techniques used, we find reinforcement learning, which can dispense with the specific properties of the material and partially its structural characteristics [265] and allow controls in a closed cycle [266]. The control techniques used also depend on the type of actuators used. In [102], it is possible to see a diagram of the different controllers for different driving systems and the advantages and disadvantages they present.

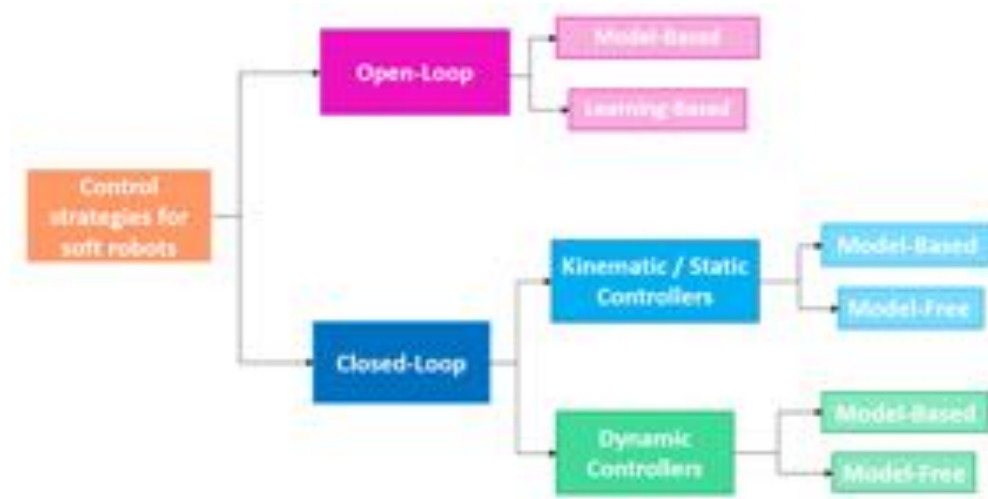


Figure 2.5 Scheme of the control strategies for soft robots.

ML techniques in soft robotics can be employed for different aims. In [267], they are categorized into main sections: sensors and actuators. A scheme of the study is presented in Figure 2.6. Usually, the expression soft robot control through ML refers to actuators' control strategies. However, in many cases, ML is helpful to extract information from sensor data or characterize or calibrate the system from a physical stimulus. The most used techniques in soft robotics, according to this study, are FF (Feedforward neural network), RNN (Recurrent Neural Network), CNN (Convolutional neural network), and kNN (k-Nearest Neighbors), among others. In addition, in the case of actuators control, reinforcement learning is also quite used, while for sensors, some unsupervised learning techniques are preferred.

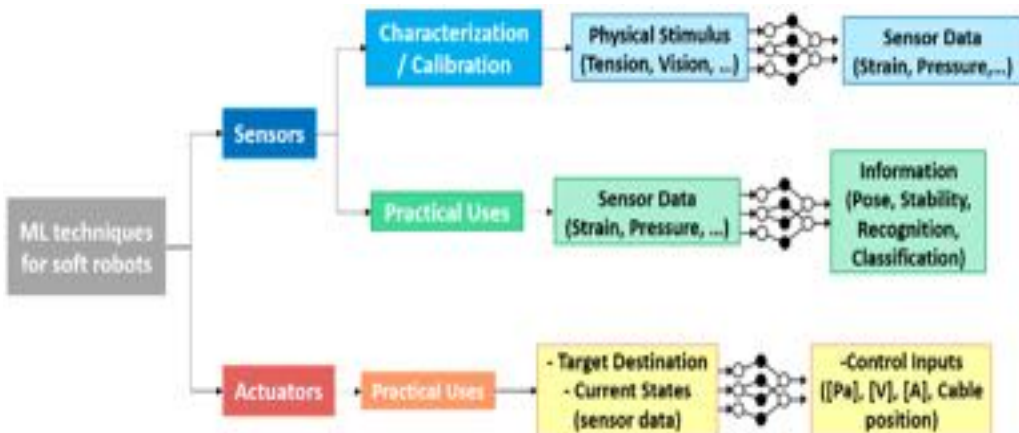


Figure 2.6 Scheme of the uses of ML techniques in soft robotics.

It is also worth mentioning a continuum-based approach for simultaneously controlling both the motion and shape of soft robots and materials (SRM) to avoid undesirable contacts. [268]

It is possible to find a detailed summary of the control for robots printed in 4D in [269]. While [270] delves into the problems of feedback in soft robots.

2.5 Conclusions

Soft robots represent the new frontier of robotics as they will allow robots to be used in fields and applications unthinkable until now. They will allow safer interactions and will be able to perform tasks impossible for traditional robots. Despite all these advantages, these robots will represent a new industrial revolution as proposed in [271], only solving all the problems and the need for advances in different aspects presented in the previous sections. For soft robots to take the step and stop being almost only investigation's prototypes, it will be necessary: (1) new materials and manufacturing techniques that allow the sensors to be embedded directly inside the robots (2) electronics and stretchable power supplies so that they do not limit the capabilities of soft robots (3) design and simulation tools suitable for soft robots and (4) new control strategies based on these advances.

Among the emerging lines of soft robotics, sustainable robots are worth mentioning, both from materials and their supply [272] and bio-hybrid robots [273].

Finally, many advances may be achieved with the union of 4D printing and FEM and machine learning techniques [269].



3. Shape Memory Alloys actuators

"Research is what I'm doing when

I don't know what I'm doing."

Wernher von Braun

This chapter presents state-of-the-art Shape Memory Alloys actuators, the principal actuators studied and employed in this work. Together with the history of this material, the advantages and challenges are explained to understand better their functioning and the decisions taken in the following chapters concerning the various spring employed.

3.1 Shape Memory Alloys

Shape Memory Alloys (SMAs) are alloys based on the shape memory transformation first reported in the 1930s when this reversible process was observed. However, it was not until 1951 that this effect was demonstrated. Later, in 1963 the Naval ordnance Laboratory developed the most famous shape memory alloys: the Nitinol alloys. This name is the union between Nickel, Titanium, and **NOL** (Naval Ordnance Laboratory).

Their employment is growing since it is possible to use these alloys both as sensors and as actuators. Also, the development of soft robotics that needs more adaptable and lightweight actuators has increased the research interest and application in various soft robots.

As it is possible to see from Figure 3.1, the number of publications is constantly increasing, demonstrating how interest in these alloys is growing despite being known and used for many years. Figure 3.2 shows which countries are mainly investigated SMA applications.

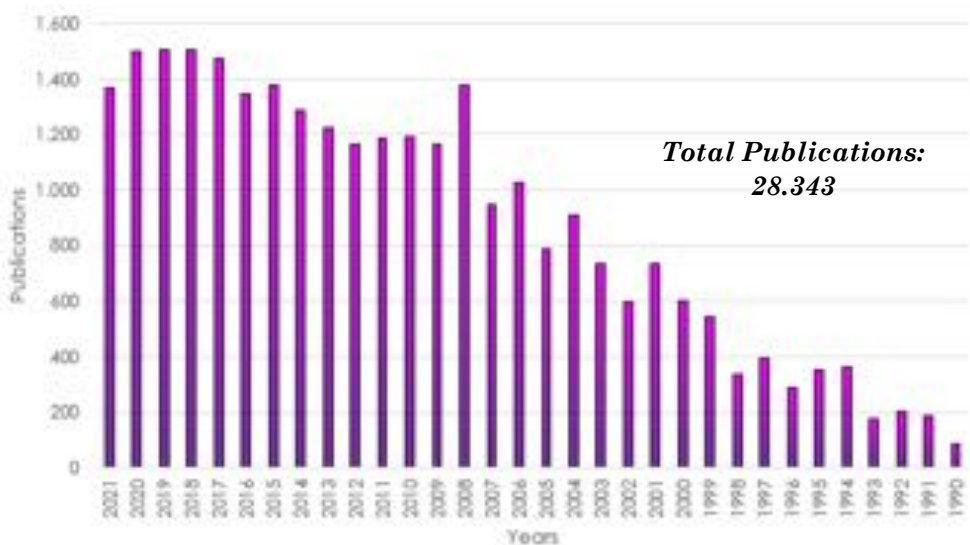


Figure 3.1 Number of articles related to “shape memory alloys” in the last 32 years. Source: Web of Science (Access Date: 30/11/2021).



Figure 3.2 Diagram of the top fifteen countries for publications in SMA (1º China, 2º USA, 3º Japan, 4º Germany, 5º Russia, 6º France, 7º India, 8º Spain, 9º Italy, 10º South Korea, 11º Iran, 12º Canada, 13º England, 14º Poland, 15º Australia)

SMA have been used in many different applications due to their characteristics. In Figure 3.3, the main categories of publications in Web Science are presented. This diagram shows how studies related to these alloys are regarded, especially materials science, followed by the automation control system and robotics, optics, construction building, biomedical applications (Dentistry Oral Surgery Medicine, Surgery, Orthopedics, Cardiology), and acoustics.

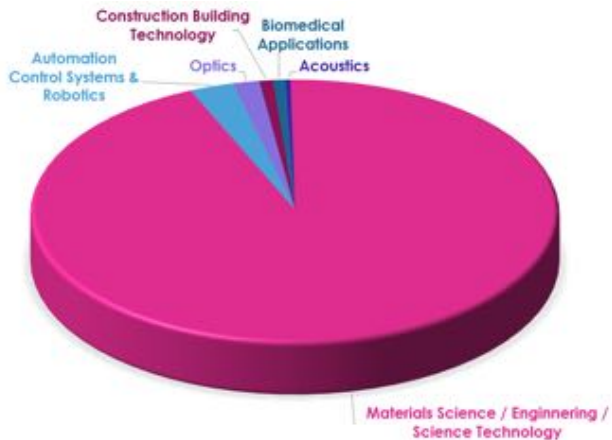


Figure 3.3 Main categories of publications. Source: Web of Science (Access Date: 30/11/2021).

Other applications fields are automotive and aerospace. In robotics they have been applied in bio-inspired robots [274], miniature robots [275], wearable robots [276], origami robots [277], reconfigurable robotic end-effectors [278,279], self-reconfigurable modular robots [280], medical applications [281,282], between many others. In [283], a review of shape memory alloy applications is available.

Shape memory alloys have the ability to remember a shape and return to this shape after deformation. SMAs can be “plastically” deformed at low temperatures, but this “plastic” strain can be recovered by heating the alloys. This is called the shape memory effect (SME).

This effect is based on the presence of two stable crystalline phases: martensite (or α -phase), which is thermodynamically stable at a lower temperature, and austenite (or β -phase), which is the parent phase stable at higher temperatures. Martensite presents a crystal structure with low symmetry, which type depends on the composition of the alloy, while austenite has a higher symmetry usually based on a cubic lattice. [284] (Figure 3.4)

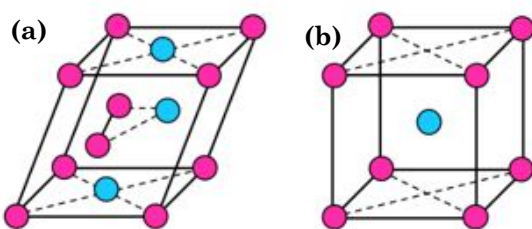


Figure 3.4 Crystal structure of martensite (a) and austenite (b). [284]

At low temperature, the alloy is in the martensite phase (M_f) and it is relatively soft and easily deformable. The molecular structure in this phase is twinned, as shown in Figure 3.6. Applying a force, this phase changes in detwinned. Thus, to recover the memorized shape is necessary to heat the alloy, the temperature A_s (Austenite start) marks the beginning of the austenitic transformation until A_f (Austenite finish), that corresponds to the complete recovery of the shape and the moment in which SMA can realize force. The alloy starts to cool and M_s (Martensite start) marks the beginning of martensitic

transformation until M_f (Martensite finish). These temperatures are shown in Figure 3.5. ΔT_H represents the transformation temperature hysteresis, and it is the difference in the transformation temperatures (from martensite to austenite, and from austenite to martensite). The transformation hysteresis can be defined as the difference between the temperatures at which the material is 50% transformed to austenite upon heating and 50% transformed to martensite upon cooling. Typical values for binary NiTi alloys are about 25 to 35 °C. [285]

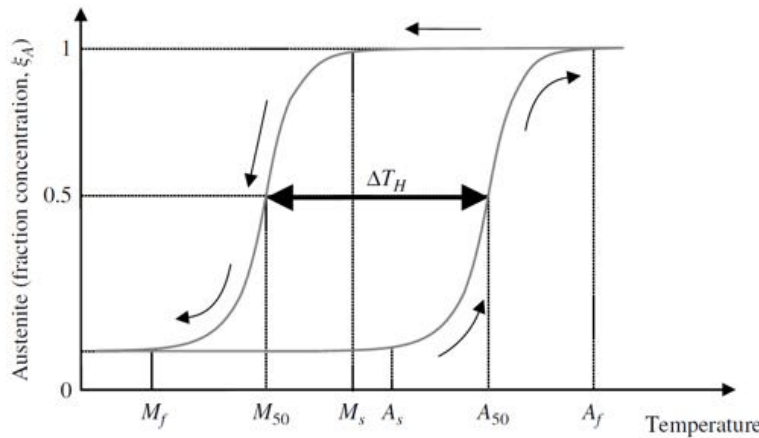


Figure 3.5 Transformation temperatures in shape memory alloys. [286]

As it is possible to see in Figure 3.6, the transformation from austenite to martensite needs a rearrangement of the alloy microstructure. Martensite presents two structures: one when undeformed and not subjected to forces (Twinned Martensite, point 1), and one when deformed and subjected to a force (Detwinned Martensite, point 2). The deformation also remains when the load is removed (2-3). The temperature progressively increases to recover the shape until the austenitic phase; the shape is maintained when the alloy cools down. [287]

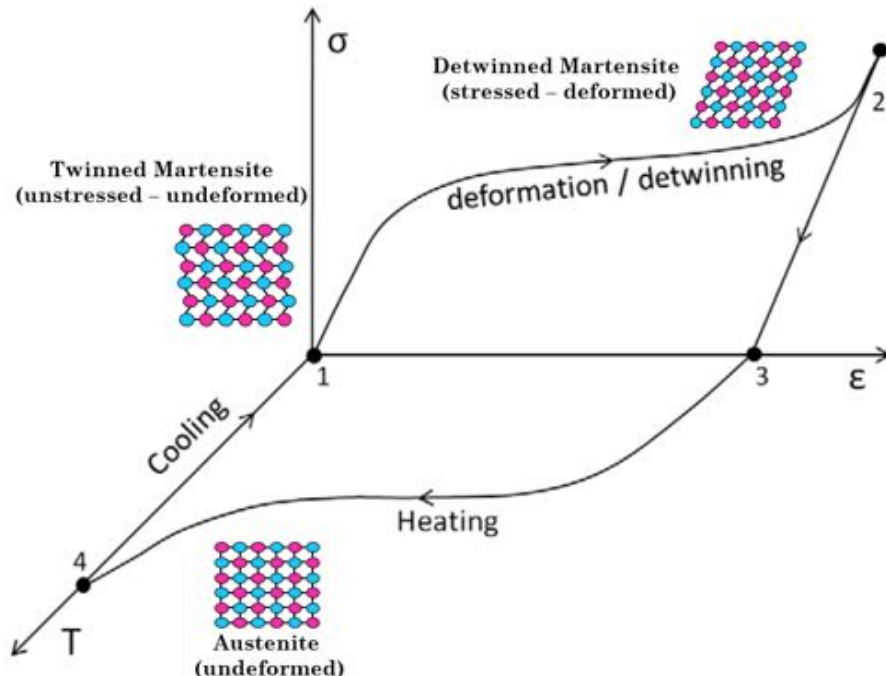


Figure 3.6 Representation of the thermo-mechanical behavior of an SMA, showing the dependency among temperature, T , stress, σ , and strain, ε , and the related crystal structures.[287]

Many properties change during the phase transformation, as explained in [288], like electrical resistivity, thermoelectric power, electromotive force, Yield strength, Young's modulus, damping, internal friction, thermal conductivity, heat capacity, and latent heat.

SMA alloys do not show all the same behavior, but they can present the following properties depending on the martensitic transformation they realize [289]:

- (1) **One-way shape memory effect.** It is the most common SMA alloy able to recover the high-temperature austenitic shape upon heating. However, to observe this transformation, it is necessary to deform the material in the low-temperature martensitic state.
- (2) **Two-way shape memory effect** (or reversible shape memory effect). These alloys can recover a preset shape upon heating above the transformation temperatures and return to another shape upon cooling.
- (3) **All-round shape memory effect.** It is a particular case of previous and differs from it for a more significant amount of shape and symmetry between the high and low-temperature shapes.
- (4) **Hysteresis behavior.** The Martensite to austenite occurs over a higher temperature range than the austenite to martensite transformation. The considered temperature is that at which the half transformation has already happened.
- (5) **Superelasticity.** These alloys can return to their original shape upon unloading after substantial deformation.
- (6) **Vibration damping capacity.** SMAs exhibit all-metal materials' highest vibration damping properties [290].

Other essential aspects of SMA are the life cycles. They depend on a stress-strain trade-off. As it is possible to see in Figure 3.7, when strain increases, stress has to decrease to achieve a good fatigue performance

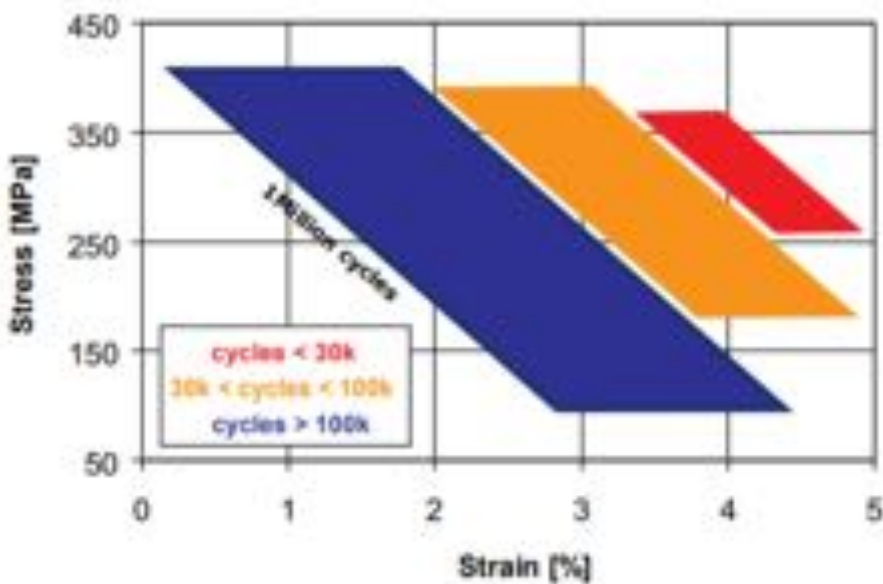


Figure 3.7 Fatigue behavior [291]

As already said, the two principles configuration of SMA are wires and springs. The graphs below (Figure 3.8 and Figure 3.9) show that SMA actuators present a very high specific working output confronting other actuators' technologies. It is also interesting that springs exert lesser force than wires with the same diameters. However, wires can only present a

contraction equal to 2%-5% of their original length, while springs can be deformed more significantly, allowing a greater displacement. This explains why in this work, only SMA springs have been employed.

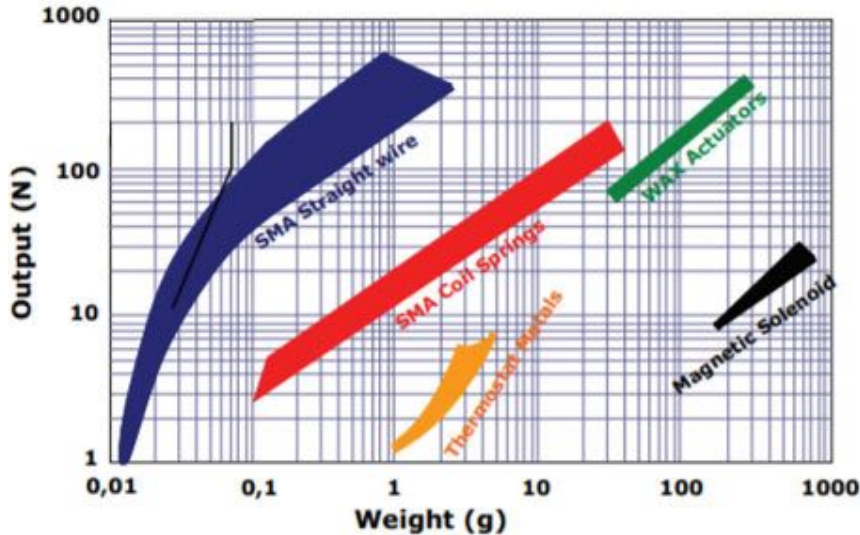


Figure 3.8 Comparison of different actuators technologies [291]

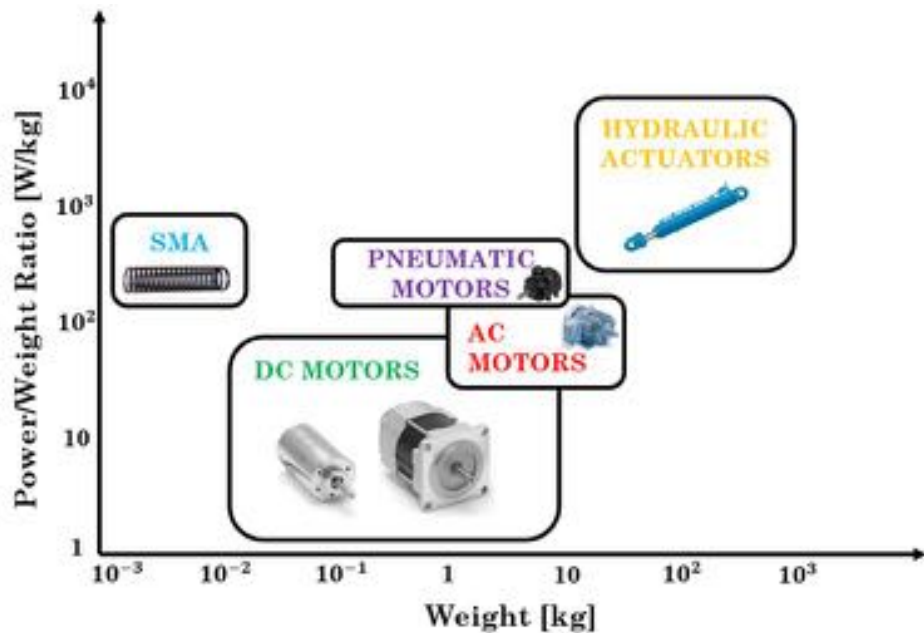


Figure 3.9 Adapted from [292] The power/weight ratio versus the weight of different actuation technologies.

As already mentioned, the SMAs' speed functioning is highly affected by the cooling process, which is greatly affected by heat sinking and design features. As Dynalloy indicates [293], one of the simplest ways to improve cooling speed is to use a smaller diameter wire since the more surface to mass the wire has and the faster it can cool. For this reason, it is better to use multiple wires in parallel to exert the same force of a single wire with a greater diameter. A higher temperature wire also improves the cooling time due to the higher temperature differential between room temperature and the wire temperature, causing a faster rate of heat loss.

It is also possible to improve cooling with external methods as forced air, heat sinks, increased stress (to raise the transition temperature), and liquid coolants. Combinations of

these methods are also effective. Considering all the above, cooling time can range from several minutes to fractions of milliseconds by effective and proper heat sinking.

Figure 3.10 shows how spring shape changes during phase transformation. Initially, the spring is stretched (1); when temperature increase, it starts to recover the shape (2) partially, until (3), when springs cannot contract more. From this moment, spring begins to cool down (4) until room temperature (5), but it maintains the memorized shape. To start a new cycle, it is necessary to deform the spring again.

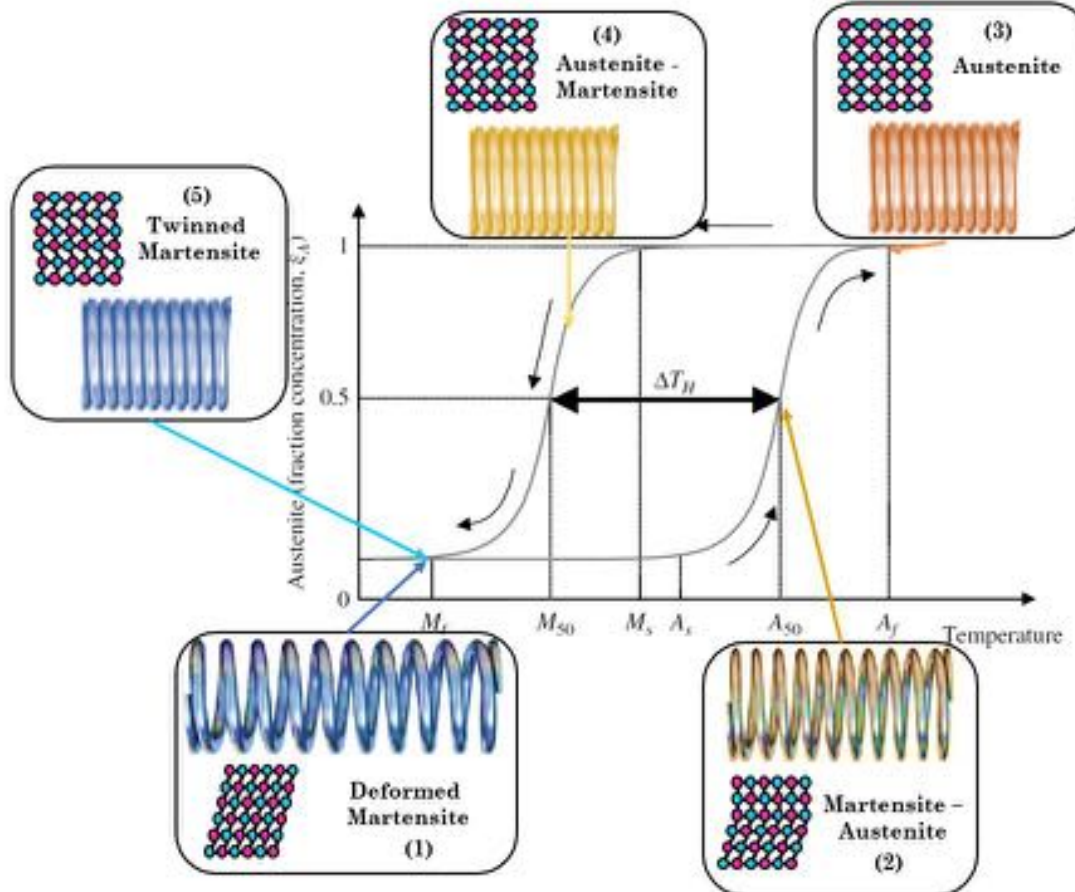


Figure 3.10 One-way shape memory effect in a Nitinol spring.

The SMA spring can operate as a two-way actuator, as explained in [294], placing a bias spring with a fixed-grip on one side of the SMA favors the recovery of the spring since, as it cools and gives way, the system will return to its initial disposition (or at least close to it) (Figure 3.11).

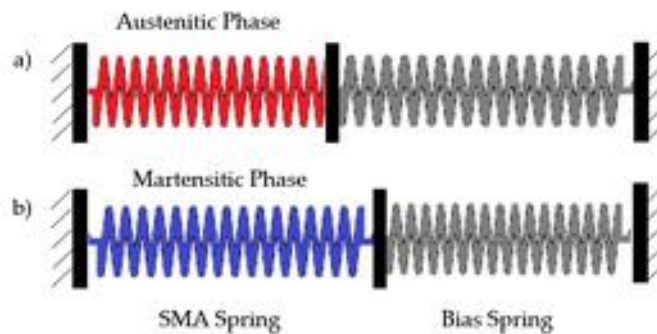


Figure 3.11 Bias spring concept

Figure 3.12 shows load-deflection curves of an SMA spring and bias spring. The slopes of the SMA spring and bias spring's load-deflection curves are spring constants and have opposite signs since they move in opposite directions. For instance, if there is an external force, the stroke is shortened to S_t' , for example. It also shows that a larger stroke can be obtained when the spring constant is small.[295]

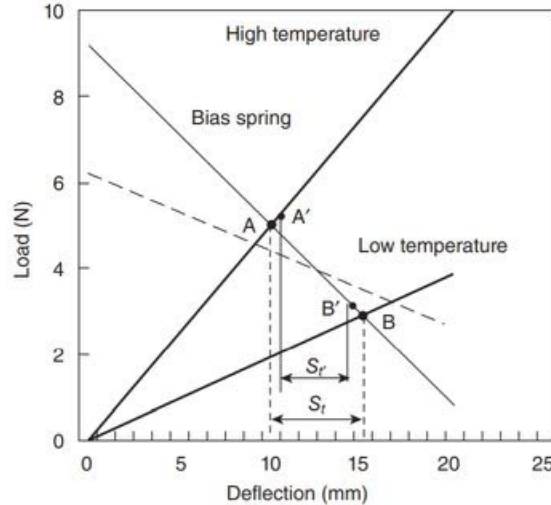


Figure 3.12 A load-deflection diagram for the SMA spring and bias spring in the two-way SMA actuator.[295]

3.2 Fabrication of SMA springs

SMA can be fabricated using different techniques, as shown in [296]. The most used are the melting techniques (vacuum melting, electron beam melting and plasma melting). Other techniques are powder metallurgy, thermal spray, thin-film fabrication, and heat treating. SMAs can usually be acquired as threads or springs. Threads through a thermal treatment can memorize a new shape depending on the application. In some prototypes shown in the following chapters, like the starfish Asforb, the jellyfish JellyRobcib, or the soft manipulators Ruăn, the springs used were manufactured from threads undergoing heat treatment.

The force that a spring produces at a given deflection depends linearly on the material's shear modulus. SMAs exhibit a significant temperature dependence on the material shear modulus. The relationship between shear modulus and temperature for SMAs is given by (Equation 3.1) [297]:

$$G = \begin{cases} G_M & \text{when } T < M_f \text{ and } T < A_s \\ G(\gamma, T) & \text{when } M_f \leq T \leq A_f \\ G_A & \text{when } T > A_f \text{ and } T > M_s \end{cases} \quad (3.1)$$

Where G is the shear modulus of SMAs.

When the SMA wire is heated or cooled, the heat balance equation is

$$\rho_1 c V \frac{dT}{dt} = -hA(T - T_f) \quad (3.2)$$

where ρ_1 is the mass density of SMA, c is the specific heat, V is the volume of SMA exposed in air, t is the time, h is the heat exchange coefficient, A is the superficial area of SMA, and T_f is the temperature of airflow.

In a typical steel coil spring, the relationship between the axial force F and the deflection δ can be described considering the torsional moment [298]:

$$F = \frac{Gd^4}{8D^3n} \delta \quad (3.3)$$

Where D is the spring diameter, d is the wire diameter, n is the number of active coils, and G is the shear modulus (Figure 3.13).

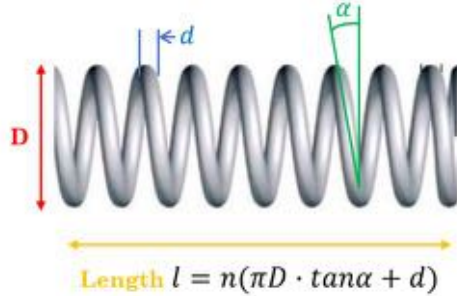


Figure 3.13 Geometric parameters of SMA spring

For a large deformation of the SMA coil spring actuator, the torque, bending moment, coil spring pitch angle, and spring diameter reduction are all assumed to be nonzero. The shear force, axial force, and coil spring curvature effect are ignored since they are small compared to the torsional and bending moments [297]

The shear stress is described as:

$$\tau = k \frac{8FD}{\pi d^3} = k \frac{8FC}{\pi d^2} \quad (3.4)$$

Where C is the spring index $C = D/d$ and k is the Wahl correction factor

$$k = \frac{4C - 1}{4C - 4} + \frac{0.615}{C} \quad (3.5)$$

τ and G are related as following with the shear strain γ

$$\tau = G \gamma \quad (3.6)$$

The stretch of spring under the load F is:

$$\delta = \frac{8FD^3n}{d^4 G} \quad (3.7)$$

The relationship between compressed length δ and shear strain γ for SMA spring is given by

$$\delta = \frac{n\pi D^2}{d} \gamma \quad (3.8)$$

The wire diameter for the actuator can be obtained from (3.4) for acceptable values of C ranging from 3 to 12:

$$d = \sqrt{k \frac{8FC}{\pi \tau}} \quad (3.9)$$

The number of turns in the spring can be obtained from (3.8):

$$n = \frac{\Delta \delta d}{\pi \Delta \gamma D^2} \quad (3.10)$$

Once geometrical parameters have been selected, it is necessary to manufacture SMA springs. The process recommended consists of three steps [299]:

1. Constrain the Nitinol in a metal fixture in the desired final shape (in this case, it was a screw, as shown in Figure 3.14)
2. Heat the part and fixture for 10 minutes in an air furnace (Figure 3.15) at a temperature of 500 °C (it is important to remember that time depends on wire diameter) and
3. Quench the part and fixture in room temperature water to define the heating time and avoid aging effects sharply.



Figure 3.14 Nitinol wire constrain in a screw with two nuts.



Figure 3.15 Air furnace used.

Custom springs present many advantages. The first is that the commercial supply of wires is greater than that of springs, so the range of available diameters makes it possible to choose the one that best suits the application developed. Springs' length can also be selected. The wire is also cheaper, and it is possible to fabricate multiple actuators from it. However, it is not easy to know precisely the parameters to carry out the memorization process correctly, and although the springs thus manufactured have proven to work properly, they lost shape memory quite quickly.

Moreover, it was not possible to perform reliable simulations since between springs performed at different times, even with the same procedure, it was noted that not all showed precisely the same behavior (some recovered their shape more quickly upon reaching the transformation temperature than others). For these reasons, all wearable prototypes have been fabricated with SMA springs industrial manufactured to obtain a

more homogenous behavior. FEM analysis has been realized to verify if they can realize the necessary strength to choose these springs.

3.3 Finite Element Analysis of SMA springs

Shape memory alloys can be modeled differently, as explained in [300], since any framework can consider the multiscale physical phenomena of SMA deformations today. Thus, four categories have been individuated, (1) the macro-phenomenological (FEM), (2) micromechanical, (3) molecular dynamics (MD), and (4) first principles models (Density Functional Theory- DFT).

These models present differences in the lengthscale-wise considered governing principles, modeling emphasis, and core assumptions. In this work, the first category was employed to model the springs used since finite element analysis have been performed. These analyses consider macroscale attributes like stress, strain, temperature transformation, and fatigue properties. The mathematical formulation is based on phase transformation, metal plasticity, and thermodynamics. The empirical values of the specific SMA are necessary to run a proper simulation (e.g., Young's moduli, transformation stress and temperature, strain). As in many other cases, FEM simulations allow reducing costs associated with trial-and-errors experiments and allow choosing the correct spring for the application. It is important to highlight that this type of simulation does not consider microscopic deformation phenomena like the grain-level deformation phenomena.

FEM analysis was realized with Ansys software [301]. The second-order tensor, E_{in} , is defined as transformation strain to measure the strain associated with the phase transformation:

$$0 \leq \|E_{in}\| \leq \varepsilon_L \quad (3.11)$$

where ε_L is a maximum value norm of E_{in} in the phase transformation after fully transformed.

The stress, σ , is therefore expressed in terms of strain:

$$\sigma = L:(E - E_{in}) \quad (3.12)$$

During the transformation, the transformation stress is defined as:

$$X_{tr} = \sigma - [\tau_M(T) + h\|E_{in}\| + \gamma] \frac{E_{in}}{\|E_{in}\|} \quad (3.13)$$

Where $\tau_M(T) = \beta(T - T_0)$ is a positive and monotonically increasing function of the room temperature, T, and the material-dependent temperature, T_0 , below which no twinned martensite occurs. β is a material parameter. The material parameter h is associated with the hardening of the material in the phase transformation.

γ is defined by:

$$\gamma \begin{cases} 0 & \text{if } 0 \leq \|E_{in}\| \leq \varepsilon_L \\ \gamma \geq 0 & \text{if } \|E_{in}\| = \varepsilon_L \end{cases} \quad (3.14)$$

The evolutionary equation for E_{in} has the following form:

$$E_{in} = E_{in}(n) + \Delta\xi \frac{\partial F}{\partial \sigma} \quad (3.15)$$

where the limit function F is given in terms of the transformation stress X_{tr} and the elastic domain radius R in the form of the Prager-type limit function:

$$F(X_{tr}) = \sqrt{2J_2} + m \frac{J_3}{J_2} - R \quad (3.16)$$

Where:

$$\begin{cases} J_2 = \frac{1}{2}(X_{tr}^2 : 1) \\ J_3 = \frac{1}{3}(X_{tr}^3 : 1) \end{cases} \quad (3.17)$$

In addition to Young's modulus and Poisson's ratio of martensite and austenite, six other parameters are defined: M, R, h, T0, β, and ε_L

Nitinol spring characteristics are shown in Table 3.1.

Table 3.1 Nitinol springs' characteristics.

Nitinol Springs Dimensions	
Total length including eyelets	25 mm
Outer diameter	6 mm
Cable diameter	0.75 mm
Number of coils	21
Activation temperature	65 °C

A first estimate of the spring force has been calculated with Equation (3.8) [298]:

$$F = \frac{\tau_a \pi d^3}{8D} \quad [\text{N}] \quad (3.18)$$

The maximum force that the spring could carry out was about 12 N, being τ_a the maximum shear stress, d the wire diameter, and D the spring diameter. Unfortunately, the seller did not provide the mechanical properties of the material. So, the maximum shear stress ($\tau_a = 450$ MPa) provided by another seller (in this case by the SAES getters group [291]) was used.

Finite element simulations were realized to validate this value. For the same reason as before, the values recommended by Ansys in their guide [301] have been used. They are shown in Table 3.2.

Table 3.2 Material parameters used for simulation of SMA helical spring.

Material Properties for a Spring Actuator	Values
Density (kg m ⁻³)	4650
Elastic modulus for austenite phase (MPa)	51700
Elastic modulus for martensite phase (MPa)	51700
Poisson's ratio	0,33
H (Hardening Parameter) (MPa)	1000
R (Elastic Limit) (MPa)	140
B (Temperature Scaling Parameter) (MPa K ⁻¹)	5,6
T ₀ (Reference Temperature) (K)	250
M	0
Maximum Transformation Strain (mm mm ⁻¹)	0,04

The force exerted by the spring does not depend directly on the number of turns, as shown in the formula (1). Therefore, the simulated spring (shown in Figure 3.16) presented a lower number of turns (5 instead of 21) to reduce the computational cost and simulation time. The spring had fixed support at one end, while it presented a force that acted by stretching the spring at the other (Figure 3.16a).

A nonlinear static analysis is performed using large-deformation (NLGEOM, ON) and unsymmetric matrices for the full Newton-Raphson method (NROPT, UNSYM). The simulation consists of 4 main steps: (1) the spring is deformed by applying about 10 N of force at room temperature; (2) the force applied is removed, and the spring does not recover its shape and maintains the plastic deformation; (3) no force or heat was applied to the spring, thus simulating its normal operating condition once mounted on the glove; and (4) the activation temperature provided by the seller was applied and, the spring fully recovers its shape, leaving zero initial deformation. Figure 3.17 shows how to change the spring shape during simulation. Figure 3.18 shows the force and thermal conditions applied and the resultant deformation.

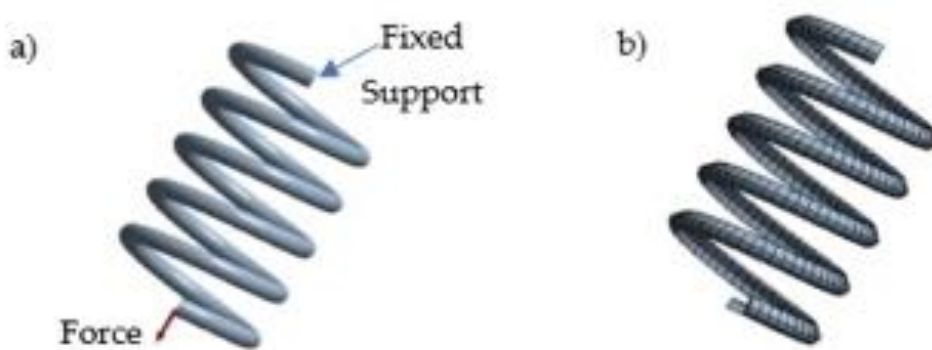


Figure 3.16 Model of the SMA spring (a) the geometrical model and boundary conditions, (b) finite element model (SOLID185 elements).

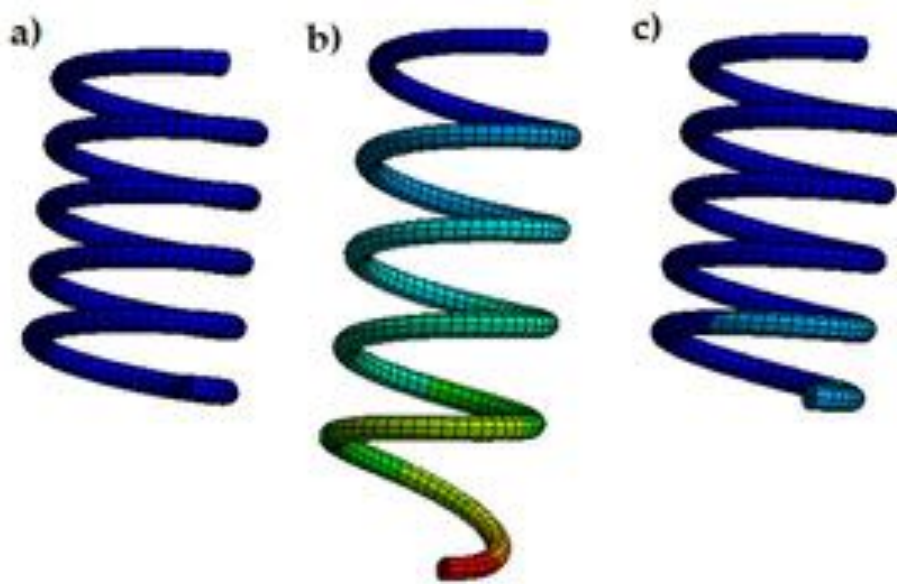


Figure 3.17 Deformed shape compared with undeformed shape. (a) spring at the initial step 0, (b) deformed spring after step 1, (c) the spring recovers its shape after heating.

After applying an initial force of 12 N, the spring does not fully recover its shape. Therefore, the first estimate of the force was quite correct.

Several simulations have been performed, varying the initial load to which we subjected the spring, and therefore varying its initial deformation and keeping the thermal excitation the

same, we observed that the contraction varied. It gave rise to variations in the resultant force as a function of the initial deformation, verified experimentally later. Simulations also showed a higher deformation in the areas furthest from the anchor, as we will see in the tests.

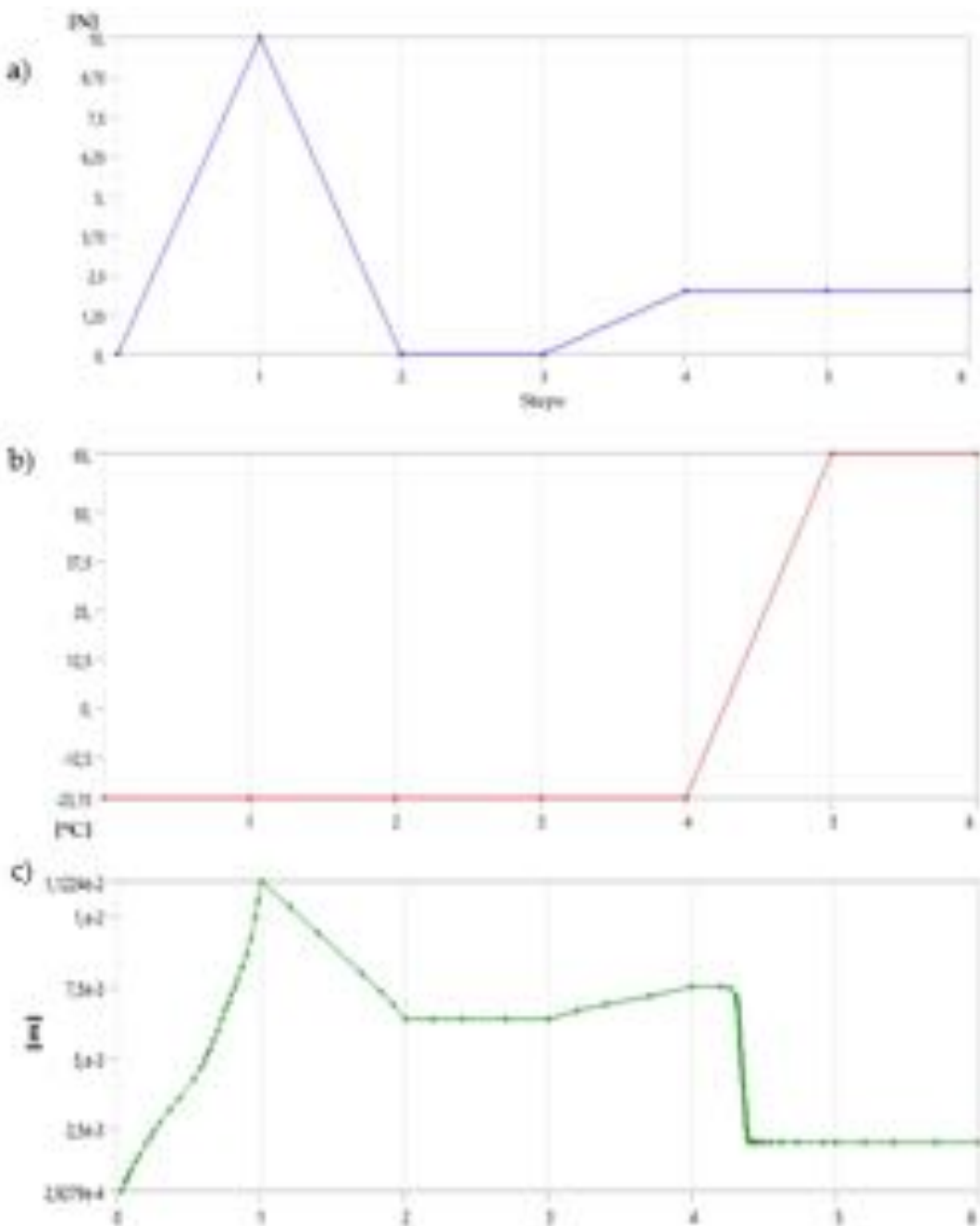


Figure 3.18 SMA spring analysis. (a) the force applied for each step, (b) thermal conditions applied for each step, (c) total deformation.



4. Bio-inspired soft robots

*" Science may set limits to knowledge,
but should not set limits to imagination."*
Bertrand Russell

Bio-inspired soft robots are the first group of soft robots discussed as bio-inspiration is the starting point of this field. Here the development of soft starfish and jellyfish are presented. The design, actuation, and control are presented for each of them.

Further information on this section can be found in original scientific publications [16].

Also, an explanatory video of some of these robots can be found in the Electronic Supplementary Material (Video [S. 1](#)).

4.1 State of the art

Many animals like octopuses, worms, or caterpillars, have been studied to learn how their body can be so soft and hard at the same time and how to reproduce it in a robotic version.

Soft materials allow soft bioinspired robots to replicate the movements of animals in both terrestrial and marine habitats. In the case of the underground environment, some of the most significant prototypes are worm-like robots [302–304], caterpillars [23], snakes [305,306], insects [146], and bat wings [307,308]. In the case of the underwater environment, research focuses on the development of prototypes that replicate the movement of fishes [309–313], octopuses [18,314,315], and jellyfishes [316–319]. Other interesting prototypes are the quadruped robot that walks underwater [320], the Manta swimming robot [321]s, biomimetic underwater robots based on dielectric elastomer actuators [322], or rajiform swimming robot [323]. These robots present different actuation systems that can be summarized into three main categories: variable length tendon, fluidic actuation, and electroactive polymer (EAP) [324]. The first category (variable length tendon) comprises robots actuated with traditional tendons and motors [325]and robots actuated with shape-memory alloy (SMA) [326,327].

One of the most famous robotic starfish is the pneumatic starfish realized by Harvard University. It was a lightweight robot that could perform fast movements (4 cm per sequence) [75]. It presented four limbs; each of these legs was actuated independently. Robotic starfishes that employ SMAs actuators try to imitate the movements of a starfish by moving its tentacles. In [110] was presented a starfish made up of SMSs (independent modular units for soft robots) capable of generating a planar, fast, and high bending range movement via the SMA wires embedded in their multilayer structure. SMA springs have been employed [22] or [328] in other cases. This last starfish stands out for its excellent results. It is capable of going in different soils with good performance in sandy soils. Exists also a starfish actuated by motors. It can move the limbs independently, allow movement by performing wave sequences, and support loads of up to 350 grams [105].

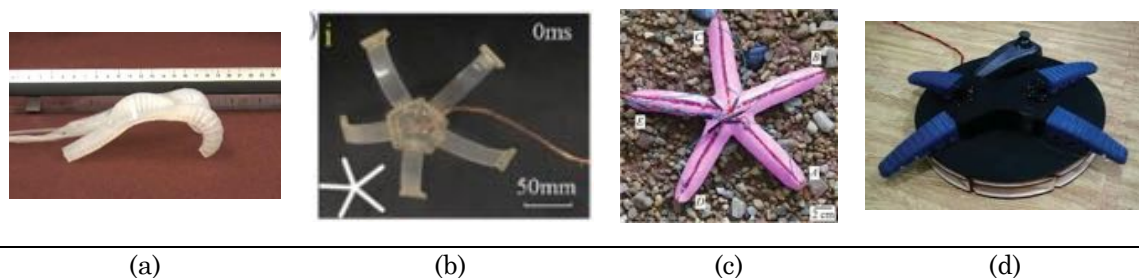


Figure 4.1 (a) The multigait soft robot [75] (b) The SMSs starfish [110] (c) Starfish with SMA springs [328] and (d) the quadrupedal starfish robot [105]

One of the first jellyfish prototypes, developed by the University of Kagawa (Figure 4.2a), used the conductive ionic polymer film (ICPF) as an actuation system [315]. It generates contractions using an articulated mechanism. The Virginia Center of Investigation realized the subsequent representative development that created a jellyfish using SMA named “Robojelly” (2011). It has a polyethylene coverage, inspired by the *Aurita Aurelia* species. When the SMA is activated, it produces a reaction with the water that generates hydrogen that helps the displacement [316]. A jellyfish robot was implemented based on a spring retraction mechanism (Figure 4.2b) [317]. It was controlled by servomotors and had a silicone body capable of generating a unilateral contraction. Another prototype based on the same operation principle, but actuated by elastomers producing an expansion to expel the water, is presented in [318]. Within the most recent developments in 2018, the University of Atlantic Florida implemented a jellyfish operated by air microvalves, capable of generating a lateral movement limiting airflow to four of the eight tentacles (Figure 4.2c)

[319]. In 2019, a jellyfish operated by SMA capable of moving vertically was developed thanks to a central SMA (Figure 4.2d) [320]. One of the last works developed is a soft jellyfish with a diameter of 3 mm actuated through an external oscillating magnetic field, capable of generating movements with a degree of vertical inclination of the body.

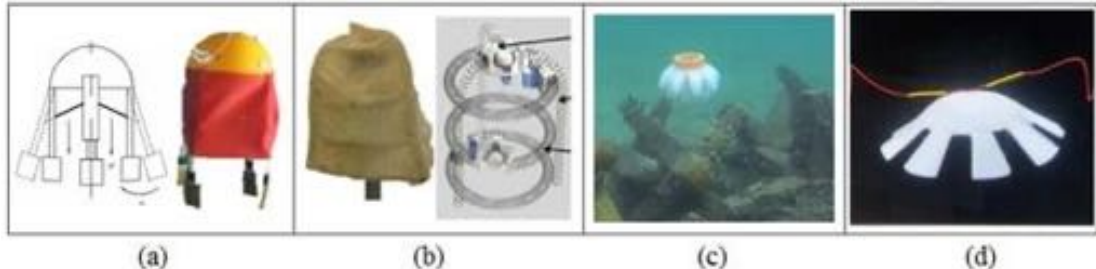


Figure 4.2 (a) Bell-shaped mechanism that generates a contraction. (b) Jellyfish actuated by spring retraction. (c) Jellyfish act pneumatically. (d) Jellyfish capable of performing only vertical movements using a shape-memory alloy (SMA).

Despite various developments focused on jellyfish with different performances, no significant progress was made in obtaining lateral movements, especially in the control algorithms. Furthermore, implementing control systems to generate coordinated movements through defined trajectories, especially SMA, has not been emphasized. Additionally, previous works have not focused on specific applications for this kind of robot.

4.2 Asforb, a bio-inspired soft robotic starfish

Asforb is inspired by the Forbes Seastar (or *Asterias Forbesi*, a species of starfish in the family Asteriidae). It usually presents five arms (sometimes 4 or 6) and grows to about 15cm in diameter with an arm length of about 6 centimeters. Starfish dimensions are generally ranging between 12 and 24 cm.

Starfish present on the lower part some tiny tentacles, as can be seen in the following figure with which they realize the displacement. It has served as inspiration for the spring placement (Figure 4.3).



Figure 4.3 From the starfish to Asforb. (a) Forbes Seastar. (b) Asforb underside. (c) Asforb topside.

The soft robot designed (Asforb) presents five limbs. The number of limbs was chosen according to the results shown in [328]. In that work, starfish with different numbers of limbs were realized (from 1 limb up to 5 limbs). The conclusion shows that the addition of limbs improves performance and that the soft robot with five limbs can move faster than the other prototypes.

Silicone was the material selected to realize the body of the starfish due to its softness and elasticity. Two different types of silicone were considered: the Ecoflex™ 00-30 and the Silastic™ 3483. They are two of the most used silicones in soft robotics. In the following table (Table 4.1), the main characteristics of the two materials are compared.

Table 4.1 Comparison of material properties between Ecoflex 00-30 and Silastic 3483

Properties	Ecoflex™ 00-30	Silastic™ 3483
Colour	Translucid	White
Mixed viscosity [mPa s]	3000	16.000
Curing time [hours]	4	24
Hardness (Shore A)	0-30	13
Tensile strength [MPa]	4.5	3.9
Elongation at break [%]	300	680
Tear strength [kN/m]	8	25
Relative density at 25°C	1.07	1.16
Linear shrinkage [%]	< 0.1	0.2-0.4

The final decision fell on the Silastic 3483 since the body needed not to be as soft as using the Ecoflex 00-30 without losing its softness or the ability to bend the limbs effortlessly. In all cases in which the body of the soft robot is made up almost entirely of soft material, it is necessary to find the material that gives the best compromise between rigidity and softness and allows the body to support itself.

To confirm that this choice was correct, it was decided to realize two Asforbs with both materials. Therefore, a mold in which poured silicone was designed with the CAD software Autodesk Inventor.

The design consists of an internal 18 cm circular concentric pattern. It represents the final starfish dimension. Regarding thickness, which is the depth of the mold, it is 0.7 cm, although later it was reduced to 0.5 cm. The length of each limb taken from the vertex to the center have a value of 7 cm. Limb's width varies along its length. In the center, it is almost 3 cm. The mold was 3D printed in ABS.

In the following figures (Figure 4.4), the printed mold and its CAD model are shown.

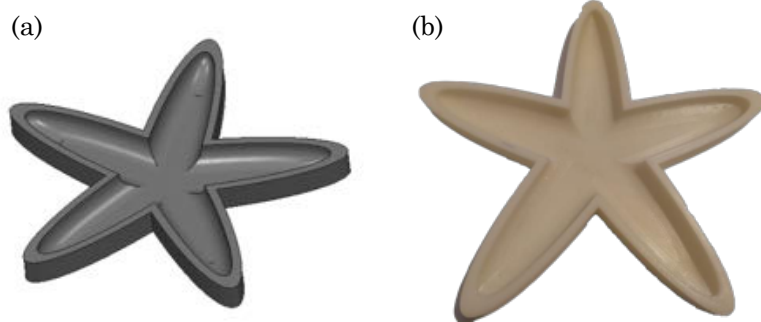


Figure 4.4 Mold. (a) CAD model of the mold. (b) the 3D printed mold

The actuators chosen for the star are SMAs springs. The choice of actuators has been explained in chapter 3. Therefore, only the design and use of them in this prototype will be explained in this chapter.

Experiments with one limb are carried out with springs of two cable diameters: 0.3mm and 0.5mm in diameter. They led to the conclusion that a 0.5 mm diameter had enough force to compress the leg but needed more voltage. On the other hand, the cable with a smaller diameter did not have enough force to realize the compression of the leg.

The electronic system is actuated by an Arduino UNO board that supplies five PWM outputs with which the five limbs of the robot are activated. Due to its low voltage, SMA springs cannot be activated by Arduino, so an additional power source (12 V and 12 A) is needed.

The primary electrical circuit is outlined in Figure 4.5. It presents a 540N MOSFET transistor, a resistance, an Arduino, and a power source. The MOSFET is used to switch the signals and thus control the voltage that enters the Nitinol.

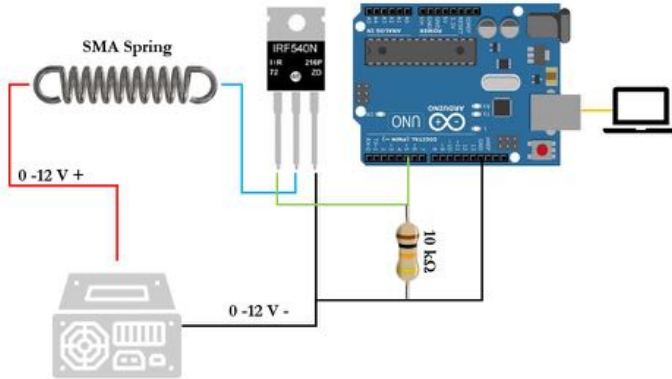


Figure 4.5 Scheme of the primary electrical circuit

As shown in Figure 4.6, five circuits similar to the previous one are realized for the five limbs since each actuator is independent of the others. The global circuit present also a led (and its resistance) connected to each Mosfet to verify the proper functioning of the circuit.

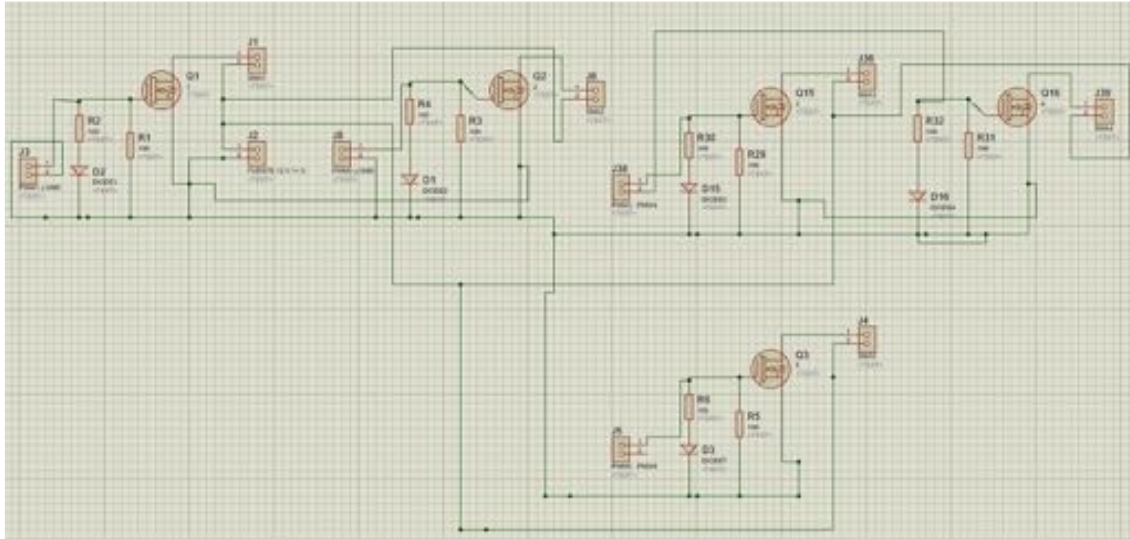


Figure 4.6 The electric circuit for the five limbs

Then the circuit has been realized with a PCB with the necessary components. The final result is shown in Figure 4.7.

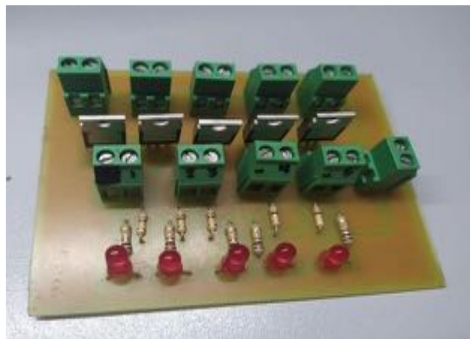


Figure 4.7 The final circuit

The connection between the SMA and the wire is realized with a staple that catches them together. In Figure Figure 4.8, it is possible to see with more detail this connection.

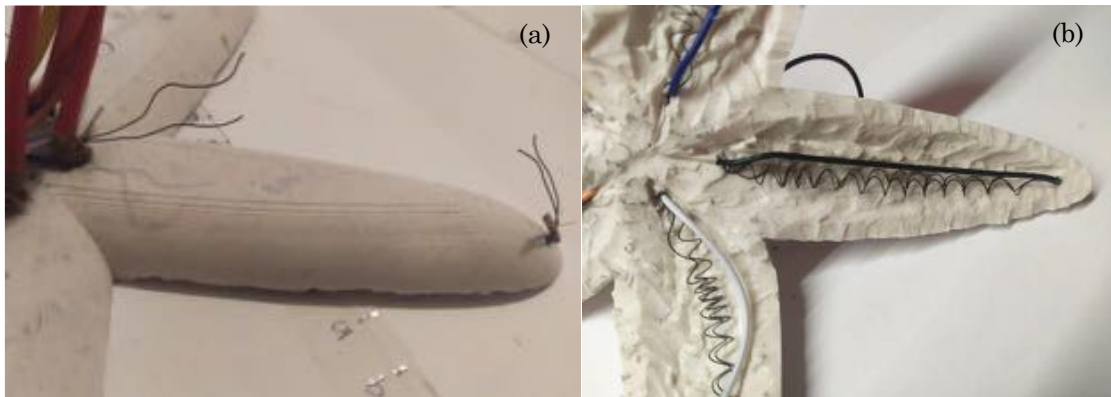


Figure 4.8 Detail of the connection between the SMA and the cable. (a) Topside view. (b) Underside view.

The control of the robot, as explained above, will be carried out through the emission of PWM signals by an Arduino UNO board. The code is written in the default Arduino application, Arduino IDE. The PWM signal is translated into the Nitinol reaction speed due

to proportionate current intensity. The objective is that around 2.5 A circulates through the Nitinol actuator, although it will be seen that it could be necessary to work with more or less amperage. Also, this value depends on the type of spring. The following Figure 4.9 shows the variation of the contraction speed with the amperage supplied to a 0.3 mm spring.

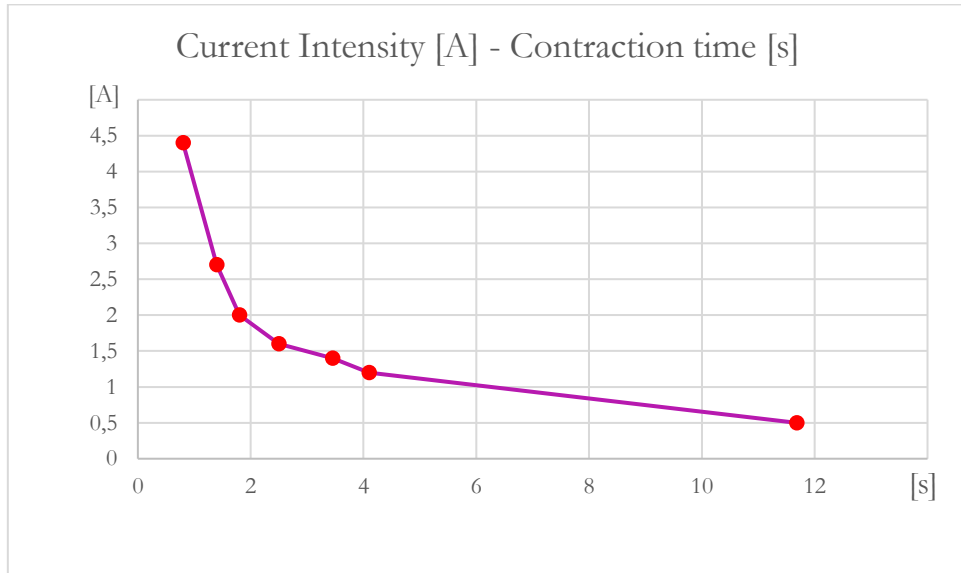


Figure 4.9 Graph of the variation of the contraction speed with the amperage supplied to a 0.3 mm spring.

4.2.1 Choice of movement patterns

For the choice of movement patterns, previous projects have been taken into account, and two types of movement patterns, as shown in the following Figure 4.10, have been tested.

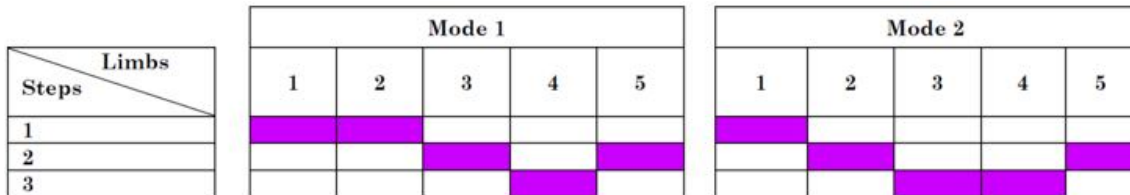


Figure 4.10 Scheme of the two possible activation modes

In mode 1, extremities 1 and 2 initially move, and once they are contracted, the same process is carried out for 3 and 5, and finally, the contraction of limb 4. Theoretically, the process is simple. However, the heating and cooling times have to be considered. During the activation of 3 and 5, 1 and 2 have to continue to be activated. In the same way, proceed to lift leg number 4, since 1, 2, 3, and 5 must be activated. The actuators' cooling process is realized following the same order. The only difference is that the cooling speed of SMA cannot be controlled. For this, currents keep all the extremities active except those that need to be lowered. An example of this is the flow of current through 3, 4, and 5 while 1 and 2 are cooled by natural convection.

On the other hand, Mode 2 is performed analogously by varying the order of limbs' movement. This process is more beneficial for other prototypes of stars explained above. In this robot, the results were null or even negative when movements were realized in this way. Therefore, this second option was rejected.

Pattern 1 (shown in Figure 4.11) allows advance in the desired direction, obtaining a useful clearance between friction and the center of mass. During the first two stages of the heating

process, it is desired to move the center of mass while reducing friction so that the extremity that makes the last movement can drag the star in its path. In the same way, during cooling, 1 and 2 go down in pairs to fix higher friction and ensure that the robot does not move backward when the next legs relax.

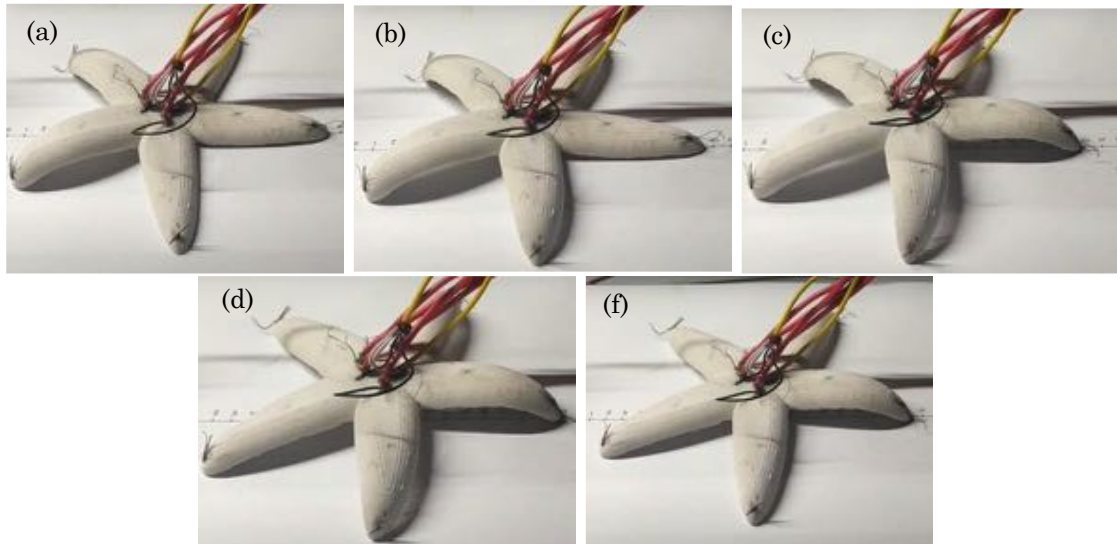


Figure 4.11 Movement patterns realized by Aforb from Step 1 (a) to Step 5 (f)

Another possibility consisted of activating all the limbs together at the same time. The star can stand upright by force exerted on all the springs simultaneously and therefore perform the movement. For this, tiny impulses have been sent sequentially to activate all the legs simultaneously. Once they are all raised, a small current maintains the temperature of these springs. In other similar projects, it is used, for example, to avoid obstacles.

Finally, it is possible to take advantage of the small advance that the contraction of independent limbs supposes, as seen with other models. In Figure 4.12, Asforb drags itself, moving only two limbs.

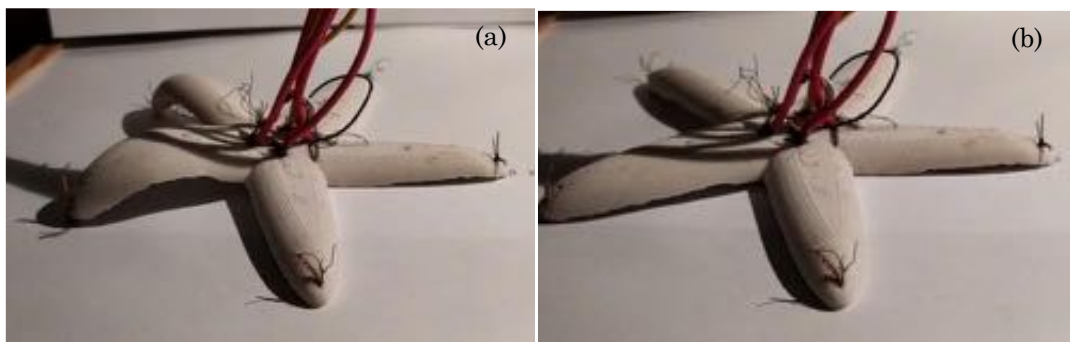


Figure 4.12 Drag movement. (a) The two limbs contract and (b) drag the body

It is interesting to highlight the importance of the weight of the wiring. As it supports so much amperage, typical ARDUINO cables cannot be used since they do not withstand much temperature and melt. Therefore, a 3mm cable has to be employed to withstand temperatures of around 70°C. It implies more weight that the star has to drag apart from itself.

4.2.2 First method: constant pulses

Pattern 1 was realized by sending independent impulses and empirically seeing the development and progress (Figure 4.13). In addition, to add speed and take advantage of the possibility that the chosen power supply, with a maximum amperage of 12A, tried to

send simultaneous impulses. With this, a more uniform and faster movement is achieved by not having waiting times between impulses; that is, while limb two is activated, limb one has become deactivated, so it is then necessary to reheat it a little to not decay in totality.

With this method, a considerably rapid displacement was observed concerning other projects; however, this was very irregular. During a cycle of about 40s, it could advance about 2cm in the best conditions.



Figure 4.13 Experiment with constant pulses

The advantages are the speed of this and the simplicity of programming. As for disadvantages, it is necessary to consider the variability of results that sometimes arrive due to temperatures or external air currents. It is also worth noting the fragility of the circuit when operating for a long time due to the high currents that are overheating MOSFETs. Furthermore, it has also come to screw up Arduinos.

In short, the constant appearance of problems makes the disadvantages outweigh the significant advantages this system has.

Using a larger SMA spring diameter and a spring of the same diameter but with an activation temperature of 45°C were evaluated.

The larger diameter spring allowed a very high compression force and speed; however, the silicone could not exert the necessary force for stretching. So the spring always stayed in the compressed form, which made it impossible to work with it.

The spring with a lower activation temperature instead did not have enough compression force to compress the end of the star.

The proposed solution was to apply two springs per limb to increase the compression force. In this case, the actuators exerted more force, but at the same time, the silicone was capable of stretching when the springs were not activated.

Initially, the PWM signal is sent simultaneously to both legs, but as has already been explained, overheating problems have meant this is not a viable option. Tests have also been developed to assess this method's virtues despite the drawbacks.

For this, the signal from the Arduino serial was used, and we associated a key to a movement cycle. In this way, the theoretical movement pattern would be made, activating five simultaneously. Figure 4.14 shows a schematic of the PWM signals send to each limb during a cycle. Only limbs 1 and 2 are activated during the first step, and their activation is simultaneous. Then, in step 2, the PWM sends to limbs 1, 2 decreases, while limb 3 starts to be heated, and so forth.

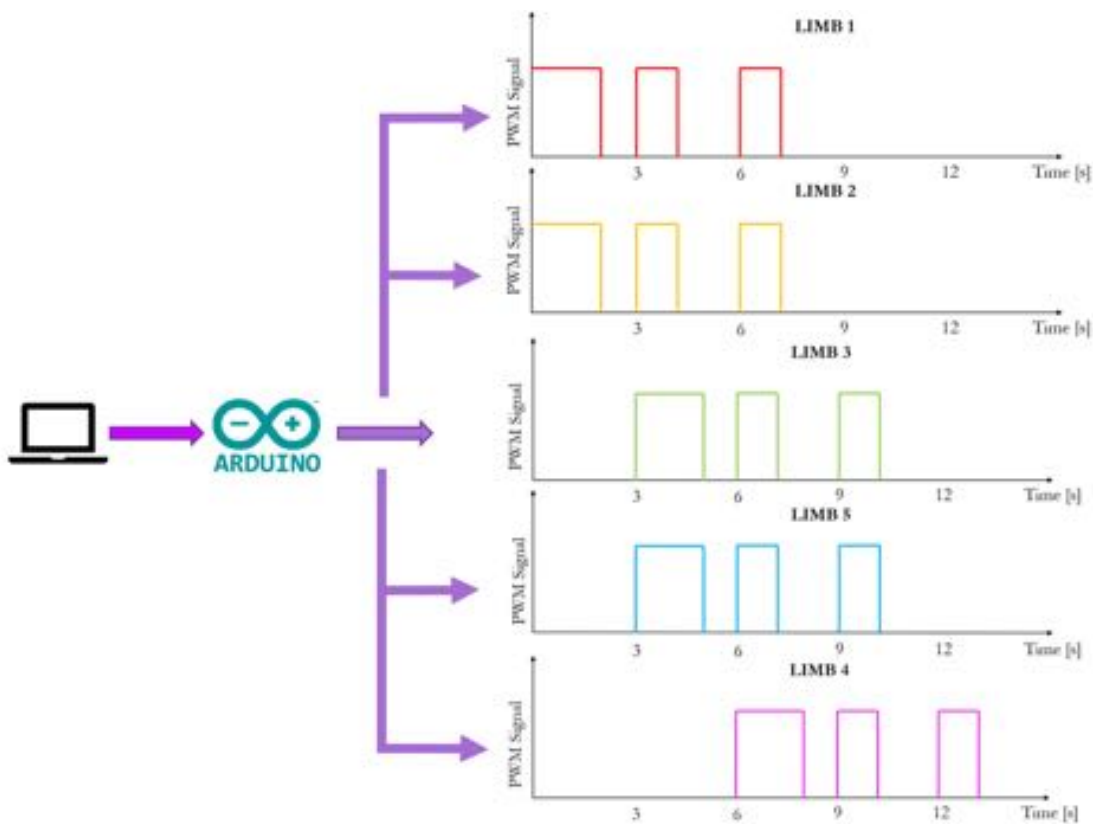


Figure 4.14 PWM signals send to each limb during a cycle in the case of constant pulses

However, the results are not appropriate due to the differences in temperatures to which they are finally subjected and the overloading of the cables. They end up reducing the life of the springs and damaging the electronic power system. The displacement is null by not making the real pattern well.

After this test, the next possibility consists of sending the control signals using pulses that avoid overheating and thus reduce a problem. For this, two options are analyzed: impulse sending in pairs or to individual limbs. In this project, the second option was implemented.

4.2.3 Second method: impulses sent to individual limbs.

The following Figure 4.15 shows a simple diagram with the steps of this previously explained pattern. It can be seen how during 0.4 seconds, the first signal is sent to the first two legs, which are reintroduced in a loop that makes it repeat 15 times. The equal process is carried out successively for limbs 2 and 3, with longer pulses to compensate for the more idle time. This time that does not emit intensity to these extremities is explained by the need to keep the anterior springs 4 and 5 contracted, and therefore impulses are sent for short periods. By means of this system, the same is continued for the last limb, sending small signals, in this case, to the other 4.

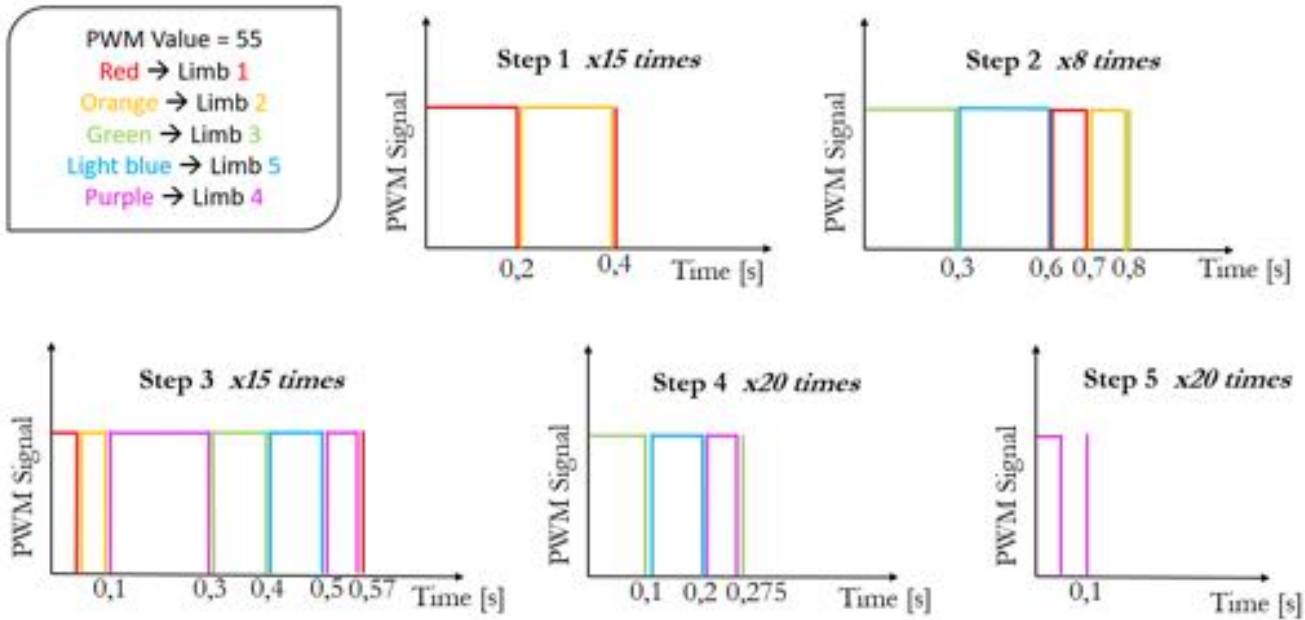


Figure 4.15 PWM signals send in each step to each limb and their repetition during a cycle

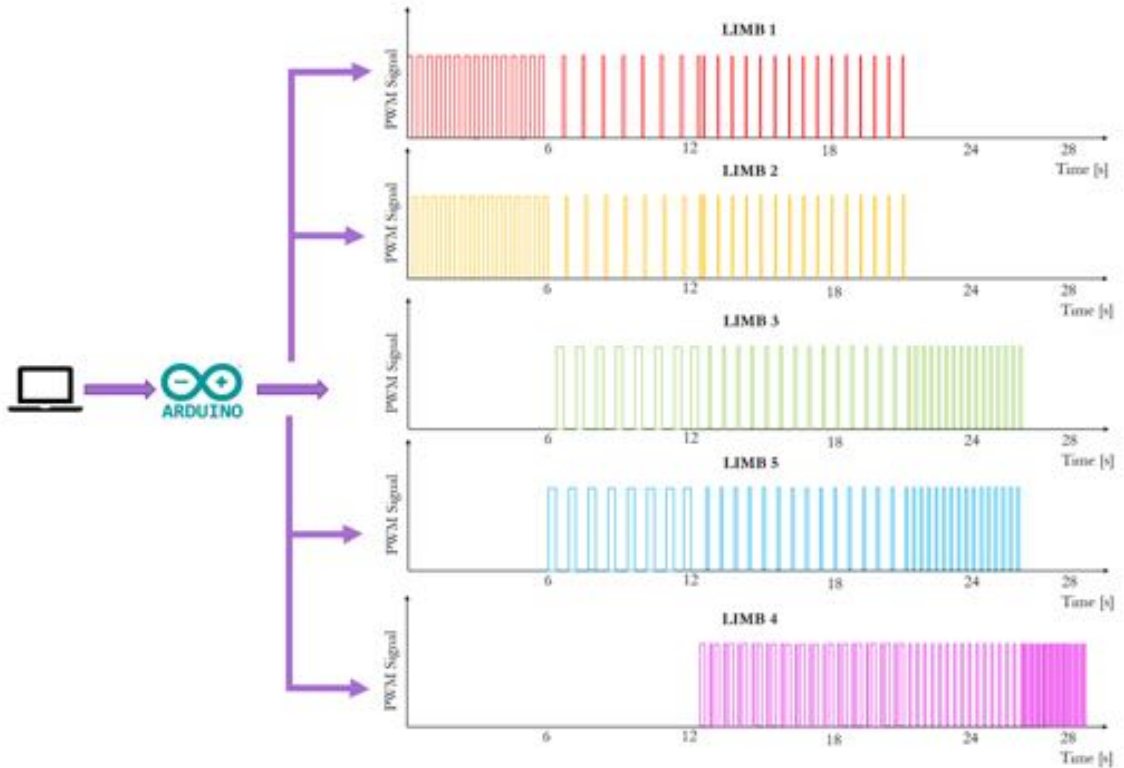


Figure 4.16 PWM signals send in each step to each limb during a cycle

The combination shown in Figure 4.16 is the optimal one. Different experimental combinations have been developed to obtain it, varying the number of the loops (n) of each heating step, the delay times and, the intensities transmitted. In the following tables, these experimental attempts are summarized.

In the first attempt (Option 1) Table 4.2, the values provided in the while loop are all the same. Regarding the time values, they are approximations of tests done independently. Time 1 represents the first step of the pattern (heating limbs 1 and 2), time 2 represents

the second step of the pattern (heating limbs 3 and 5), and time 3 represents the third step of the pattern (heating limb 4).

Table 4.2 First attempt to implement the control by impulses sent to individual limbs

Option 1						
	n loops	PWM	Time 1 [s]	Time 2 [s]	Time 3 [s]	Total time [s]
Step 1	20	70	0,4	0	0	8
Step 2	20	70	0,2	0,6	0	16
Step 3	20	70	0,1	0,2	0,275	11,5
Step 4	20	70	0	0,2	0,075	5,5
Step 5	20	70	0	0	0,1	2
						43

Favorable results have been obtained, reducing the value of the PWM to 55, as shown in Table 4.3.

Table 4.3 Second attempt to implement the control by impulses sent to individual limbs

Option 2						
	n loops	PWM	Time 1 [s]	Time 2 [s]	Time 3 [s]	Total time [s]
Step 1	20	55	0,4	0	0	8
Step 2	20	55	0,2	0,6	0	16
Step 3	20	55	0,1	0,2	0,275	11,5
Step 4	20	60	0	0,2	0,075	5,5
Step 5	20	55	0	0	0,1	2
						43

Therefore, the next step was to reduce the number of loops to obtain the same results in less time. So, the value of the loops of the heating phase of limbs 1 and 2 was reduced from 20 cycles to 15. In this way, two seconds are saved, as is shown in Table 4.4.

Table 4.4 Third attempt to implement the control by impulses sent to individual limbs

Option 3						
	n loops	PWM	Time 1 [s]	Time 2 [s]	Time 3 [s]	Total time [s]
Step 1	15	55	0,4	0	0	6
Step 2	20	55	0,2	0,6	0	16
Step 3	20	55	0,1	0,2	0,275	11,5
Step 4	20	60	0	0,2	0,075	5,5
Step 5	20	55	0	0	0,1	2
						41

In the fourth attempt (Table 4.5), the number of loops of steps 2 and 3 was reduced. This reduction in the number of cycles allows the reduction of more than 10 seconds of the total time.

The selection of the number of loops is empirical. Different values are due to the different responses of SMA spring during the heating phase. So, for example, springs in limbs 3 and 5 needs fewer loops to heat than the springs in limbs 1 and 2. This difference can be due to

many reasons, for example, their creation process (time and shape) or their connection with the wiring.

Table 4.5 Fourth attempt to implement the control by impulses sent to individual limbs

Option 4						
	n loops	PWM	Time 1 [s]	Time 2 [s]	Time 3 [s]	Total time [s]
Step 1	15	55	0,4	0	0	6
Step 2	10	55	0,2	0,6	0	8
Step 3	15	55	0,1	0,2	0,275	8,625
Step 4	20	60	0	0,2	0,075	5,5
Step 5	20	55	0	0	0,1	2
						30,125

The final version made it possible to reduce the total time to 28,5 s (Table 4.6). Every step happens as precisely as possible so that there are no dead spots between them, avoiding lost time. It is important to remember that the time is dependent on the room temperature since the cooling process is not controllable by code. For this reason, steps four and five are remarkably longer to allow first springs to relax and stretch.

Table 4.6 Last attempt to implement the control by impulses sent to individual limbs

Option 5						
	n loops	PWM	Time 1 [s]	Time 2 [s]	Time 3 [s]	Total time [s]
Step 1	15	55	0,4	0	0	6
Step 2	8	55	0,2	0,6	0	6,4
Step 3	15	55	0,1	0,2	0,275	8,625
Step 4	20	60	0	0,2	0,075	5,5
Step 5	20	55	0	0	0,1	2
						28,525

4.2.4 Results

The results that will be presented in the graph in Figure 4.17 are the outcome of the different tests discussed above. The graph shows only the results from the implementation of option five are shown here.

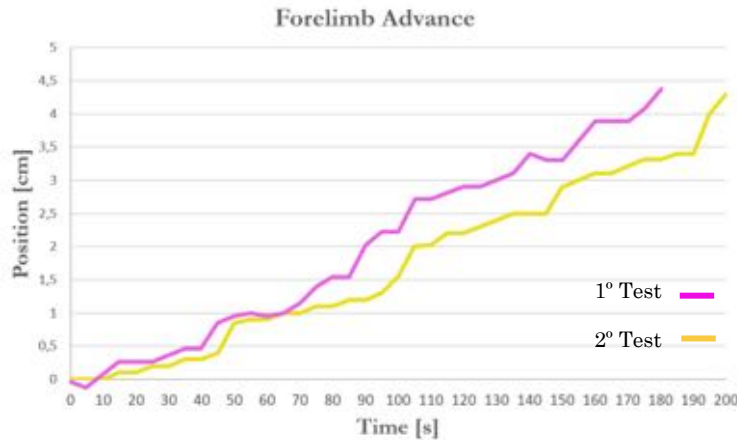


Figure 4.17 Graph Time-Position of two different experiments.

The displacement data is taken by referring to the advancement of the forelimb. Data are recollected every 5 seconds. The operating period is variable, close to three minutes to complete four full cycles. The following graph shows two different tests realized in two different moments; the differences are due to the other factors explained, among which the temperature and the surrounding air currents should be highlighted.

The moment the most significant displacement is made is very localized; it occurs when the limb is stretched. During the heating of this spring, the displacement is usually zero or even negative since the other legs exert force on the surface, which means that it cannot move back when contracted. However, the advance can be seen here when the last leg is stretched, as the others are relaxed, inducing more contact and, therefore, greater friction.

There is a significant difference to the theoretical one regarding the time per cycle due to the uncontrolled cooling. It has gone from taking about 30 seconds to values around 45.

Logically, it is understood that this displacement is not the same in each limb, as it contracts and stretches at different times in the cycle. Therefore, in the same way, a test is carried out with one of the extremities that perform the first contraction. The average speed of Asforb is 1.8 cm/min.

A final test employing paired pulses was realized to verify if it allows better results than unit pulses. In this case, limbs 1-2 are activated and deactivated simultaneously, and the same is done with limbs 3-5. These pulses are shown in Figure 4.18.

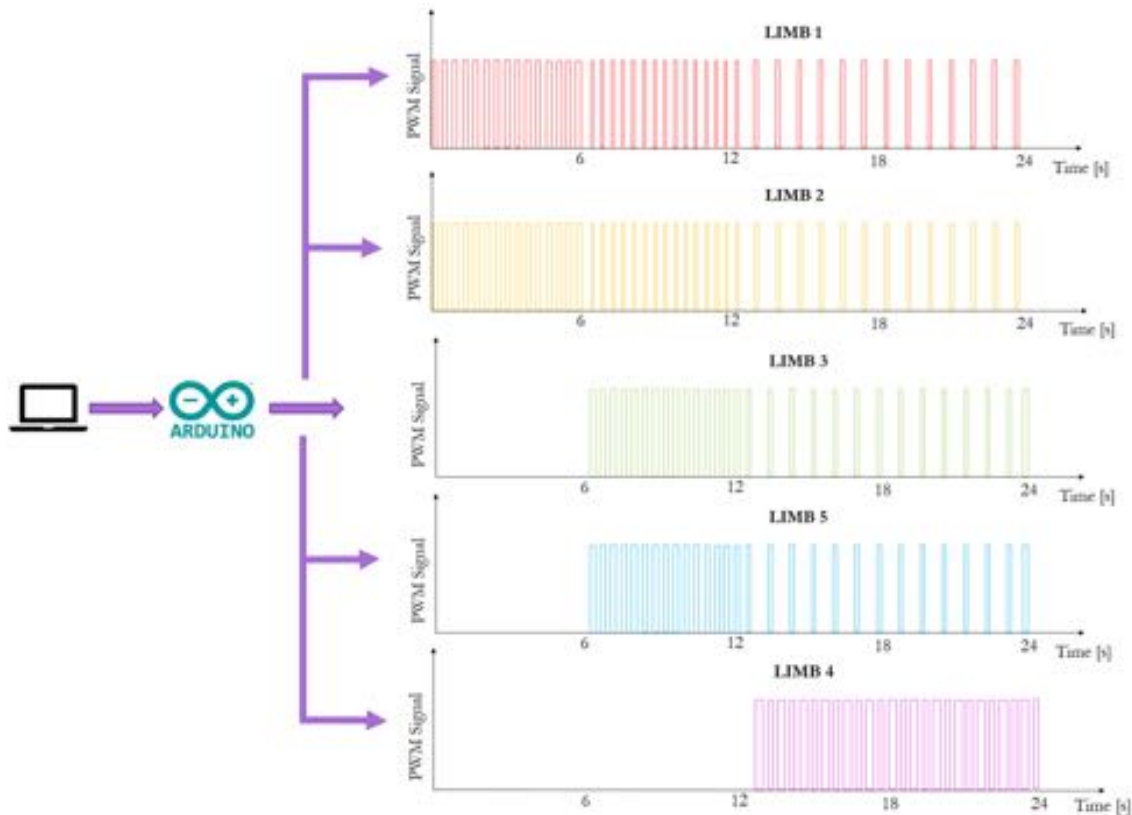


Figure 4.18 PWM signals sent to each limb during a cycle in the case of paired pulses

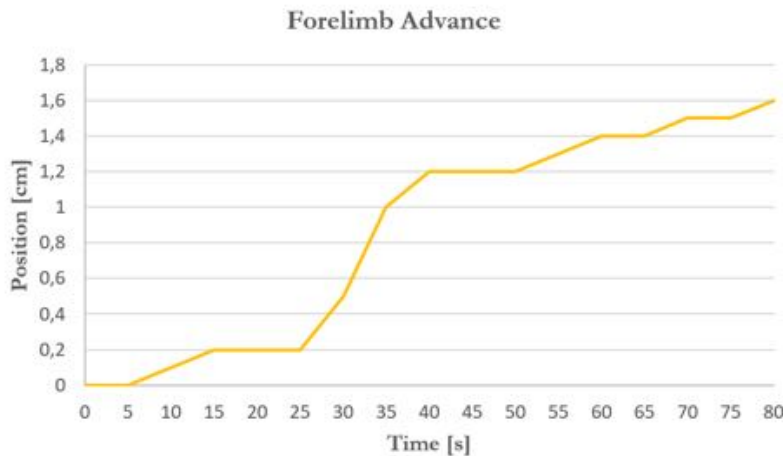


Figure 4.19 Graph Time-Position of the experiment realized with paired pulses

With this method of paired pulses, slightly better results can be achieved than with individual pulses (Figure 4.19). The result of this comparison between the two methods is a much higher heating rate of the springs when simultaneously exposed to high temperatures. It supposes a more significant contribution of power by the battery and overloading of the transistors. On the other hand, minor burns begin to occur by having less cooling time in each cycle. The effective displacement is similar, although in the second case, it causes more problems during its execution, and the time is reduced by about 5 seconds compared to the previous system, and it represents the only practical advantage.

4.3 JellyRobcib, a soft jellyfish

JellyRobcib is a soft underwater robot based on the movement and anatomical study of the jellyfish species “*Chrysaora hysoscella*.” The body measurements were taken based on an adult stage jellyfish (22–30 cm). The total weight, including the actuation systems consisting of SMA springs, is 110 g. Its speed is in the range of 2.5–2.8 cm/s. It also presents a temperature sensor for monitoring purposes.

4.3.1 Design

The CAD model developed for analysis and simulations was generated in Solidworks based on a behavior study for jellyfish species *Chrysaora hysoscella*, typical of the Mediterranean Sea and has several representative characteristics of most jellyfish (bell delimited and pronounced tentacles) [329]. Figure 4.20 shows the analysis carried out on an adult-sized *Chrysaora* jellyfish (diameter of approximately 23 cm), for which ten uniformly distributed points were established along its bell to analyze the evolution of the extreme areas (4 points) and middle zone (6 points) during the process of relaxation and contraction.

The described movement consists mainly of two stages: the first one of relaxation, Figure 4.20(a,b), at which stage the central bell is extended, and the second phase of contraction, which happens in a range of reduced time concerning relaxation (around 21% of the relaxation time); the contraction phase is from the state shown in Figure 4.20(c,d), which is in the range of 0.7 s and allows it to expel the fluid inside the bell, achieving movement. The points in Figure 4.20 [P1–P10] represent distributed points on the surface of the jellyfish body. They have been placed to visually reference the body states during the contraction and relaxation phases.

Additionally, it has been identified that the tentacles contribute with an additional fluid displacement that generates vertical movement.

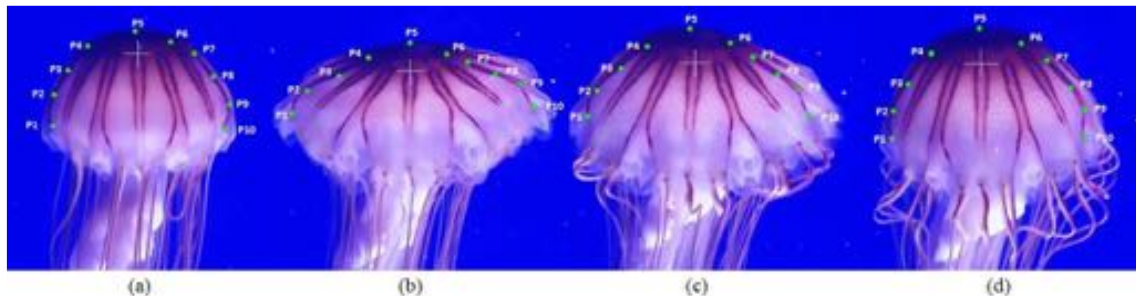


Figure 4.20 *Chrysaora* jellyfish movement cycle. (a,b) correspond to the state of relaxation, and (c,d) correspond to the rapid contraction phase.

The robot body has been made with a highly flexible Ecoflex® silicone base, and it has an average diameter of 22 cm. Figure 4.21a shows a central cross-section, and Figure 4.21b is a photograph of the final prototype. A 3D printed mold (Figure 4.21c) in ABS generated from the jellyfish CAD model was made to cure the silicon for the body of the implemented robot (Figure 4.21d). The central SMA and the tentacles were added during this curing process.

The robot consists of 5 SMA spring actuators placed so that one SMA is in the center of the body (350 microns) with a ring shape of an 80 mm diameter and four lateral SMAs (500 microns) of 75 mm length are located radially, anchored in the center and on the periphery with 90 degrees of separation, as reflected in the cross-section of Figure 4.21a. In this way, the controller can determine the degree and contraction time to produce the relaxation and contraction to expel water.

The implemented actuators have been selected based on their desirable characteristics for the movement, specifically to generate rapid contractions, which are their reduced size and their weight which does not represent a significant load. Their activation temperature is 50–65 °C + –5 °C.

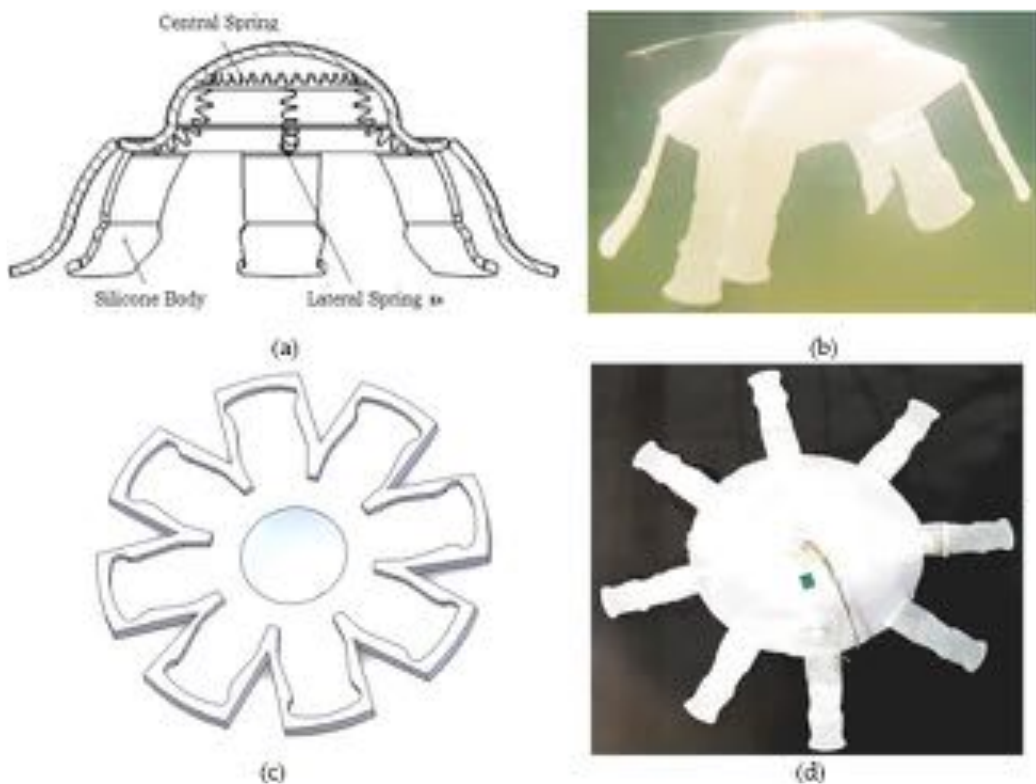


Figure 4.21 Computer-assisted design (CAD) model implemented in Solidworks: (a) cross-section of the CAD model. (b) Robotic jellyfish implemented inside the test pool. (c) 3D-printed mold. (d) Extended body.

The SMA springs employed have been manufactured. The manufacturing process is based on winding the SMA wire in a screw and fastening it with nuts at the ends; then it is introduced into the oven where it reaches 600 °C, for 15 min, before a subsequent cooling process (Figure 4.22a), thus obtaining the SMA with the spring memory. The subjection of the four lateral SMAs was carried out externally. SMAs had been previously encapsulated (Figure 4.22b) with a thin layer of Ecoflex Silicone, leaving them completely sealed, and with the cables for the control board, their anchorage to the jellyfish body was made employing thin metallic joints that cross the SMA cover layer and the body, being fixed by pressure. On the other hand, the central SMA was fused to the body, placed during the drying process, laying the cables for control on the outside.

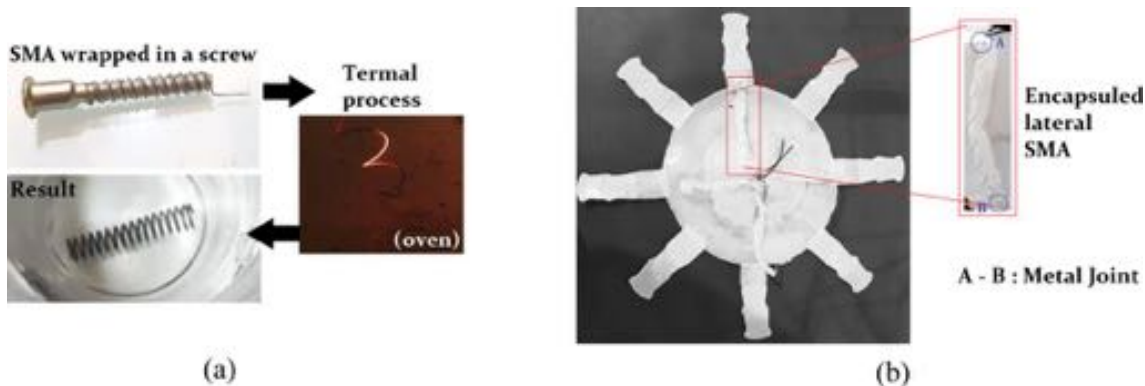


Figure 4.22 (a) Manufacturing of the SMAs. (b) Detailed section of encapsulated lateral SMA

4.3.2 Modeling

Three types of analysis were carried out to verify robot functionality before its implementation. These analyses allowed the evaluation of (1) the material behavior against the SMAs' contraction, (2) the volume displaced by the jellyfish during the contraction, and (3) the pressure generated during the contraction inside the jellyfish bell and the needed pressure for a positive displacement.

A simulation of the jellyfish body material behavior was carried out (Figure 4.23) to evaluate the displacement generated and the amount of water that can be evacuated with each contraction. The amount of water displaced was used as data for the CFD analysis. The SMA spring's return to its extended form is due to the design of the tensioned silicone body. After the contraction is generated and the temperature in the SMA is reduced, its state becomes malleable so that the silicone body itself extends it.

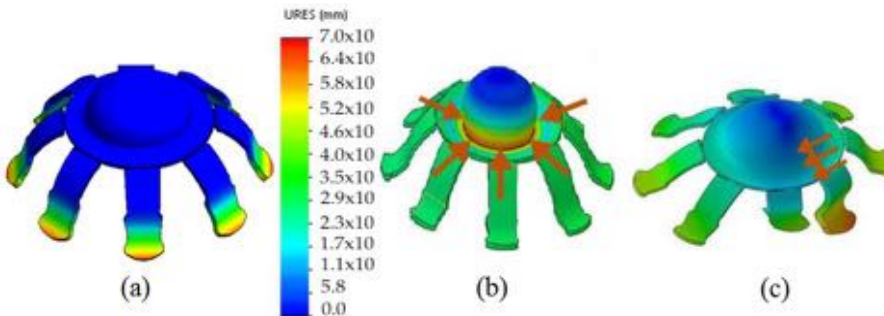


Figure 4.23 Simulation of the jellyfish body displacement when the central SMA contraction is applied:
(a) before contraction; (b) after the central contraction; (c) after lateral contraction

Using Equation (3.1)[298,330] that relates the shear modulus of the SMA material (G) [$\frac{N}{m^2}$], SMA diameter (d) [m], variation of displacement during contraction (x) [m], springs' turn diameter (D) [m] and the number of spring turns (N), it is possible to calculate the maximum force that the central SMA will make during the application of contraction.

$$F = \frac{G \cdot d^4 \cdot x}{8 \cdot D^3 \cdot N} \quad (3.1)$$

The equation only allows “estimating” the force due to the complexity of modeling the entire actuation system. Although the stress-strain produced is directly considered, the term in the equation “G” relates to both types of stress since both are in function of the Y (Young’s modulus) as established by Pons [286]. When working with Nitinol, there is shear stress and normal stress, but since both efforts are partially present simultaneously, it is considered that $G = Y$.

The previously calculated force is represented by a cyclic force exerted by the central SMA and was applied to the CAD model (the force is represented by the brown arrows for the two cases in central Figure 4.23b and lateral Figure 4.23c), which is assigned the parameters of the material (Ecoflex Silicone 00-30): viscosity 300 cps, shore hardness 00–30, breaking strength of 900%, tear-resistance of 38 (6654 Nm/m), Shore hardness 00-, specific volume (26 cu.in/lb), maximum temperature 450 °F (232 °C). Simulation results show a maximum displacement of 70 mm in the central bell after contraction, representing a volume of displaced water equal to 557 cm³. The zones with a red color range represent greater displacement produced in the bell by the central SMA.

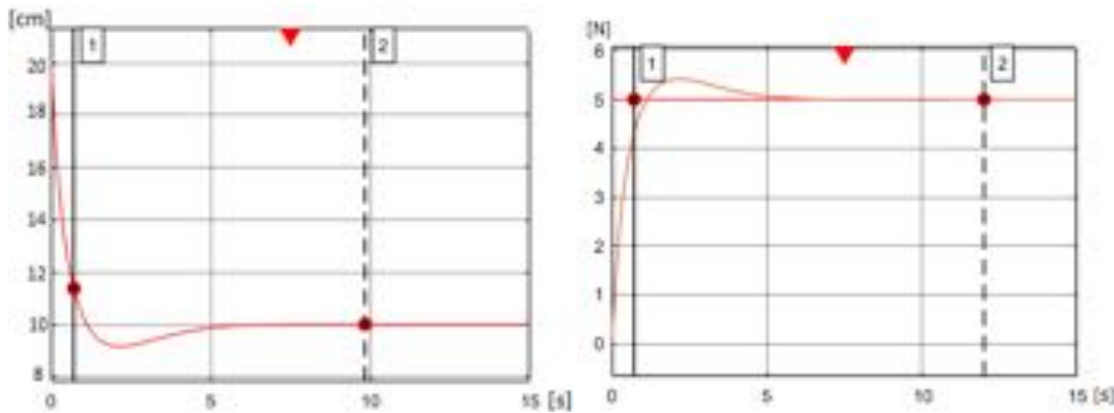


Figure 4.24 Responses to parametric modeling to a reference. (a) Contraction of the jellyfish bell. (b) Force produced by the SMA.

Figure 4.24 shows the behavior of jellyfish modeling; Figure 4.24a shows the contraction of the jellyfish bell for a reference of 10 cm, where the system response is extremely fast, achieving the reference in the first 2 s, and keeping it constant because of the fuzzy controller. For its part, Figure 4.24b shows the response of the force generated by the SMA to a 5 N reference signal; here, the sudden increase of the force is due to the sudden contraction of the SMA.

Figure 4.25 shows a comparison of the diameter variation for two contractions. During the first 0.7 s, it quickly shrinks in size due to the force of contraction exerted by the SMA. After that, it returns to its relaxed state again while the SMA is cooled. The curve shown in blue differs slightly from the yellow one, mainly due to the data capture and filters applied in the vision system.

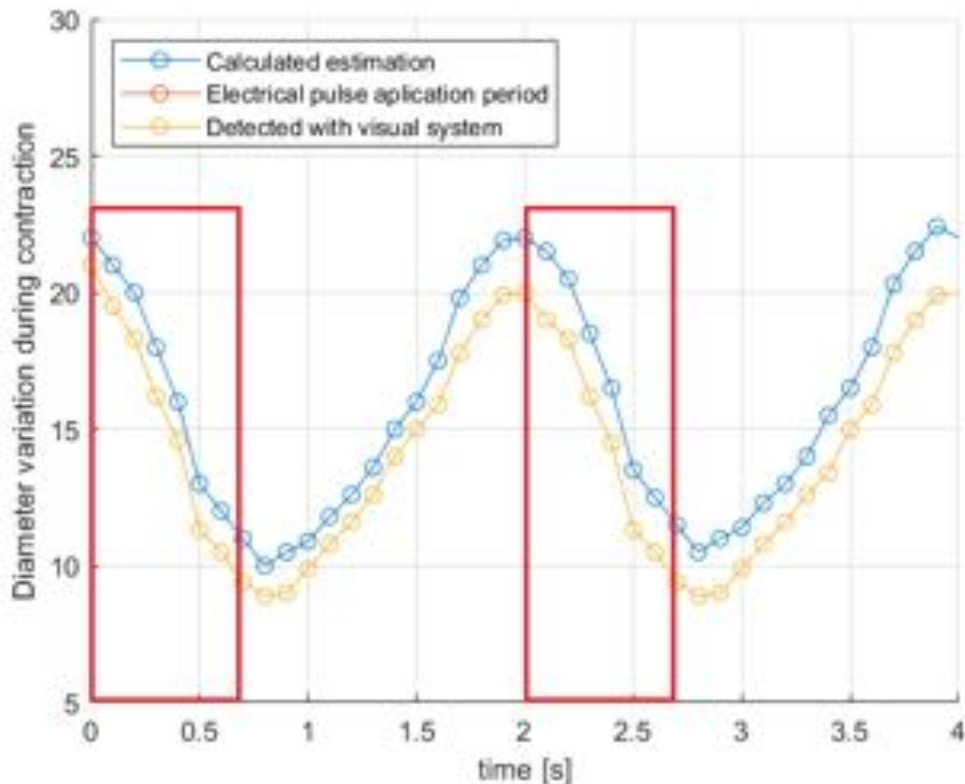


Figure 4.25 Diameter of the jellyfish bell variation comparison.

Its propulsion system generated by contractions produces the Jellyfish displacement. When these happen, their body generates a vortex, which is forcefully expelled and thrust forward. To keep the movement constant, a series of pulsations must be generated. To validate the geometry model, all forces involved in the displacement of a body in the water, such as drag coefficient, added-mass coefficient, and Reynolds number, are analyzed [331]. Together with the data obtained from the CFD, they allow evaluation of the instantaneous acceleration produced by the contraction and determine if jellyfish can advance [329].

During the simulation development, gravity has been used as an operational parameter because its use implies the action of buoyancy. Figure 4.26(a,b) shows the fluid displacement (water) during the vertical and lateral contraction, respectively represented by spheres. There is a variation in the sphere color according to the velocity generated during the process, the spheres being red for high-speed areas and blue for negative velocity areas. The accelerations are shown with lines in Figure 4.26(c,d) for vertical and lateral contraction, respectively.

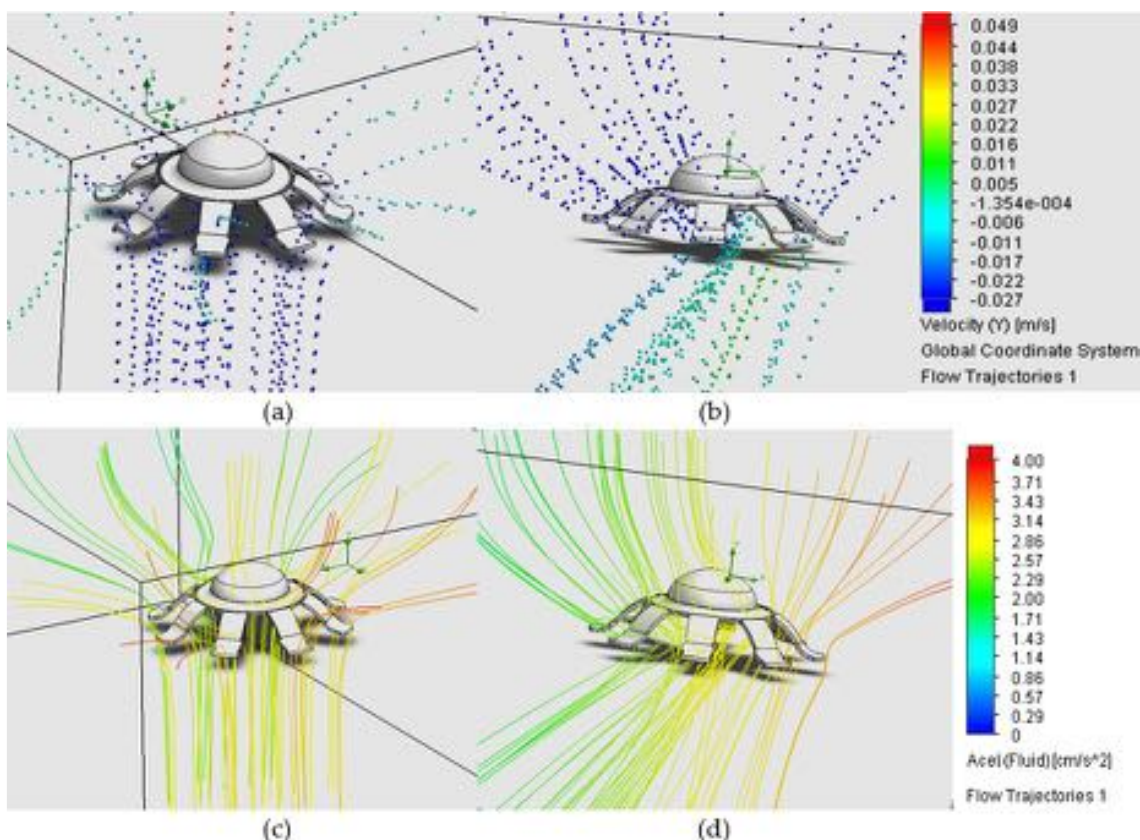


Figure 4.26 Representation of fluid displacement during jellyfish contraction using the Solidworks-Flow Simulation plug-in: (a) vertical displacement—speed (m/s); (b) lateral displacement—speed (m/s); (c) vertical Acceleration (cm/s²); (d) lateral acceleration.

The simulation verification is performed based on Equation (3.2) [332], which evaluates the average acceleration to determine if a positive displacement is generated. This expression involves the water jet thrust under the hood (T_i) [$\text{g} \cdot \text{cm}/\text{s}^2$], the drag force (D_i) [$\text{g} \cdot \text{cm}/\text{s}^2$], the weight (W) [N] and the effective mass of the jellyfish (E_i) [g]. This equation does not consider the presence of tentacles because of their complexity. For that reason, a known model was considered to represent the most relevant part of the body (around 92% is modeled as a bell shape). The calculation without including the tentacles shows that there will be a positive displacement, while the simulation corroborates that tentacles generate an additional impulse because of the positive vortices generated at the ends after each contraction. In this study, the robot presents a slow motion, and the positive feedback on

thrust associated with “added-mass variation” is very small and has not been considered [333].

$$A_m = \frac{T_i \cdot (D_i + W)}{E_i} \quad (3.2)$$

which are calculated, respectively, from the expressions: Equation (3.3) for (T_i), Equation (3.4) for (D_i), Equation (3.5) for (E_i) and Equation (3.6) for (α_i) [332,334–336].

$$T_i = A_v \cdot \alpha \cdot j_i^2 \quad (3.3)$$

$$D_i = \frac{1}{2} \cdot \rho \cdot u_i^2 \cdot \pi \cdot h_i \cdot \frac{d_i}{4} \cdot C_{D,i} \quad (3.4)$$

$$E_i = V_{b,i} \cdot \rho \cdot [1 + \alpha] \quad (3.5)$$

$$\alpha_i = 0.5 \frac{d_i}{h_i^{1.4}} \quad (3.6)$$

The variables involved are bell hole area (A_v) [cm^2], water density at 25 °C (ρ) [g/cm^3], fluid velocity (j_i) [cm/s] instant jellyfish speed (u_i) [cm/s] jellyfish bell height (h_i) [cm], jellyfish diameter (d_i) [cm], drag coefficient ($C_{D,i}$), the volume inside the jellyfish bell ($V_{b,i}$) [cm^3] and the added mass (α). Equations (3.7)–(3.9) were used to calculate the previous values:

$$j_i = \frac{1}{A_v} \cdot \frac{dV_{s,i}}{dt} \quad (3.7)$$

For Equation (3.3), where [cm/s], is the jet speed at the time i , [cm^2] is the umbrella’s whole area, and [cm^3] is the instantaneous volume under the umbrella.

$$u_i = \frac{(x_{i+1} - x_{i-1})}{2t} \quad (3.8)$$

In Equation (3.4), where [cm/s], is the speed at time i , x [cm] is the position for the respective time and t [s] (time)

$$C_{D,i} = \frac{24}{Re^n} \quad (3.9)$$

For Equation (3.5), $C_{D,i}$ is the drag coefficient, the Reynolds number, and “n” depends on the value of Re , with $n = 1$ if less than 1 and $n = 0.7$ if $1 < Re < 500$.

Based on these expressions, an acceleration equal to 3.38 cm/s^2 has been determined, similar to the CFD result of 3.8 cm/s^2 (Figure 4.26c). Therefore, the displaced fluid resulting from the contraction will generate an acceleration greater than zero, and consequently, the displacement will create progress and not regression.

Figure 4.27 shows a comparison between the displacement of the given volume for the quasi-analytical simulation (modeled on Equations (3.2)–(3.9)) and the CFD output volume for a contraction, where the accumulated volume was included as a reference to see how it changes during the contraction. Figure 4.27 shows the displaced volume at each moment and the total accumulated volume for each defined case. Thrust modeled with CFD is higher from the analytical model because viscous effects associated with the vortex ring formation and added-mass-variation effects are neglected in the analytical model.

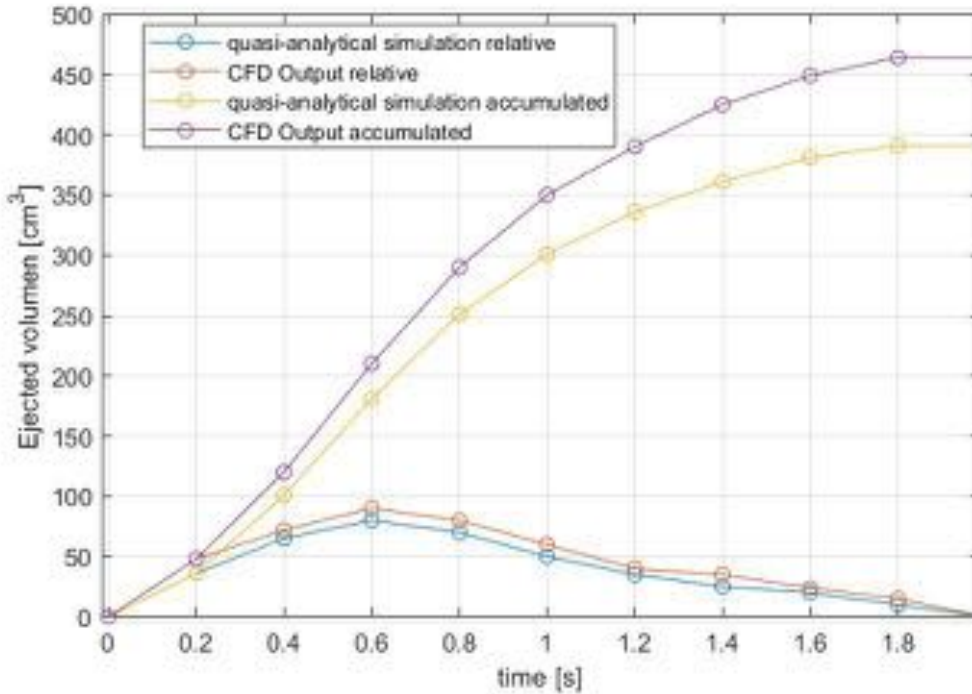


Figure 4.27 Comparison of the volume ejected, using CFD and the analytical model.

4.3.3 Control

The experimental system shown in Figure 4.28 allows robot movements, acquiring location data, and monitoring thermal data. It consists of 6 steps.

- **Step 1** is responsible for acquiring the images of the robot through a wireless camera and sending them to the central computer (a vision system was developed and tested by MBARI in a real situation in deep waters [337]).
- **Step 2** corresponds to the control interface for movement control and the establishment of virtual points. Data monitoring is carried out with a temperature sensor. It was placed on the robot's top according to the CFD. The displacement of fluids in this area is less than in any part of the body, acquiring a more reliable measurement.
- In **Step 3**, the robot is located inside the aquatic environment. The vision system applies object segmentation and digital image processing techniques.
- In **Step 4**, errors are calculated and provided to the fuzzy controller based on the current position and virtual path points.
- **Step 5** (power stage) supplies the current in a controlled manner to contract the SMAs depending on the errors calculated in the previous step. (The potency card shown has been designed and implemented based on the power required to handle currents of up to 6 Amps with 36 Volts).
- Finally, **Step 6** corresponds to the robot within the aquatic testing environment and the execution of movements.

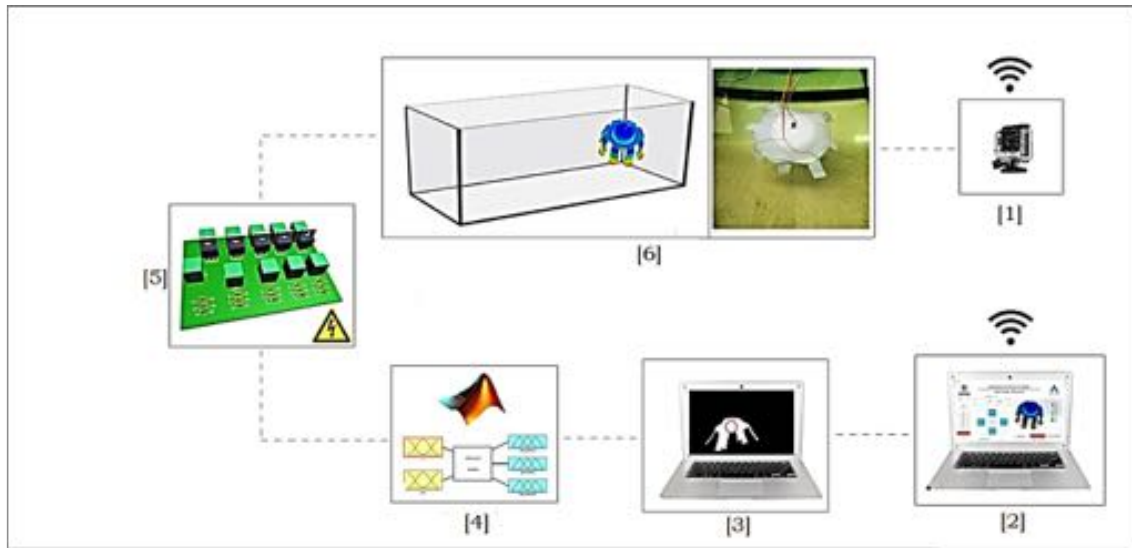


Figure 4.28 Experimental assembly of the system for the execution of tests.

For the development of movements, a MATLAB interface was developed through which the robot is monitored, and different parameters are calibrated (Figure 4.29).



Figure 4.29 Interface for control and configuration in MATLAB

It has two modes of operation. The first one is a manual method and allows the robot to be teleoperated through the threshold configuration for PWM value and image threshold.

The operator executed the independent movements using the buttons on the panel (forward, backward, right, left, ascent), and the temperature values were acquired as required by the user; the results of the manual movement were captured on video examined in MATLAB.

The second mode is autonomous and requires the establishment of virtual points to form a monitoring path. Figure 4.29 shows the location of four virtual destination points (P1, P2, P3, P4) so that the robot forms a square trajectory and performs thermal monitoring in that area, with an established uniform sampling time of 500 milliseconds.

A fuzzy control system was implemented because a control (PID) is not feasible due to the lack of a precise model. After all, the body does not have a rigid structure and the nonlinear and discrete relationship between SMA control and resulting contraction.

The control loop (Figure 4.30) has as input the virtual destination point consisting of two coordinates (x_{ref} , y_{ref}). These values (given in millimeters according to the previously performed calibration) are subtracted from the current values of the robot position given by the vision system, determining an $error_x$ and an $error_y$, respectively. These values are sent to a fuzzy controller with two inputs and generate three outputs, whose rules are detailed in Table 4.7. The variables in the table are defined as ($e +$) positive error, ($e -$) negative error, (z) zero, (SMA_{R-C-L}) right, center, and left SMA actuator, respectively.

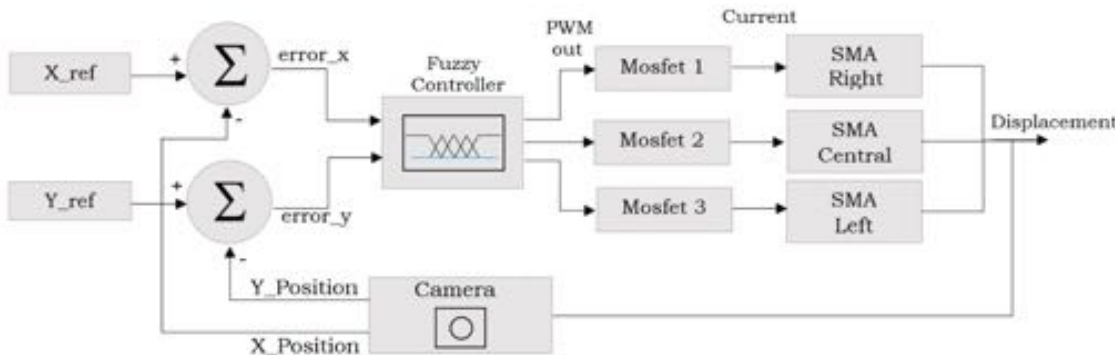


Figure 4.30 Fuzzy Control loop, two inputs, and three outputs

Table 4.7. Rules for the fuzzy controller, with two inputs (errors) and tree outputs SMA_{R-C-L}

Error "x"					
	e-Big	e-Small	z	e+Small	e+Big
SMA_R	$null_{PWM}$	$null_{PWM}$	$null_{PWM}$	Med_{PWM}	$High_{PWM}$
SMA_R	$null_{PWM}$	$null_{PWM}$	$null_{PWM}$	$null_{PWM}$	$null_{PWM}$
SMA_R	$High_{PWM}$	Med_{PWM}	$null_{PWM}$	$null_{PWM}$	$null_{PWM}$
Error "y"					
	$null_{PWM}$	$null_{PWM}$	$null_{PWM}$	$null_{PWM}$	$null_{PWM}$
SMA_R	$null_{PWM}$	$null_{PWM}$	$null_{PWM}$	Med_{PWM}	$High_{PWM}$
SMA_R	$null_{PWM}$	$null_{PWM}$	$null_{PWM}$	$null_{PWM}$	$null_{PWM}$
SMA_R	$null_{PWM}$	$null_{PWM}$	$null_{PWM}$	$null_{PWM}$	$null_{PWM}$

The PWM output values have been raised based on the observation and analysis of the robot's behavior through manual operation, determining that PWM values greater than 200 (78% of the cycle) generate a quick contraction response in the SMA, where corresponds to 255, is 175 and is 0, in a range of [0–255] of the duty cycle.

Based on the fuzzy conclusion generated from the rules, the respective output of the PWM is generated toward one of the Mosfet in potency card: (Mosfet 1) for displacements to the right, which acts on the respective lateral SMA (Mosfet 2) for vertical displacements, which acts on the central SMA in the form of a ring and (Mosfet 3) for displacements to the left, using the respective lateral SMA.

The maximum peak current operated by the potency card is up to 6 Amps, which is applied for a maximum time of 500 milliseconds—enough time to produce the molecular state change in the SMA, returning to its initial form of contracted spring, generating the displacement of water by compressing the respective area in the jellyfish body.

After that, there is a recovery time of 2 s, in which the jellyfish passes to the state of relaxation. During this time, the SMA, with the help of the low water temperature (24 °C), reduces its temperature and changes its state again before executing the closed-loop control again.

The controller is conditioned by external programming to correct the errors “x” or “y” one by one since, according to the CFD analysis, the impulse generated after each contraction would be lost if it is performed in a combined lateral way and vertical or first lateral and then vertical. Therefore, the best option was to correct first in “x” then in “y” or conversely.

The proposed experiments consist of establishing trajectories through virtual points through the developed interface. The robot can follow them due to the motion controller and perform periodic temperature measurements to generate thermal maps and analyze the parameters of the jellyfish movement.

The environment of tests to carry out the experiments was a pool with measures of $1.30 \times 1.50 \times 2.50$ m. Table 4.8 shows in its three sections the results of the three types of movements carried out and the main variables measured during the execution of the monitoring movements.

Table 4.8 Variables measured from a data set of experimental tests of Figure 4.29 movements.(No CT = Number of Contractions)

	Distance Traveled [cm]	SMA_L N° CT	SMA_C N° CT	SMA_R N° CT	Time [s]	Peak speed medium [cm/s]	Peak acceleration [cm/s ²]
a	114	0	14	0	61.6	2.51	5.01
a	116	0	16	0	64.8	2.53	5.2
a	120	0	15	0	68.2	2.47	5.34
a	117	0	15	0	65.2	2.52	5.21
b	91	0	0	15	41.4	1.28	4.86
b	92	0	0	16	43.1	1.14	4.92
b	95	14	0	0	44.2	1.08	5.04
b	93	16	0	0	42.4	1.35	4.89
c	245	4	12	8	142.2	2.14	6.72
c	241	5	13	7	136.3	2.07	7.01
c	239	5	13	8	148.2	2.10	6.82
c	242	4	12	9	139.6	2.24	6.92

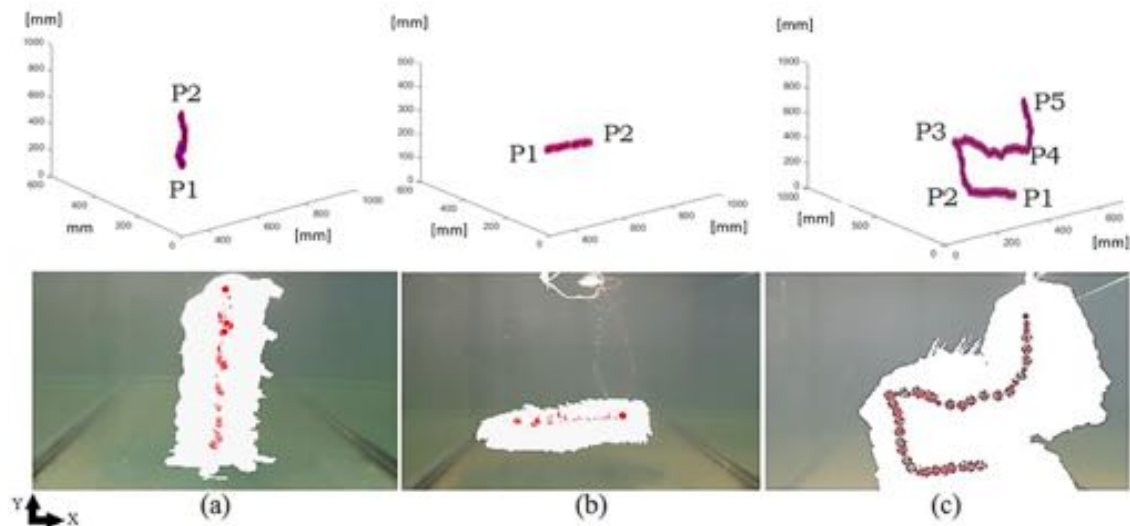


Figure 4.31 The three figures show the jellyfish overlap during the movement along the entire trajectory and the central point of the jellyfish in each moment. Movements developed: (a) vertical displacements; (b) lateral displacements; (c) trajectory composed of several points.

Figure 4.31 shows the visual system location result, where the red points show the jellyfish centroid for each moment, while the blank areas correspond to the jellyfish segmented and superimposed for each moment so that the path of passage is defined.

Over the trajectory in Figure 4.31(a–c), the points established for the path are shown, all starting from P1. In Figure 4.31a, an ascent movement has been made starting from the

pool bottom and a destination point at the top; Figure 4.31b has its starting point on the left side and concludes in the right area, and Figure 4.31c shows the lower right central area of the pool and begins its trajectory towards the established trajectory points that end in the upper right.

In this way, several individual tests were carried out with different destination points for each case.

4.3.4 Experiments

The results of the kinematic parameters of experiments developed to validate the controller and movement of the jellyfish are shown. Data concerning speed were filtered using the Savitzky–Golay method. In Figure 4.32 and Figure 4.33, red points represent data captured by the vision system at each moment, and the blue curves were used to represent the peaks of data with a higher value produced by contractions.

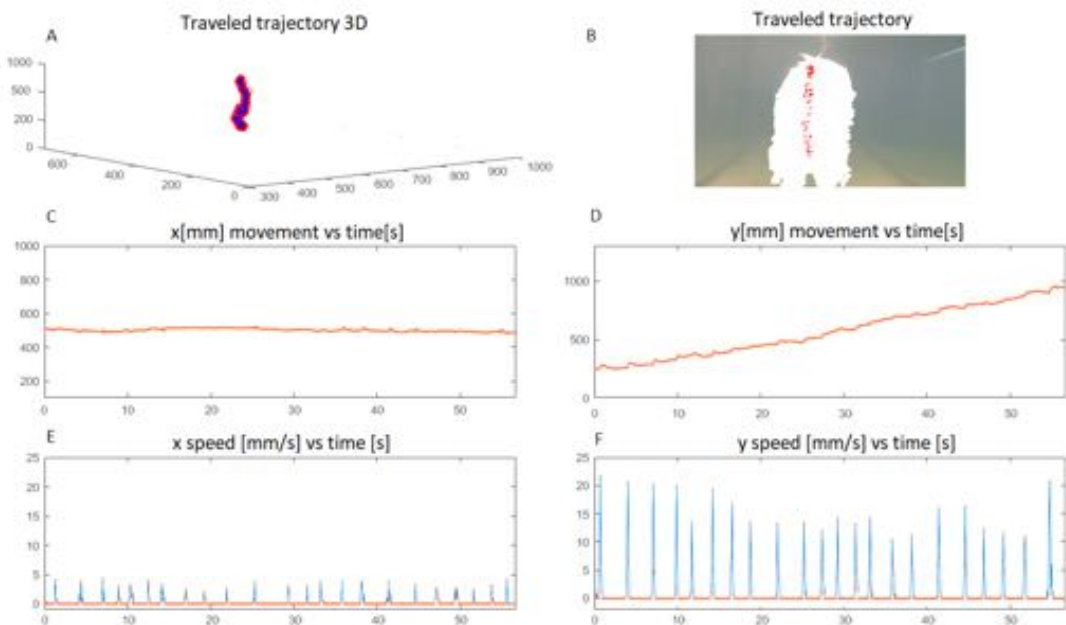


Figure 4.32 Experimental kinematic parameters based on vertical displacement. (A) Shows the 3D traveled trajectory; (B) Shows the jellyfish positions along the path; (C) Shows x position; (D) Shows y position; (E) Corresponds to x speed; (F) Shows y speed

Figure 4.32 shows vertical movement developed to travel a distance of approximately 1 m; Figure 4.32F shows the speed peaks generated with each contraction (22 in total), and Figure 4.32D shows the ascent path, in which after each contraction there is a slight increase in the ascent, which is due to the propulsion generated after the expulsion of the water. Figure 4.32E shows a slight variation of the x speed after each contraction.

Figure 4.33 shows horizontal movement to travel a distance of approximately 25 cm, Figure 4.33E shows as red rectangles the electrical pulses to produce the contractions (5 in total) and as blue curves, the speed peaks, and Figure 4.33F shows the acceleration, where the peaks coincide to the instants where the contractions were executed.

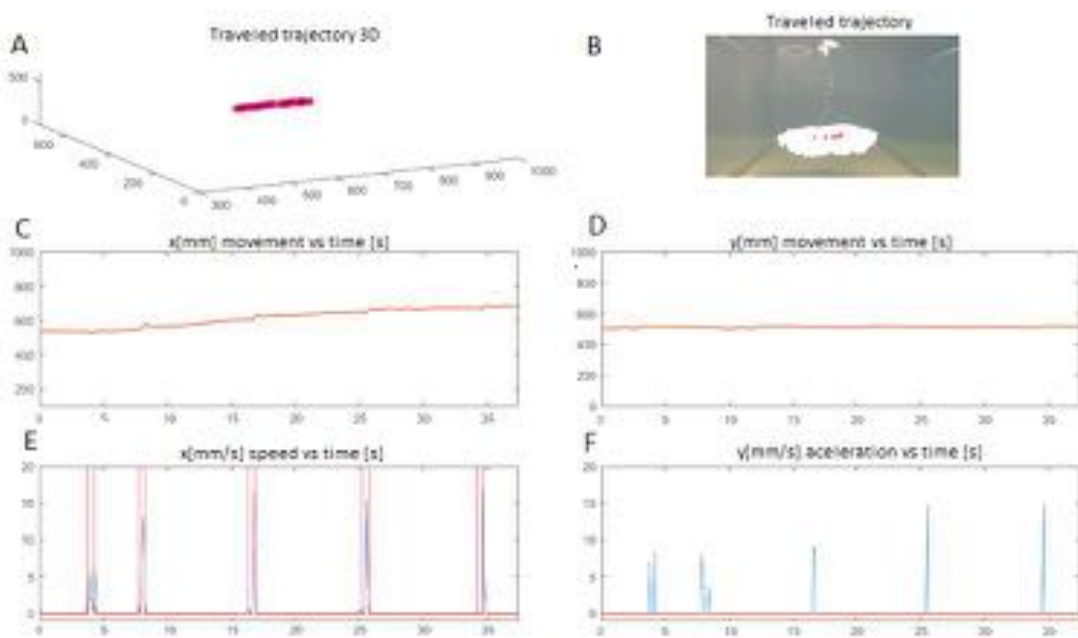


Figure 4.33 Experimental kinematic parameters based on horizontal displacement. (A) Shows the 3D traveled trajectory; (B) Shows the jellyfish positions along the path; (C) Shows x position; (D) Shows y position; (E) Corresponds to x speed and red rectangles are the electrical pulses given; (F) shows y acceleration.

4.3.5 Thermal Maps Generated through Path Tracking

One of the possible applications for the Soft Jellyfish Robot proposed is to monitor not only temperature but also other environmental variables (pH, contamination (turbidity)). The temperature was chosen to demonstrate this idea.

During the trajectory journey, through the virtual points given through the interface shown in Figure 4.29, temperature measurements were carried out at different points along the path that traveled with a sampling interval of 500 milliseconds to subsequently generate a thermal map of the area, based on the temperature gradient and the focused position of each measurement in an instant. To carry out these tests, boiled water (around 90 °C) poured from the test pool top was used to generate a heat source that disperses and allows the water temperature to be modified uniformly.

The average time required to travel a trajectory at an average speed of 2 cm/s is 52.3 s; during this time, a constant flow of water was maintained from the top with a manually reduced flow, which is why it reaches the lower part with a temperature of around 33 °C in the lower areas.

Jellyfish bell movement affects the uniform distribution of the water, but the sensor has been placed on top, just where the movement of the water is greatly affected.

Thus, Figure 4.34a refers to a map generated from real measures taken by Robotic Jellyfish, while Figure 4.34b to a map generated from two thermal sources of dispersion in the upper corners. Water was poured in each spot with a high temperature at 90 °C, and the graph shows the temperature transfer tendency to the lower temperature zones, reaching a maximum of 50 degrees and a minimum of 25 in the areas where there was no temperature transfer.

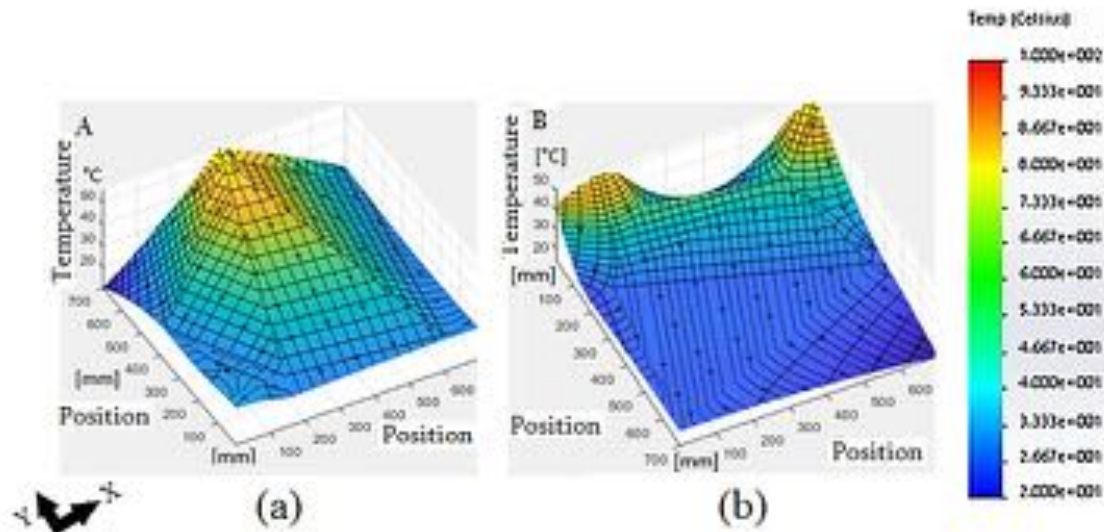


Figure 4.34 Thermal maps generated from the thermic measurements with the robotic jellyfish: (a) map with a thermal focus on the upper central part; (b) map with two thermal bulbs in the upper corners.

4.3.6 Results

The vertical jellyfish displacement has been taken as a reference since it is the movement typically performed by the species, with which we can make a comparison. Figure 4.35 shows in the first column the results of velocity, displacement, and acceleration of the developed jellyfish actuated with SMA, while the other three columns correspond to the research developed by Sean Colin in the study of morphology to develop a model of propulsion called “hydromedusa” [332].

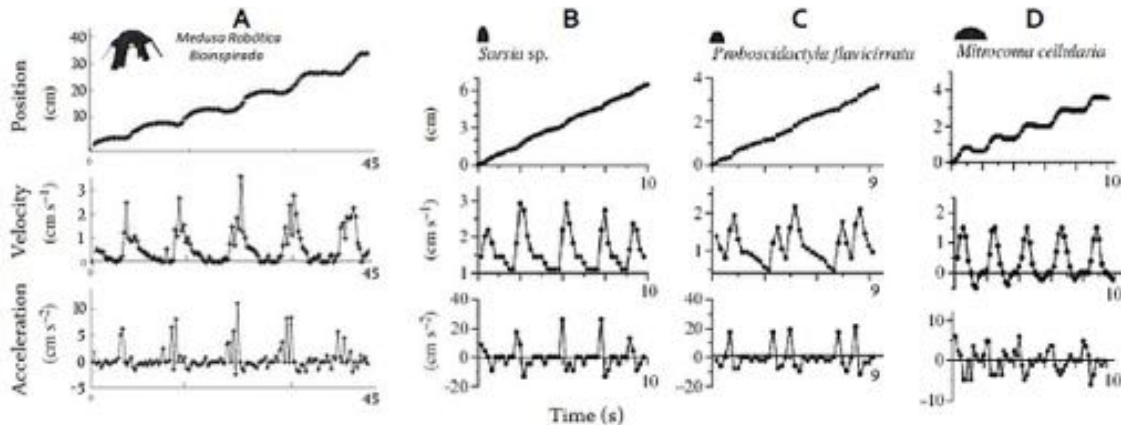


Figure 4.35 (Column A) Comparison of movements and variables of robotic jellyfish developed, compared to jellyfish species: (Column B)[139] *Sarsia* sp.; (Column C) *Proboscidactyla flaviderrata*; (Column D) *Mitrocoma cellularia*.

The displacement made by the robotic jellyfish presents oscillations for the rise and fall with each contraction. The slight downward displacements are mainly generated by the weight and recovery time of the SMAs after heating to generate the contraction, while the ascending curves of the real jellyfish show significant similarity, showing a similar decrease after contraction. The velocity curves are highly similar in all four cases; the soft robot reaches an average peak velocity of 2.54 cm/s, while the second, third and fourth reach 2.53, 1.95, and 1.24 cm/s, respectively; acceleration behavior in the same way in all cases presents a remarkable similarity.

On the other hand, the use of equations for CFD and model of bell selected gave satisfactory results, showing similar values for the acceleration value that is reflected with an

acceleration of 3.8 cm/s^2 using the CFD and 3.38 cm/s^2 in the calculated values. This difference is due to the tentacle presence because CFD shows that the tentacles generate an additional impulse after each contraction because of the positive vortices generated at the ends. This means that tentacles contribute 11.05% of the total acceleration.

One of the methods applied to minimize the cables' influence consisted of introducing elements to improve buoyancy; however, the results were not good since they generated instability after each movement. For this reason, there is no buoyancy compensator; it is also important to indicate that the consumption of the robot is 0.185 W for the trajectory in Figure 4.36A.

Based on the results in Table 3, an analysis of accuracy and controller repeatability was performed. Accuracy and repeatability for vertical (lateral) movements are equals to ± 2.165 (± 1479) cm and 0.973 (0.944), respectively.

Figure 18 shows a compendium of results (3 tests of the whole dataset from Table 4.9 are shown); the results of the analysis made by MATLAB are shown when establishing a target point (in blue) for all cases, to evaluate the results and obtain the values of accuracy and repeatability.

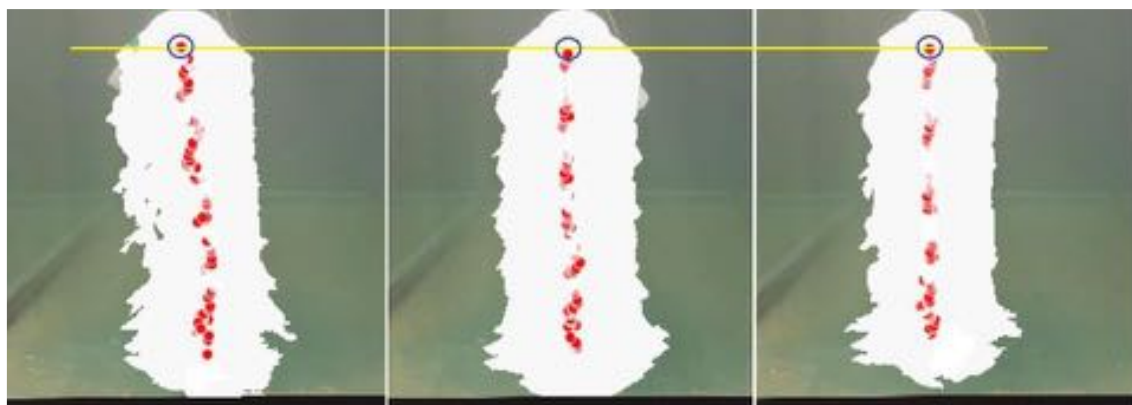


Figure 4.36 Comparison of movements and variables of robotic jellyfish developed.

The SMAs are encapsulated in a silicone layer so that external temperature has little influence on the alterations in the SMAs' state.

Among the advantages of using robotic jellyfish as a means of monitoring are mainly the quick contraction for propulsion, its low weight, and the cost of implementation, which is highly reduced compared to that of an underwater exploration structure or the hiring of diving equipment, with constant and reliable monitoring.

A comparison has been made between the displaced water volumes, with data obtained with CFD and quasi-analytical modeling, obtaining as main results that there is a difference between them, although both follow the same trend shown in Figure 9. In CFD, ejected volume is higher than the analytical model because viscous effects associated with the vortex ring formation and added-mass-variation effects are neglected in the analytical model. A similar situation occurs with other parameters, such as the Reynolds number.

4.3.7. Conclusions

This work shows the design and implementation of a soft, autonomous robot actuated by SMA, capable of performing vertical and horizontal movements to travel along given paths in the water; this robot is controlled by a fuzzy visual control and is applied in thermal monitoring, representing measured data as thermal maps.

Robot development has an analytical background, beginning with the analysis of the jellyfish *Chrysaora hysoscella*, from which a CAD model was obtained, the basis for this model. A CAE and CFD analysis were done, validating the design, and CFD equations showing similar values for the acceleration that are reflected with a value of 3.8 cm/s^2 using the CFD and 3.38 cm/s^2 in the calculated values. The jellyfish body implemented was made with flexible silicone and consists of five spring-shaped SMAs: a central one in a circular shape and four lateral springs radially separated 90 degrees anchored from the center to one end of the bell.

A fuzzy controller was implemented to control the robot movements because the jellyfish body is made of soft material. In addition, the behavior of the SMA has bidirectional hysteresis when changing phase, so finding an exact model is highly complex, and the fuzzy controller implemented generated a low error range, generating an accuracy of $\pm 2.165 \text{ cm}$ and repeatability of 0.973 for vertical movements and an accuracy of $\pm 1.479 \text{ cm}$ and repeatability of 0.944 for lateral movements, after tests were applied. Data from the controller (PWM output 0–255) were used as input for the control board and power control board (specifically the Mosfets IRF540-N) that regulate the current supplied to the respective SMA, generating the movement.

The kinematic parameters produced during the movement of the jellyfish show that after each contraction, there are peaks of velocity, increases in movement, and acceleration. The jellyfish bell diameter shows a fast variation during the first 33% of the total contraction time. Comparing the displacement data (vertical movements) of the robotic jellyfish against jellyfish of the species *Sarsia* sp. and *Proboscidactyla flavicirrata*, it can be emphasized that in the curves generated with the results for displacement, speed has highly similar behavior, achieving speeds of up to 2.5 cm/s (Robotic Jellyfish), compared to 2.8 cm/s of the mentioned species.

The use of MATLAB as an interface allowed temperature data acquisition, robot location, control of autonomous movements, generation of thermal maps, and identifying the jellyfish state and monitoring its temperature status.

The Jellyfish robot is proposed to monitor not only temperature but also other environmental variables (Ph, contamination (turbidity)). The temperature was chosen to demonstrate it due to its ease of management and the fact that it is reversible, not contaminating the water and thus allowing the opportunity to repeat experiments without changing it.

4.4 Plant-inspired design for explorative soft robots

Plants have been rarely considered in robotics as a model of inspiration for designing and developing robots. This is probably due to “their radically different operational principles compared to animals and their difficulty studying their movements and features.” [338]

However, plants present an incredible ability to respond to various signals or external stimuli and adapt to changing environmental conditions. For this reason, they realize movements characterized by energy efficiency and high density to reduce energy consumption during motion.

New materials are necessary to realize robots inspired in plants. Natural materials are based on a limited number of basic components (i.e., cellulose, hemicellulose, lignin, and pectin) that provide all the properties mentioned above due to their hierarchical organization. One famous material inspired by plants is Velcro [339]. Many other interesting industrial solutions resulting from the study of plants like bamboo, lotus or pomelo, are summarized in [338].

Macroscopic plant movement results from a coordinated and reversible modulation of intracellular turgor (pressure) to tune their stiffness. Thus, in [340], a soft robot plant was proposed, it presents a reversible osmotic actuation based on the electrosorption of ions on flexible porous carbon electrodes driven at low input voltages.



Figure 4.37 Tendril-like soft robot able to climb [340]

This work has realized an initial study about the possibility of designing an explorative soft robot taking inspiration from the morphology and movements of climbing plants that follow environmental stimuli to orient themselves, find supporting structures, and direct their growth for enhancing light exposition and survival.

The apical extremities of climbers, especially in twiners, are the most active in exploration and growth. They show the specific architecture of tissues with fibers that re-orient to convey twining, coiling, and nutation movements. Water flow is the motor pump in these aerial parts, with growth motions driven by environmental light.

The aim is to investigate a biomimetic design for the generation of environmentally-driven behaviors in a soft plant-inspired robotic arm, and mimic elongation and bending capabilities of the apical regions of twiners, taking advantage of a custom-made functional material, already available in the Bioinspired Soft Robotics laboratory of Istituto Italiano di Tecnologia, Italy, able to respond to humidity and light.

The material can be combined with, e.g., SMA to transduce the energy collected by the material into a 3D motion. In this case, SMA shows advantages and disadvantages, e.g., long cooling time, which needs to be exploited and addressed to confer the motion's fast (range of few minutes or seconds) reversibility. Other possibilities can be exploited, including microfluidic, origami-like configurations, or tensegrity systems.

In the following figures, the first design proposals are shown. At first, it was considered possible to realize a structure formed by different levels, as shown in Figure 4.38. The structure will comprise two different materials: the black will be the functional material mentioned above, while the other will be soft like PDMS. The black material, equally spaced to allow bending movements in every direction, can be arranged in two ways: perpendicular (Figure 4.38a) or inclined 45° (Figure 4.38b) to the green part. However, the two solutions were not suitable since the thickness of black material needs to be tiny (a few mm) to realize its function correctly, and the structure could not stand on itself. Moreover, a design solution made from a single material will be preferred, not two as in this case.

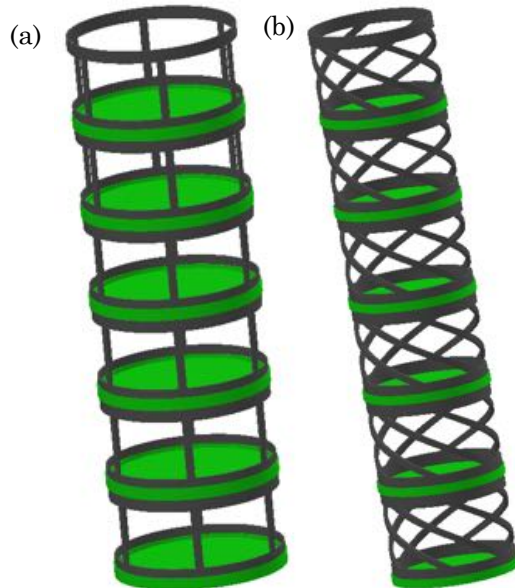


Figure 4.38 First design proposal. The black parts represent the functional material, while the green one the inactive structure. In (a), the functional material is perpendicular to the structure, while (b) is inclined 45°.

Thus, the next idea was to realize a structure capable not only of being able to bend but also elongate. One approach could have been that of origami, but given the characteristics of the material, it was not possible to create folds. Since it naturally tended to return to its original position without needing to be activated. In literature, in similar cases, the adopted solution has been to realize the structure in various parts and join them with the functional material. So, when activated, it actuates the other inactive components of the structure. In this case, it was not a solution contemplated since it was pretty evident that the material could realize movements but do not support the weight of other parts. However, starting from the origami idea, a design was proposed composed of a single piece that presented some incomplete cuts that generated fold lines along which the structure was weakened (Figure 4.39).

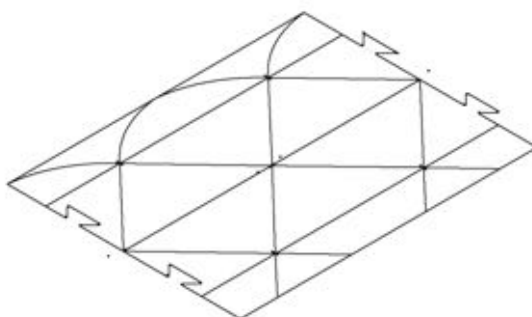


Figure 4.39 Design based on origami. The incomplete cuts represent weakness along which fold the structure.

The idea was to realize these cuts with laser cut. The final structure will be a cylinder folded that would have elongated and bent by activating the material.

After testing this idea, it was possible to notice that the structure could not be folded despite the cuts. It is important to remember that the structure has a thickness of a few millimeters, so the cuts present a depth lesser than 1 mm. For this reason, the desired effect is probably not obtained while it is obtained by applying the same idea on greater thicknesses.

The final proposed design consists of a mixed version of the previous ones (Figure 4.40). In this case, the robot consists of only one part, the design is realized with laser-cut, and the final shape is a cylinder. This structure seems to be a viable option, but further studies are needed.

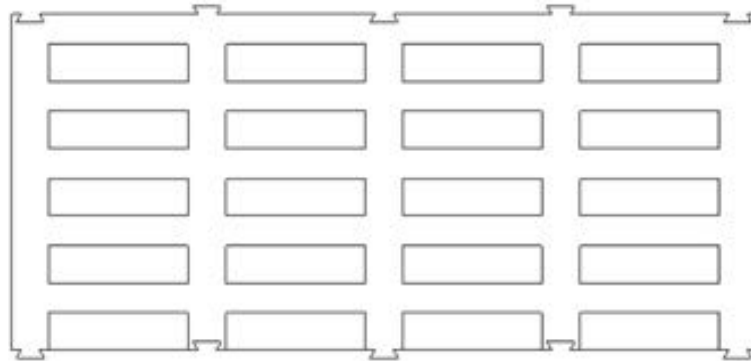


Figure 4.40 Final proposal design.

4.5 Discussion

The study of bio-inspired robots allows understanding better nature and how to reproduce the characteristics and capabilities of certain animals that, despite being very soft, can exert significant force or move very quickly.

It is not always possible to faithfully reproduce living beings since nature is complex, and millions of years of evolution have been necessary to reach what they are today. However, it is essential to consider some of the characteristics that define them to make more similar prototypes in terms of capabilities. For this reason, the starting point of these prototypes is their natural counterparts. Thus, the real dimensions of a starfish and a jellyfish have been considered. Moreover, each prototype has chosen different silicones to reproduce each body's different elasticities and consistency.

The jellyfish has been shown to have more satisfactory results than the starfish. Something that has influenced these results has been the environment in which the tests were carried out. Many larger soft animals generally move in a medium such as water or underground. Therefore, the jellyfish can realize proper displacements in the water while the starfish finds it challenging to move on a surface.

The biggest objection would be that the starfish is also an aquatic animal, so it probably could have moved without problems in the water. However, the objective was to reproduce a starfish that could move out of the water, supporting its weight.

The choice of SMA as the actuator has proven to be suitable as it does not add significant weight to the body. Water also represents a substantial aid in cooling the SMA, speeding up its operation. While in the case of the starfish, an external cooling system would be necessary since the starfish's speed is greatly affected by the cooling time.



5. Soft robotics manipulators

"Each problem that I solved became a rule which served afterwards to solve other problems."

Rene Descartes

Manipulators soft robots are the second identified group of soft robots. They represent probably one of the most crucial fields in soft robotics due to the many applications this type of robot can potentially realize with a significant advantage to conventional manipulators. The biggest problems are the modeling and control, as already explained in state of the art. In this chapter, two prototypes will be analyzed, and the modeling strategies applied in each case will be studied. The first will be a tendon-driven continuous robot (Kyma), while the second (Ruān) is a continuous soft robot actuated with SMA springs.

Further information on this section can be found in original scientific publications [341–343]

Also, an explanatory video of some of these robots can be found in the Electronic Supplementary Material (Videos [S.3](#) and [S.4](#)).

5.1 State of the art

In the late 20th century, Gregory S. Chirikjian made fundamental contributions to developing continuous manipulator robots. He proposed a modeling strategy for this robot by approximating its shape to a curve [236]. This methodology was checked in a hyper-redundant manipulator of 30 DoF, also used to study obstacles avoidance, various forms of locomotion, and some gripping algorithms [344].

Later, at the beginning of the 21st century, there were numerous advances in the design and modeling of this type of robot thanks to Walker and his research group from Clemson University, which proposed a manipulator inspired by an elephant's trunk. He also studied the theoretical foundations of continuous robots [238] and proposed a model to approximate them, assuming that their sections are constantly curved [4]. This robot can also be considered hyper-redundant, discrete, and underactuated.



Figure 5.1 Elephant's trunk by Hannan and Walker [238].

Continuous robots offer multiple advantages against other such as the ability to surround objects with their whole body. However, continuous robots usually present complex controls. For this reason, Walker argued combining continuous elements — to adapt with the environment— and rigid ones — to achieve more accurate positioning— [345].

Medicine is one of the fields in which continuous robots have a greater impact. For example, for minimally invasive surgeries [346,347], endoscopies [68], or colonoscopies [348]. Many miniaturization efforts for this type of robot have been achieved in recent years.

Another example of a continuous robot with a significant impact on the research field is Tendril made by NASA. It is a manipulator robot designed for minimally invasive tasks in space missions. Its peculiarity is based on an eccentric morphology with great length and small diameter compared to other models made up to that time. The greatest inspiration for its design comes from those made for medical applications, although such models did not reach similar lengths. It consists of two joints provided with springs to make prismatic movements and a set of cables that allow their rotation. The springs provided some consistency to maintain the robot structure and were also used to control its compression. The cables were connected using two motors and pulleys for each joint so that the retraction of a tendon enabled the extension through the other end [349].

Over the years, hybrid systems were also studied, either because of the actuation strategy, such as the case of ET Arm —using both pneumatic actuation and tendons— [350], or either because of the materials —partially soft and rigid— [351]. This methodology comes from the idea of Walker of finding a balance between the properties of different types of robots. For example, the ET Arm (Elephant Trunk Arm) was designed to present a new system of actuation not composed either by cables or by pneumatic actuators. It was made up of two segments; each provided multiple elastic structures, artificial skin, and three artificial muscles. Besides, it was actuated by a series of motors arranged in its base, allowing the continuous movement of its structure.



Figure 5.2 (a) *Tendril, made by NASA to perform minimally invasive tasks in space [349].* (b) ET ARM, actuated by artificial muscles [350].

Moreover, other continuous robots were designed without using elements as springs within the structure, such as the robot of the University of Nottingham. It was conceived inspection and reparation tasks in wind turbines. It is a very flexible model, and, just like Tendril, it has a high eccentricity regarding the length-to-width ratio. It has 25 DoF and is capable of navigating in unstructured environments. Also, it has a camera on its end-effector to allow in-situ interventions. Additionally, it presents a compact and innovative mechanical structure, which uses pairs of cables to minimize the number of actuators and joints to allow high accumulative bending angles. A set of innovative control algorithms allows its navigation and generates the end-effector trajectory [352].



Figure 5.3 *Robot with 25 DoF for inspection and reparation tasks in wind turbines [352]*

After studying the continuous robots, traditionally made from rigid materials, new types of flexible structures were considered to allow other types of interactions with the environment. These robots, commonly called soft robots, promise greater adaptability, versatility, and security advantages compared to traditional continuous ones.

Other types of actuation, such as the pneumatic, not so used up to that time, suffered a remarkable growth alongside this paradigm shift. Some examples of robots that used this type of actuation are the KSI Tentacle Manipulator [353], Air-Octopus [30], or the OctArm [4]. Years later, the Festo company also made a relevant industrial manipulator with pneumatic actuation with high performance: the Bionic Handling Assistant (BHA) [31].

First, the Air-Octopus featured a hybrid performance, provided by a central camera pneumatically pressurized and by external tendons. It consists of two pneumatic sections, mainly used to grant consistency and flexibility at the same time. One of the advantages of this design is the hollow design used to conduct tendons and sensors. These cables are arranged in angles of 120° and can only exert traction forces. A combination of these three

cables allows rotating each section in all directions. This configuration gives 2 DoF, and the soft structure provides a third prismatic one.



Figure 5.4 Air-Octor, a continuous manipulator robot with multiple sections [30]

On the other hand, the robot OctArm V is provided by 12 DoF actuated by pneumatic McKibben muscles. It is constructed from latex, covering the tube with a double helicoid fabric of plastic mesh. These actuators present a large strength-weight ratio, ideal for soft manipulators.

Furthermore, the Octarm V can grasp objects surrounding them with its structure. It can move with high precisions, and it can carry heavy loads. Morphologically, it is divided into three sections, each one with two axes of rotation and one prismatic movement, making 9 DoF. The length of each section was designed to achieve an accumulative bending angle of 360° in order to manipulate a wide range of objects with different sizes.

In addition, it can grasp and manipulate objects with a much higher dexterity than Air-Octor. Moreover, it is very flexible, elastic, and has good load capacity, but it is not easy to construct and control. However, Air-Octor has a much simpler mechanical design and is easier to control.



Figure 5.5 Octarm V, a soft robot inspired in an octopus tentacle [4].

As previously mentioned, another relevant soft robot is BHA, made by Festo. It is pneumatically actuated and almost entirely made by polyamide; as a result, it is very flexible and lightweight —around 1.8 kg in weight—. It has three main sections, each with three pneumatic actuators, one spherical joint, and one gripper with three fingers acting pneumatically. The total length of the robot is 75cm. When the bellow structure receives pressure, it can perform either prismatic or rotational movements. At maximum pressure, the robot can get a total length of 1.2 m. Besides, the robot configuration can be obtained using 12 length sensors. It is capable of stably moving to carry heavy loads. It is intended for cooperative applications and manipulation tasks because of its inherent safety.



Figure 5.6 *Bionic Handling Assistant (BHA) is a pneumatic soft robot with high dexterity made by Festo [31].*

Pneumatic systems have proven to be a solid actuation system for hyper-redundant robots. However, air compressors, needed for such systems, are often bulky, complex, consume lots of energy, and have high fabrication and maintenance costs [350].

From 2010, the growth of lighter and easy-to-reproduce soft robots increased. It is possible to find some of these examples in [6], of which many models were developed inspired by the octopus tentacle [18,65,103]. In addition, the appearance of these robots has promoted the study and application of novel methods of actuation, using materials with variable stiffness as in [230].

Some of the most representative examples of this genre are from the University of Pisa. One of them is a manipulator with a silicone structure actuated by a flexible steel cable to provide prismatic movements and by a nylon one to provide gripping and flexibility capabilities. Both types of cable are actuated using servomotors. Furthermore, it can adapt its shape around the different sizes and shape objects [354].

Subsequently, these mechanical models were improved over the last years by implementing a new way of actuation. It is a soft robot composed of a very flexible braided plastic fiber structure, actuated by an arrangement of SMAs, set through both transversal and longitudinal directions to provide the desired deformations [158]. Accordingly, it is an entirely soft prototype able to perfectly mimic the movements of an octopus tentacle [18].



Figure 5.7 (a) *Soft robot inspired in a tentacle [103]. (b) Continuous and soft hyper-redundant robot composed by a braided cover and actuated by SMAs [18].*

5.2 Kyma, a tendon-driven soft robot

Kyma is a continuous soft manipulator composed of 4 modules for a total length of 120 mm. (Figure 5.8).

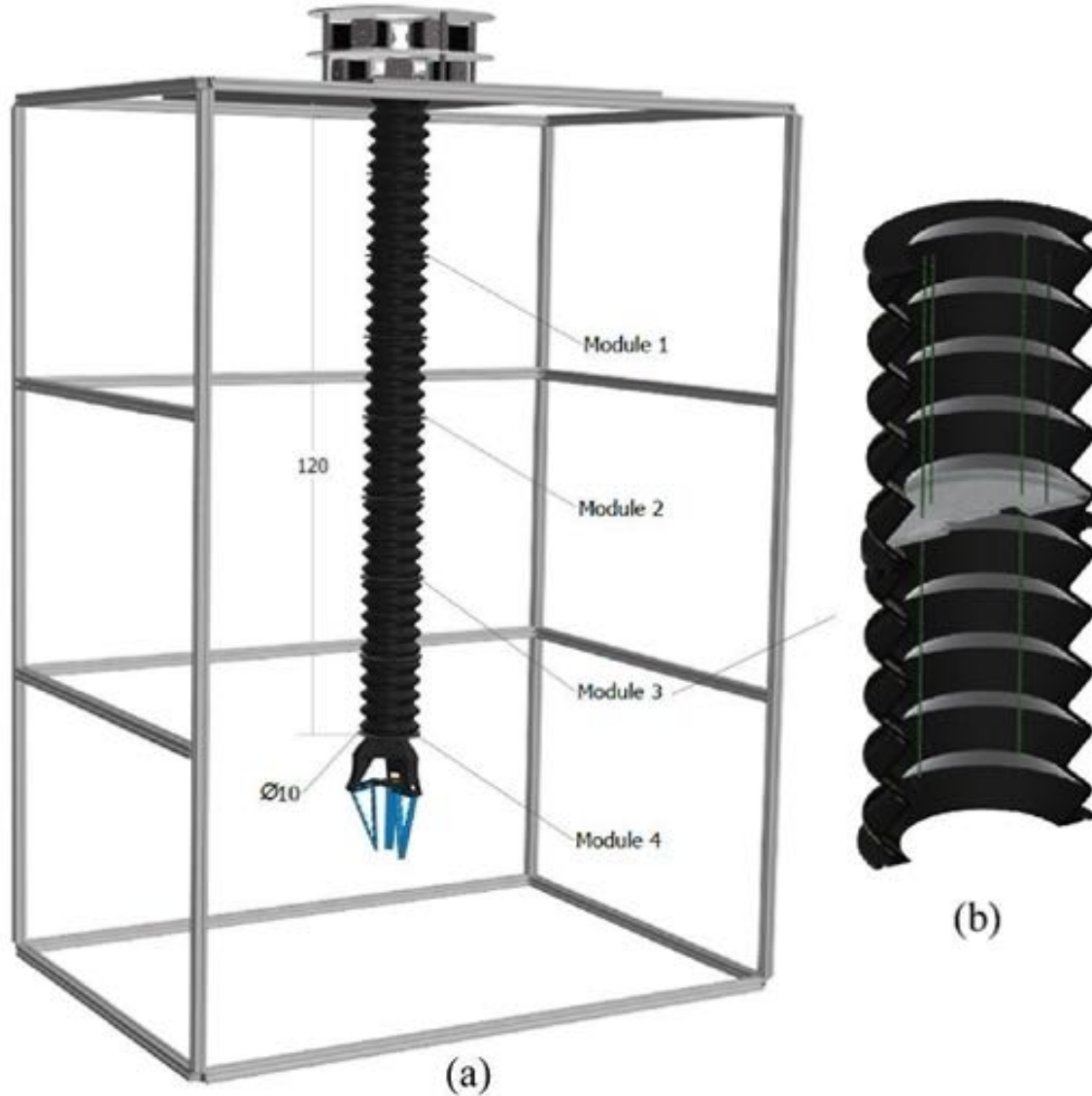


Figure 5.8 (a) Mechanical model of the soft manipulator Kyma, composed by four equispaced modules actuated by tendons. (b) Detail section of one module. Dimensions in centimetres.

5.2.1 Design

The main element of the Kyma structure is a set of wavy bellows that allow both bending and prismatic movements. The second one allows the robot to shorten up to 25% of its total length of 120 mm. Since bellows are made with flexible Polyvinyl Chloride (PVC), it is possible to affirm that it is a soft robot. As they are very flexible, when a single actuator makes a displacement, it usually combines both bending and prismatic movements, complicating notably the model. Bellows present an external diameter of 100 mm and a thickness equal to 2 mm. (Figure 5.9).

A 3D-printed ring was designed to join bellows together (Figure 5.10). This joint allows a quick and easy connection without adding significant weight or rigidity to the whole structure.

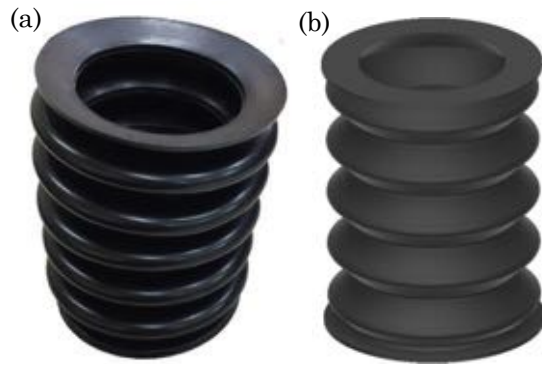


Figure 5.9 (a) The soft bellow used to realize Kyma's structure. **(b)** The CAD bellow model used in later simulations and mechanical design

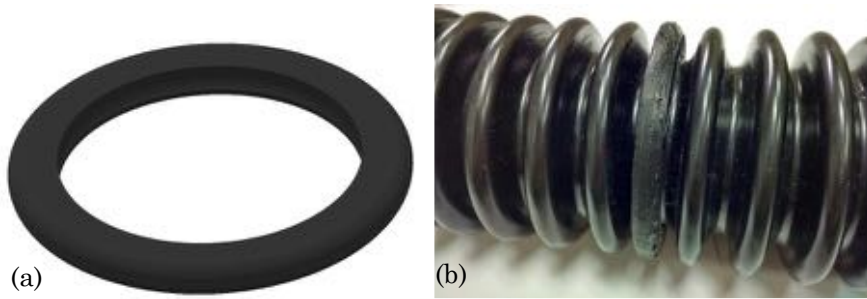


Figure 5.10 (a) CAD model of the ring connection **(b)** Detail of the connection between two bellows

Each module of Kyma's body comprises a bellow and a fiber-reinforced plastic disc (Figure 5.11) that fits perfectly in one of the pleats of the bellows without the need for any other mechanical connection.

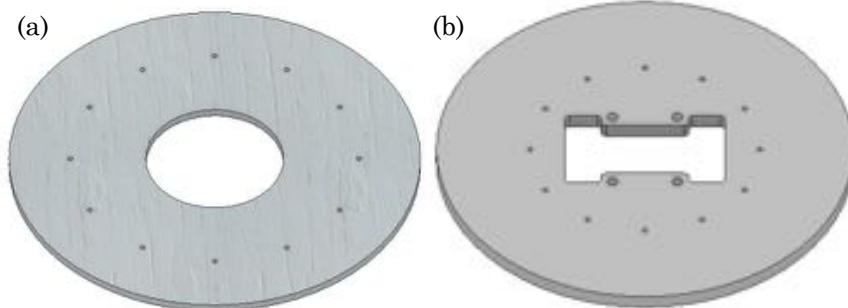


Figure 5.11 (a) First design of discs **(b)** The final design of discs

The holes in the discs allow anchored tendons that actuate the body. Tendons are a 0.8-millimeter diameter fishing line made of an ultra-resistant eight-fiber braid of polyethylene (Ultra-High Molecular Weight Polyethylene -UHMwPE), a robust and light fiber capable of holding up to 70 kg without breaking. The upper extremity of tendons is connected to its corresponding motor through a custom-designed pulley shown in Figure 5.12.

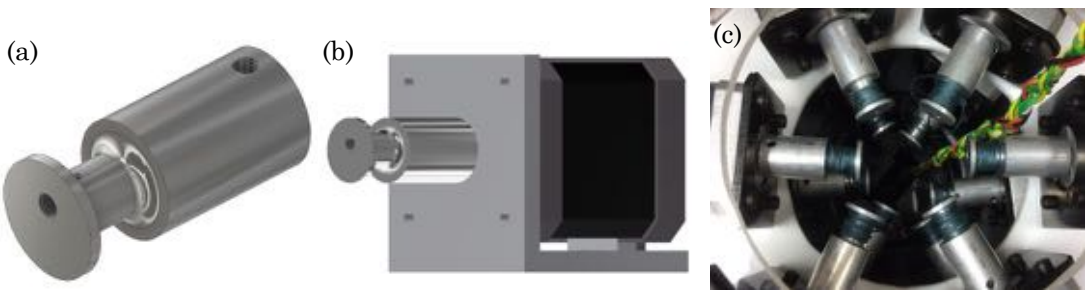


Figure 5.12 (a) Custom-designed pulley (b) The assembly between the pulley and the motor (c) Pulleys assembled in Kyma structure

Three angularly equidistant tendons actuate each one of the four sections at 120° , made. Other geometrical combinations were also tested but showed less stability and lower torques (Figure 5.13).

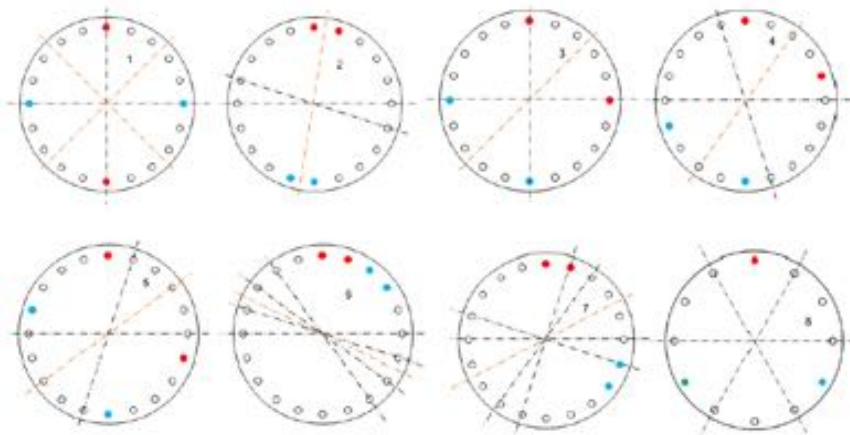


Figure 5.13 Different configurations to distribute the cables in a single module. The same color dots represent the movement of a motor and a cable in two directions; the black axis represents independent actuation rotations, and the orange one the combination of all of them.

Kyma relies on a total of 12 stepper motors in the external actuation box, capable of pulling the 12 tendons in a controlled manner (Figure 5.14).



Figure 5.14 The actuation box with the 12 stepper motors divided in two levels

The total DOFs of the robot are 12: 8 rotational and 4 prismatic. In fact, it is possible to obtain two rotational DOFs combining tendons' lengths one by one or in pairs and one prismatic DOF when the three of them act simultaneously for each section.

Tendons' lengths are independently controlled through the motors, all synchronized using a hierarchical control structure composed of 1-master and 3-slave processors. Furthermore,

the robot is equipped with a soft end-effector/gripper that allows carrying out pick and place operations which will be explained in Chapter 6.

Additionally, the robot use Inertial Measurement Units (IMUs) placed in the center of each disc to capture its pose in real-time.

5.2.2 Modeling

The high flexibility of Kyma's body difficult its control and modeling significantly. Therefore, it was challenging to choose a model technique to represent its highly no-lineal behavior properly.

As explained in state-of-the-art, the main strategies to solve the modeling issue for continuous and soft robots are model-free and model-based approaches.

Model-based approaches can be subdivided into kinematic and dynamic models. One approach for each one of these two categories has been applied to Kyma. The first one was the PCC (Piecewise Constant Curvature) method, while the second one was a numerical modeling strategy based on a Finite Element Method (FEM) using SOFA, an open-source library.

The PCC method was applied with an online correction of an IMU array sensory system. The PCC method was firstly computed (the theory of this method will be deepened in the next section of this chapter), while the robot was disposed of with a set of IMUs that provide the Kyma's absolute rotation at a specific point. All the information from the IMUs was collected with a multiplexor connected by the I2C communication. Minor deviations in each module can lead to high errors in the end-effector since, in serial manipulators, the error is accumulative from the base to the tip. From the comparison between the PCC and data, it was possible to correct the first one. So, it is possible to consider it a hybrid method since it does not entirely predict the robot movements but corrects the pose with online information. Results were obtained at very high frequencies and reduced the relative errors to 3%. This method is very cheap and relatively easy to implement. However, it would not be feasible to predict the robot movements beforehand.

However, the second strategy allows a better representation of Kyma since it can deal with its wavy morphology that allows its prismatic capabilities. All other methods neglect the geometrical design of soft robots. Additionally, this strategy allows contact response and compliance analysis. The SoftRobots Plugin of SOFA has been used. The theoretical foundations for this tool for deformable objects are the ones of continuum mechanics for the material modeling, Lagrangian multipliers for constraints solving, and Signorini's law for contacts. [355]

The system is based on Newton's second law, which models the dynamic behavior of a body as shown in Equation (5.1).

$$M(\mathbf{q})\ddot{\mathbf{v}} = P(t) - F(\mathbf{q}, \mathbf{v}) + \mathbf{H}^T \boldsymbol{\lambda} \quad (5.1)$$

Here, $\mathbf{q} \in R^n$ is the vector of generalized degrees-of-freedom, the displacements of the mesh nodes; $\mathbf{v} = \dot{\mathbf{q}} \in R^n$ is their corresponding velocity vector; $M(\mathbf{q})$ is the inertia matrix; F represents internal forces applied to the simulated object depending on the current state, such as the deformation law; P collects other known external forces; \mathbf{H}^T is the matrix with the constraint directions; and $\boldsymbol{\lambda} \in R^n$ is the vector of Lagrange multipliers containing the constraint force intensities, such as the force applied by actuators like tendons or pneumatic pressures. The backward Euler is applied to solve this equation. As a result, the element's force fields, masses, contacts, and constraints give place to the position and velocity outputs.

The main steps of this method are summarized in Figure 5.15.

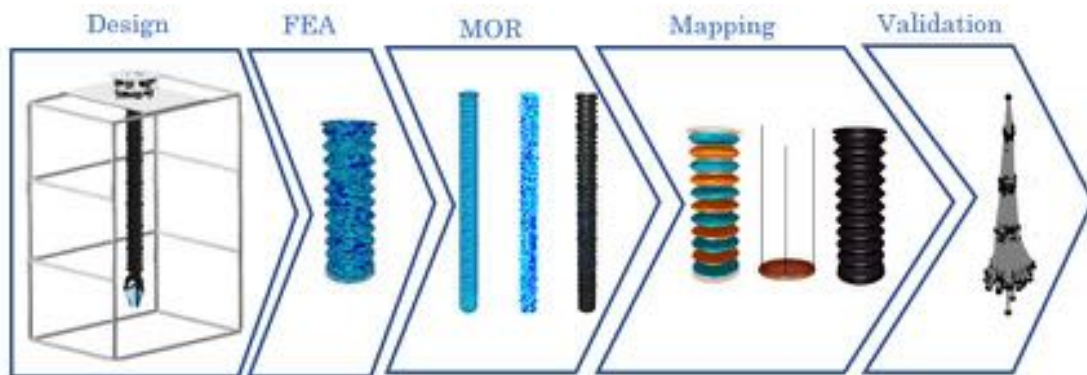


Figure 5.15 Framework of Kyma modeling.

The Finite Element Analysis (FEA) comprises different models to recreate Kyma's behavior as well as possible: the deformation model, the collision model, the actuation model, and finally visual model. To clarify the method's implementation, a scheme with the main components to construct the model (Table 5.1) and the main features of Kyma (Table 5.2) are presented.

Table 5.1 Main node hierarchy and a bullet list of the principal components to model Kyma in the SOFA environment alongside their descriptions.

Root node	SoftRobots plugin
<code>RequiredPlugin</code>	SofaPython plugin
<code>RequiredPlugin</code>	SOFAMiscCollision plugin
<code>RequiredPlugin</code>	Visual appearance of the scene
<code>VisualStyle</code>	Constraint solver
<code>FreeMotionAnimationLoop</code>	Constraint solver
<code>GenericConstraintSolver</code>	Collision detection by pair-wise tests
<code>BruteForceDetection</code>	Set distances to consider collisions
<code>LocalMinDistance</code>	
Kyma node	
<code>EulerImplicit</code>	Time integrator
<code>MeshGmshLoader</code>	Mesh loader for Gmsh file format
<code>MechanicalObject</code>	Mechanical state vectors
<code>UniformMass</code>	Define the element's mass
<code>TetrahedronFEMForceField</code>	Tetrahedral finite elements
<code>RestShapeSpringsForceField</code>	Elastic springs used to anchor the robot
Kyma visualization node	
<code>OglModel</code>	Visual model for OpenGL display
<code>BarycentricMapping</code>	Mapping using barycentric coordinates
Kyma collision model	
<code>MeshSTLLoader</code>	Mesh loader for STL file format
<code>MechanicalObject</code>	Mechanical state vectors
<code>Point</code>	Collision model based on points
<code>Line</code>	Collision model using a linear mesh
<code>Triangle</code>	Collision model using a triangle mesh
<code>BarycentricMapping</code>	Mapping using barycentric coordinates
Disks node (x4 units)	Simulation of the inter-modular disks
Tendons' node (x12 units)	Actuation cables anchored in the disks
<code>MechanicalObject</code>	Mechanical state vectors
<code>CableConstraint</code>	Tendons used to actuate the robot
<code>BarycentricMapping</code>	Mapping using barycentric coordinates
<code>PythonScriptController</code>	External code source based on python
Obstacles (optional)	Obstacles for interacting purposes

Table 5.2 Main parameters of Kyma to construct the FEM model and a heuristic adjustment to decrease the computational cost.

Variables	Real values	Heuristic tuning
Exterior diameter	100 mm	
Total length	1200 mm	
Thickness	2 mm	10 mm
Material	PVC	
Density	1160 kg/m3	
Mass	1.10 kg	2.5 kg
Young's Modulus	10 N/mm2	
Rupture strain	400 %	
Actuated sections	4	
Number of tendons	12	

The first and most important of them, the deformation model, requires choosing the proper type and dimension of mesh elements. Concerning the shape, a tetrahedron shape has been selected for being the best to fit in generalized volumes (Figure 5.16(a)). Another essential aspect to consider is the balance between the resolution and accuracy of the mesh to obtain reliable results with an appropriate number of elements. Generally, the higher the number of elements, the better the accuracy and the higher the computational cost, especially in terms of time. This second aspect is crucial to realizing a real-time model. So, the number of elements has to be the perfect balance between simulation accuracy and time. Analyzing previous works, it is possible to see that the SOFA Framework begins to perceive relative frame-rate decreases for more than 2000 elements. Therefore, the deformation model of Kyma should not exceed that value. However, the number of elements was very high due to Kyma's morphology. Two techniques have been applied to reduce them: the heuristic method and the Model Order Reduction (MOR) technique.

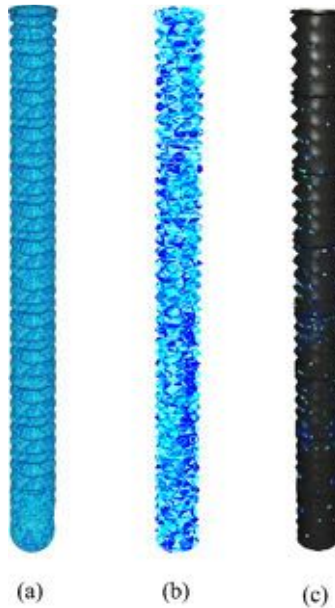


Figure 5.16 (a) Full-order deformation mesh with 120000 tetrahedra, infeasible for real-time applications. **(b)** The heuristic method adapts a model with 1650 elements to match the real robot behavior. **(c)** The Model Order Reduction decreases the number of state variables of the model to 1886 while retaining its original characteristics

The principal aspects that affect the number of elements (120 000 at first, later reduced to 11 000 decreasing the CAD resolution) are the robot's wavy morphology and thickness, which equals 2 mm. These force to have a very high number of interconnected elements. So, through the Heuristic method, the walls' thickness was increased to decrease the number of elements, keeping Kyma's behavior and obtaining a real-time model.

The model similarity (S) was obtained by a min-max normalization of the evaluated thickness (r) compared to the real one (r_{min}) and the maximum possible ($r_{max} = 50\text{ mm}$), as shown in equation () . The results of the different tests are presented in Table 5.3

$$S = 100 \cdot \left(\frac{r - r_{max}}{r_{min} - r_{max}} \right)$$

Table 5.3 Analysis of the model thickness versus the number of FEM elements.

Model thickness	Number of tetrahedra	Similarity
2 mm (real)	11 000	100%
3 mm	9000	98%
5 mm	2500	94%
10 mm	1650	83%
50 mm (solid)	600	0%

The similarity decreases significantly with the increase of thickness, but the computational cost also decreases considerably. The thickness value of 10 mm was selected as the proper compromise between similarity and feasibility. The model needs to be adjusted to the real robot with changes in the mass, but the macroscopic properties are quite similar.

The greatest weakness of this model was that robot characteristics are not perfectly retained. For this reason, the MOR technique was implemented. It retains the exact robot characteristics and uses a set of offline simulations to reduce the number of state variables of the model. In this second case, the starting model (the full-order model) needs to be highly accurate to represent the real soft robot, so the CAD model with 11 000 tetrahedra was used. MOR techniques comprise many different methods. In this work, the *Proper Orthogonal Decomposition* (POD) method was applied since it is a powerful and effective MOR method that aims at obtaining the most important components of a high-dimensional complex system by using a few proper orthogonal modes [356]. It maps the high-dimensional system to a low-dimensional subspace. The *ModelOrderReduction* plugin was used to implement this method, which reduced the number of state variables of the model to 1886 while retaining its original characteristics.

This deformation model will be the basis for all other models adopting the pose through a Barycentric Mapping [357].

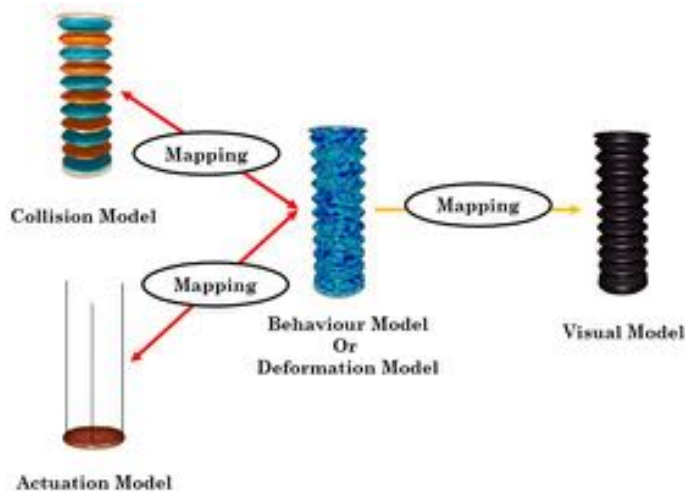


Figure 5.17 The multi-model representation in SOFA.

The actuation model (Figure 5.18) defines the set of twelve tendons that virtually exert displacements from a prefixed pull point to an anchor point. Their movements are consistent with the bellow deformation through a Barycentric Mapping. Moreover, they are guided through a set of intermediate points to avoid the collision with the bellow. (Figure 5.19)

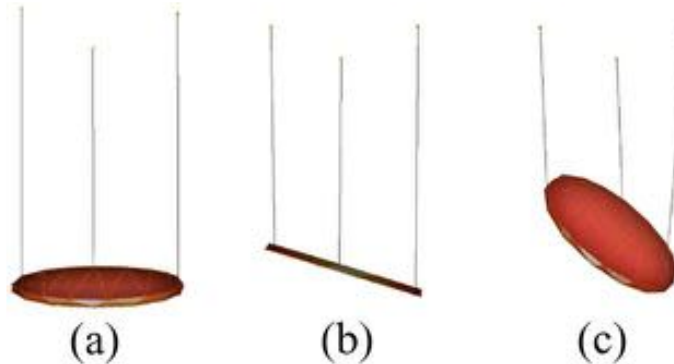


Figure 5.18 Actuation system based on three tendons per section. (a) Not actuated, (b) side view of the left-tendon displacement and (c) multiple-tendon displacement.

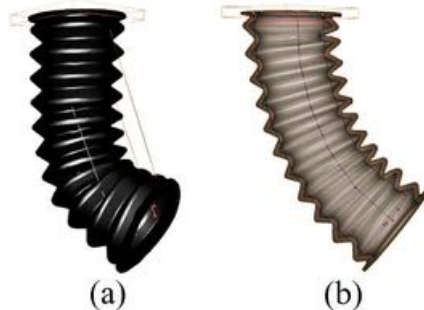


Figure 5.19 Transmission system based on (a) tendons without guidance and (b) the same system restricted to the robot morphology.

The collision model was implemented for two main reasons: self-collisions and interactions with the environment or other objects. If the self-collisions were not considered, the robot deformation model would overlap the bellows in a non-realistic way (Figure 5.20).

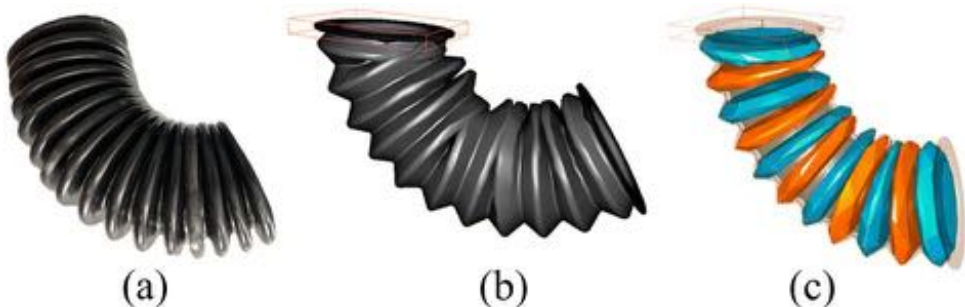


Figure 5.20 Difference between (a) the real robot behavior with physical restrictions, (b) the undesired model without self-collision restrictions, and (c) the simplified collision model based on two different subsets.

It is recommended to deal with each collision system independently for better results. Thus, as Kyma is made with eight bellows provided with six folds each, it will be expected to have 48 independent collision models to consider all the possible permutations. However, it was possible to reduce this number to a set of two, as shown in Figure 5.20(c), since it was experimentally deduced that interactions between neighbor folds are enough to recreate the

robot behavior. Consequently, the computational cost is widely reduced while still obtaining good results.



Figure 5.21 Front and perspective view of the Kyma model interacting with its supporting structure in a zero-gravity environment and with an object.

Finally, the visual model is the simplest node of the system since it is used to represent the real appearance over the deformation model, which is the one that truly computes its movement. Thus, the visualization node is created as a Child of the deformation node. A BarycentricMapping component is again used to move this model according to the deformation one in real-time. The final effect looks like the visual model is moving, while the truth is only represented.

5.2.3 Models validation

Both previously explained models, the heuristic and the MOR one, have been tested by comparing the real robot behavior. Two metrics have been studied to analyze the model feasibility: computational time and accuracy.

The real-time capability has been tested for the first metric by actuating the model slightly higher than the prefixed motors' maximum speed (120 rpm). Under these circumstances, the model provides its outputs at an adequate frequency of 20 Hz to compute the robot dynamics. This value may not depend just on the number of elements of the deformation model but also on the computer system, the collision model, or the visual one, among other parameters. The wavy morphology of the robot Kyma influences the computational cost of the collisions management. The following tests were conducted in a computer with Intel® Core™ i7-8700 at 3.70 GHz, ×64 architecture, and 16 Gb of RAM. Higher frequency rates could be obtained using a computer with better specifications.

Regarding the accuracy, both the soft robot Kyma and the real-time FEM models have been equally actuated to compare their whole-body configurations. For that purpose, a set of 100 random robot poses has been compared to evaluate the model accuracy within its entire workspace. To measure the exact pose of Kyma, an OptiTrack motion tracking system has been used. Thus, several passive markers made of retro-reflective material have been deployed on the robot's surface to capture its shape by using an array of infrared-sensitive cameras and light sources (Figure 5.22). The motion capture system works at 250 frames per second, and its accuracy is below 0.1 mm. Because of this, the obtained results by the motion tracking system can be considered the ground truth.



Figure 5.22 Three of a total of twelve infrared-sensitive passive markers used by the motion capture system to obtain the robot pose.

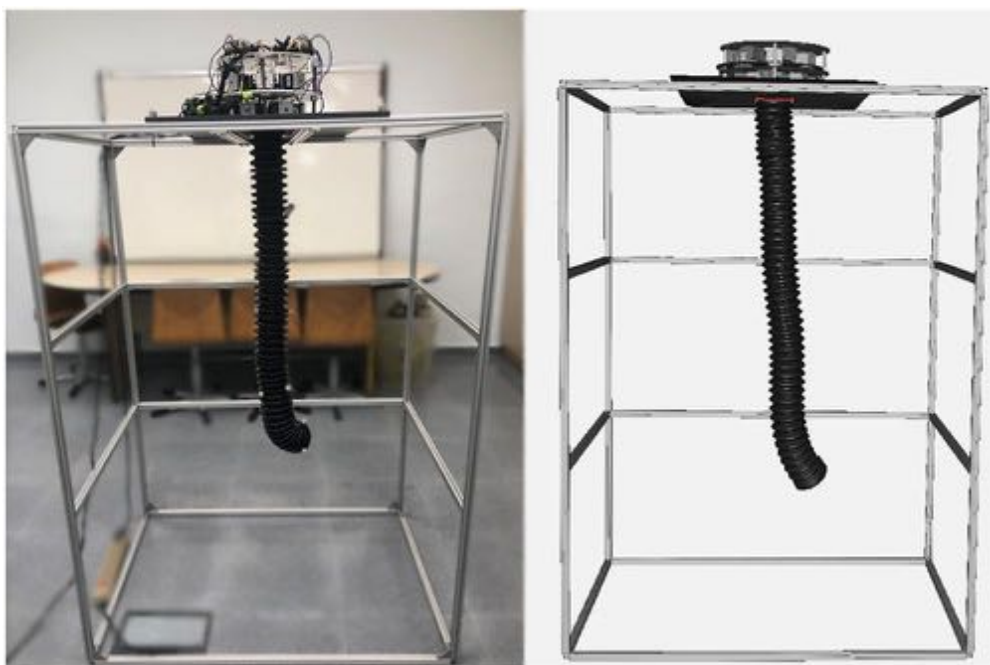


Figure 5.23 Comparison of a single test of the real robot (left) versus the obtained model (right).

Then, both the robot and the FEM models are equally actuated, as shown in Figure 5.23. If all the tracked poses are combined in the same graphic, it is possible to show the explored workspace (Figure 5.24). The exact results are exhibited in Table 5.4. Here, the mean, minimum and maximum errors are calculated and analyzed concerning their maximum distance from the robot's zero position. It is essential to clarify that the primary purpose of soft robots relies on easily adapting or safely interacting with their environment. However, not precise enough models can result in an infeasible closed-loop control. Thus, accuracy must be studied in soft robot models, but it should not be evaluated with the same yardstick as for rigid ones.

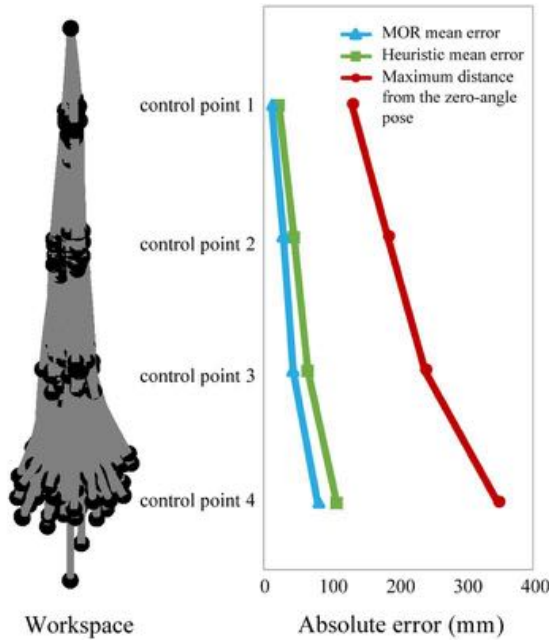


Figure 5.24 Real robot workspace representation for 100 iterations and validation of the FEM model. The absolute error is compared to the maximum Euclidean distance of the robot from a non-actuated pose.

Table 5.4 Validation results of the FEM Model for 100 random pose iterations.

Control Point	h	D_{max}	\bar{x}_1	\bar{x}_2	x_{min}	x_{max}
1 (base)	300	130	22	20	3	66
2	600	183	44	40	6	89
3	900	239	64	59	10	124
4 (tip)	1200	348	107	99	46	195
All:	-	348	59	56	3	195

It can be seen in Table 5.4 that the heuristic model locates its first control point with an accuracy of 22 mm on average while getting maximum ones up to 3 mm. Similarly, the MOR model obtains a mean accuracy of 20 mm for the first control point. Likewise, in all serial manipulators, the error is accumulated from previous to following control points. Thus, the tip gets higher errors than those control points close to the base. Additionally, the MOR model presents a slightly higher accuracy than the heuristic one, but both of them are quite similar. The MOR technique relies on the characteristics of the real robot and proposes a general solution without any human intervention. However, the heuristic method is less reliable since it depends highly on the robot and a specific decision-making process.

Considering the maximum Euclidean distance of each control point from its non-actuated state, it is possible to infer the relative error. In similar works, such as [247], a 1.4 mm mean error is obtained using the same framework for a smaller robot that works in a workspace of 32 cm³ ($4.37 \cdot 10^{-2}$ mm/cm³). However, the current work obtains mean errors of 59 mm for the heuristic model and 56 mm for the MOR one within a workspace of 152 000 cm³ (around $3.75 \cdot 10^{-4}$ mm/cm³). Thus, the presented models present two orders of magnitude higher accuracy than the workspace sizes when the data is normalized. Surprisingly, the accuracy obtained from a bigger soft robot model based on real-time FEM does not decrease proportionally to a bigger size. On the other hand, if the mean errors are relative to the entire length of the robot, they are around 5% for both the heuristic and the MOR model.

5.2.4 Teleoperation

The last work realized with Kyma was its teleoperation through an immersive interface. The aims were to analyze if immersive interfaces enhance the telepresence and efficiency against conventional ones; and if natural language reduces workload and improves performance against other conventional tools. A population of 50 people has tested a total of 2 interfaces and six interaction tools.

The system arrangement will rely on bilateral communication (the information is exchanged between the user and the robot in both directions) (Figure 5.25). The user sends information to operate the robot, whereas the robot transmits information to the user to report its current pose, both in real-time. In the presented system, this bilateral communication performs a cycle with a frequency of 10 Hz, high enough to test the capabilities of the interfaces.

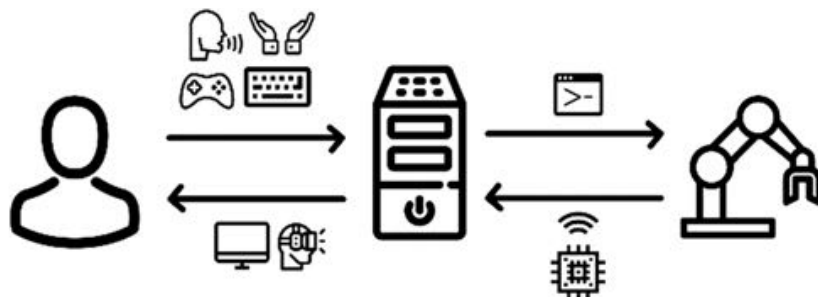


Figure 5.25 Bilateral scheme for the robot teleoperation.

The bilateral controller implemented in this work follows a position–position scheme. Thus, the robot will move to a determined position previously commanded by the user.

The two interfaces (conventional and immersive) have been created based on the same constitutive elements in Unity3D. A good interface would be clear, concise, familiar, responsive, consistent, aesthetic, efficient, and forgiving. With these features, an interface could provide high situational awareness that can be defined as the perception of elements in the environment within a volume of time and space, the comprehension of their meaning, and the projection of their status in the near future [358]. The conventional interface shows the information on a regular monitor, and the immersive one uses a virtual reality headset to display the same information.

Since Kyma is divided into four sections, teleoperating this robot will rely on four input positions. Additionally, a computer is used to host the interfaces and control the robot movements. It uses different peripherals to transmit or capture information from the user, such as a display monitor, a VR headset (HTC Vive), a keyboard, or a gaming controller. The robot feedback to the user will be visual to display its shape, obtained from the onboard sensory system based on Inertial Measurement Units (IMUs).

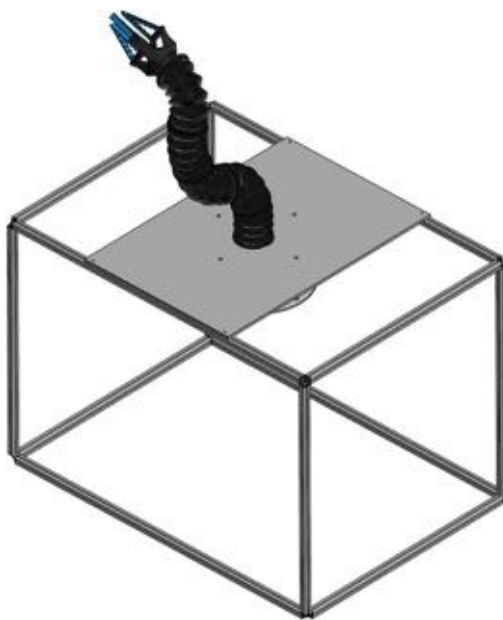


Figure 5.26 Kyma

The teleoperation of this type of robot requires a relatively high number of inputs to manage their shape [359] appropriately. However, human beings perform better, paying full attention to one thing at one time [360]. Therefore, the most convenient interface maximizes efficiency, which is the ability to maximize precision and speed by commanding a robot to perform a determined task.

The number of inputs will be highly dependent on the number of DOFs. In the case of Kyma (Figure 5.26), it has four sections, so the number of inputs will be the same, although the virtual robot will rely on a model based on Piecewise Constant Curvature (PCC) to reconstruct its shape.

In both interfaces, the user is expected to move the input towards five predefined positions, and, in case of making a selection, the robot will move accordingly. The robot's pose will be updated in the interface in real-time using the onboard sensory system.

In the conventional interface, the user is sitting looking at the monitor and can use the keyboard to move in 3D a sphere that symbolizes the position where the robot's end-effector is commanded to move (Figure 5.27). The real robot was located in the same space so the users could see the robot being commanded. However, in a real scenario, the robot could be located in a remote environment, so the robot's current pose is adequately displayed in real-time using the bilateral scheme explained before.

The same information is displayed in the immersive interface, but in this case, an immersive headset with three-dimensional (3D) stereoscopic vision is used. The user is asked to stand up and make small movements to command the robot position for this practice. Here, the user moves the 3D sphere that symbolizes the end-effector position by pushing it with bare hands, tracked by the Leap Motion device (Figure 5.28).

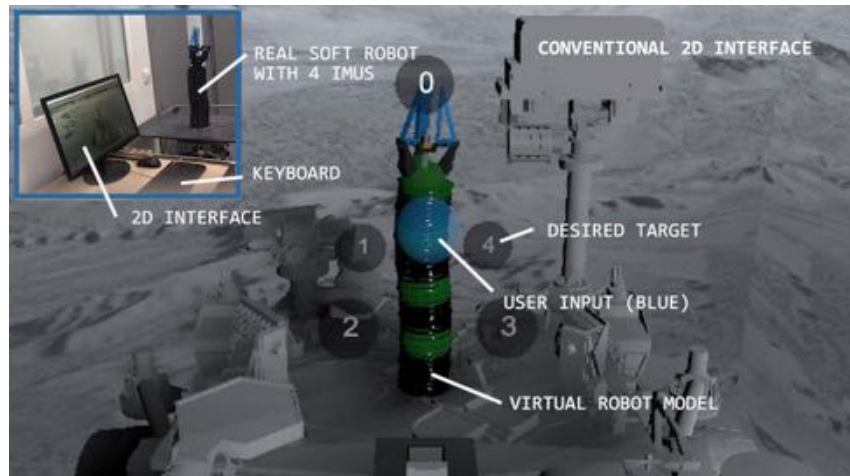


Figure 5.27 Conventional interface.

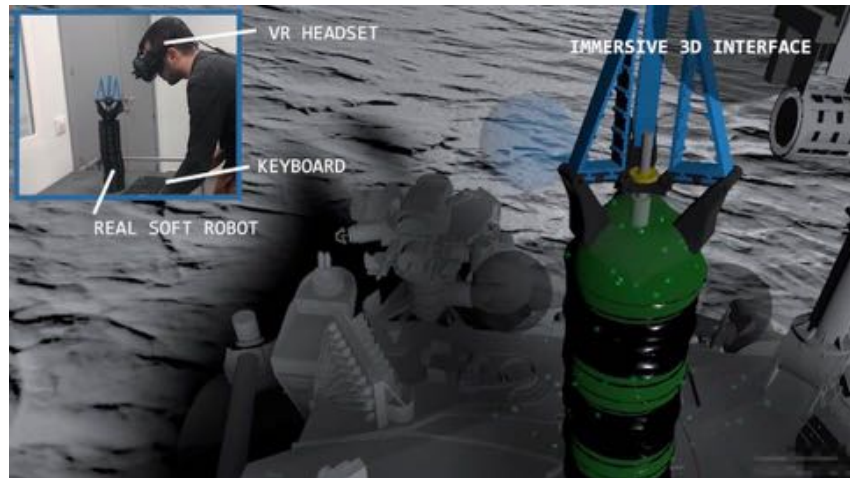


Figure 5.28 Immersive interface.

Six different approaches have been developed in Unity3D, making use of a computer, the HTC Vive VR headset, and, in some cases, Xbox or Leap Motion controllers to determine which strategy is more appropriate to teleoperate soft continuous robots in an immersive interface in terms of efficiency and workload,

These strategies are the following:

- **Controller.** The user is provided with a VR headset and an Xbox gaming controller to teleoperate the robot. The desired joint must be selected using some buttons, and then it can be moved along the Cartesian directions using the controller's axis. The implementation allows simultaneous inputs so the user can combine the three directions to perform 3D movements. The joints' speed can be adjusted by the quantity of displacement in the axis. (Figure 5.29)

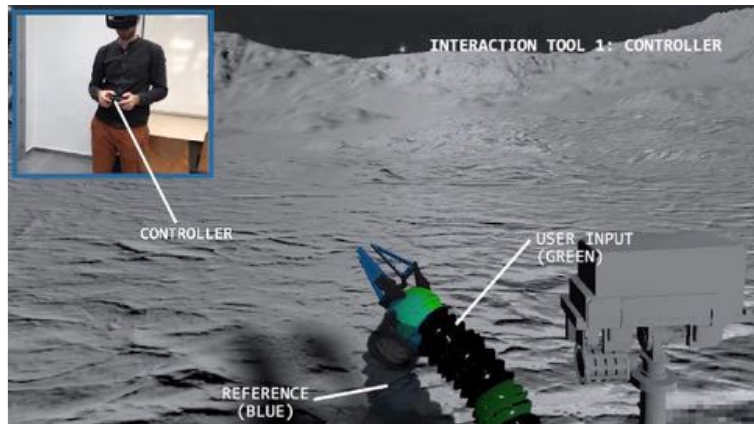


Figure 5.29 Controller strategy.

- **Master-slave.** A virtual master with the same features as the slave has been created. The user's hands were tracked using the Leap Motion controller. Thus, users with two hands can move the master, and consequently, the slave will be moved the same way as the master is being manipulated. (Figure 5.30)

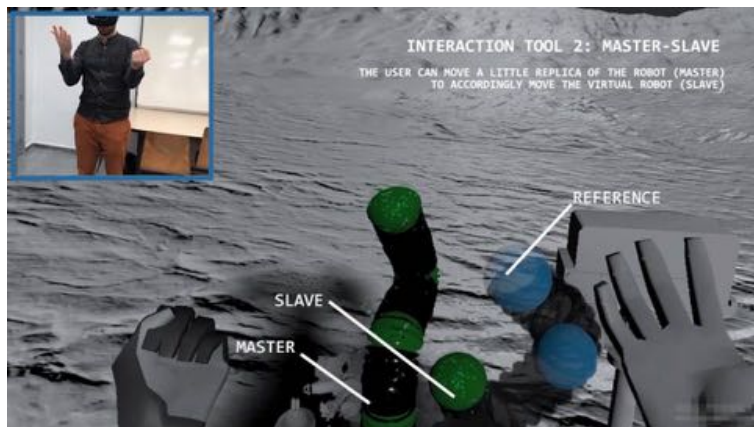


Figure 5.30 Master-slave.

- **Local gestures.** This strategy also uses hand tracking to capture gestures. However, the main difference is that the user must approach the virtual real-size robot and use the hands to push the robot joints towards the desired reference by direct contact. It was found that pushing enhanced efficiency and reduced workload against grabbing, so the joints could not be grabbed but only pushed using this approach. (Figure 5.31)

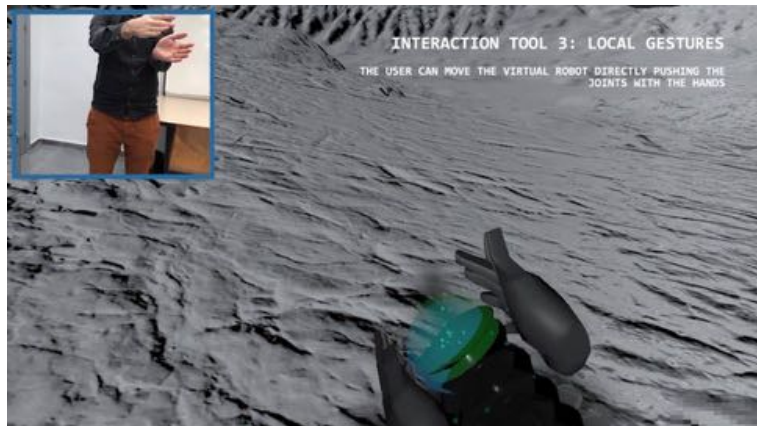


Figure 5.31 Local gestures strategies.

- **Remote gestures.** Like the master-slave strategy, it allows the robot to be moved without direct contact with the virtual robot model. The user can open the index finger on the one hand, so a virtual laser appears as an extension to easily select the joint to move. Then, when the other hand is opened, it will move the selected joint accordingly to its own movement. When this hand closes, the joint does not move. Since this strategy relies on remote gestures, the operator is not expected to move a lot. (Figure 5.32)

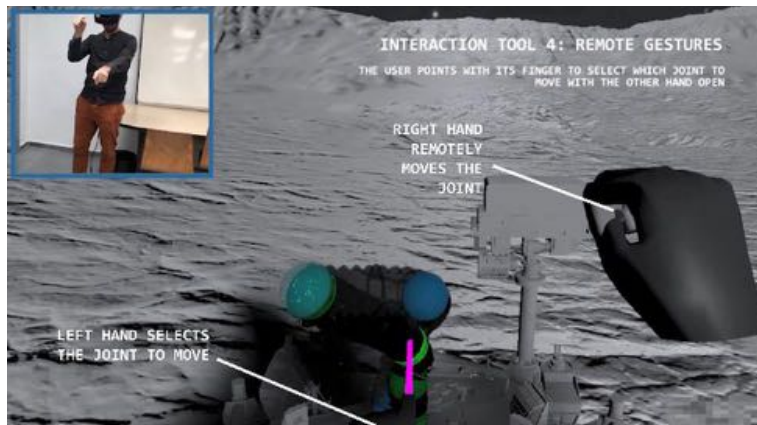


Figure 5.32 Remote gesture strategies.

- **Voice commands.** It is based on speech recognition to command the robot movements. This approach was created to teleoperate the robot even if the hands are busy or their movement is hindered. Therefore, the user needed to remember some intuitive commands previously defined in a dictionary. Such commands could activate the movement of the robot continuously by defining when to start and stop. The joint to move is first selected by pronouncing numbers, in this case, from 1 to 4. Then, the speed can be defined as a slow, medium, or fast. Finally, the user can speak in which direction to move the selected joint among left, right, forward, backward, up, and down. (Figure 5.33)

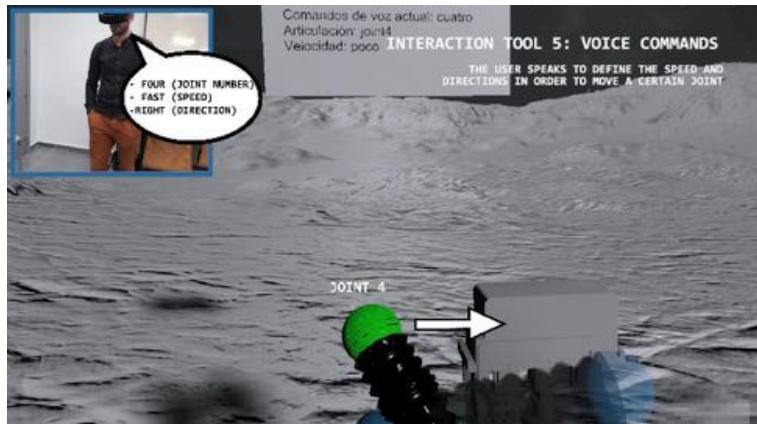


Figure 5.33 Voice commands strategy.

- **Hybrid approach of gestures and voice recognition.** Voice Commands are programmed to select the desired joint by pronouncing which joint to move from 1 to 4. Then, similarly to the Remote Gestures strategy, the user can raise the hand to move the joint with reindexing, as explained before. Hence, the voice is proposed as an alternative of pointing with the other hand to select the joints unequivocally, and gestures are selected to move the joint efficiently. (Figure 5.34)



Figure 5.34 Hybrid approach of gestures and voice recognition.

In every method, the user has to exploit all the available resources to adequately manage the pose of a virtual robot, which has to be approached towards a predefined virtual reference. The 50 participants needed to complete the tasks as fast and precise as possible in all these experiments. Experiments can be divided into two phases: (1) human-robot interfaces and (2) Interaction tools.

In the first phase, to test the objective efficiency of the developed interfaces in terms of precision and time, the participants were asked to move a blue sphere as a representation to where the end-effector of the robot is desired to move. This input could be moved towards five numbered and predefined target positions, depicted by grey spheres of the same size. The participants could practice for a while until they felt ready to minimize the learning factor between interfaces. They could press a begin button and move the input towards 3 of the five target positions previously specified. Then, a timer began to run, and the precision was measured as the mean of the Euclidean distances between the input and the desired targets. Both time and precision variables were first rescaled—min-max normalization—among the data relative to both interfaces to allow further comparisons, then averaged, and then rescaled again.

By this method, speed and precision are measured the same to test efficiency since both parameters can be considered equally important to teleoperate a generic soft continuous robot. However, it must be remarked that one variable could be more important than the other depending on the robot and its purpose. As a result, the efficiency is 33.55% higher on average, and the variance a 41.98% lower for the immersive interface than for the conventional one (Figure 5.35a). The results show that situational awareness is 73.71% higher in the immersive interface than in the conventional one (Figure 5.35b). Concerning the visual feedback evaluation, the participants could see the real robot and the model within the interface simultaneously and in real-time to make reliable comparisons between them. As a result, they perceived that the visual feedback was 39.47% higher for the immersive interface than for the conventional one on average (Figure 5.35c). To finish, and regardless of previous questions, the participants were asked to subjectively choose between both interfaces assuming they had to perform the same task. Consequently, 94% of the participants preferred to use the immersive interface (Figure 5.35d). Therefore, both subjective and objective parameters agree to select the immersive 3D interface to teleoperate hyper-redundant robots as the best to enhance efficiency and telepresence.

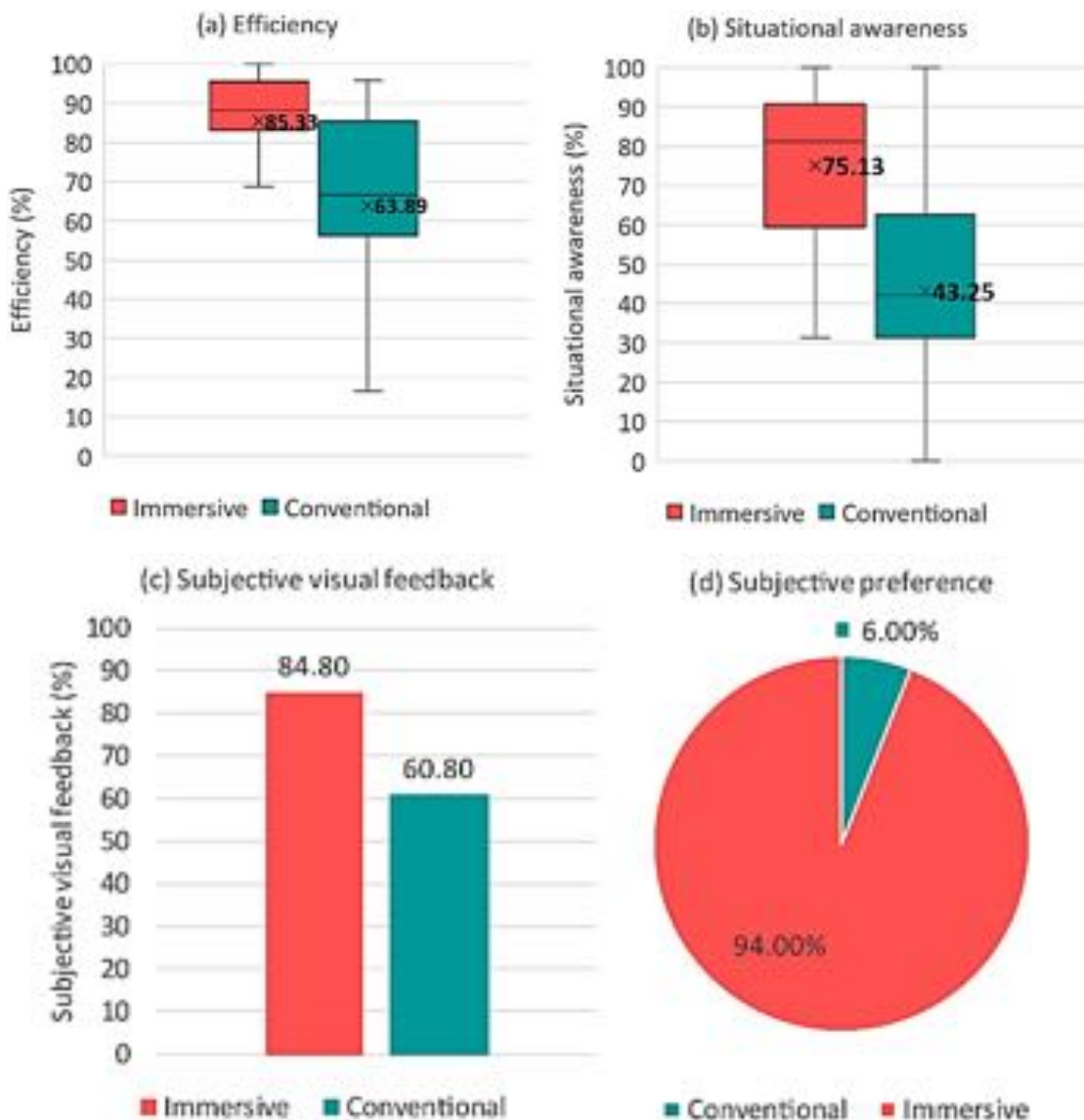


Figure 5.35 Results for the human-robot interfaces test. (a) Efficiency in terms of precision and time, (b) situational awareness, (c) subjective visual feedback, and (d) subjective preference

The second phase is based on selecting which interaction strategy is better within this immersive reality for the same purpose. As a reminder, there are six developed strategies: controller, master-slave, local gestures, remote gestures, voice commands, and gestures and voice. In this test, the participants used a VR headset to command the movements of a hypothetical virtual robot towards a randomly defined set of references by using the previously mentioned interaction approaches. On the one hand, the efficiency was similarly measured using both elapsed time and precision.

For each of the approaches, the user could also practice before the timer began to reduce the learning factor. Moreover, the precision was measured and averaged as the Euclidean distance between every four sections of the virtual robot and the relative ones of the reference, differently colored to ease comprehension. The user had to repeat the process three times in all the strategies, moving the virtual robot towards different references to increase data normalization. Such references were randomly defined but bounded to a predefined and limited space to not differ too much from one participant to another. Therefore, the virtual robot joints were moved 3600 times in total in these experiments. Accordingly, the learning factor was minimized, whereas the randomness and repetitions standardize the data to achieve generalization. Similar to the previous experiment, the speed and time were first rescaled, then averaged, and then rescaled again, giving place to the previously defined efficiency.

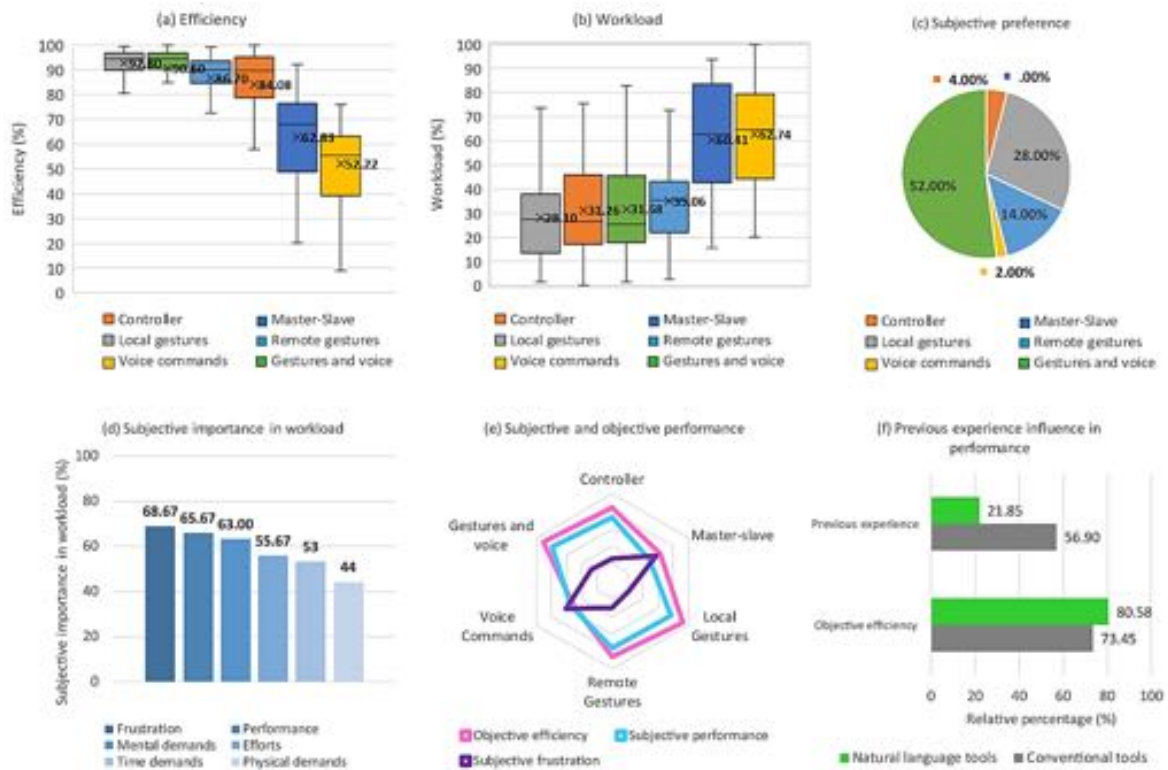


Figure 5.36 Results for the interaction-tools test. (a) Efficiency in terms of precision and speed, (b) workload, (c) subjective preference, (d) subjective importance of variables in workload, (e) subjective and objective performance comparison, and (f) previous experience influence in performance

Therefore, as seen in Figure 5.36a, the efficiency is indistinguishably the best for local gestures and voice, with mean values of around 90%. They are closely followed by remote gestures and the controller, indistinguishable with efficiencies of around 85% on average. Furthermore, finally, the master-slave and the voice commands are, respectively, the ones with less objective efficiency.

On the other hand, the most common method to determine the workload (W) of a mission is the NASA Task Load Index (NASA-TLX) [361,362]. It is based on rating 6 variables related

to the influence of workload: mental demands, physical demands, temporal demands, performance, efforts, and frustration. Thus, local gestures, controller, gestures and voice and remote gestures have half of the workload compared to master-slave and voice commands with mean values of approximately 32% and 61%, respectively. Besides, the participants selected frustration as the most critical factor influencing workload, followed by performance, mental demands, efforts, time demands, and physical demands, as shown in Figure 5.36d.

Furthermore, it is possible to compare the objective efficiency in Figure 5.36a with the subjective performance obtained from the workload test. Surprisingly, the participants were very accurate in evaluating their performance, and it was found to be highly influenced by the level of frustration (Figure 5.36e).

The participants were asked about their previous experience in VR and AR, robotics, and video games. If that experience is averaged and plotted against the objective mean efficiency for both tests, the variables are found as directly proportional (Figure 5.37). Therefore, previous experience can be understood as a significant factor in achieving a high-efficiency level.

Despite having less experience with natural language than conventional tools, the results show that the participants performed better using the first ones against the last ones (Figure 5.36f).

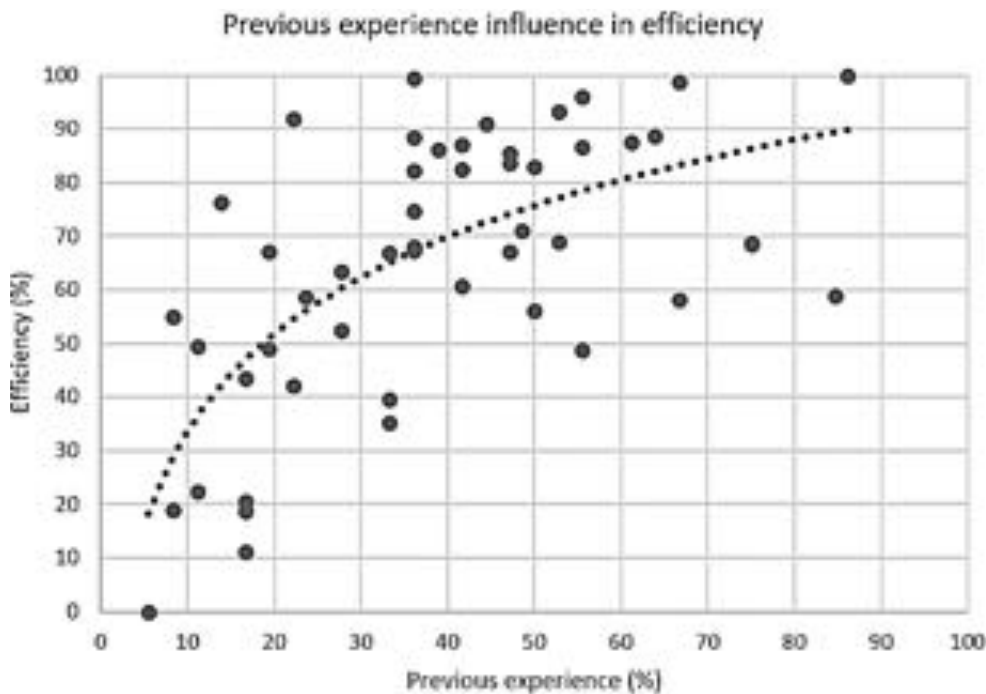


Figure 5.37 Previous experience influence efficiency both for the human–robot interfaces and the interaction tools experiments

Finally, regardless of previous results, the participants were asked to choose among their preferred interactions. More than half of the participants, precisely 52%, chose the gestures and voice strategy, followed by local gestures with 28% and remote gestures with 14% (Figure 5.36c). If the number of conventional and natural-language tools were the same, 92.31% of the participants would have preferred to use a natural-language tool against a conventional one.

5.2.5. Conclusions

The initial hypothesis of this work stated that a state-of-the-art strategy could constitute a reliable source to model the presented robot, Kyma. While some model-based methods rely on many assumptions, such as uniform shapes or negligible dynamics, the FEM approach was chosen to extract the irregular morphology of the robot and model robot–object interactions.

Likewise, many soft devices, Kyma, are composed of a thin body, usually difficult to model using FEM because of requiring many elements, often unsuitable for real-time applications. This is an important issue that had to be addressed to define the deformation model. Two methods are presented to optimize the FEM method efficiency and reduce the computational time. First, a heuristic method proposes to tune a model with fewer elements to match the behavior of the real robot. Secondly, the MOR technique may be the most promising one from the state-of-the-art. The heuristic method aims to solve this issue by slightly reducing the robot model accuracy instead of experimentally adjusting other parameters to capture the macroscopic deformations in real-time. On the other hand, the MOR uses a set of offline simulations to reduce the number of state variables, retaining the main characteristics of the robot. In both scenarios, an actuation system based on tendons and a collision model has been developed to manage self and possible robot–object interactions.

Real-time models based on FEM are highly dependent on computer graphics capabilities. The technological barriers are improved year by year, but the computer resources are still limited to reduce the gap between the real world and the virtual models. The higher the complexity of the environment, the higher the computer graphics requirements. This work presents the modeling process of a complex soft robot with numerous challenges such as very thin walls in a big structure, a strong dependence on its wavy morphology, the appearance of both bending and prismatic movements, or a high number of actuators. Using the presented techniques can help to dramatically reduce the computational cost of these simulations, making possible to model environments otherwise impossible to describe accurately.

Additionally, this work features a brief study of the compliance of the models since soft robots are usually devised for that purpose. Consequently, the developed models exhibit high dexterity and good capabilities to surround or lift objects using the robot's body. It is also concluded that the relation between the characteristics of the robot and the properties of the objects is crucial to performing specific tasks. Thus, simulation results show that soft robots also have much potential in space exploration activities where the action of gravity is negligible.

To finish, both models have been validated using a precise motion tracking system and making comparisons with the real robot. As a result, the control points were properly located with lower mean errors than in similar previous works. The MOR model presents a slightly higher accuracy than the heuristic one, and results obtained from the first one are more reliable than those from the second one since they are obtained without making any manual adjustment. Additionally, it can be deduced that this work studies the real-time FEM method for much bigger robots. Furthermore, most importantly, the accuracy obtained from the model validation does not decrease proportionally to a higher robot size. Moreover, both models exhibit accuracies up to three times higher than previous methods such as PCC. However, future works should not lose sight of other approaches like two-dimensional shell elements since they may also provide low computational costs for thin morphologies [363].

With these results, it is possible to discuss whether a very complex real-time FEM model can be valid or not. As usual, it will highly depend on the application. In this context, soft

robots are intended to adapt to their environment safely. Moreover, the obtained models manage to capture the main macroscopic shapes of a very complex device, opening the way for a promising future to control soft robots.

On the other hand, the teleoperation work aims to clear the path to focus the future research of hyper-redundant robots' teleoperation. This kind of robot has numerous degrees of freedom, so their spatial understanding is often difficult to perceive.

On the one hand, this work aimed to determine whether immersive 3D interfaces are better or worse than conventional 2D ones to teleoperate hyper-redundant robots. Experiments with 50 participants show that immersive interfaces exhibit 33.55% mean higher efficiency in terms of speed and precision and 73.71% mean higher situational awareness than conventional ones. As a result, immersive interfaces were chosen to teleoperate this kind of robot by 94% of the participants. On the other hand, the same population tested some interaction tools to determine which strategy is better suited for the same purpose within an immersive reality. A total of 6 methods were developed: controller, master-slave, local gestures, remote gestures, voice commands, and gestures and voice. In this case, efficiency is indistinguishably the best for both local gestures and gestures and voice, with mean values of around 90%, closely followed by remote gestures and controller. Also, a workload test showed that local gestures, controller, gestures and voice and remote gestures have half of the workload than the other two approaches. Besides, the participants were very accurate in evaluating their performance, which was found to be highly influenced by their level of frustration.

Moreover, results showed that natural-language tools are more intuitive since they exhibited higher performance despite the less previous experience. Finally, more than half of the users chose the gestures and voice strategy as the preferred one. This is understandable since we, as human beings, are used to communicating by simultaneously gesticulating and speaking. Moreover, 92.31% selected an interaction tool based on natural language against a conventional one. Therefore, this work concludes that immersive realities and natural-language tools should play an important role in the near future of hyper-redundant robots and their teleoperation.

5.3 Ruǎn, a continuous soft manipulator

Ruǎn is a continuous and soft manipulator robot since its body is made almost entirely of silicone and actuated with SMA springs (Figure 5.38).

The design of Ruǎn is based on the following requirements:

- dimensions limited in diameter and length, similar to [18,103]
- segments actuated independently to obtain a significant range of movements
- segments capable of being joined easily to allow a quick replacement in case of damage or to add segments

The final design of Ruǎn is a three segments robot. Each segment is cylindrical and is actuated with three SMA springs Figure 5.39 placed inside cavities that cross the cylindrical segment longitudinally. Cavities are not in the center of the cylinder but are offset towards the outside of the segment. Springs are placed symmetrically at 120°. Cavities present a diameter greater than the outer diameter of the springs to allow their correct contraction movement from which SMA springs exert force. Integrating the spring within the segment allows obtaining a more compact design.



Figure 5.38 Ruǎn

The individual or combined action of the springs allows the segment to bend around multiple axes. Thanks to this combination, each segment consists of 3 DOF, three actuators whose end position can be defined in a 3D space, and two rotations for the axes perpendicular to the central axis of the segment when found at rest.



Figure 5.39 SMA springs disposal

A single segment operated in this way can position its end on a surface similar to a sphere cap. The sphere's radius depends directly on the length of the segment, as shown in Figure 5.40. As previously indicated, the end of the segment could vary its position in X, Y, and Z and perform rotations about the X and Y axes.

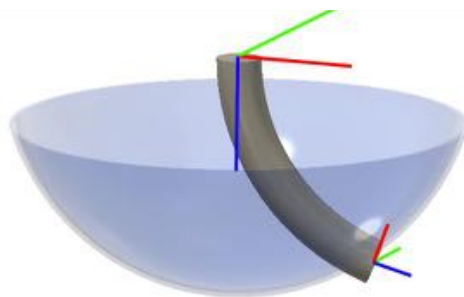


Figure 5.40 Motion of range of a segment

The composition in three segments widens the range of movements represented in Figure 5.41. The concatenation of the movements of the different segments generates a range of movements like the one shown below.

In this case, there are three springs for each segment, that is, three controllable DOFs. Since the complete set consists of three segments, 9 DOFs are obtained by which the position and orientation of the free end can be controlled. Therefore, it can be stated that the design corresponds to a redundant robot, and since the segments are arranged one after the other, it is a continuous robot. Figure 5.41 shows examples of the robot's configurations and the ranges of movements of each of the segments.

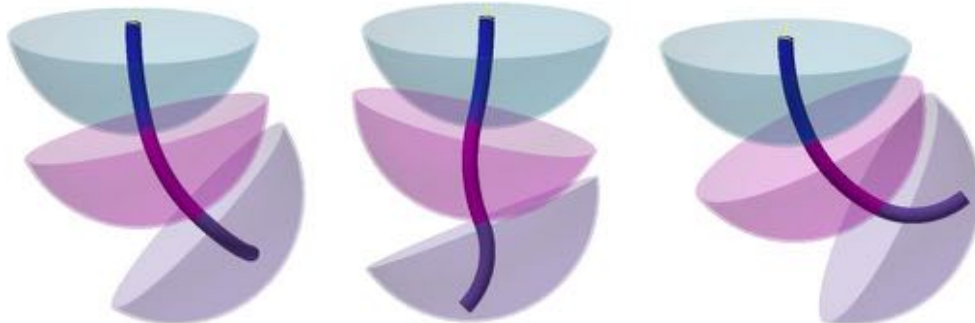


Figure 5.41 Motion range of three segments.

Each segment is actuated independently, so the actuators extend within the length of each one (they start and end at the top and bottom of segments). Therefore, connection parts between segments are necessary to secure the extremities of each actuator properly. These parts are integrated within the silicone body to achieve a compact design.

Small magnets are arranged at the ends of each segment to join them together easily and quickly.

5.3.1 Design

The main elements of the design are the rigid elements that are integrated into the silicone body. These are discs printed by a 3D printer in PLA arranged at the ends of each segment (Figure 5.42). These discs realize three essential functions: (1) join segments together, (2) provide the rigid support necessary to anchor the ends of the SMA springs, and (3) determine the position of the cavities in which both the SMA springs such as power cables are placed.

Each disc presents:

- A hole in the center for the central cavity (15 mm diameter).

- Nine through holes corresponding to the cavities of the silicone body (6 mm diameter).
- Nine holes for the cylindrical magnets that realize the union system.
- Three cavities to place the SMA anchor parts (stops).



Figure 5.42 Discs

The three segments present the same assembly. The process to realize one of them begins with the placement of the magnets and stops on the discs. The magnets are glued to the discs to ensure they do not separate during robot operation. On the other hand, the stops can be removed later to place springs. In Figure 5.43, the detail of this initial assembly is shown. Each segment contains two discs with the elements arranged as indicated.

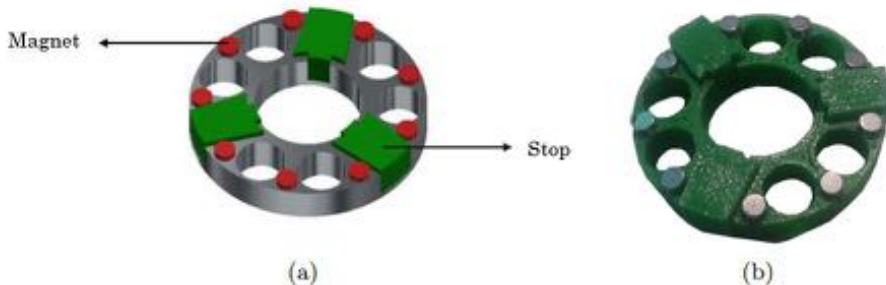


Figure 5.43 Disc with magnets and stops (a) CAD model (b) Real disc

Then nine cylindrical rods plus a central rod are arranged coinciding with the holes in the discs. The discs are located at the rod's ends to coincide with the holes for the upper and lower disc stops, as shown in Figure 5.44.



Figure 5.44 Rod and disc structure

The structure is introduced into a cylindrical mold sealed at the bottom, where later the silicone is poured. The silicone used is translucent platinum silicone, Platsil GEL-0030. Once the silicone is dry, the mold is removed as the rods and stops. Figure 24 shows the silicone-covered structure once it has cured. Figure 5.45 shows the silicone segment without all these elements.

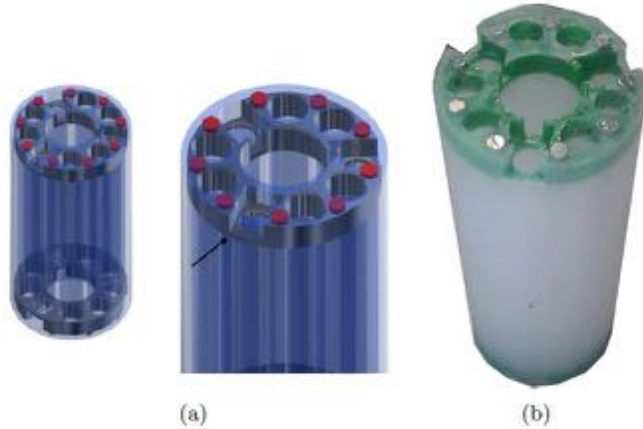


Figure 5.45 The silicone segment

The positions in which the stops were located are those that house the SMA springs. Some new stops will still be placed in the first ones, as indicated in Figure 26, to secure springs. Finally, the power cables, highlighted in red and black in Figure 5.46, are attached to each one. At the top of the segment, each SMA spring is attached to the power supply. At the bottom, the cables return from each spring to the connection point with the transistor. These second cables are routed through the central cavity of the segment, up to the top.

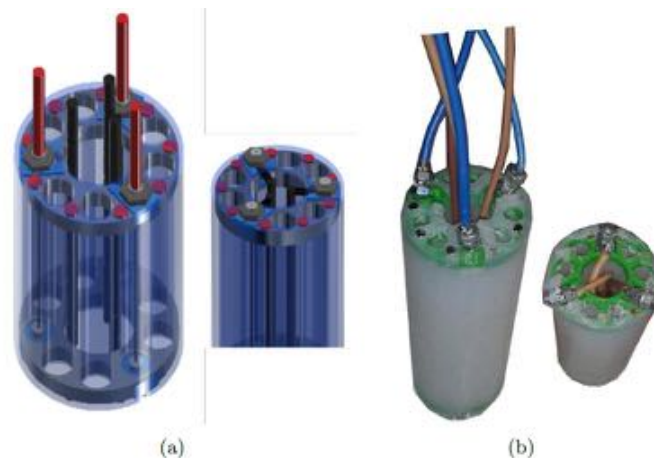


Figure 5.46 Power cables connection.

Once connected to the lower module, the power cables of the three SMA springs run through the two upper segments. The positions that the springs occupy within each of the modules are 40 degrees out of phase. It is necessary to ensure that the power cables have an obstacle-free passage to the top of the set.

Manufacture of springs

The springs used in this work were manufactured from SMA cable to obtain springs with characteristics that most closely approximate the design requirements.

The springs that actuate the silicone segments must meet two main requirements: (1) they can perform a contraction that allows bend segments silicone to the desired position, and (2) they can develop the strength necessary to realize the bending movement.

The spring's length needs to contract is directly related to the length of the segment itself and with the angle bending desired. The length of the segment is 80 mm. Therefore the spring will have a length of 80mm when the segment is at rest. A 20 and 30 mm contraction is required to reach the desired inclination between 30 and 40 degrees. These values are obtained from the same test in which the length of the segment is analyzed. An average value of 25 mm contraction is set to perform the calculations.

The SMA wire selected is a Nitinol wire with a diameter of 0.5 mm. Different trials with cables of smaller diameters provide negative results regarding the necessary force. Wire with greater diameter has not been contemplated not to increase segment size.

Once the proper calculations have been made, the specifications of the spring to be manufactured are known. The first step to manufacturing a spring from an SMA cable is to wind the cable to get the arrangement in turns; two crimp-type pieces are used at the ends to secure the cable Figure 5.47. The process explained in [287] has been taken as a reference to realize this process. With the cable wound on the rod and its ends secured, the heat treatment is carried out. It is necessary to raise the temperature of the SMA cable to 500 degrees for it to "memorize" the spring arrangement. When the target temperature is reached, it is maintained for 15 minutes and then cooled to room temperature. With this last process, the manufacture of the SMA springs is concluded.



Figure 5.47 Springs manufacture

The following calculus has been realized to know the necessary length of springs. The equations by which the calculations are made can also be found in [287]:

$$F = \Delta x \cdot K \quad (4.3)$$

$$F = \frac{G \cdot d^4 \cdot x}{8 \cdot D^3 \cdot N} \quad (4.4)$$

Where:

- $\Delta x = 25 \text{ mm}$ is the elongation of the spring.
- $F = 981 \text{ N}$ is the elongation force used. It is an experimental approximation of the force that performs the silicone segment to return to its resting position.
- K is the spring constant of elasticity
- $G = 10.8 \cdot 10^9 \text{ N/m}^2$ is the shear modulus of the material with which the spring is manufactured
- $d = 0.5 \text{ mm}$ is the diameter of the wire with which the spring is manufactured
- $D = 4 \text{ mm}$ is the outer diameter of the spring
- N is the number of turns of the spring.

From the established parameters, using equation (4.3), it can be deduced that:

$$K = 39240 \text{ N/m} \quad (4.5)$$

With the elasticity constant obtained and equation (4.4), the number of turns can be calculated:

$$N = 33.6 \cong 34 \text{ turns} \quad (4.6)$$

The length to which these 34 turns should extend is:

$$\Delta x = l - l_0 = 80 - l_0 = 25 \text{ mm} \rightarrow l_0 = 55 \text{ mm} \quad (4.7)$$

The length of cable used in the manufacture of this spring is:

$$\pi \cdot d_{avg} = l_{oneTurn} \rightarrow \pi \cdot 3 \cong 9.5 \text{ mm} \quad (4.8)$$

The d_{avg} is the mean spring diameter. Therefore, the length of the cable used in this spring is:

$$9.5 \text{ mm} \cdot 34 = 323 \text{ mm of cable} \quad (4.9)$$

Diameter justification

The thickness of the walls is 2mm to achieve the maximum possible bending. Walls are the areas between the cavities and the exterior of the silicone body or the peripheral cavities and the central cavity. Achieving a thickness of less than 2 mm is complicated in the manufacturing process since the molds cannot be perfectly aligned. In addition, a minimal wall thickness could not suppose the destruction of the segment before minor cuts derived from its manipulation. On the other hand, a greater thickness implies more resistance to bending the segment, which implies a more significant effort for the springs.

Another determining factor is the force that the magnets have to withstand. In a state of rest, the magnets must ensure that the segments are attached. In this case, the force they have to support is the weight of the segments hanging from them. Each segment weighs about 50 grams. During the robot's operation, the forces generated tend to separate the points of union. Therefore, it is necessary to distribute the junction points on the contact surfaces so that the effort is distributed among several points and not concentrated on just one. At the same time, it must be ensured that the segments can be separated comfortably without damaging the elements. Due to this, the magnets cannot present a too great bonding force. After carrying out different tests with different numbers of magnets distributed over the contact surface between the segments, it was concluded that the best solution was to distribute small cylindrical magnets. The space selected to locate the magnets is the one between the cavities of the segments. Neodymium magnets with a diameter of 3mm and a height of 2mm have an attractive force of 252 g. Nine of these magnets distributed on the contact surface between the segments ensure that the segments are joined during the robot's operation.

The outer diameter of the SMA springs is 4mm. According to this, the SMA springs' cavities must have a diameter greater than the springs to ensure their correct contraction. Hence, cavities must have a diameter of 6 mm to ensure correct operation.

All the dimensions stated above are reflected in the discs placed at the ends of the segments. Both give the justification of the diameter of the segments for the size of the discs. Keep in mind that the discs are surrounded by silicone, so to the outer diameter of the disc (33 mm), it is necessary to add 2 mm corresponding to the thickness of the outer walls, which makes the outer diameter of the segments 35 mm.

Justification of segment length

The segment's length must compromise the desired inclination at the free end of a segment and the force that the SMA springs can develop. A segment with the same characteristics as the one exposed was built and tested to encounter this value. The test consists of subjecting this segment to the forces of bending realized through different masses. For this, threads are introduced through the cavities in the same way they will be arranged SMA springs (three wires spaced 120 degrees). One end of each thread will be attached to the segment's bottom, while the other end will come out through the segment's top. Two of the wires ensure the rest position of the segment, while the third present a mass to bend the segment. The resultant bending is a function of the mass and length of the segment.

The length variation of the segment is achieved by removing a certain amount of silicone for each trial. Therefore, it is a destructive test. The masses vary from 0 to 1000 grams at 50-gram intervals. Each segment is tested three times with all masses, bending each time in a different segment orientation. Repeating the test in different directions of the segment allows minimizing errors due to the manufacture of the body of silicone. The mean inclination values obtained from the three tests performed for each length are presented in Figure 5.48.

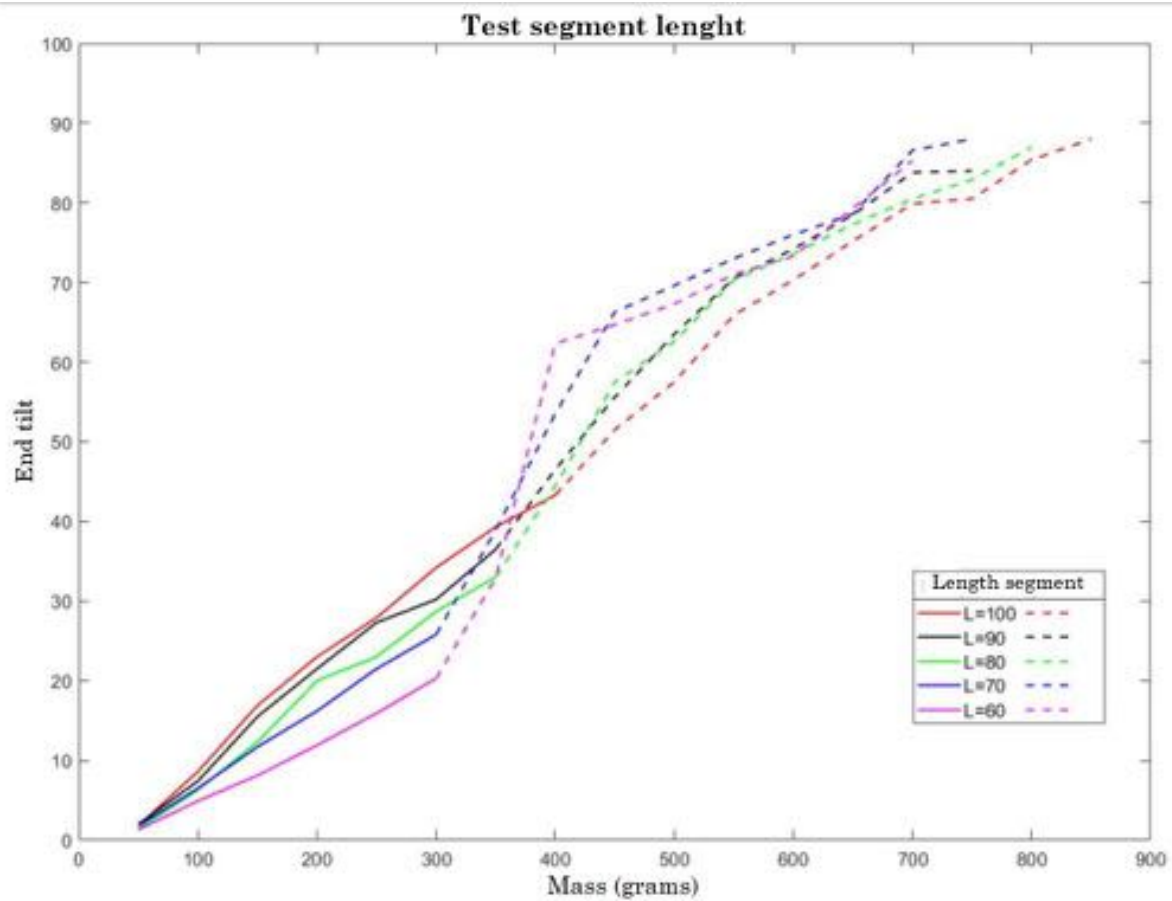


Figure 5.48 Tests segment length

The curves relate the force exerted by the mass to the inclination of the end of the segment. Each line shows a discontinuity from certain values. This discontinuity corresponds to the appearance of folds in the silicone segment (Figure 5.49). Due to these folds, the relationship between the mass and the segment inclination ceases to be progressive, provoking a sudden change in the segment inclination.

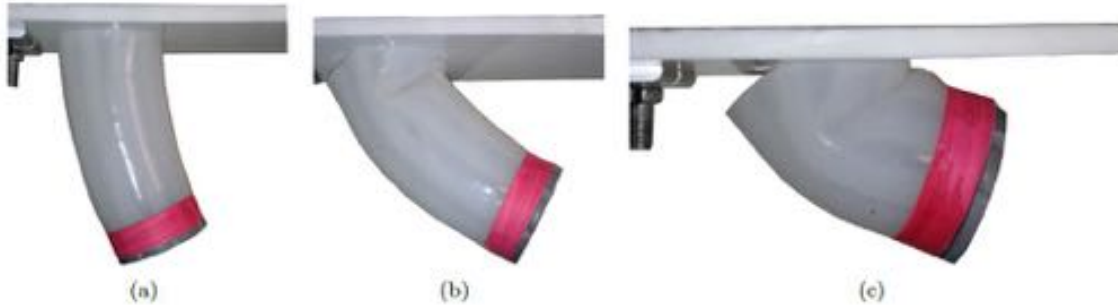


Figure 5.49 (a) controlled bending of the segment b) Appearance of folds at the base of the segment. c) Fully bent segment with folds

The segments' lengths vary from 100 mm to 60 mm, reducing 10 mm each time. The tests carried out show that when the length of the segment is reduced, the folds appear with lesser forces. Since for the 60 mm segment, it is not possible to bend the segment of 30 degrees with stable behavior; it makes no sense to reduce more the segment length.

According to the data, the minimum length to reach an inclination of 30-40 degrees before the appearance of folds is 80 mm. A mass of between 300 and 400 grams is necessary to reach the desired inclination.

Electronics

The elements used are Two Arduino UNO boards, 9 IRF 540N MOSFET transistors, 9 10K resistors, 9 SMA springs, and a 12V and 18A power supply.

As shown in the diagram in Figure 5.50, the same structure is used nine times for the nine springs. It is necessary to point out that two amperes are necessary to activate each spring, so only up to a maximum of 6 springs can be activated in each movement, two for each segment. With this, it is concluded that the power supply capable of delivering up to 18 amps is enough to power the robot.

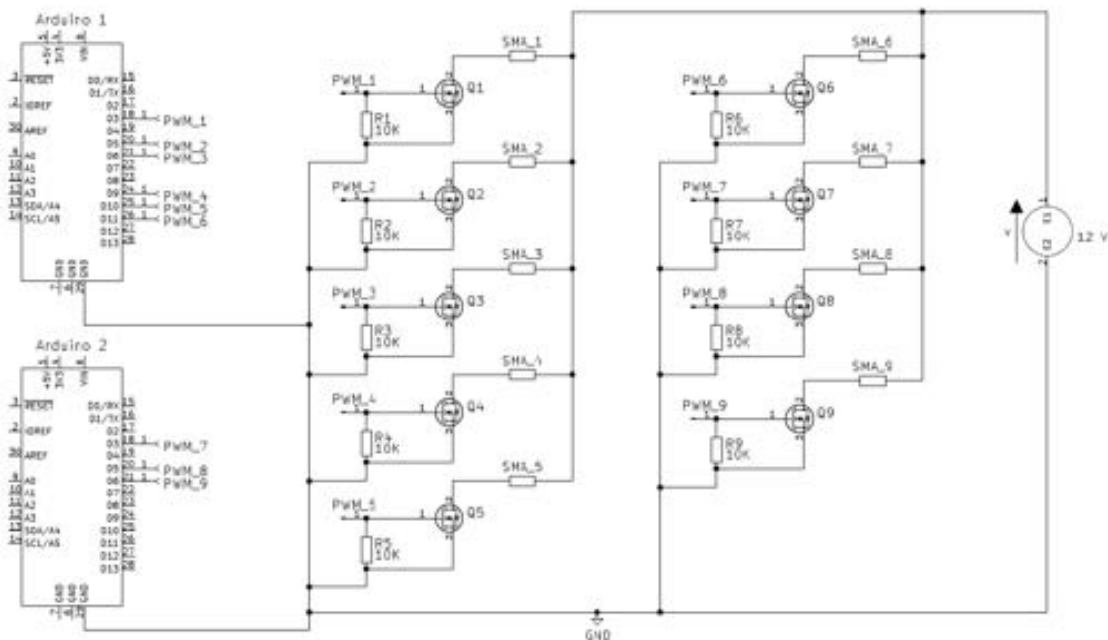


Figure 5.50 Electric circuit

There are different methods for activating SMA actuators. In this case, MOSFET transistors connected to the power supply and controlled by a PWM signal coming from the Arduino Uno boards are used. PWM outputs allow modulating the output pulse to an intermediate voltage between 0 and 5. The output signal from each of the PWM pins comes from the programming implemented in the central computer. As previously indicated, each PWM activation signal is connected to the input of the MOSFET transformer. In this way, the current that passes from the source to the drain can be controlled. This source-drain current is the one that circulates through the SMA spring, so it is the one that allows springs to reach their activation temperature (45 °C in this case). All these elements have been placed as independent blocks on a PCB board.

5.3.2 Open-loop control

Vision system

A vision system capable of detecting the different positions of the robot's segments and the end-effector was implemented to know if the movements performed by the robot meet the initial specifications.

The idea of positioning flexion sensors on the outer walls of the robot was discarded not to add resistance to the body and so difficulting bend movement. On the other hand, the interpretation of the variation of the resistances with the bending will be complex and will not provide information on the position of the ends of the segments.

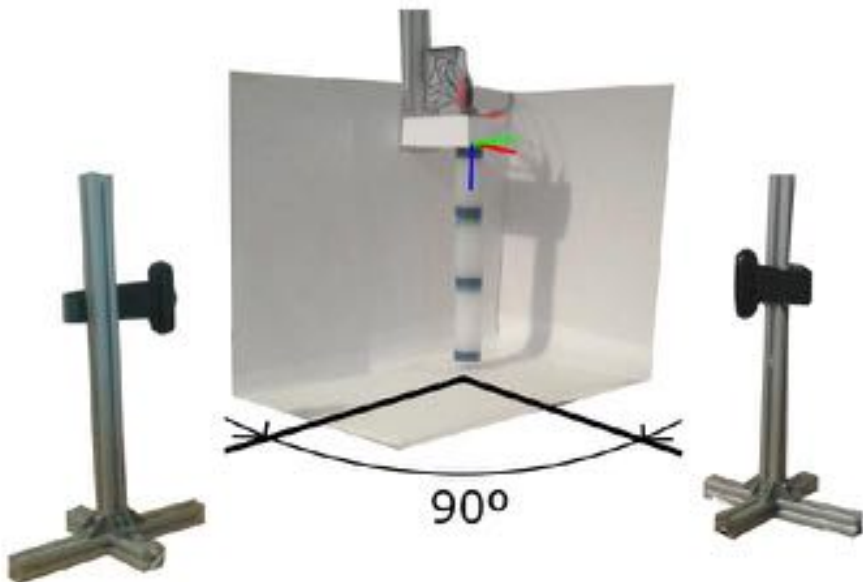


Figure 5.51 Vision system setup

It was decided to arrange marks on the robot to calculate the positions that it can achieve. As the robot can perform movements in three dimensions, two cameras were used to obtain two different perspectives of the robot. Each of the cameras captures the robot's displacement in the corresponding plane, as shown in Figure 5.51. The data obtained from each camera are put in common to obtain the position of the marks concerning a reference system located in the upper part of the robot. The marks are rings surrounding the ends of the segments. In captured images by the cameras, these rings are perceived as rectangles. By treating the images, it is possible to determine the rectangle axis inclination, and therefore the inclination of the end of the segment. The vision system has been implemented in Matlab.

Each segment consists of three springs, so the combination of their movements sets the different positions that the robot's end-effector can reach. Since experiments have been realized with only two segments, 49 different positions can be realized. These positions result from combining the seven positions (counting the rest position) that can reach the first segment by activating its springs individually or not with the seven positions of the second segment. Figure 5.52 shows examples of the test performed.

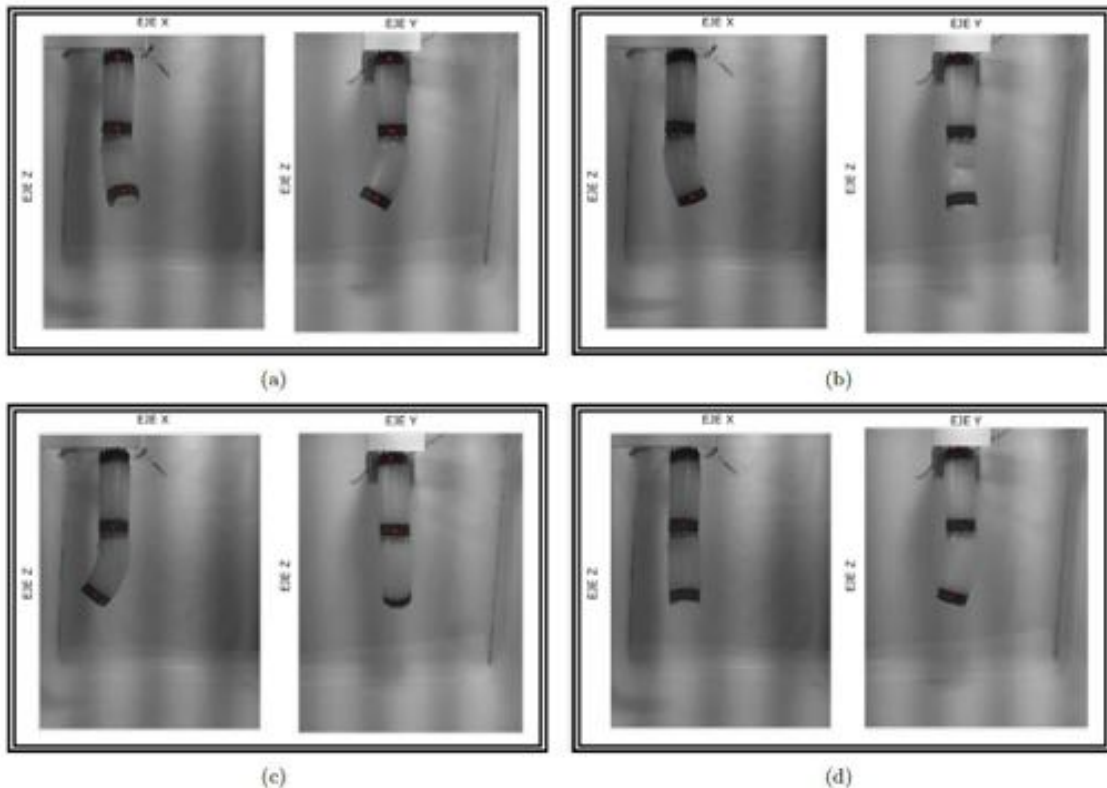


Figure 5.52 Tests

As shown in Figure 5.53, the activation of the springs produces a fold in the silicone body instead of making a uniform bending. This effect was analyzed in previous trials and highlighted the difficulty of obtaining a reliable model of the presented robot. Of all the tests carried out, the different positions of the end effector are shown in the graph in Figure 5.54.

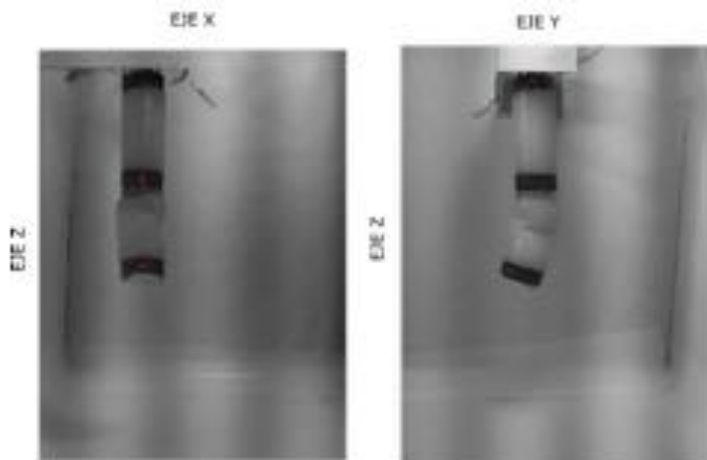


Figure 5.53 Folds in the silicon body during actuation.

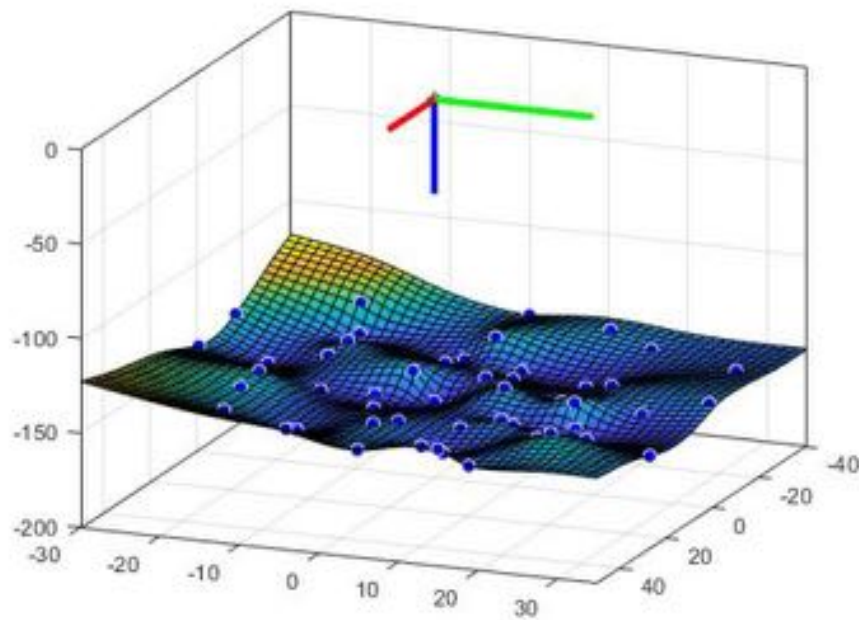


Figure 5.54 Free-end positions

In the XY plane, the end effector can realize a maximum displacement of 40 mm in the direction negative of the X-axis and a maximum displacement of 55 mm in the positive one. Regarding the Y-axis, the displacement in the negative direction of the axis can reach 30 mm, while in the positive direction, it reaches 40 mm. Concerning the Z-axis, establishing a minimum height of 160 mm corresponding to the robot's position at rest, the action of the springs can raise the end effector to 135 mm, that is, can realize a 45mm offset.

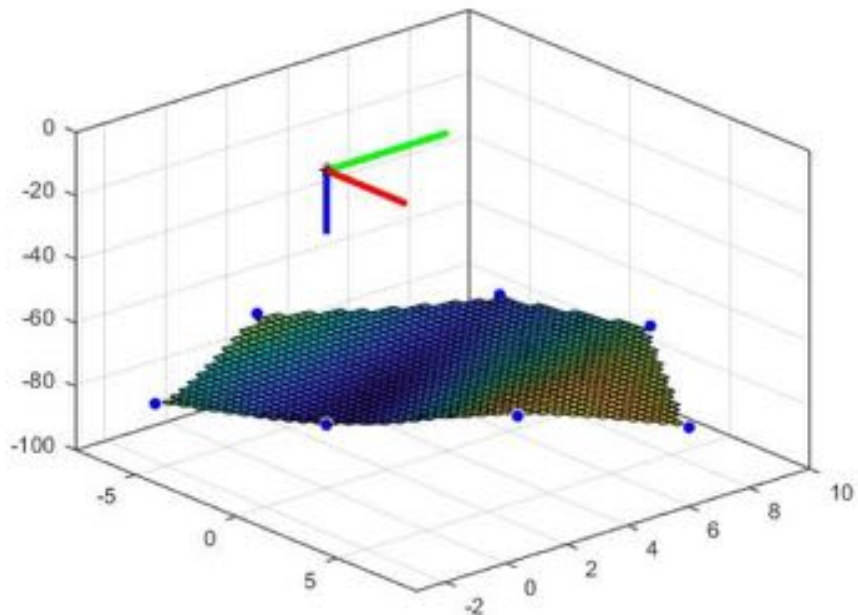


Figure 5.55 First end segment positions

In addition, Figure 5.55 shows the seven positions assumed by the end of the first segment. It is necessary to emphasize that the springs of the first segment must overcome the force necessary to bend this segment and raise the second segment. Due to this, the total displacement of the first segment is less than that of the robot's end-effector. It realizes a -8

and 9 mm displacement in the X-axis and -3 and 10 mm in the Y-axis. In the case of the first segment, the lower bound on the Z-axis is 80 mm, and the maximum displacement observed is 7 mm in the direction upward. Moreover, the inclination that the first segment can reach is less than that of the second, presenting a maximum angle of 20 degrees. The end of the second segment reaches 35 degrees incline with the first segment at rest.

Once the positions have been determined, a matrix is generated. It relates the end effector positions with the springs that need to be actuated to move. Therefore, the control performed is an open-loop control in which the positions are found default.

As the graphs of the range of movements represent, there is no normalization of the range in different directions. It is because the springs included in each segment do not always exert the same force. To this effect is added the silicone behavior of the body, which may appear folds that make the resulting position vary.

Interface and operation

The interface aims to show real-time information on the robot's status; it also allows users to establish the orders of movements desired.

By superimposing dots on the images captured by both cameras, it is possible to verify that the vision system correctly captures and interprets the marks placed on the robot.

Both images are presented in the interface to track the robot from both points of view (Figure 5.56). The information on the position of the marks is presented in the data table. It is also visible the inclination of the end of each of the segments.



Figure 5.56 User interface

In the interface, there are two menus, the user and the Development menu. The User menu (Figure 5.57 (a)) allows selecting a point from the 49 that the robot can reach. Once selected, the Move button activates the springs needed to bring the robot's end to the desired point. The relationship between the points to which the robot can move and the springs necessary to activate was established in the position mentioned above matrix. The Development menu (Figure 5.57 (b)) allows users to select the springs to actuate independently.



Figure 5.57 (a) User and (b) development menus

Since the destination points are known, the possible discrepancy between the selected point and the position reflected in the data table will be due to the error made by the vision system.

5.3.3 Towards a closed-loop control

As explained in the previous section, the first control of Ruăn was an open-loop control. Consequently, it was necessary to improve it and realize a closed-loop control. This control allows users to send the robot's end-effector to a destination without knowing how each segment needs to move to reach the final position. First of all, it was necessary to realize the kinematic modeling of the robot and know the relationship between the actuators' actions and the resulting arc curvature of the robot. This information will be used to feed a neural network and realize the control. Three techniques have been employed to realize this work: the Piecewise Constant Curvature (PCC) kinematics, finite element analysis (FEA), and artificial neural networks (ANN).

The starting point was the mapping proposed by [364] in constant curvature kinematics and shown in Figure 5.58. The PCC approach allows for simplifications in kinematic modeling as explained in Section 4.2.2, but, as in Kyma's case, necessary assumptions to use this method do not significantly affect the final model. Moreover, thanks to these assumptions, we work with modular kinematic transformations that can be decomposed into two separate mappings: one from the actuator space to configuration space and another from configuration space to task space.

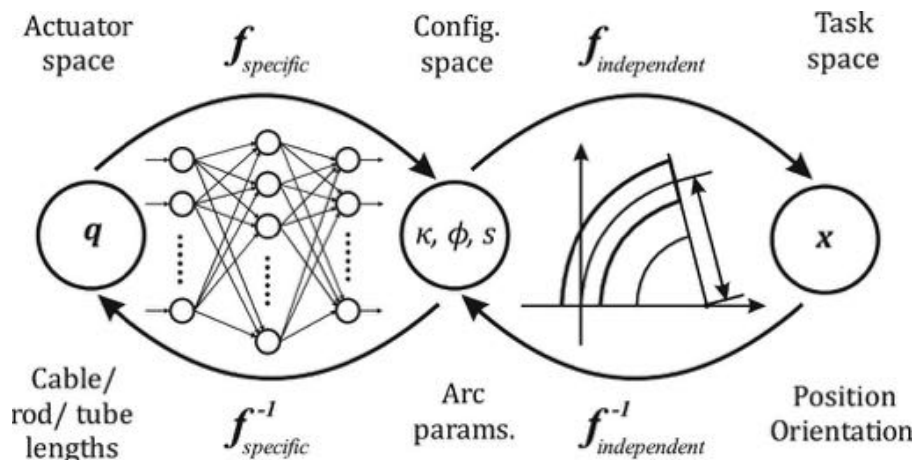


Figure 5.58 Mappings in constant curvature kinematics [364]

As shown in Figure 5.58, the first mapping involves the transformation of the actuator space \mathbf{q} , towards the configuration space whose parameters $\mathbf{K}, \emptyset, \mathbf{S}$ describe the arcs of

constant curvature. The second mapping involves the transformation of the configuration space to the task space \mathbf{x} , which describes the position and orientation of both the backbone and the tip of the robot.

The actuator space \mathbf{q} is represented by the variables that describe the action of the actuators (length of the cables for a tendon-driven robot or pressure level for a pneumatic one). In the case of Ruan, the actuator space \mathbf{q} consists of the variables that describe the action of the SMA springs. These variables are correlated with those of the configuration space ($\mathbf{K}, \emptyset, \mathbf{S}$) through the mapping $f_{specific}$, that highly depends on the specific robot. On the contrary, the second mapping $f_{independet}$, between the configuration space and the task space (x) does not depend on the robot, which means it is the same for all robots that meet the requirements of the PCC formalism.

Consequently, the forward kinematics transformation can be expressed as:

$$\mathbf{q} \xrightarrow{f_{specific}} \mathbf{K}, \emptyset, \mathbf{S} \xrightarrow{f_1} \theta, d \xrightarrow{f_{D-H}} \mathbf{x}$$

The $f_{independet}$ mapping is decomposed in two mappings: the first links arc parameters and Denavit–Hartenberg (D–H) parameters, the second relates D–H parameters to task space variables \mathbf{x} . The inverse kinematic mappings f^{-1} can be used for motion control of the robot.

In this case, the $f_{independet}$ is derived using PCC kinematic relations, as already mentioned. While the $f_{specific}$ is obtained from FEA. The main reasons are the complexity of analytical calculations and the significant amount of experiments necessary to derive it experimentally. Finite element simulation provides an accurate representation of the behavior of the physical robot despite its complex structure. However, this method is computationally expensive in terms of time and resources, and it cannot be used in real time. Therefore, data generated by FEA simulations can be generated offline and used to train an ANN later.

The PCC method was proposed by Hannan and Walker in 2000 [237]. Their work suggests that after activating the actuators, the curves generated in the robot's body can be approximated as a series of arcs of constant curvature ("piecewise constant curvature") tangent to each other. Likewise, these curves are described using the parameters of arc \mathbf{K} , \emptyset, \mathbf{S} belonging to the robot configuration space and illustrated in Figure 5.59.

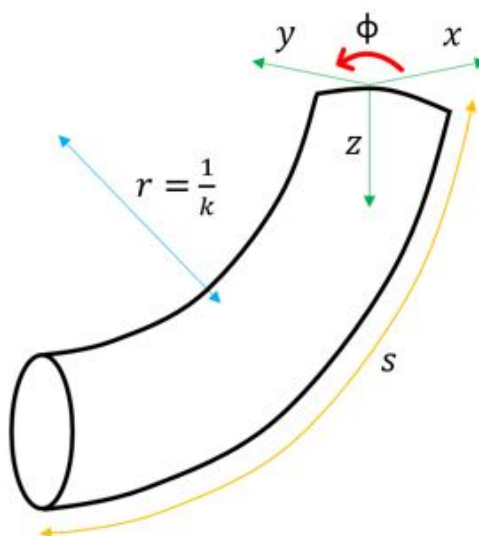


Figure 5.59 Kinematic modeling using PCC approach.

As can be seen, K is the curvature (inverse to the radius of the circumference that describes the arc), \emptyset the angle between the x-z plane and the plane containing the arc, and S indicates the length of the arc.

Webster and Jones demonstrated in [365] that the segment could be represented as a rigid link with two rotational joints at the base, a prismatic joint in the middle, and two other rotational joints at the tip of the segment, as shown in Figure 5.60.

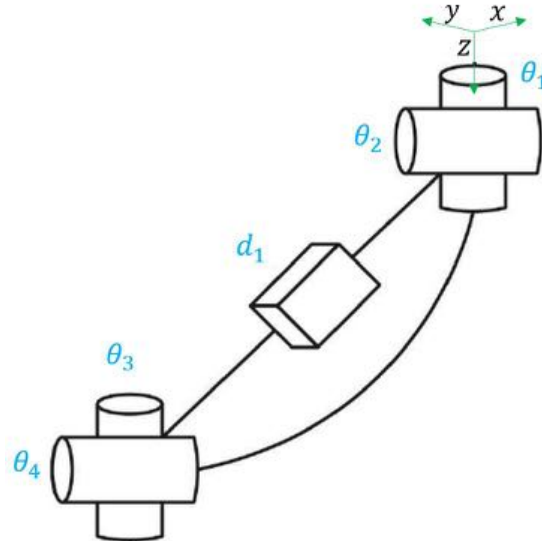


Figure 5.60 Hypothetical rigid link model of a flexible robot [365]

The parameters d_1 , θ_1 , θ_2 , θ_3 , θ_4 correspond directly to the Denavit-Hartenberg parameters, so they can be used to define the homogeneous transformation matrix T (d , θ). Therefore arc parameters can be applied directly in the transformation matrix, being T_{PCC} (d_1 , K , \emptyset , S). This matrix can be simplified since $\theta_3 = \theta_2$ and $\theta_4 = \theta_1 + \pi$, as demonstrated in [366] by Jones and Walker. So the final T_{PCC} that represents $f_{indipendet}$ is:

$$T_{pcc} = \begin{bmatrix} \cos^2\emptyset(\cos KS - 1) + 1 & \sin\emptyset \cos\emptyset(\cos KS - 1) & \cos\emptyset \sin\emptyset & \frac{\cos\emptyset(1-\cos KS)}{K} \\ \sin\emptyset \cos\emptyset(\cos KS - 1) & \cos^2\emptyset(1 - \cos KS) + \cos KS & \sin\emptyset \sin KS & \frac{\sin\emptyset(1-\cos KS)}{K} \\ -\cos\emptyset \sin KS & -\sin\emptyset \sin KS & \cos KS & \frac{\sin KS}{K} \\ 0 & 0 & 0 & 1 \end{bmatrix} \quad (4.10)$$

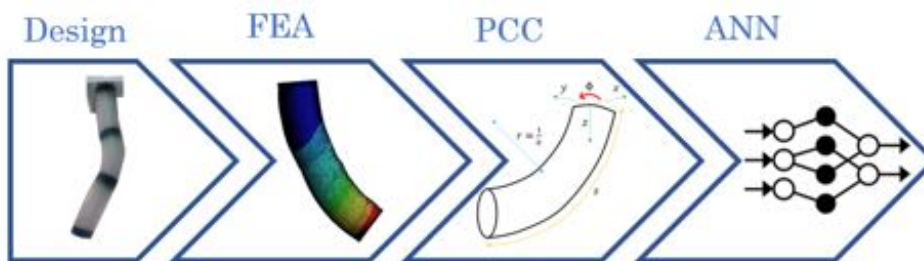


Figure 5.61. Design and kinematic modeling framework for soft robotic systems.

Figure 5.61 summarizes all the following steps.

4.3.3.1 Modeling

In the case of the development of the kinematic model of continuous robots, the equation of motion given by continuous mechanics (4.11) cannot be solved since it involves an infinite number of degrees of freedom.

$$\nabla \cdot \sigma + \rho f = \rho \left(\frac{\partial v}{\partial t} + v \cdot \nabla v \right) \quad (4.11)$$

Due to the high calculation times required by the FEA, the model was first developed for a single segment and, once the results were satisfactory, the system was adapted for two robot segments concatenated. For the same reason, the model's geometry was simplified. All FEM simulations have been realized with ANSYS Mechanical.

The first simplification involves the disc, as shown in Figure 5.62.

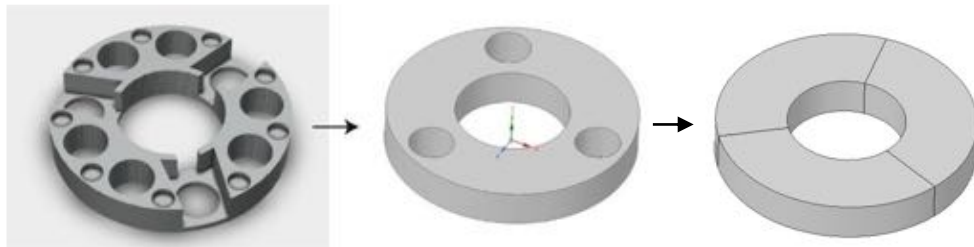


Figure 5.62 Simplified design of the discs

In addition, both discs and the robot's body were divided into three equal parts to reduce time calculations, as shown in Figure 5.63.

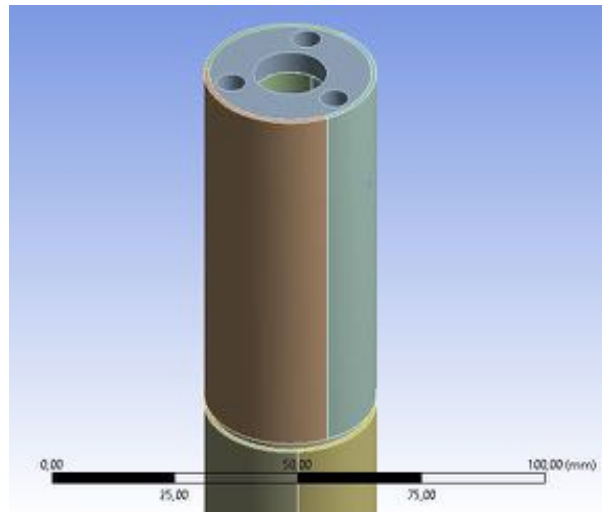


Figure 5.63 Simplified section of the body

SMA springs were replaced by threads or tendons of a standard material, which are displaced vertically during activation (Figure 5.64). The threads were defined by generating lines of 0.5 mm diameter centered in the longitudinal cavities sides of the silicone body.

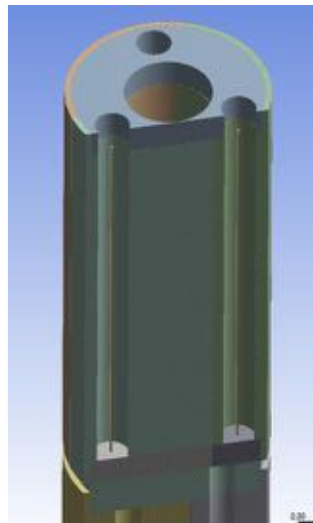


Figure 5.64 Tendons inside the body

The materials applied in the simulations were EcoFlex 00-30 for the body, Nylon 6 for the threads, and PLA for the discs.

The EcoFlex 00-30 material is not presented in the Ansys material library, so it is necessary to create it. Silicones are hyperelastic materials, and several models of them exist, among them the Yeoh model 3rd order is used to represent the Ecoflex 0030 silicone is the Yeoh model, which is defined in a general way by equation (4.12):

$$U = C_{10}(I_1 - 3) + C_{20}(I_1 - 3)^2 + C_{30}(I_1 - 3)^3 \quad (4.12)$$

Where U is the strain energy density function, C_{10} , C_{20} , C_{30} are the polynomial coefficients, and I_1 is the strain invariant.

In this case: $C_{10} = 1.27 \cdot 10^{-2}$, $C_{20} = 4.23 \cdot 10^{-4}$, and $C_{30} = -1.45 \cdot 10^{-6}$. (4.13)

The size of mesh elements considers the minimum number necessary to realize a proper simulation in a minor calculation time. A significant number of elements in the silicone body increased the calculation time at unsustainable levels and generated the folds that the real robot presents by bending its segments, as shown in Figure 5.65. Even though these folds are part of the physical robot's behavior, they are not desired, affecting its movement and convergence ability.

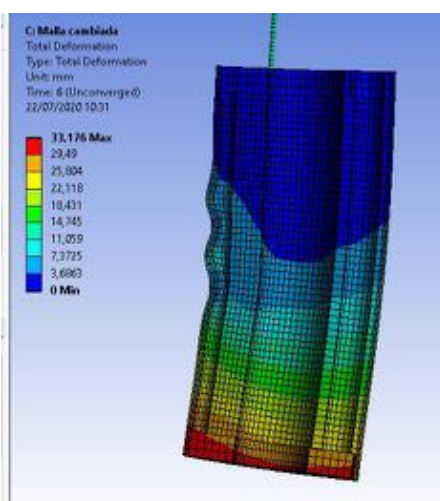


Figure 5.65 Segment simulation with folds

The meshing of the threads greatly affected the lack of convergence. The amount of elements in them affects their level of flexibility; the more elements the threads have, the more flexible they will be. Moreover, as mentioned above, they need to be flexible enough to adapt to the curve of the silicone body after deformation; that is, it is sought that the threads curl together with the silicone body Figure 5.66.

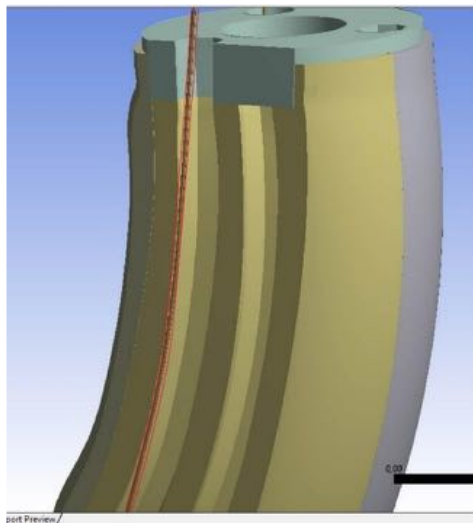


Figure 5.66 Desired behavior of tendons

However, many elements also negatively affect the interaction of the threads elements with the body. If the mesh of the threads is very fine, its elements turn out to be small ones that are ignored by the mesh of the silicone body going through it at some points, as shown in Figure 5.67.

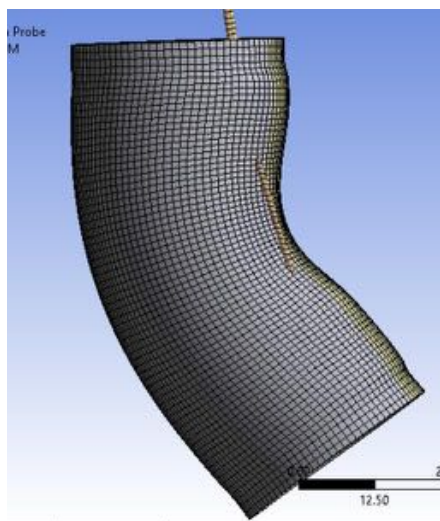


Figure 5.67 Tendons penetration

The type of elements in both the silicone geometry as in the discs was changed to Solid185

The model presents fixed support to the upper rigid disc of the first segment, that is, at the robot's base. While the tip of the second segment is free and the only added charge is standard gravity. Both segments are joined via a bonded type joint. Each wire is connected to the robot segment through a joint at each end. The lower joint, which joins the thread to the lower rigid disk, is of the fixed type, while that the upper joint, which "holds" the thread in place, is prismatic or Translational; the latter ensures that the thread can only move

vertically. Finally, joint displacements are placed at the end top of each thread (Figure 5.68).

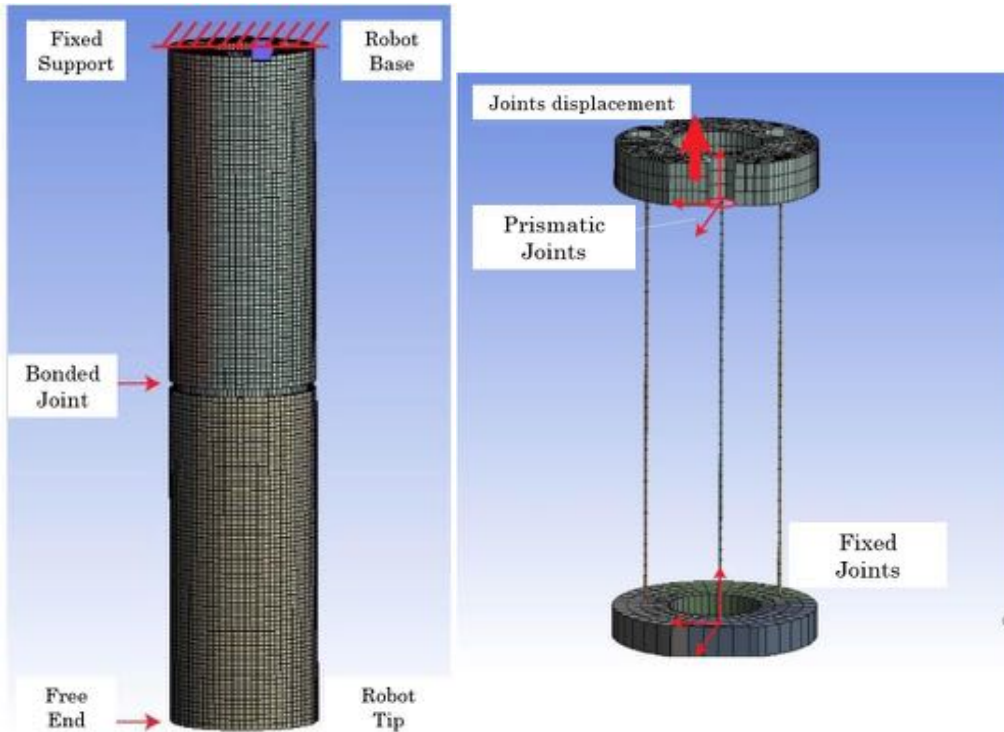


Figure 5.68 On the left boundary condition in simulation. On the right, joints and displacements in the threads.

Steps' simulation determines which threads will be displaced and the value of the displacements. Threads are activated in pairs, and each pair corresponds to a letter. Table 5.5 shows Configuration A in the second segment.

Table 5.5 Tendons displacements. Configuration A.

Second segment activation				
Steps	Thread 1	Thread 2	Thread 3	Configuration
5	4	4	0	
6	8	8	0	
7	12	12	0	A
8	13	13	0	
9	0	0	0	

Table 5.6 All possible activation combinations

Segment 1			Segment 2		
Configuration	Activated threads		Configuration	Activated threads	
A	Thread 1	Thread 2	A	Thread 1	Thread 2
			B	Thread 2	Thread 3
			C	Thread 3	Thread 1
B	Thread 2	Thread 3	A	Thread 1	Thread 2
			B	Thread 2	Thread 3
			C	Thread 3	Thread 1
C	Thread 3	Thread 1	A	Thread 1	Thread 2
			B	Thread 2	Thread 3
			C	Thread 3	Thread 1

For Configuration A of the second segment, threads 1 and 2 displace 4 mm upwards while thread three does not move. In Step 6, these offsets in wires 1 and 2 increase to 8 mm while wire 3 remains 0. And so on until that wires, 1 and 2 reach their maximum displacement to return to 0, the state of rest. These trigger settings allow each segment to perform three different movements since our robot has two segments; it can perform nine different movements. All possible combinations of these activations between the two segments are shown in Table 5.6.

The bending angle was calculated by defining a point remote control on the lower disc of each segment and calculating their rotation in the X, Y, and Z directions. Results were compared to the ones obtained in the first phase of the work. The physical robot reached a maximum angle of approximately 20° at the tip of its first segment, while the second segment reached an angle maximum of approximately 35°.

The tests showed that the required bending angle in the first segment is achieved with a vertical displacement in the threads of -12 mm. On the other hand, the bending angle required in the second segment is reached with a displacement in the threads of -13 mm. Figure 5.69 represents the deformation of the soft body of the robot under the action of the threads.

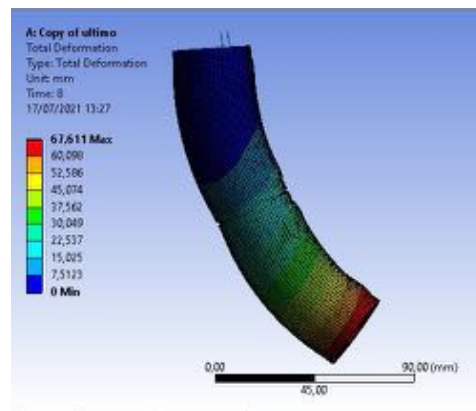


Figure 5.69 Deformation of the soft body of the robot under the action of the threads.

Once the results had been considered acceptable, data were extracted. The data extracted define the curves and relate their bending with the activation of the actuators. Consequently, three equidistant paths were defined along the outside of each silicone segment, as seen in Figure 5.70.



Figure 5.70 Paths of deformed nodes.

The data extracted comprises (1) threads' displacements in millimeters and (2) node rows' displacements after deformation. These are divided according to the segment from which the data was extracted, its Step, and its activation settings.

Microsoft Excel was used as a tool to save and process the data. The backbone curves were calculated for each segment and Step, through the coordinate of nodes before and after deformation. To verify these backbone curves, they were graphed in Matlab.

Matlab was also used to apply the PCC method and calculate the parameters K , \emptyset , S in each Step. For this, it has been developed a function arcParameters that includes within itself all the necessary calculations.

The function arcParameters takes the first segment configuration, the Step, the first segment backbone, the second segment backbone, and finally, the displacements of the threads. It returns the arc parameters for the first and second segments. Besides this, it generates a table in Excel where calculated data are saved and organized to later use in the neural network.

The multilayer perceptrons or MLPs were chosen for the neural network since they have been successfully applied to learn robots' forward and inverse kinematic models.

MLPs are pre-powered neural networks with a minimum number of 3 layers composed of nodes (the input layer, the output layer, and at least one hidden layer). Each node of one layer is connected to all the nodes of the next layer through a weight w_{ji} . Furthermore, all nodes except those belonging to the input layer have an activation function. The activation or step function takes the output of the previous node and acts as a filter or limiting function by modifying the result value. The learning process consists of calculating the error of the final output of the network in order to update all the weights w_{ji} . These weights can be updated by backpropagating the error δy_i between the desired value and the actual output of any neuron.

Matlab provides a tool (Machine Learning) that, through the function *feedforwardnet* (*hiddenSizes*, *trainFcn*), generates an MLP with the desired hidden layers and training function. It also provides functions to train the network based on an input data set and a data set of the desired results.

In this case, the input data set consists of the SMA spring displacements in mm, while the result data set consists of the arc parameters K , \emptyset , S .

The number of hidden layers was decided considering the results presented in the paper [367], where it was demonstrated that a multilayer network compared to a single hidden layer network did not present a significant improvement. For this reason, it was decided to use six hidden layers in our network.

Another important aspect is that the neural network can only approximate continuous functions; however, the rotation angle \emptyset is not continuous because from 0° it jumps to 360° . For this reason, it was decided to replace the value of \emptyset by $\sin \emptyset$ and $\cos \emptyset$.

The training data set saved in an external Excel table was divided between the input matrix and the matrix of expected results. However, the first tests gave erroneous results because certain parameters belonging to the first segment interfered with the parameters of the second segment. These problematic parameters are those taken during the rest state of the segments. Since they do not present a curve because there is no activation of the actuators, the arcParameters function; hence it produces miscalculations in these specific situations.

The solution chosen to this problem because it is the simplest was to use two different neural networks, one for each segment and obviating the data that contains zero

displacements in the threads. Although the second segment's position depends on the movements performed by the first segment, the arc parameters, these now being K , $\sin \phi$, $\cos \phi$, S , they only describe configuration space and not position in the workspace.

Even if these changes represent a considerable reduction in the training data, The results obtained were satisfactory in several tests.

The work carried out was validated through comparisons with the previous data, as shown in Table 5.7.

Table 5.7 Comparison of the displacement ranges between the second segment of the flexible robot and the simulation.

In-plane displacement ranges (mm)							
	X		Y		Z		
	Max	Min	Max	Min	Max	Min (Rest)	
Real Robot	55	-40	40	-30	135	160	
Simulation	35.88	-56.7	52.48	-45.79	131	162	

The minimum value of displacement in the Z-axis equals the rest position of the tip of the free segment. The coordinate being at rest Z from the free end tip will be 160-162 mm. At the same time, the maximum value is equal to offset in the direction toward the origin, as the robot will always flex upward. The displacement value can be obtained by subtracting the idle value minus the maximum value.

The most considerable discrepancies observed in Table 5.7 are given by the difference between the physical robot's orientation and the robot model's orientation in the simulation. However, considering the absolute values of the displacements values being quite close.

Table 5.8 Total displacement of the free end of the robot.

Total displacement capacity (mm)			
	X	Y	Z
Real Robot	95	70	25
Simulation	92.58	98.27	31

As shown in Table 5.8, the free end of the physical robot can move a distance on the X plane of 95 mm in total, while the simulation shows a displacement of 92.58 mm in total. Regarding the displacement in the Y-axis, the asymmetry of the physical robot affects results. In the case of a perfectly constructed robot, the displacement in the Y-axis would be practically equal to the displacement in the X-axis, as the data shows simulation.

So the other errors are considered to be within acceptable ranges, thus concluding that the simulation represents with a good fidelity level the behavior of the flexible robot.

After the phase training, tests were carried out to verify the accuracy of the approximations with some data reserved for these checks. In Table 5.9 and Table 5.10, the comparison between the expected values and the obtained values is shown.

Table 5.9 Comparison of neural network results for the first segment.

	First segment			
	S	$\sin \phi$	$\cos \phi$	K
Expected Data	76.0837	0.8656	0.5008	0.0055
Data Obtained	73.3643	0.9612	0.2007	0.0029

Table 5.10 Comparison of neural network results for the second segment.

Second segment			
	S	$\sin \phi$	$\cos \phi$
Expected Data	74.1405	0.8649	0.5020
Data Obtained	74.3726	-0.2829	0.2421

These results show that, while some of the parameters are approximate almost exactly, others have a somewhat considerable deviation, as is the case of the sine and cosine. Experience leads to determine that this happens by the amount of data training that was provided.

5.3.4 Conclusions

Ruǎn is a soft continuous manipulator actuated with SMA. The use of SMA springs as actuators has allowed the development of a compact and functional robot, and it represents a pretty good alternative to a conventional tendon-driven system.

The presented design has explored a robot consisting of three segments, but it can incorporate new segments. In this way, robot length can be controlled to achieve a greater adaptation to the task to be carried out. The joining system by magnets could be used in the same way in this hypothetical design, but it will be necessary to explore different ways of feeding the springs.

The vision system through which the position is captured presents a significant error concerning the range of movements that the robot can develop. It will be necessary to increase the accuracy of the system.

It has been possible to simulate the nonlinear behavior of Ruǎn as a segment unique and as the set of two segments, thus providing a data source for relating the behavior of the actuators to the bends presented in the body of silicon.

The MLP neural network approximates nonlinear functions but requires a large amount of data to obtain results with an acceptable margin of error. Thus, the development of an application that automatically extracts data from the finite element simulation effectively is necessary.

This strategy has allowed direct, fast, and energy-efficient kinematic modeling through finite element simulations with machine learning tools.

However, before all these considerations, it will be appropriate to redesign the robot to avoid folds during its bending. For this, it will be necessary to study materials and the body's behavior when deformed.

Moreover, another task to be carried out would be the improvement of the physical robot supervision system. The implementation of flexible sensors such as Flexim or IMUS allows proceeding with the development of the control system.



6. Soft Grippers

*"Experiment is the sole judge
of the validity of any idea."*
Richard P. Feynman

This chapter presents a comparative study of four types of soft grippers. In this case, SMA actuators have not been applied since the aim was to realize a highly efficient soft gripper. The four presented grippers can be divided into two main groups: the mechanicals and the pneumatics. After the design explications, a series of experiments are presented to verify which of the four was the most robust and versatile. Twelve objects have been selected to represent different dimensions, weights, and shapes. Also, the objects have been tested in three environments to measure how they can affect the proper functioning of grippers.

Further information on this section can be found in the original scientific publication [368].

Also, an explanatory video of some of these robots can be found in the Electronic Supplementary Material (Videos [S. 5](#)).

6.1 Introduction

Robotics grippers are one of the essential components in the industry because of their capability to manipulate objects. They realize transportation tasks and perform quality control to optimize robotic work cells [369]. They can be used in several applications, such as industry, medicine, space exploration. Each application presents different characteristics and needs specific solutions, so grippers can be divided into categories based on their function as described in [370]. Thanks to the advance in soft materials and soft actuators, soft grippers have gained relief in soft robotics in the last years.

Traditional hard robotic grippers consist of mostly rigid joints and links [371] that have to adapt to the object not to damage it precisely. Consequently, their use is limited to a specific item type. If a variety of objects need to be manipulated, it will be challenging, if not impossible, to grasp them with the same rigid gripper.

The solution is to increase the degrees of freedom of the fingers that form the gripper, using, e.g., flexible materials for finger fabrication. It allows grippers to adapt to objects passively. Gripping tools with greater robustness can be developed using the principles of soft robotics. It implies that they do not require changes in their programming or construction to manipulate different objects, and the precision needed to make the grips is reduced.

6.2. State of the Art

Although the development of soft robotics is relatively recent, a variety of soft grippers exist, as seen in [44].

Rigid gripping tools with electromechanical actuation are the first step toward soft robotics. Using a chain of rigid elements, grippers can adapt to the shape of the objects. The greater the number of elements composing the chain, the better the finger profile approximates a continuous line. This is interesting because a larger contact area between the gripping tool and the object leads to a reduced pressure exerted on that area, thus resulting in a lower risk of damaging delicate objects. A prototype based on this idea was developed in 1978. This gripper could adapt to objects of almost any shape and size and grip them with uniform pressure along with the whole finger. Moreover, it presented a relatively simple mechanism and control implemented only with a pair of wires [372].

An evolution of the previous example is a tendon-driver gripper fabricated through shape deposition manufacturing, which presents joints formed by an elastomer and actuators and sensors incorporated in hard rigid polymers [208]. In another case, two different types of silicone have been used to realize the gripper's fingers: one more rigid for the base and another more flexible for the section to be in contact with objects. The actuation is realized only with a cable to allow an easier adaptation of the gripper to objects [373]. Other examples are [36,374–377].

Increasing the contact surface between the finger and the object is also the idea behind the grippers that use passive structures actuated with external motors. In this case, cables are not required because when grippers deform, they adapt to the geometry of the objects. The fourth gripper presented in this study and in [378] is based on this concept.

Another large family of soft grippers is the one using pneumatic actuators. In general, they have deformable pneumatic chambers realized with different types of silicone or other elastomers. What distinguishes them is the shapes of the pneumatic chambers. Examples of this type of gripper can be seen in [379–384].

Two interesting types of pneumatic soft grippers use the pneumatic system to create the vacuum and grasp objects by suction, such as [385,386], and those that exploit the principle

of jamming transition, such as [41,387–389]. The fabric-based soft grippers are also worth mentioning; these pneumatic actuators present advantages over others due to their high flexibility, stiffness customizability, and the high force-to-weight ratio [390–392].

Apart from these two categories into which the four grippers described in this research fall, many other technologies have been used: electro-adhesion [39,393,394], Gecko-adhesion [395,396], dielectric elastomer actuators (DEAs) [40,397–399], fluidic elastomer actuators (FEAs) [131,400], magnetorheological (MR) fluid [401], and shape-memory materials [402]. In some cases, two different types of actuation are implemented in the same gripper to allow stable and reliable grasping under different working environments as in [403], which presents the combination of the suction and traditional linkage-driven grippers or in [383], which presents the integration of an electro-adhesive system and a pneumatic actuator.

All these last technologies have achieved good results, although, to date, they are not yet used, especially in the industrial sector, since they do not have the same performance as pneumatic and mechanical grippers.

This work presents a review and comparison of different technologies for soft robotic grippers to highlight the more robust mechanical design. Usually, specific robotic gripper designs are presented and tested to demonstrate their effectiveness. Nevertheless, soft robotic grippers present the interesting ability to grip various objects, so it is useful to know the best option and why robustness is the first requirement. Our results have the purpose of showing how different types of mechanical actuation systems and material selection can influence gripping capability.

6.3 Mechanical Design of Grippers

In this work, four soft robotic grippers have been recreated starting from commercial products, except the third one. Each gripper has been designed from scratch, thus partially modifying its original design but always aiming for the finest quality. Two actuation systems (pneumatic and electromechanical) and four design solutions have been chosen to realize an effective comparison. Two grippers employ a pneumatic actuation system, while the other two utilize an electromechanical actuation system. In addition, grippers present similar sizes and fit the UR3, the robotic arm used in the experiments.

In the first part of this section, each gripper will be described in terms of its design and actuation. The two types of actuation systems are separately described, being common to every pair of grippers.

6.3.1. Pneumatic System

The two pneumatic grippers use the actuation system shown in Figure 6.1.

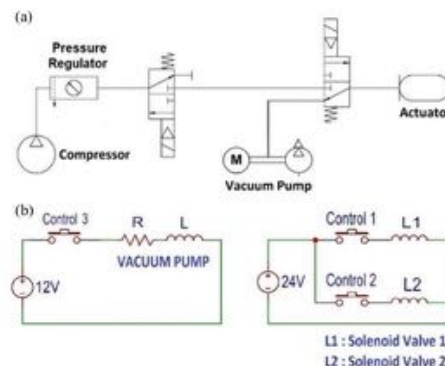


Figure 6.1 Pneumatic system. a) Connection diagram. **b)** Wiring diagram control. Signals 1, 2, and 3 are the cables that connect to the UR3 for control.

The pneumatic module is composed of two solenoid valves. One solenoid valve connects the path that carries the pressurized air to the gripper with the air extracted with the vacuum pump. The other solenoid valve connects the tube from the pressurized air reservoir with the inlet of the first solenoid valve and a blind tube. It operates as an open/close valve. Finally, a pressure regulator controls the pressure that is administered to the gripping tools. A compressor with a small tank is used for compressed air, whereas an electric vacuum pump is used for vacuum generation.

5.3.1.1. Gripper 1

The first gripper, shown in Figure 6.2, is a pneumatic gripper based on the one commercialized by Soft Robotics [38]. They developed several configuration solutions depending on the application. In this work, the four-finger solution, with fingers symmetrically spaced around the center of the gripper, has been adopted.

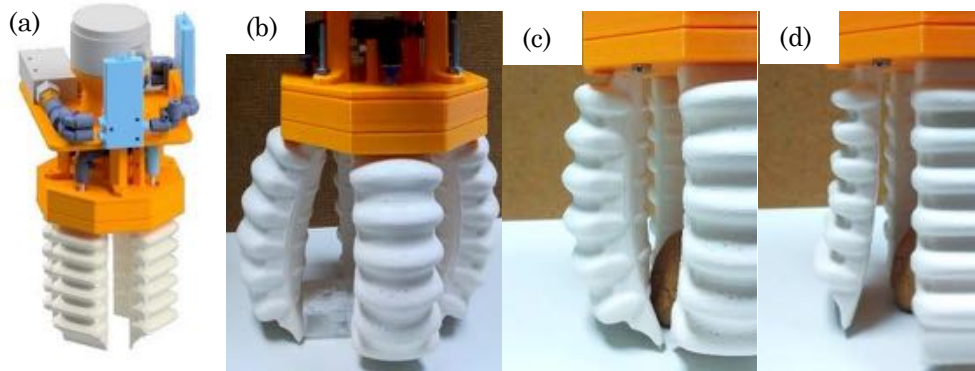


Figure 6.2 First gripper. (a) CAD model, (b) Gripper during the operation, (c) Fingers flexed, (d) and Fingers in extension.

The most important aspect of the design of fingers is their asymmetry along the lengthwise plane. This is necessary to allow movements. The inner side presents a flat surface with small reliefs that stick out to improve gripping capacity. The outer side presents six chambers that inflate when pressurized air is introduced, generating the contraction movement. Vice versa, creating a vacuum inside, they contract and generate the extension movement.

At one end, the finger has a section that allows it to be held at the base of the gripper and allows air to enter and exit the chamber. On the other end, a section with greater rigidity and with a triangular profile has been added to the finger. This provides a relatively straight section at the end of the finger to perform a better grip with the extremity. Fingers measure 11 cm in length and 4.5 cm in width.

For the creation of this prototype, two parts can be distinguished: manufacturing silicone fingers and the 3D printing of the rest of the pieces that form the base of the gripping tool (all 3D printed parts are made with the thermoplastic polyester PLA).

A mold has been realized with 3D printing to obtain a silicone finger, as shown in Figure 6.3. It comprises three different parts: a male that provides the internal shape of the finger, and two females, which provide the exterior. The silicone used is the Silastic® 3483, with a cure time of one hour.

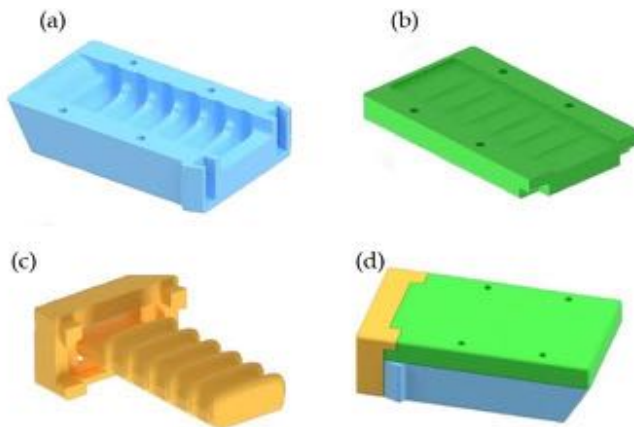


Figure 6.3 Mold for manufacturing silicone fingers: (a) Mold for inner side, (b) Mold for outer side, (c) Male mold, (d) The assembled mold.

This silicone allows getting the desired characteristics concerning stiffness, while other silicones such as Ecoflex® 00-30 have proved too soft for this application.

The working pressure of the gripping tools is around 2 bars.

5.3.1.2. Gripper 2

The second gripper, as shown in Figure 6.4, is also pneumatic and is based on the Versaball, which is a gripper produced by the company Empire Robotics Inc. [70]



Figure 6.4 Second gripper: (a) CAD model of the gripper, (b) Gripper during the operation.

Its operation is based on the jamming process by which granular materials increase their viscosity when the density of particles increases.

The gripper presents a spherical chamber made of an elastomeric plastic membrane filled with granular material. It is possible to get the liquid and solid pseudo-states when pressurized air and vacuum are applied, respectively.

To grab an object, a small amount of air has to be introduced in the chamber so that the granular material acts similar to a liquid. Then, the gripper has to be pressed against the object, adapting the contents of the chambers to the outer shape of the object. Finally, the vacuum is created inside the chamber to solidify its interior and maintain the shape of the object. As long as the vacuum is maintained, the object is held by the gripper. Subsequently, it is enough to fill the chamber with air again, return to the “liquid” state and release the object. This method of gripping requires that the object size be approximately half of the diameter of the pneumatic chamber.

This gripper comprises the previously described pneumatic module, a piece to join this module with the claw, two pieces to keep the filter in place, and two final pieces that hold the pneumatic camera.

As in the previous case, the pneumatic chamber is the essential element of the gripper. A latex balloon of approximately 1-mm thickness and about 8 cm in diameter has been chosen to realize it. The chosen thickness provides the chamber with resistance against the abrasive action of the granular material and ensures that it is not damaged when coming into contact with objects. At the same time, a smaller thickness adapts easier to the minor irregularities of the objects, besides gaining flexibility and elasticity.

Several options of granular materials have been tested, such as ground coffee, fine sand, and breadcrumbs. After testing ground coffee and breadcrumbs, it has been observed that the chamber adapts much better to objects with ground coffee. This is the same material used in the research previously mentioned.

A filter is necessary to allow air to pass in both directions and maintain the granular material isolated from the pneumatic system. The filter is composed of a felt circle with the same diameter as the upper section of the base and a thickness of approximately one millimeter. The working pressure is around 1 bar.

6.3.2. Electromechanical System

The other two grippers are mechanical and use a 6 V DC motor with a reduction gearbox. To calculate the reduction, two parameters must be considered: the approximate closing time of the gripper and its generated torque.

For the third gripper, a great reduction ratio is necessary since the torque generated by the motor must be enough to pull the three cables of the three fingers of the gripper simultaneously, so a reduction of 1:298 is necessary at least.

Indeed, a fourth gripper presents a spindle nut system that generates a suitable torque for this application. Thus, the reduction is chosen only based on the gripper closing time and is equal to 1:125.

The same structure is used to mount the motors on the two grippers, as the motor size is identical despite the different reduction ratios. This structure is composed of two parts: a base and an adapter for the robotic arm UR3. The base part houses the motor inside and is designed to be tightened to prevent its longitudinal displacement.

Finally, the simplified electrical scheme is shown in Figure 6.5. The LR group represents the DC motor, and the H bridge is composed of the four bipolar signals and the two control signals. These are the ones that connect to the input/output panel of the UR3.

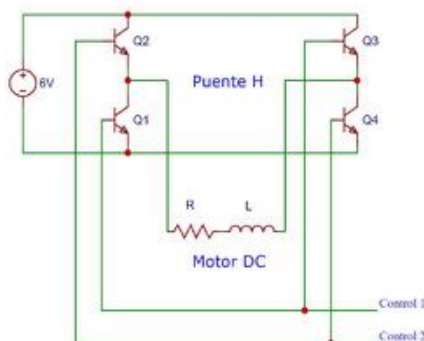


Figure 6.5 Wiring diagram of the electromechanical system.

5.3.2.1. Gripper 3

The first mechanical gripper, as shown in Figure 6.6, presents articulated fingers actuated by cables. When the cables are pulled by a motor connected to a pulley, the fingers are flexed.

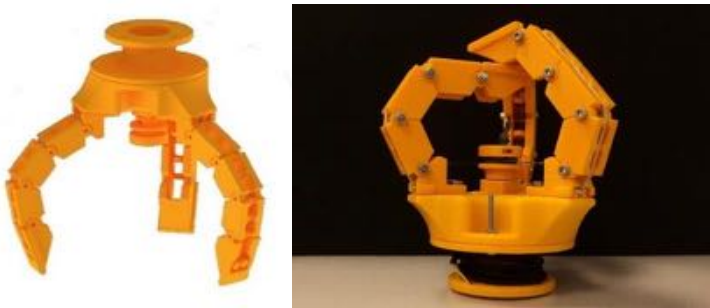


Figure 6.6 Third gripper: (a) CAD model of the gripper, (b) Real Gripper.

The shape that fingers adopt is a function of the object to be grasped; the links of the finger will adapt to the object's outer surface.

Here, the number of fingers selected to achieve optimum grip is three, arranged at 120 degrees. To work correctly, the three fingers must perform their movements simultaneously.

To carry out this movement, the three cables (one for each finger) are wound on the same pulley that collects or releases the cables, generating thus the flexion or extension of the fingers based on the rotating direction.

The pulley represents a crucial part of the design since it is responsible for synchronizing the movement of fingers. It has an inner section in which a nut is inserted to fasten the pulley to the flat face of the motor shaft. The pulley is designed with a small diameter to generate a good torque for the application but large enough to be printed in 3D and not too fragile. It also has a duct with a circular section that connects the outer face of the pulley, where the cables are wound, with the underside of the pulley.

The three fingers are held on a base, and an adapter connects to the robot. Each finger comprises three base modules, one end, and a tip. Modules are joined with screws that allow their relative rotation. Each finger measures 12 cm in length and 2.5 cm in width.

5.3.2.2. Gripper 4

As shown in Figure 6.7, the fourth gripper is based on the MultiChoice Gripper product manufactured by the FESTO® Company [404]. This design is based on the mechanics of the human hand, where the thumb serves to impose an effort in the same direction but opposite orientation as the rest of the fingers. To adapt to different object typologies, the tool developed by FESTO can reorient the fingers and obtain different configurations. For example, objects with round perimeter are placed with ternary symmetry. However, for objects with parallel faces, one finger is placed in opposition to the other two.



Figure 6.7 Fourth gripper: (a) CAD model of the gripper, (b) Gripper during the operation.

Nevertheless, for the reproduction of this prototype, this feature has been obviated to focus attention on the design of the fingers: passive structures capable of adapting to the objects that deform them. This gripping tool comprises three fingers of a flexible material. The fingers are triangular with thin walls and, longitudinally, they present a nucleus formed by rigid parts that prevent the walls of the finger from approaching. With this morphology, the tip remains approximately the same place when trying to deform the finger, but the body bends around the object. This deformation of the finger allows it to adapt to the shape of the object's surface with which it will make contact, and, thanks to its flexibility, it will deform before damaging it. In this case, the choice of the number of fingers that form the gripper could have been two, three, or four. The number three has been selected because the spindle mechanism moves perfectly synchronized, and it is unnecessary to complicate the design by adding a fourth finger, although it might be useful to have it in some scenarios.

The gripping tool consists of three flexible fingers and a rigid base. The fingers are made from the elastomeric thermoplastic produced by the company Recreus [405] called FilaFlex, and they measure 11 cm in length and 1.5 cm in width. Two pieces form the base: the main one on which the fingers are mounted, the motor is coupled, and a secondary one that joins the gripping tool with the UR3. Furthermore, the mechanical actuation comprises a direct current motor, a flexible coupler, a spindle, a nut, and a handle attached to the nut, the finger connector, and the motor support.

Each finger can be held with rotational joints at both ends of its base to generate the grip movement. By maintaining the position of the outer ends of the finger bases and changing the height of the inner ends, the opening and closing movement is achieved. This movement, which can be generated in many ways, is done with a spindle nut mechanism. A motor rotates the spindle, which causes the nut to move up and down when its rotation is prevented. The inner ends of the fingers are connected to the nut by connectors, which allow the possibility of movement while preventing the rotation of the nut.

The rigid sections that form the internal structure of the finger have been made with a wire. This wire has enough rigidity to allow the deformation of the finger but at the same time allow it to return to its initial position.

6.4. Experiments

The objective of this work is to test the robustness of the gripping tools and their grasp stability. To test these parameters, an experiment has been designed in which the ability of the gripper to grip a specific object, hold it while the robotic arm realizes a trajectory, and successively release it, is evaluated (as illustrated in Figure 6.8). The test is deemed

successful if the object does not fall either during the grip or the displacement and if the object is not damaged after gripping action.

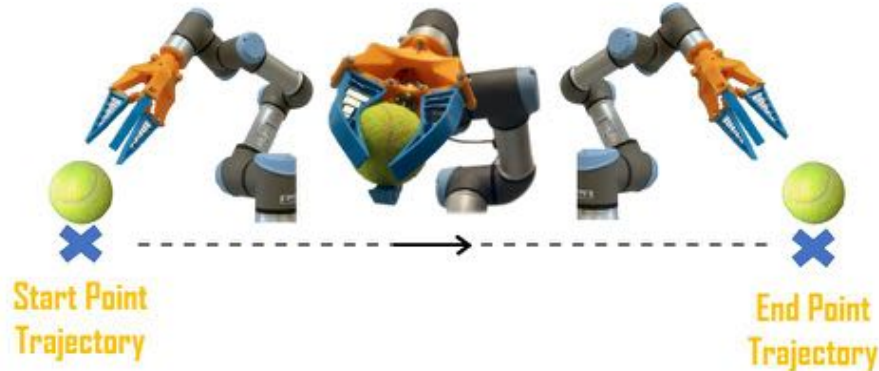


Figure 6.8 Test execution: the gripper picks up one of the twelve objects in a predetermined position and place it in the desired location.

Since one of the most important aspects is the capability of grippers to manipulate objects with different characteristics, i.e., different shapes, rigidity, and fragility, twelve objects, as shown in Figure 6.9, have been chosen for experimentation. Each of them presents different characteristics to represent a wider range of objects. The weight and dimensions of objects are limited by the capacity and dimensions of the grippers.



Figure 6.9 Selection of objects for experimentation with its identification number. (a) Tennis ball #1, (b) Screen Cleaner #2, (c) Vaseline Container #3, (d) Metallic Container #4, (e) Nut #5, (f) Rock #6, (g) Tomato #7, (h) Egg #8, (i) Glue Stick #9, (l) Dish Sponge #10, (m) Broccoli #11, and (n) Candy Box #12.

Objects are oriented in different ways not to facilitate any gripper. For example, object #9 (see Table 1) is arranged vertically, whereas object #12 is arranged horizontally. In some cases, external elements have been used to ensure the correct positioning of the object, such as for the egg (#8) (as can be seen in Figure 10 or for the tennis ball (#1), which would have slipped once placed on the surface due to their physical characteristics).

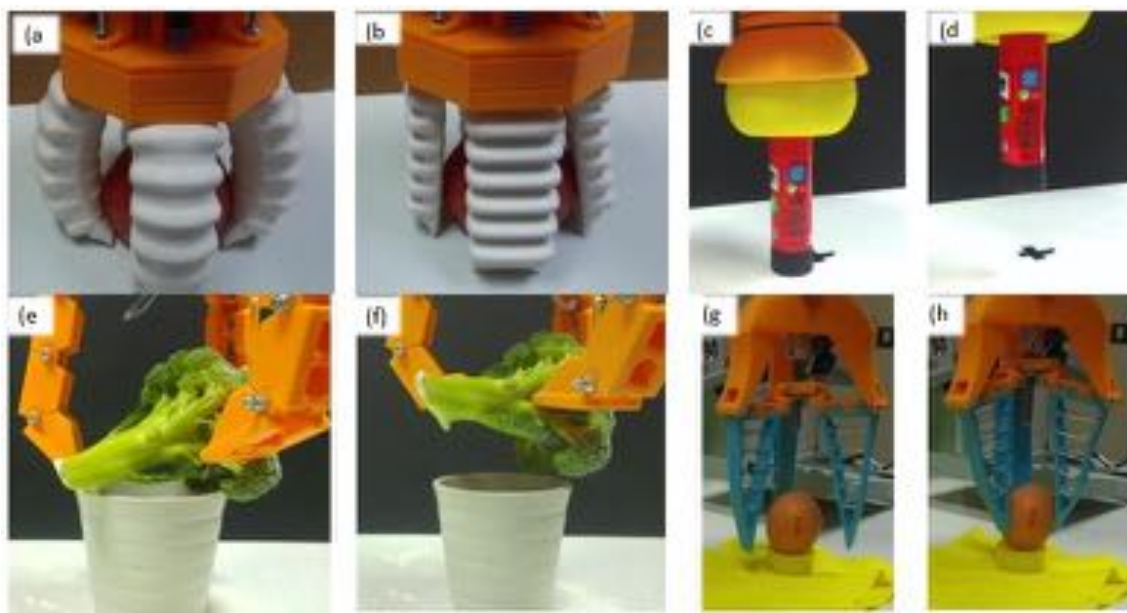


Figure 6.10 Test execution with Gripper 1 (a,b), Gripper 2 (c,d), Gripper 3 (e,f), Gripper 4 (g,h).

In the following table (Table 6.1), each object's identification number is assigned to simplify the result tables.

Table 6.1 Selection of objects for experimentation. Each object has been assigned a number to facilitate the subsequent display of results (first column). The “Dimensions” column shows the significant dimensions of each object, and the “Weight” column shows the weight of the objects used in the experiments. In the last column, “Relevant Aspects,” the aspects that differentiate each object from the others are highlighted.

Identifier	Object	Dimensions	Weight	Relevant Aspects
1	Tennis ball	70 mm diameter	57,6 g	Quite rigid and with a rough surface
2	Screen Cleaner	80 mm diameter 30 mm thickness	12,8 g	Considerably soft and deformable
3	Vaseline container	80 mm diameter 50 mm height	147 g	Very smooth surface
4	Metallic container	85 x 50 x 30 mm	47,9 g	Prismatic form with some irregularities, smooth surface
5	Nut	35 mm diameter 45 mm height	14,4 g	Very small and lightweight
6	Rock	25 x 15 x 10 mm	12,9 g	The smallest object of the experiment
7	Tomato	90 mm diameter 70 mm height	229,6 g	The heaviest object of the experiment
8	Egg	50 mm diameter 65 mm height	71 g	Hard but very fragile
9	Glue Stick	25 mm diameter 100 mm height	19,6 g	Svelte with irregularities at the ends
10	Dish Sponge	105 x 80 x 25 mm	10,2 g	Considerably soft and deformable with a slightly stiffer surface
11	Broccoli	90 mm diameter 120 mm height	130,4 g	Irregular object that should not be deformed
12	Candy box	60 x 35 x 15 mm	7,9 g	Little gripping surface (except for the second gripper)

The experiment has been carried out in three different environments: normal, humid, and dusty. The normal environment is achieved without changing the properties of the environment. In this case, objects are not damp or dusty.

The humid environment consists in moistening both the gripping tool and the object. The presence of humidity causes greater effects on some objects than on others, depending on the object's surface and how much the water can wet it. For instance, while a plastic container with smooth walls may only slightly be affected by a humid environment, the properties of a sponge, such as its weight and surface adhesion, significant change in such an environment. Finally, the dusty environment is simulated by spreading a generous amount of flour to both the tool and the object. The last two situations can occur in agriculture or specific industrial processes.

For each experiment, 20 repetitions have been performed. This means that 60 repetitions have been performed with each tool for each object, and twenty have been performed for each environment, which is 240 for each gripper and object. Being twelve objects, a total of 2880 repetitions are performed. In Figure 6.10, it is possible to see some captions of these experiments.

The time used for successful gripping is different for each of the grippers. In the case of Gripper 1, this time is in the range of 1–2 s since the fingers must be inflated to a greater or lesser extent according to the object's size. In the case of Gripper 2, this time is about 3 s since it is necessary that the gripper first adjusts to the object's shape to perform the vacuum subsequently. In the case of Gripper 3 and Gripper 4, this time is less than or equal to one second.

6.5. Results

The data obtained from the experiments are presented in the following graphics and Table 6.2, Table 6.3, Table 6.4, and Table 6.5.

Table 6.2 Experiments with Gripper 1. On the left, the table with a success rate for every object, in the last column, the average for every object is calculated, and at the end of the table, the average success rate for every environment is determined. On the right, the graphic representation of Table 2 is reported.

Obj.	Experiments with gripper 1			
	Normal	Humid	Dusty	Average
1	100 %	100 %	100 %	100 %
2	100 %	100 %	100 %	100 %
3	100 %	100 %	0 %	67 %
4	100 %	95 %	65 %	87 %
5	100 %	100 %	100 %	100 %
6	20 %	30 %	0 %	17 %
7	95 %	95 %	5 %	65 %
8	0 %	0 %	0 %	0 %
9	100 %	100 %	100 %	100 %
10	80 %	100 %	75 %	85 %
11	95 %	100 %	95 %	97 %
12	100 %	100 %	100 %	100 %
Avg				
	83%	85%	62%	77%

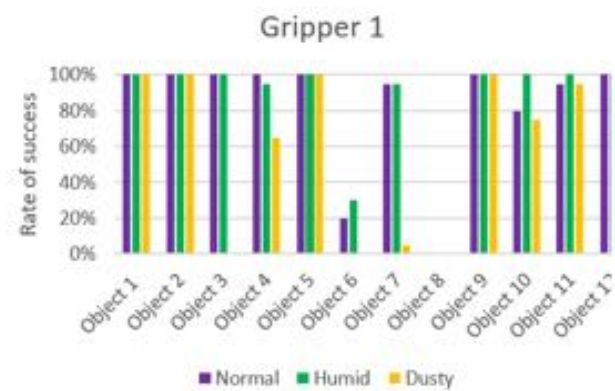


Table 6.3 Experiments with Gripper 2. On the left, the table with the success rate for every object, in the last column, the average for every object is calculated, and at the end of the table, the average success rate for every environment is determined. On the right, the graphic representation of Table 3 is reported.

Obj.	Experiments with gripper 2			
	Normal	Humid	Dusty	Average
1	0 %	0 %	0 %	0 %
2	0 %	0 %	0 %	0 %
3	0 %	0 %	0 %	0 %
4	0 %	0 %	0 %	0 %
5	70 %	90 %	60 %	73 %
6	85 %	90 %	0 %	58 %
7	0 %	0 %	0 %	0 %
8	0 %	0 %	0 %	0 %
9	100 %	100 %	95 %	98 %
10	0 %	0 %	0 %	0 %
11	0 %	0 %	0 %	0 %
12	95 %	100 %	100 %	98 %
Avg	29%	32%	21%	27%

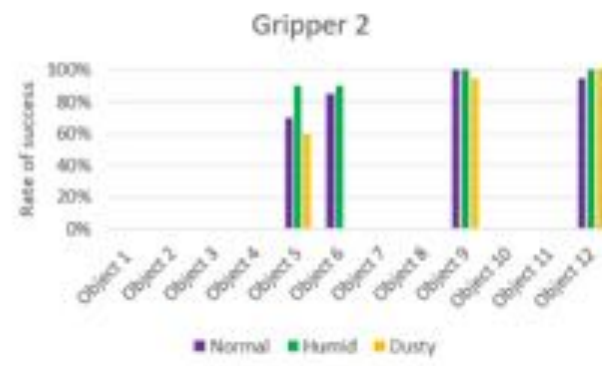


Table 6.4 Experiments with Gripper 3. On the left, the table with the success rate for every object, in the last column, the average for every object is calculated, and at the end of the table, the average success rate for every environment is determined. On the right, the graphic representation of Table 4 is reported.

Obj.	Experiments with gripper 3			
	Normal	Humid	Dusty	Average
1	50 %	55 %	20 %	42 %
2	100 %	30 %	95 %	75 %
3	0 %	0 %	0 %	0 %
4	0 %	0 %	0 %	0 %
5	0 %	0 %	0 %	0 %
6	0 %	0 %	0 %	0 %
7	100 %	80 %	100 %	93 %
8	0 %	0 %	0 %	0 %
9	30 %	20 %	10 %	20 %
10	85 %	20 %	65 %	57 %
11	85 %	70 %	50 %	68 %
12	0 %	0 %	0 %	0 %
Avg	38%	23%	28%	30%

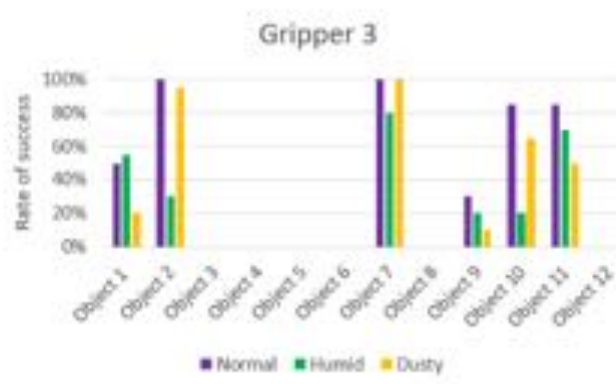
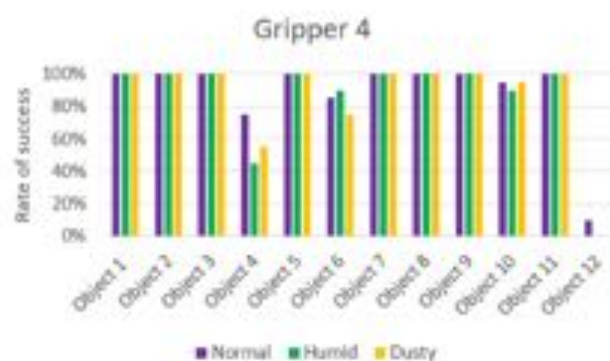


Table 6.5 Experiments with Gripper 4. On the left, the table with the success rate for every object, in the last column, the average for every object is calculated, and at the end of the table, the average success rate for every environment is determined. On the right, the graphic representation of Table 5 is reported.

Obj.	Experiments with gripper 4			
	Normal	Humid	Dusty	Average
1	100 %	100 %	100 %	100 %
2	100 %	100 %	100 %	100 %
3	100 %	100 %	100 %	100 %
4	75 %	40 %	50 %	58 %
5	100 %	100 %	100 %	100 %
6	85 %	90 %	75 %	83 %
7	100 %	100 %	100 %	100 %
8	100 %	100 %	100 %	100 %
9	100 %	100 %	100 %	100 %
10	95 %	90 %	95 %	93 %
11	100 %	100 %	100 %	100 %
12	10 %	0 %	0 %	3 %
Avg	89%	85%	85%	86%



The first three columns of data correspond to the success rate of the gripping tools in the three scenarios: normal, humid, and dust. The average column of success rates for each object in all scenarios is presented in the fourth column. In the last row, the average success rate for each environment is calculated, and the global success rate is calculated as

the average between the rates of each object in each scenario. A histogram accompanies each table to display the data more intuitively.

From the results (Figure 6.11), it can be seen that the success order of the grippers is as follows: Gripper 4, Gripper 1, Gripper 3, and Gripper 2.

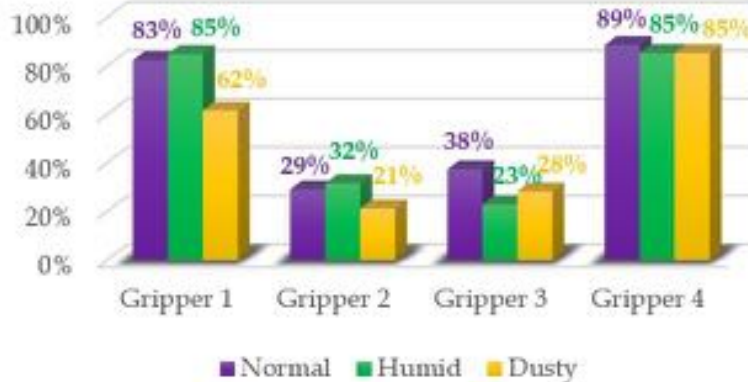


Figure 6.11 Summary of test results for the four grippers in the three environments.

Gripper 1, with 77% of the global success rate, is the best of the two pneumatic grippers and ranks second among the four presented grippers. Table 6.2 indicates that Gripper 1 can grab eight of the 12 objects with a success rate equal to or greater than 85% and that only in two cases, with objects #6 and #8, it has not been able to grasp them. This is because the size of object #6 (the stone) was too small for this type of gripper, while the surface of object #8 (the egg) was the most slippery, besides the impossibility of applying high forces to avoid breaking the object. The best performance is achieved in a humid environment. This is because the silicone of the fingers has increased adhesion in the presence of moisture. Vice versa, the friction coefficient decreases in the presence of dust, and therefore, the worst results are obtained in the third scenario.

Gripper 2 presents the lower global success rate, which is equal to 27%. This was expected due to the restriction that it cannot take objects more than 50% of its diameter. It achieved good results only with the smallest and lightest objects, but also, in this case, it did not do better than the other grippers. For the same reasons as in the previous case, the humidity seems to indicate better performance.

Gripper 3, with 30% of the global success rate, is slightly better than Gripper 2. However, it is evident from Table 6.4 that it is not better. Despite its ability to grab many of the objects, it fails to complete the task in most cases. It reached 100% only in three cases: with object #2 in the normal environment and with object #7 in the normal and dusty environment. These results indicate that this gripper is suitable for large objects and is not affected by weight. Unlike Gripper 2, it is unable to grasp small or rectangular objects, and the presence of humidity, in general, worsens its performance (as in the case of objects #2, #7, and #10).

Gripper 4, with 86% of the global success rate, is the best gripper of this study. As shown in Table 6.5, its performances, with a success rate of 89% in the normal environment and 85% in the other two cases, are not significantly influenced by the type of environment. It is capable of grasping both small and light objects as large and heavy objects. Fingers adapt to objects by applying uniform pressure without the need to exert much force. The gripper presents problems only with two objects, #4 and especially #12. In both cases, it is a rectangular object with smooth surfaces (in the case of #12, the thickness is the least). In this case, the gripper, with its three fingers, is unable to surround the object and adapt to it.

In summary, Gripper 1 can grab many different objects with similar performance. Its limitations proved to be the dimensions below those of the nut and the thin objects. In the case of delicate objects such as #7 and #11, the gripper has left them intact. Gripper 2 can grab little and lightweight objects, better if with regular surfaces, as in the case of objects #9 and #12. Almost certainly, some improvements in the realization of the gripper would allow achieving better results, but due to the limitations mentioned above, it would still not be the most robust gripper among the four proposed. Gripper 3 is suitable for grabbing sufficiently large and heavy round objects that cannot escape laterally. In general, it did not cause damage to the most delicate objects; however, it is necessary to generate more force on the object's surface to ensure a firm grip. Finally, Gripper 4 proved to be the most robust gripper of the four proposed. It is able to grasp objects without exerting a significant force, so it is suitable for delicate objects, and it has been seen that neither the tomato nor the broccoli has been dented.

In Figure 6.12, comparison graphs have been realized to highlight the most significant differences.

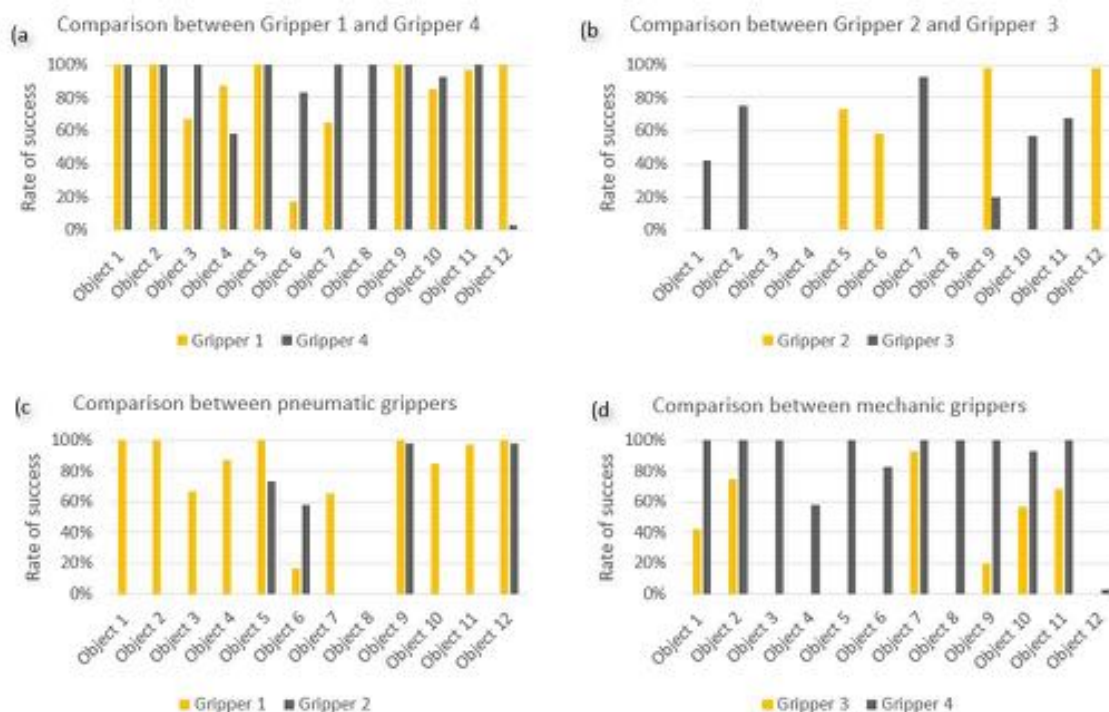


Figure 6.12 Graphics comparison between (a) Gripper 1 and Gripper 4. As can be seen from the graph, the two grippers generally have similar performances. **(b) Gripper 2 and Gripper 3.** These are the two grippers with the worst performances, and each one proved to be suitable only for a specific type of object. **(c) Graphic comparison between Gripper 1 and Gripper 2 (the two pneumatic grippers).** As can be seen from the graph, Gripper 1 works significantly better than Gripper 2. **(d) Graphic comparison between Gripper 3 and Gripper 4 (the two mechanic grippers).** As can be seen from the graph, Gripper 3 works significantly better than Gripper 4.

Figure 6.12a compares the performance of Gripper 1 and Gripper 4, the two best grippers. Both exhibit acceptable behavior with most objects. This indicates that, in general, they are very robust tools of grip. Interestingly, the two grippers compensate, as with objects #8 and #12, and in part with #4 and #6. Although the shape of approaching the object is similar, the presence of a fourth finger in Gripper 1 makes the difference in grabbing rectangular objects, even if the dimensions of these same fingers are prejudicial for grasping small objects.

Figure 6.12b compares the two grippers with lower performances. In this case, the type of object that each can grasp is completely different.

Figure 6.12c compares the pneumatic grippers. Only with object #6 is Gripper 2 better than Gripper 1.

Finally, Figure 6.12d compares the mechanical grippers. In this case, Gripper 4 is always better than Gripper 3. Electromechanical grippers behave best in the normal environment and not in a humid environment such as pneumatic grippers. This is because, with this type of gripper, the objects' grip depends to a lesser extent on the coefficients of friction.

Analyzing the data, it is interesting to observe that results are not affected by the change of environment for certain objects, while for others, they change significantly. Gripper 1, for example, exhibits a critical fall in the success rate with tomato in the dusty environment. These significant variations can be attributed to the surface properties of the object. The surface of a tomato, e.g., is perfectly smooth and not porous. As a consequence, powder remains on its surface and directly affects the grip. This effect does not occur with the tennis ball due to its surface roughness. Another example of this phenomenon occurs with the stone. The second pneumatic grip tool, with success rates of 85% and 90% in normal and humid environments, cannot grasp the stone in the presence of dust.

Object #9 (stick glue) exhibits the best results with an 80% success rate globally (in all environments and with all grippers). The three objects with the worst results have been objects #4 (metallic container), #6 (the stone), and #3 (the Vaseline container), with overall results of 36%, 40%, and 42%, respectively.

Finally, we present some considerations concerning the construction and operation of the grippers. The tool with the fastest and easiest manufacturing process turned out to be Gripper 4. In addition, its control is very simple and requires only a power supply, while in the case of pneumatic grippers, a compressor, a pressure air tank, and a vacuum pump are needed.

Another factor to consider is the noise generated by the tools during use. The two electromechanical grippers are much quieter than the pneumatic ones due to the work of the compressor and the vacuum pump, although the latter could be replaced by a vacuum ejector, which is much quieter.

The work environment is another factor that affects performance. The pneumatic tools may be a better option in the food industry due to the ease and speed of cleaning them. Another advantage is that the compressor and the tank may be away from tools and out of the manipulation environment. In contrast, in the electromechanical tools, the operating mechanisms are in direct contact with the work environment and could compromise the safety of the installation.

If the speed of action plays a paramount role in the application, as in pick and place tasks in which the speeds of opening and closing of the tools are critical for productivity, pneumatic grippers should be considered as the better option due to their higher speed.

However, from the perspective of the maintenance of gripping tools, it is not easy to determine which is the most appropriate. Although changing a component of an electromechanical gripper requires a longer time, pneumatic elements are more likely to fail than mechanic ones.

6.6. Conclusions

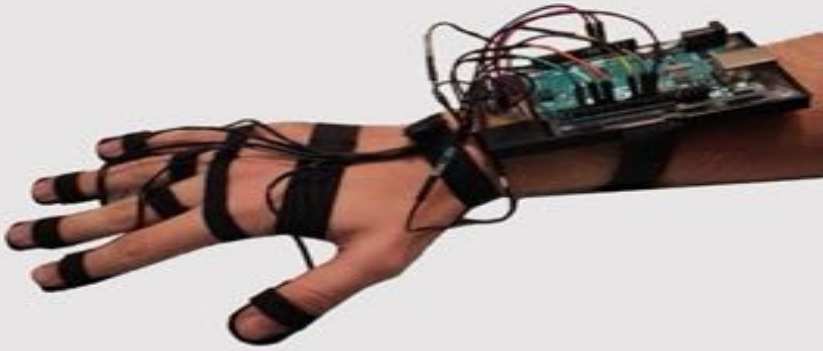
Four prototypes of soft robotic grippers, including their design and manufacture, have been developed for a later stage of experimentation. To realize a more effective comparison, two grippers use pneumatic system actuation, while the other two employ electromechanical actuation, and each of them shows a different solution design. All grippers have been tested with twelve objects in three different work environments. These objects have carefully been

selected to be a representative group of items that could be manipulated by the grippers in a real industrial work environment. This group includes objects with different geometric and mechanical characteristics in terms relative to the dimensions of the grippers. An overview of the work and real tests is available in Supplementary Materials.

From the results of our tests, it can be seen that Gripper 4 (the electromechanical gripper with passive structure) and Gripper 1 (the pneumatic gripper with chambered fingers) present the highest success rate, with rates of 86% and 77%, respectively.

Thus, it can be concluded that Gripper 4 represents the best option when robustness and good behavior for the manipulation of unknown objects are needed. Gripper 1 also represents an excellent option despite some limitations due to the dimensions of fingers that do not allow grasping certain types of objects.

It is worth noting that the improvements in the mechanical design of the other grippers may increase their percentage of success rate.



7. Wearable soft robots

"The greatest challenge to any thinker is stating the problem in a way that will allow a solution."
Bertrand Russell

This chapter presents the developments realized in the fourth category of soft robots: wearable devices. It is divided into three sections: haptic devices, exoskeletons, and virtual reality (VR) applications. It is also important to highlight that all of them have been designed for post-stroke hand rehabilitation. After a brief introduction, each device will be analyzed concerning the design, the actuation, and the results obtained. Almost all of them use SMA springs as actuators, but different sensors and actuation strategies have been employed. Finally, the application of VR pretends to improve the experience with these devices. Results show that soft robots in wearable and medical devices could constitute a concrete alternative to classical rehabilitation devices.

Further information on this section can be found in the original scientific publication [406].

7.1 State of the Art

Covering all state of the art concerning haptic devices, exoskeletons, and virtual reality applications for post-stroke hand rehabilitation, will require many pages. Therefore, only the most important results in these fields are summarized in this state of the art. Moreover, only wearable devices will be considered, omitting desktop versions.

Virtual reality in hand rehabilitation started to be used in the early 2000s. One of the first examples is the work presented in [407], in which they used a glove that detected hand motions, finger movements, and gripping, and an Xbox to realize four exercises. They worked on a different rehabilitation aspect: the first on the impairments in finger range of motion, the second on the speed of motion, the third on the fractionation, and the fourth on the finger's strength.

In [408], the use of augmented reality to realize rehabilitation exercise. The system is more complex than in previous works since a database with patients' profiles was developed, allowing rehabilitation doctors to not stay physically with patients and control progress later. Patients manipulate a tangible object that is tracked to measure their performances. In this case, a camera and various squared markers are required; for this reason, it is probably not the most comfortable solution for patients at home.

In [409], a solution with a pneumatic glove (PneuGlove) was proposed. Patients practice grasp-and-release movements either with material objects or with virtual objects. They tested their work with 14 persons affected by stroke; tests were realized both with the glove and virtual reality and only virtual reality.

In 2010, a set of serious games with vibrotactile feedback was presented [410]. It was another example of augmented reality; since vibrotactile actuators are attached to real objects, a camera and various squared markers are required, as in the previous work. Parameters evaluated were: task completion time (TCT), eye-hand coordination, motion smoothness, hand steadiness, hand motion curvature, hand range of motion, and hand strength. The games proposed were the Cannon-ball game, where patients have to receive a virtual ball with a cup, and the Air-Hockey game, where they have to play hockey against PC.

The study presented in [411] applied augmented reality to simulate daily activities like holding and tilting a mug to pour virtual water or gradually grasping random size-position circles. The proposed system involves not only the hand but also the arm and the wrist. It is a portable, low-cost home-based device. The therapist can interact remotely, and the patient can work independently.

In 2013 a novel artistic virtual reality environment was developed by the Rehabilitation Institute of Chicago [412]. Fourteen stroke survivors with chronic hemiparesis tested the virtual reality scene inspired in Alice in Wonderland, realizing different tasks to practice whole-hand grasp, lateral pinch, palmar pinch, finger extension, and finger individuation. Magnetic trackers provide information regarding head orientation and hand location. It was also employed the pneumatic glove, PneuGlove, already mentioned.

The following year, the Leap Motion controller was proposed for hand tracking in stroke rehabilitation [413]. In this case, they modified the Fruit Ninja game to allow patients to practice their finger individuation. There was no virtual reality, only the use of the sensor. On the contrary, in work presented in [414] in 2016, the Leap Motion was used with virtual reality to develop the muscle tonus and increase precision in gestures. Four games were developed: the Trash can, where patients have to collect objects and put them in the trash; the Pyramids, where they have to gather blocks and put them on shelves; and the Labyrinth, where they have to collocate a ball.

Another example of vibrotactile feedback with a virtual-reality-based interactive environment was presented in [415]. The device was equipped with small DC vibration motors, and with piezoresistive thin-film force sensors placed on the table, the therapist can evaluate the finger pressing values to evaluate rehabilitation progress. Two virtual reality-based games were developed; their aim is to hitting gophers or musical notes.

In 2017 in [416] was presented a system, based on the fusion of VR and EMG signal, processing that with support vector machine (SVM) was able to classify gestures. No camera is necessary in this case, and it is a significant advantage concerning previous works. The scene is a virtual kitchen environment in which different objects are placed to realize daily tasks.

In another work, Leap Motion, with Unity, has been used to improve patients' hand and finger motion through three games: Space, Cannon, and Piano. No HDM-VR was used, so games are 2D, and the experience was not so immersive as in others works. Other works have been summarized in [417] or in [418].



Figure 7.1 (a) [407] (b) [408] (c) [409] (d) [411] (e) [412] (f) [414]

Virtual reality allows patients to immerse in virtual experiences to realize rehabilitation exercises more enjoyably. Nevertheless, it provides only a visual and audio experience, so considering other senses is quite interesting also to provide haptic feedback based on kinesthesia or tactile interactions. Many studies over the years have proved that haptic devices realized to help in hand rehabilitation in stroke patients improve patients' conditions in terms of motor recovery and motivation [419]. One of the first studies was

conducted in 2002 with the use of two haptic force feedback devices: the Rutgers Master II (RMII) glove and the Rutgers Ankle (RA) [420]. They were both pneumatic devices, lightweight and powerful. They were tested with two chronic patients post-stroke in a virtual-reality scenario, and both demonstrated increases in strength and function. The first device Rutgers Master II has been used in another study as [407] with another famous prototype named CyberGlove. It is produced by the company CyberGlove System that has traded many versions of the glove during the years. It is often used with CyberGrasp, a lightweight, force-reflecting exoskeleton that fits over the CyberGlove [421]. Another glove that provides kinesthetics feedback is the PneuGlove [422]. It utilizes air pressure to assist in finger extension.

Concerning **tactile feedback**, existing many prototypes, but many of them are not developed with rehabilitation aims. Three techniques exist to provide tactile feedback: 1) vibrations, 2) normal indentation, and 3) lateral stretching. In the first case, possible actuators are piezoelectric, DEA actuators (as in [423]), or miniature vibrating motors. The latter actuators are the most used since they are effortless to use and control and lightweight. For example, the prototype shown in [424] allowed users to experience tactile materials' delicacy. It presents a motor for each finger, and with an Arduino Uno in the back of the hand, it only weighs 120 g, and it is sufficient a 9V battery to supply the five motors. In the second case, possible actuators are servo motors (as in [425]), voice coils, or SMA as in [426,427]. Finally, the third option is often realized with rotary motors [428], electrostatic brake [429], or pneumatic (as in [430], where bubbles regulated independently by valves provide the feeling of contact with a virtual object). Pneumatic actuation provides considerable precision and realism; however, it is bulky and noisy due to the compressor. DC motors and servo motors also provide realistic feedback, but at the same time, they are heavy, bulky, and rigid.

On the contrary, SMA and small vibration motors are lightweight, compact, and, especially SMA, flexible. The drawback is a less realistic tactile feeling than other actuators, which can be improved through the right control and a proper design. Many other models of soft haptic gloves are summarized in the followings state of the art [63,431].

In the case of **kinesthetic haptic gloves**, many models use pneumatics despite the complexity and large volume that this type of actuation requires. Increasing the number of DOF (Degrees of Freedom) presented by the glove implies a new, greater volume than the alternatives. In addition, the compressor and the noise it generates have to be taken into account. The Jamming Tubes [432] prototype simulates the grip of not-heavy objects using the principle of jamming. It is quite a bulky system for two-finger control. Depending on the desired sensation, air bladders in the palm and on the back are widely used. A recent pneumatic model is the Haptx Glove [430], which has several small bladders on both the palm and the fingertips. These are inflated independently to obtain a faithful tactile simulation that allows differentiating in the same fingertip depending on the contact location. In addition, these gloves have several motors for grip sensation.

The other most widely used actuators are DC motors in tendon-driven models, such as Hand Exoskeleton [433]. They can precisely control the range of movement with the help of an encoder. However, it is a bulky and not lightweight design. The size will be more accentuated with the increase in the DOF since they are associated with an increase in DC motors. Similarly, the more force required, the more powerful the motors. Therefore, motors end up being outside the glove for some force ranges—the TeslaSuit company [434] presented in early 2020 a haptic glove with servo motors.

In the case of the model called MRAGES [435], a magnetorheological fluid (MRF) was used inside a piston. A magnetic field was varied to control the movement and, consequently, fluid viscosity. Thus, high forces can be achieved with light equipment and safety. In this

case, the actuators provided forces up to 6 N; but simple design changes can create much higher forces. However, these types of fluids have a very high cost and a slow reaction time.

Another alternative is the use of a Shape Memory Alloy (SMA). When an SMA is heated, it recovers the shape previously memorized in heat treatment, so its length can be affected and used to restrict movement. The ExoPhalanx [436] is a glove that takes advantage of the SMA's ability to compress as a brake for the cable, making it more complicated to move around. The main disadvantage of this design is the all-or-nothing control over the force. In this way, the weight grasped in the simulation cannot be controlled and depends on the strength exerted by the fingers. The only thing that can be characterized in the simulator would be the size of the object. In the case of the prototype [427], the intermediate areas of each phalanx are compressed by SMA rings that contract when current is passed through them, causing the sensation of pressure. However, the advancement of the fingers is not impeded, so the grip it realizes is not realistic. In addition, as soon as several consecutive fingers are implemented in the glove, the rings can rub and reduce the naturalness of the movement.

A market model, widely accepted for its lightness and power, is the DextrES [429] glove. With a high voltage (2000 V) and very low amperage (500 μ A maximum), it offers forces of up to 20 N. It uses two metal bands for each finger, one fixed on the wrist and the other located along with the finger. As it moves, its band slides over the one on the wrist. When it is necessary to retain the movement, the current circulates through the metal bands, and by the electrostatic effect, the bands adhere, preventing movement. However, a costly source is necessary to get the voltage and amperage values previously mentioned.

Finally, to recreate the grip and experience a force that opposes the penetrating object, some prototypes [437] take advantage of the force generated by the user's opposing fingers using elastomeric dielectric actuators. Depending on the size of the grasped object, the actuators will lock in different positions. The main disadvantages are the inability to recreate actions that involve a single finger or the size grasp limited by the possibility of the compression of these actuators.

The most widely used models are those with pneumatic actuators and DC motors, whether desktop or wearable. Although the other actuators (MRF, SMA) are less used, they offer essential advantages when designing a soft haptic glove that is lightweight and flexible but at the same time powerful. In [63], an updated state-of-the-art about wearable haptic devices is available.

All the previous technologies can significantly help stroke survivors; however, sometimes, patients cannot move their hands correctly, and in this case, it is impossible to realize any game without the help of a therapist. So, extra help from an exoskeleton is necessary. Soft exoskeletons are being widely studied, and the most varied prototypes exist. However, we presented here only those that present a structure similar to the one presented by the second prototype, consisting of a glove without other mechanic structures, since they are relatively recent. A jointless structure for compact hand exoskeleton[438] was presented in the Conference on Rehabilitation Robotics of 2011. The device was a glove with tendons in the fingers actuated with a motor to extend the hand. This system allows to realize a force equal to 18 N; however, tasks only need 10.5 N. Exo-glove was another example of a tendon-driven glove with motors [439]. It is compact and weighs only 194 g. It realizes a pinch force of 20 N, a wrap grasp force of 40 N, and a maximum grasped object size of 76 mm. The same idea was then used in [440] with the addition of suction cups to improve adherence with hand.

Nevertheless, probably one of the better tendon-driving prototypes is shown in [441]. They use only one motor to move 8 degrees of freedom of the hand, taking advantage of the synergy of hand movements. Moreover, they use a Bowden cable transmission to locate the

motor on a belt or in a backpack. This last characteristic is essential in these devices since patients cannot carry significant weight in their hands, so we also find it in [442]. This soft, lightweight glove is controlled with electromyography that detects the patient's intention. It presents two more control modes: a physio mode and a mobile application. Actuators and controllers located on the patient's back allowed to reduce the weight of the glove to less than 0.05 kg. It realizes a force equal to 2.45 N force for each finger. Less frequently, other actuators like SMA (Shape Memory Alloy) are used in these types of devices. One example is shown in [443]; they use nine SMA spring actuators for three fingers (index, middle, and ring finger) to realize a force equal to 11 N and provide 14 DOF for four digits (the little finger is not involved). There are three control modes for the SMA spring actuators: "on," "hold," and "off." The total weight is 85 g. The major problem with SMA actuators is the cooling time that slows the functioning.

For this reason, in the ASR glove presented in [444], some fans are used to accelerate the cooling process of SMA. This glove is weightier (517 g) than the previous one, and it is provided with Artman and force sensors. Pneumatic actuators are also widely used; however, they have limitations due to the compressor requirement, making the glove not so portable as the other types. In [445], a soft pneumatic glove controlled by the movements of the healthy hand is presented. It weighs less than 0.5 kg and provides a total force of 10-15 N. Control is based on a mathematical model that relates the turned angle with the tension that must be applied to the actuators.

Due to all the aspects illustrated in this state of the art, it is easy to understand why SMA actuators have been employed to develop the following prototypes. They allow a lightweight and compact design. The drawback is the control and the actuation time. However, it is considered that in rehabilitation applications, high velocities are not so critical as the comfortability for patients and easiness of wearing them.

7.2 Haptic gloves

Human beings depend on five senses, and haptic technology focuses on touch. It arose because of the amount of information we can perceive through touch. Thanks to screens or other similar devices, information can be added to what we already perceive with other senses. However, haptics is especially interesting in medicine for delicate surgery or rehabilitation [446] or for handling highly unstable and radioactive elements to avoid exposure to certain risks. However, it also finds significant development in leisure activities, such as video games, to provide an increasingly immersive experience. Kinesthetic haptic gloves allow the simulation of the grip of objects in different ways, for example, by preventing the advancement of the fingers or by performing an extension movement.

7.2.1 Force haptic glove

This first section presents the development of a soft haptic glove actuated with SMA springs to generate a kinesthetic perception in the user. Usually, SMA actuators are used in an on/off manner. However, in this case, three different actuation levels to simulate three different sensations (three different forces) have been achieved. Results have the purpose of showing how SMA actuators could be an interesting option for haptic devices. First, the development of the prototype is illustrated, explaining all the design decisions and the components. Then, the actuators are analyzed deeply through finite element (FE) analysis. Next, the control and characterization of the system are illustrated. Finally, experiments and results are discussed.

The glove's design requirements were: soft material, soft actuators with a smooth weight/power ratio, lightweight, wearability, and portability. This device's softness is essential since the stiffness would not have allowed the realistic simulation of lighter objects.

7.2.1.1 Design

The device consists of two principal parts: (1) a glove with actuators and cables, (2) an armband with electronics and power cable. A flexible stretch sensor (Image Scientific Instruments) connects the two parts. The selected glove is made of elastic fabric (polyester and elastane) that provides elasticity and thermal insulation (Figure 7.2a).

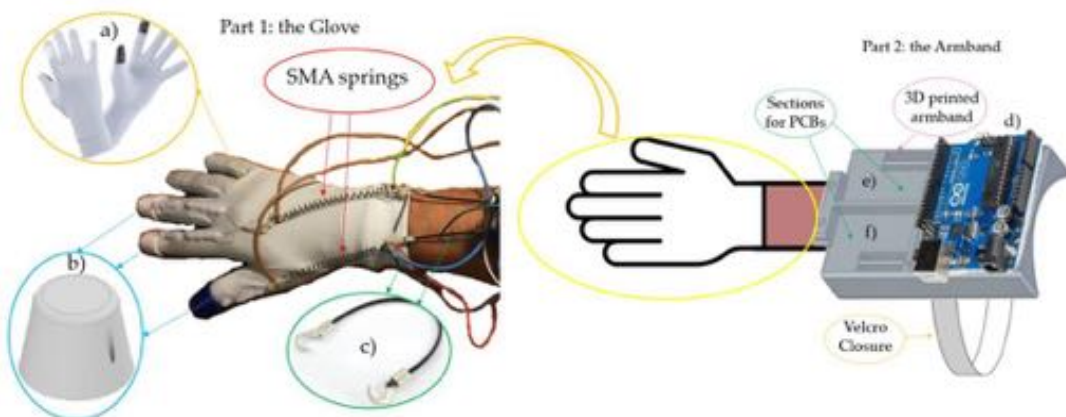


Figure 7.2 The two principal parts of the haptic glove. (a) Glove made of elastic fabric. (b) 3D printed finger cap (c) Flexible stretch sensors (d) Arduino UNO (e) electronic circuit for SMA control (f) electronic circuit for stretch sensors.

A nylon thread of 0.5 mm diameter connects the fingertips to the actuators. This material is lightweight, flexible, and robust. The nylon thread passes through a Teflon™ pipe to avoid friction with the glove and realizes a smoother movement. It presents an outer diameter of

4 mm and an inner diameter of 2 mm, and it is glued to the glove with a hot glue gun. This solution was more straightforward than the option of sewing tubes due to the fabric glove. The pipe is divided into two parts to guide the thread but not interfere with the finger's movement.

The nylon thread is not directly connected to the glove because this could tear the fabric through use. Therefore, three-finger caps have been designed and printed in 3D with PLA. They are joined to the glove as the Teflon pipe and present a small hole to realize the connection with the thread.

On the other end, the cable is connected to the SMA actuator. This connection is challenging because a higher temperature reaches SMA during this function. Therefore, to avoid fusion of the nylon (its diameter is tiny), thermal insulation with two plastic clamps is necessary.

The same insulated connection between the SMA and the flexible stretch sensor is used. In this second case, the insulation is even more important for avoiding incorrect measurements that could happen without it. Connected to the SMAs are two flexible stretch sensors.

The manufacture of the glove was straightforward. The only bespoke parts were the 3D printed finger caps and the armband (and, of course, the electronics). All other components were purchased (glove, springs, sensors).

These sensors offer reasonably precise measurements of the tension state of the cables. The total length, including the two hooks, is 5 cm. When the sensor is relaxed, the rubber has a nominal resistance of approximately 200 ohms per centimeter. According to the manufacturer, the resistance gradually increases with the sensor stretching up to 150% of its original length ($5 \text{ cm} \times 150\% = 7.5 \text{ cm}$).

By establishing a correct relationship between electrical resistance and deformation, we indirectly obtained a measurement of the tension in the sensor as long as we were in the linear zone of deformation. The procedure for obtaining these measurements will be described in detail in the following sections. The elastic property of the sensor will also facilitate the recovery of the initial state of the SMA since it will pull it back to its nominal length. Cooling is the most time-consuming phase in the SMA cycle. However, as explained in [294], placing a bias spring with a fixed-grip on one side of the SMA favors the recovery of the spring since, as it cools and gives way, the system will return to its initial disposition (or at least close to it).

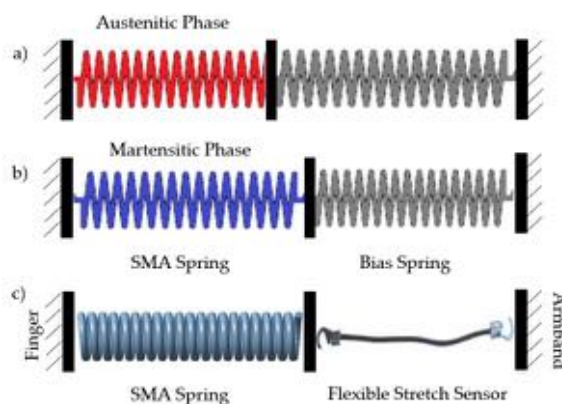


Figure 7.3 SMA-spring actuators (a,b) The idea as illustrated in [16] (c) the idea as implemented in our work

In the present work, bias springs have been changed with elastic sensors (as shown in Figure 7.3c) to provide information and fulfill this recovery function. Moreover, this design solved one of the problems of haptic glove designs with cables that pass in the upper area of the fingers: the turning radii and the need for it to have two fixed points at both ends. If the cable were to pass inside the fingers, as tendons do, this would not impede the total length required, which would always be constant. However, when these pass over the skin, some displacement at the cable ends because of the radii of gyration. This phenomenon happened when we actuated the SMA when the system was at rest. It gave rise to the appearance of a force that blocks the hands' free movement of the hands. Figure 7.4 shows this effect between two joints which, if we add it to the one produced between the other finger and the wrist, will give rise to displacements that cannot be ignored.

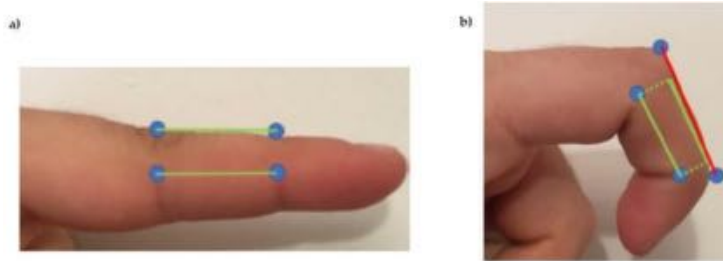


Figure 7.4 (a) Finger fully stretched (minimum distance between upper joint area). **(b)** Bent finger (maximum distance between the upper part of the joints).

Therefore, we will need some freedom at one end of the cable to move our fingers, which can be achieved by deforming these sensors or the SMA. A high elasticity constant would block this freedom since we would need a high force for a movement that apparently should be without load. On the contrary, a constant that is too low to allow the fingers to move naturally would cause that variation in the length of the SMA that the spring must absorb to result in an inappreciable force, rendering the actuator useless. It makes the selection of sensors (used in this case also as springs) crucial.

The armband provided the electronics: it consists of a single part impressed with 3D printing (PLA) (Figure 7.2).

It is possible to identify three sections, each of which houses a specific circuit of the electronic system: the largest is for the Arduino UNO, and the other two are, respectively, for two PCBs (one for the SMA control and one for the stretch sensors reading). It also presents a grip zone for the sensors. This design allows the glove to be assembled and disassembled quickly. The face in contact with the arm is slightly curved to generate comfort for the user. A Velcro closure is used to fasten the armband. In this way, each user can adjust the size. In this case, the power supply is external. It reduces mobility but at the same time allows a more lightweight prototype. It will be possible to add a battery and realize a portable device in the future.

The actuators selected to realize this prototype were SMA springs for all the reasons explained in Chapter 3. After the mechanical analysis presented in Chapter 3, we studied the electrical circuit to actuate the springs. Their electrical resistance was verified experimentally to be equal to 1.3 ohms. The source offered 12 V and 3 A, with a nominal power of 40 W. We selected the Mosfet model IRF530, channel n. With this model, we dissipated a maximum of 88 W.

Following the characteristic curve (data at 25 °C) offered by the manufacturer, for a gate-source voltage of 5 V (characteristic voltage of the Arduino pins), the drain current will be around 3 A. Therefore, we will not be able to act with duty cycles greater than 40–50% on the two SMAs simultaneously since the capacity of the source will be exceeded.

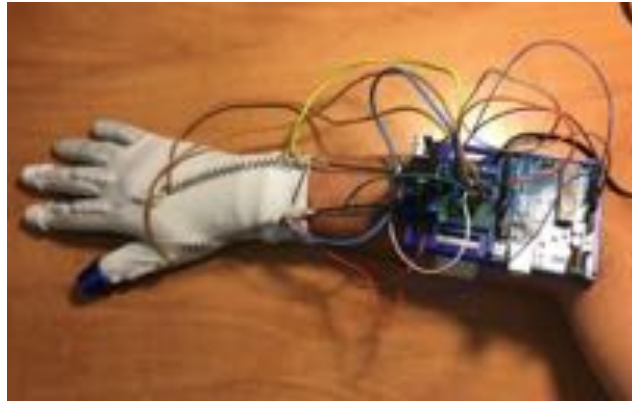


Figure 7.5 Final Haptic Glove.

The scheme used to control the Mosfet is that of Figure 7.6. The simulations have been carried out with LTspice.

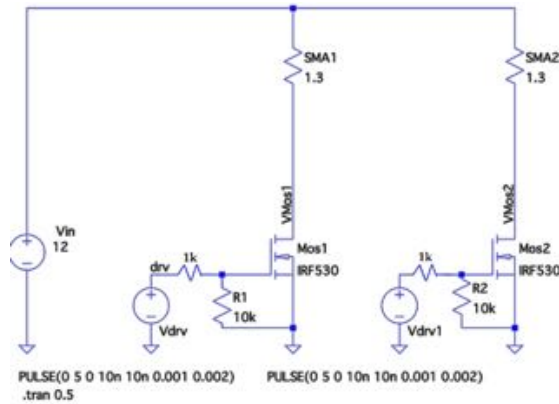


Figure 7.6 General schematic in LTspice.

To use these devices as haptic glove actuators, they have to exert different levels of force. Therefore, the SMA is usually used in an on/off manner. Consequently, the only possible states are when the austenitic transformation has been completed or not started. Analyzing any graph that shows the current-strain relationship for an SMA spring (for example, the one shown in Chapter 3 of the book in [286]), we saw that if we could position ourselves at intermediate points of the curves, we obtained different states of stress. Therefore, a perfect thermal balance had to be achieved. Depending on the dimensions of the chosen spring, it will be more or less complex. If, for example, it is small, it will heat up quickly with tiny variations in the current, making any intermediate point of the curve inaccessible. If we could access these areas of the curve, the main drawback became the hysteresis of the process. *A priori*, without a feedback system, we cannot know at which point of the curve diagram we are. One option would be to use thermal sensors that give us an idea of what percentage of the transformation has been completed and what sense we are in (heating or cooling). However, this process seems quite complex since these two curves are not always the same, and they vary, as we have seen, with initial deformation.

The most straightforward alternative would be to ignore this hysteresis and find an equilibrium point once the desired force is reached wherever we are on the curve.

We would act according to the force being carried out at all times by increasing the current if it is not enough or decreasing it if it were excessive.

We will, therefore, need a sensor capable of measuring this force.

7.2.1.3 Control

The system's control was carried out with an Arduino UNO, a closed-loop control that gives feedback from the stretch sensor that provides the tension existing in the SMA-sensor assembly.

Once the tension state of the cables has been measured, the system performance varies. Therefore, the difference between the force required and the measurement is equal to 0, or, at least, close to it.

A PWM value that provides some stabilization in the actuator temperature at room temperature should be sought. It will not be completely accurate because it will be necessary to supply different energy values depending on the desired force and different temperatures reached by the SMA to remain stable in each situation.

In addition, it will depend not only on the needed force but also on other initial factors such as the initial deformation. It will also not be possible to ensure constant factors in each use. The error is defined as:

$$E_{\text{error}} = F_{\text{sensor}} - F_{\text{required}} \quad (7.2)$$

When the force (F_{sensor}) is less than the demand (F_{required}), PWM values lower than stabilization will be necessary. If necessary, it could even correspond to a zero-duty cycle to protect the actuators. On the contrary, when the error is negative, we still have to contribute energy. In both cases, we observe that the necessary duty cycle will not exceed 4%. The PMW values depend on the calculated error, as explained later, so the control is proportional.

To reach a constant force starting from rest, we cannot use a PWM of the order of those used to stabilize because heating the SMA to its transformation temperature would be on the order of minutes. For this reason, initially, the duty cycle will be 67% (this corresponds to a current value of 2 A). The spring will heat up in seconds. Once the desired force has been reached, the duty cycle must be reduced immediately to the mentioned values (less than 4%) to avoid complete austenitic transformation.

It is also possible to reduce the duty cycle before reaching the required force by taking advantage of the thermal inertia of nitinol.

In the beginning, when the value of the PWM is 0, the SMA should enter the warm-up phase. However, the system will always remain at rest until the force to simulate is not indicated.

Once the setup was finished, we read the analog ports (corresponding to the sensors) and calculated the cables' tension. Next, we checked if the last reading from the serial port indicated a non-zero value for the force. If this were null, it returned to the beginning of the loop with the duty cycle equal to zero for both actuators.

In the case of obtaining a correct value other than zero, the SMA will be heated. Once the SMAs reach the operating point, they will be assigned a PWM that stabilizes them. In Figure 7.7, the code flow is shown.

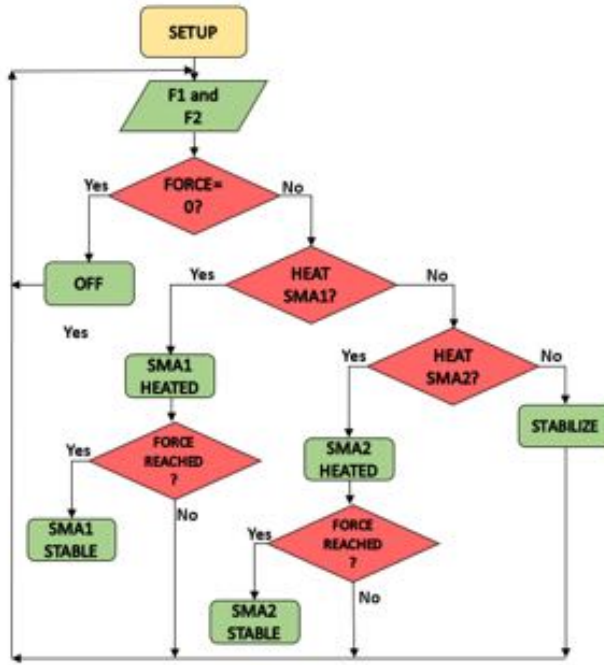


Figure 7.7 Code flow diagram in Arduino.

Several tests had to be carried out to realize this control precisely and achieve a reliable characterization of the nitinol springs and flexible sensors. The setup prepared to collect these data consists of a structure that supports a bar from which a weight of 300 g hangs. It is greater than the 2 N required for each SMA. The SMA weight (3 g) is assumed to be negligible. Under the weight is a scale. Figure 7.8 shows the assembly previously described.

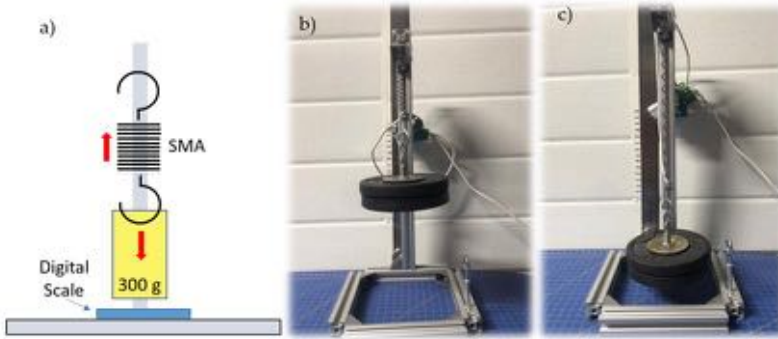


Figure 7.8 General setup for the experimental characterization of the SMA spring. (a) Scheme (b,c) Reality.

The procedure for obtaining the spring tension measurements was as follows:

1. The measure indicated by the scale was noted when there was still no current flowing.
2. The SMA was heated, and it was observed how varies the measurement on the scale until it stabilized
3. The stabilized value was subtracted from the first one noted, and the tension experienced in the spring was obtained.

In the first tests, some parameters that may have conditioned the operation of the Nitinol actuator were varied, such as ambient temperature, initial deformation, or the current that

passed through it. It was observed that there was certain repeatability in the tests if the initial stress and deformation were preserved. If this were not true, for equal values of PWM, the force exerted by the SMA differed significantly. Minor variations in ambient temperature (25–27 °C) seemed not to have had much influence. Therefore, the strength exerted by the SMA depended both on the current that circulated and the initial deformation. It made open-chain control practically impossible and complicated it in a closed chain by introducing this new variable to consider.

Then the elastic sensor was characterized to perform closed-loop control of the SMA. For this, the initial assembly was used by putting the sensor in place of the SMA. Then, with the help of a multimeter, the resistance in the sensor was measured. The data obtained can be seen in Figure 7.9.

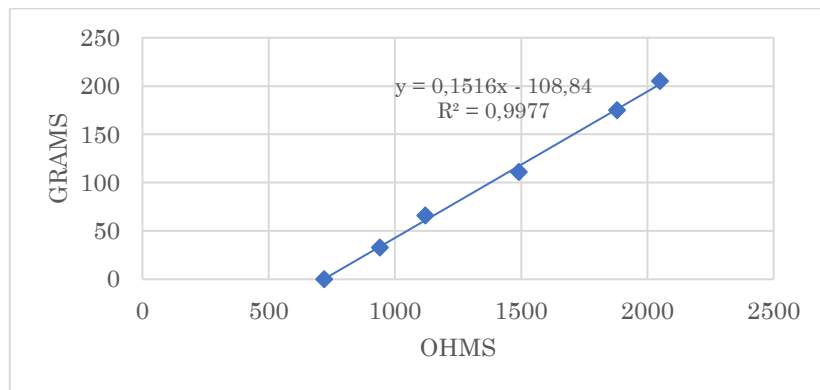


Figure 7.9 Results of the sensor characterization tests for the Resistance–Weight function elaboration with the equation of the line and correlation coefficient.

There was a clear relationship between strength and resistance where the points fit perfectly (correlation coefficient of 0.9977) to a line. The slope of the line was $m = 0.1516$. The ordinate at the origin was equal to $n = -108.84$. The equation that therefore related the voltage in the SMA-Sensor assembly as indicated in Equation (7.3) was

$$T = \frac{0.1516 \left(\frac{V_{in} R_{gauge}}{V_{A0}} - R_{gauge} \right) - 108.84}{9.81} \quad [N] \quad (7.3)$$

Gauge resistors were used to read the sensors to obtain an average of their resistance using a voltage divider and, consequently, determine the relationship between the electrical resistance and the force experienced. Therefore, the tension state of the system was defined.

The regulator designed to adjust the PWM to the requested strength worked on the error between the demanded force and the desired one. It worked in grams, as the unit of measurement of the error, for convenience.

After numerous tests at room temperature (25–27 °C), we concluded that the value 7 of the PWM provided good thermal stability to the system for the range of forces (0–2 N) and the initial deformation of the spring with which it will work.

Therefore, as long as they were within ± 1 g, this was the PWM exerted. If we were between +1 and +2, +2 and +5, or higher than +8, it was 6, 5, and 4, respectively. If we were between -2 and -1, -5 and -2, or -5 and -8, it was 8, 9, and 10, respectively. If it was less than -8, the SMA went directly to the warm-up phase.

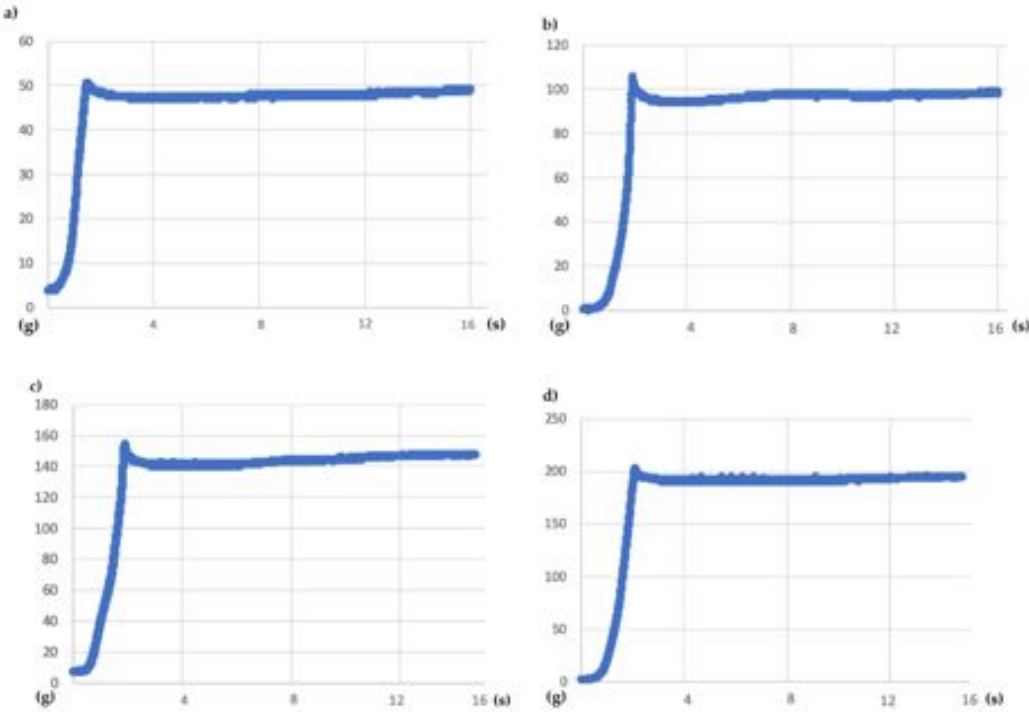


Figure 7.10 Weight vs. time graph for a 15 s test, and a demanded weight of (a) 50 g (b) 100 g (c) 150 g (d) 200 g.

The tests carried out had a duration of 15 s. Therefore, first, forces of 50, 100, 150, and finally 200 g were requested. The results are represented in the following graphs in Figure 7.10.

The existing initial peaks did not exceed 8 g of difference with the requested force, and the falls that followed them were not far from more than 8 g in any case because there would be peaks in the graphs due to entering the heating phase. Then it managed to stabilize at the indicated value. Therefore, we affirmed that it was a pretty precise system, allowing us to exercise reliable, albeit slow, control.

In the glove tests (showed in Figure 7.11 and Figure 7.12), as we did in the previous ones, we tried to obtain weight-time graphs, with the glove already mounted on the arm, to see if they corresponded to those already achieved. Each SMA is represented in a different color to illustrate the operation of both. The first thing that struck us was the delay between them, which corresponded to approximately 2 s. By not being able to heat both together, there was no choice but to accept this behavior.

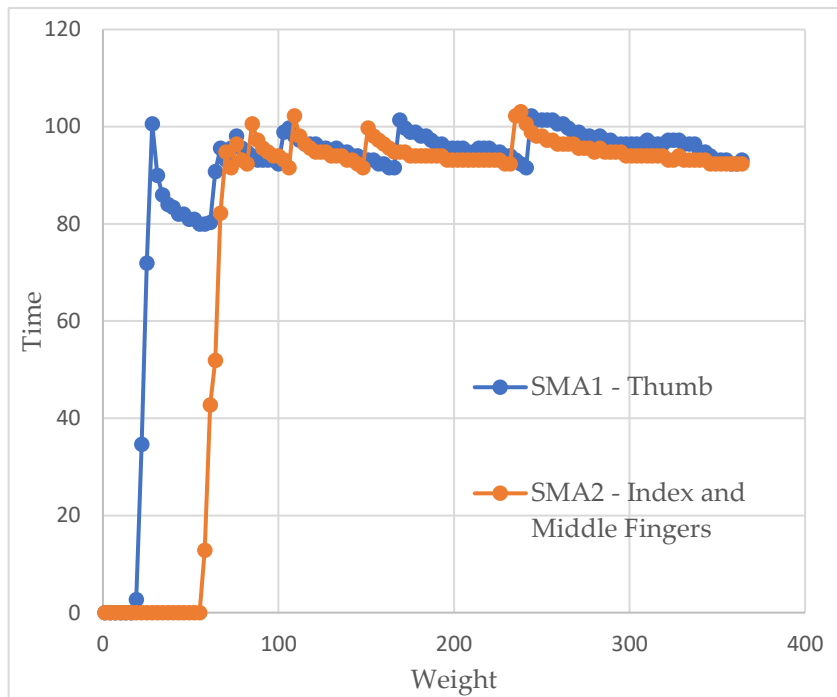


Figure 7.11 Weight vs. time graph for the glove test with a simulated weight of 100 g.

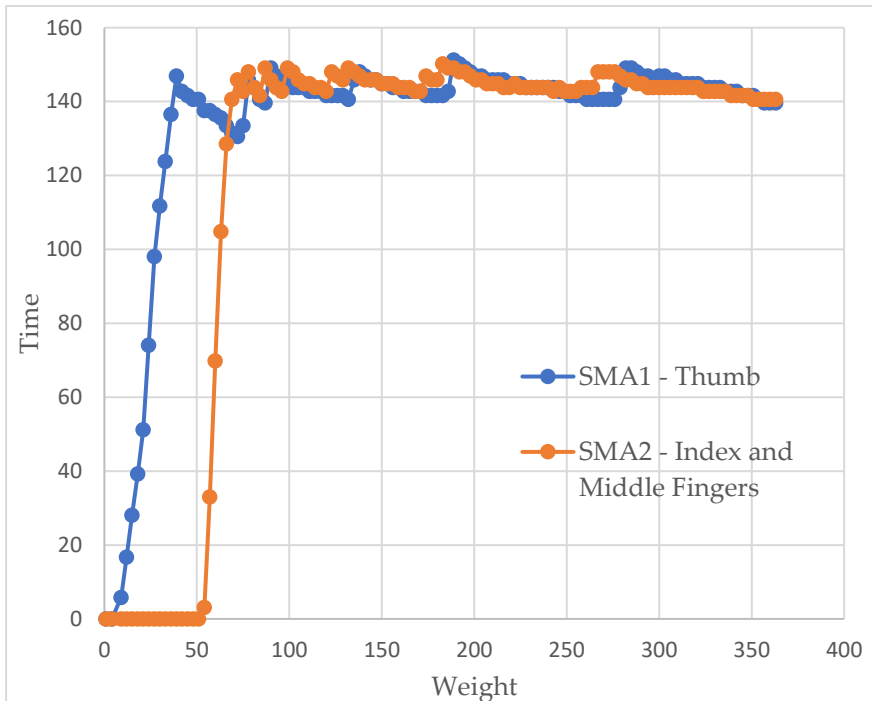


Figure 7.12. Weight vs. time graph for the glove test with a simulated weight of 150 g.

We also see how the force in the first SMA decays as the second begins to heat up since no energy is being supplied. Thus, all of it has to go to the second dock. However, once the latter has warmed up, the former recovers quickly.

As before, we saw how the force tended to stabilize a little below the desired values with slightly higher errors but still lower than 10%. However, a behavior appeared that we did not observe before. These were small peaks of force. The system detected that the springs had to be heated again because the error was in the last available window (8 g). If we looked closely, when one of these warm-ups ended, the other one immediately began.

Factors such as the person's pulse or being faced with a new sensation could have caused strange movements that ended up resulting in a loss of balance point that, finally, led to those peaks. They did not appear before as they were in a completely static system.

7.2.1.4 Tests

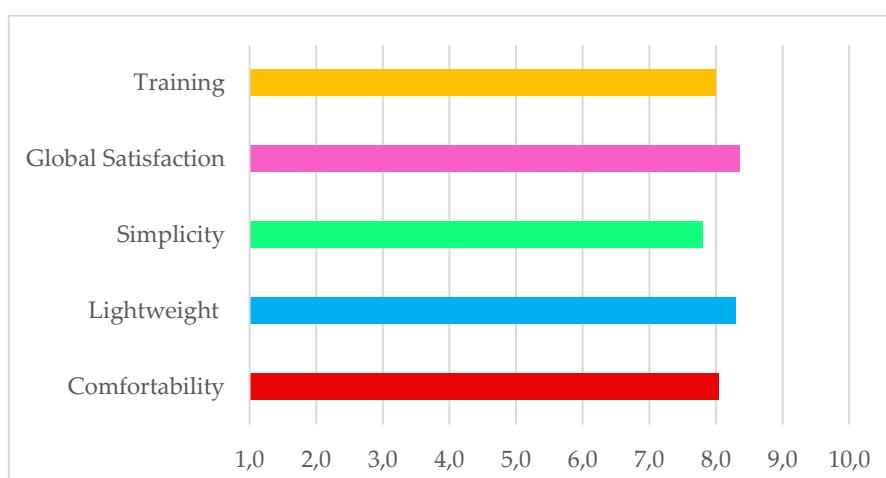
The glove was tested with 15 participants to determine if it could convey a haptic feeling of grip. Volunteers aged between 16 and 56 years (10 females and 5 males) had no previous experience with this type of device. Consequently, training was carried out. Different forces were simulated with the glove, while on the other hand, the participants held an object of the same simulated weight to notice the type of sensations to be experienced.

After the training, they experimented with the forces (in random order) with their eyes closed. The device allowed the simulation of three different forces: 100, 200, and 300 g. They had to determine which one was being simulated at any given moment. Four different types of tests were presented. In each one, the sequence of simulated forces varied. In the first test, they were simulated in increasing order (100–200–300), in the second, decreasing (300–200–100), and in the third and fourth, there was no logical order (200–100–300 and 200–300–100, respectively).

At the end of the tests, the participants answered two blocks of questions. The first questions were general, and the results are presented in Table 7.1. The diagram below Table 7.1 summarizes the results of the questions. It shows the mean between questions about the same topic (for example, between questions 1 and 5) to calculate a single value for the essential characteristics of the glove. The participants assigned a value from 0 to 10 to each question. Zero corresponds to total disagreement with the proposed proposition and, ten corresponds to complete agreement.

Table 7.1 Results of questions about general aspects in a scale of 0 to 10 (where 0 = worst, 10 = best).

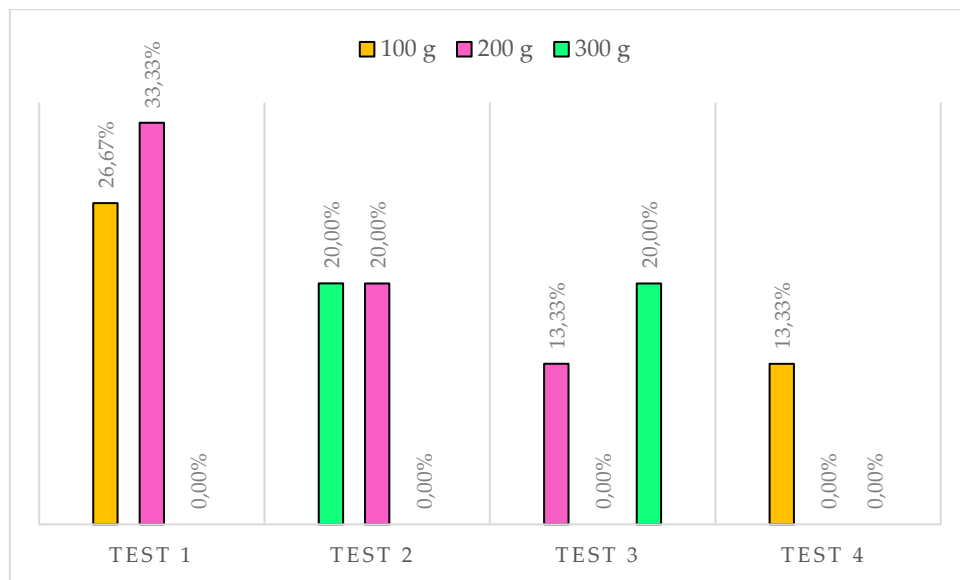
Questions	Avg.	σ
1) I feel comfortable wearing the device	7.3	1.94
2) The device is lightweight	8.3	1.83
3) The device is easy to put on and take off	7.0	1.41
4) The device is easy to use	8.6	1.06
5) The device has not caused me any kind of discomfort (heat, weight, etc.)	8.8	2.08
6) The device performs the function it promises	7.8	1.32
7) I have been able to appreciate the different forces that the device performs clearly	9.0	1.46
8) I am satisfied with the overall experience	8.3	1.23
9) Previous training has been helpful	8.0	1.06
10) Sensitivity has improved with the use of the device	9.5	0.64



In the second block, the answers during the test were annotated. The absolute error is shown in Table 7.2. The diagram below Table 7.2 graphically describes the results of the tests. Each color corresponds to a specific weight, and the percentage of errors is shown.

Table 7.2 Results of tests.

Test	Simulation Order (g)	Error	Avg. Error
Test 1	100	26,67%	20%
	200	33,33%	
	300	0,00%	
Test 2	300	20,00%	13,33%
	200	20,00 %	
	100	0,00%	
Test 3	200	13,33%	11,11%
	100	0,00%	
	300	20,00%	
Test 4	200	13,33%	4,44%
	300	0,00%	
	100	0,00%	



The percentage of success in the tests was 83.7%. It would improve considerably if more tests were carried out since, as we saw, results improve markedly with use, going from an error of 20% in the first test to 4.44% in the last. Most mistakes were made by confusing the force of 200 with that of 300. Specifically, the simulation of 300 g had correctness of 86.7% and that of 200, 73.3%. Many of these errors ended up being recognized by the participants.

This result was satisfactory since it was not easy to distinguish two forces of this type even with objects if they were not taken consecutively. The percentage of success with 100 g amounted to 91.1%. It was an expected result: the relative jump from 100 to 200 was 100%, and the one between 200 and 300, 50%. In addition, the participants perfectly distinguished between a minimum level of action (100 g) and no actuation.

Considering the questions asked, we concluded that the level of satisfaction was high, especially in questions regarding the development of the tests. Comfort was the second most penalized factor in voting. Because the participants had short forearms, the bracelet had to be placed above the elbow for some tests because, as we said before, there had to be a

minimum length in the spring–sensor assembly to ensure correct operation. It created some discomfort.

7.2.1.5 Conclusions

The soft haptic glove presented allows simulating small forces. The SMA springs were used as actuators because of their excellent power-to-weight ratio. In addition, the device is soft, lightweight, and easy to put on.

The glove allowed the simulation of three different forces (100, 200, and 300 g) and generated the sensation of holding an object in the user. To re-feed the glove, elastic sensors were used. Thus, they had a double function: on the one hand, they helped the springs recover in the cooling phase, and on the other, they provided us with information about the force being exerted. In addition, several experiments were carried out to characterize the springs used in the prototype to carry out correct control of them.

Tests with real users were carried out to validate the device. In the first phase, users with the glove on experienced different forces in causal order. People guessed the force they were experiencing with an initial precision of 80% and a final 95.56%. It showed that after a few uses, people recognized without problems the sensation they were experiencing. Users were also asked about their experience with the glove to determine the level of comfort. The answers showed a high level of satisfaction with the device and an overall good experience.

In conclusion, the SMA springs combined with elastic sensors allowed more precise control of this type of actuator. Nevertheless, the device needs some improvement in the design. For example, adding a cooling system to speed up the cooling process will allow users to grip different objects faster. Another interesting future work would be to develop an application with virtual reality.

7.2.2 Tactile, haptic gloves

After the promising results of the first haptic prototypes, the next aim was to test SMA actuators for tactile, haptic devices. So, two soft haptic tactile gloves that give feedback in the fingertips and palm have been developed. The glove's design is relatively minimal to leave the hand relatively free and facilitate their wearing as much as possible and proportionate a more natural experience. It is also important to remember that it was developed with a rehabilitation purpose; therefore, patients possibly do not have enough muscular tone or present muscular stiffness, so a lightweight and easy-to-wear device is essential.

As explained in state-of-the-art, three techniques exist to provide tactile feedback 1) vibrations, 2) normal indentation, and 3) lateral stretching. In our study, we have realized two of them, the first through small vibration motors and the second through a tendon-driven system actuated by SMA springs that generate pressure on the fingertip.

From a medical point of view, four main mechanoreceptors provide information to the central nervous system about touch, pressure, vibration, and cutaneous tension: Meissner's corpuscles (rapidly-adapting, respond to low-frequency vibrations and fine touch), Pacinian corpuscles (rapidly-adapting, respond to deep pressure and high-frequency vibration), Merkel's disks (slow-adapting, respond to light touch), and Ruffini's corpuscles (slow adapting, respond to skin stretch). [447] In our case, the first three types are stimulated by the glove.

7.2.2.1 Design

The glove comprises three parts: the fingertips, the palm, and an armband. All the components are 3D printed with PLA and independent of each other. Two types of fingertips have been developed: one uses vibration motors, and the others a tendon-driven system actuated by SMA springs. So, the name that will be used when referring to the first prototype will be the vibrotactile glove, while for the second, it will be the SMA-tactile glove.

The three parts of the vibrotactile glove are shown in Figure 7.13: each thimble (Figure 7.14) houses a small vibratory motor, while a small elastic band allows it to adapt to different hands. The palm houses five motors. The selection of these motors' positions is based on previous works and medical papers that show the hand's zones with more tactile receptors. [448,449] It also presents the elastics band.

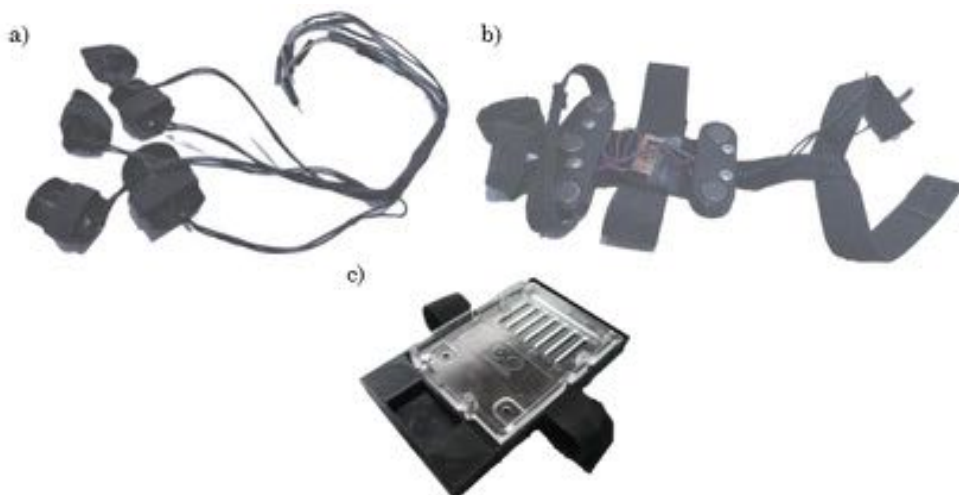


Figure 7.13 The three parts of the vibrotactile glove: (a) thimbles, (b) palm, and (c) armband

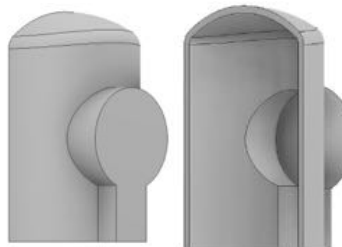


Figure 7.14 Thimble design.

The armband houses the Arduino and the electric circuit. An adjustable stiff webbing with a plastic buckle secures it to the arm. The final version of the vibrotactile glove is shown in Figure 7.15.

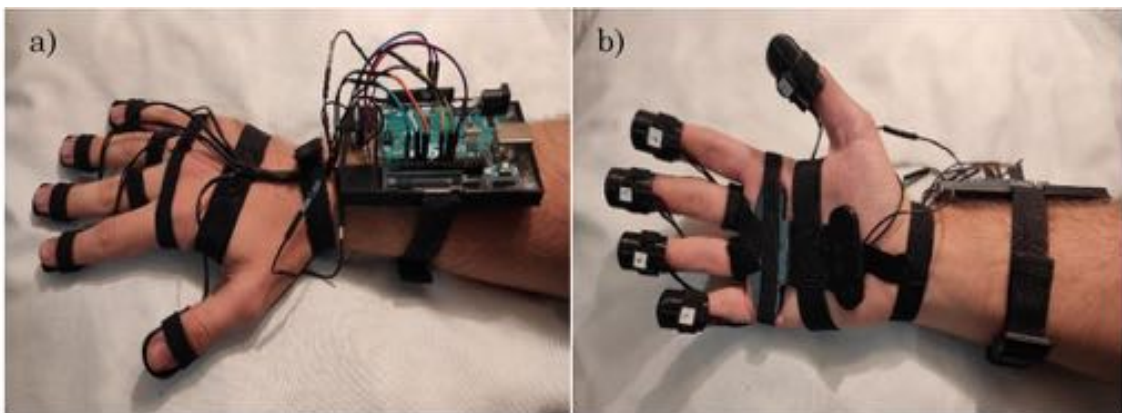


Figure 7.15 Final version of the vibrotactile glove (a) dorsal view and (b) palm view

The circuit is primary. The ten motors (five for fingertips and five for the palm) operate with an input voltage of 3V. Each of the fingertip's motors is associated directly with a PWM pin to set the vibration value for each user. The remaining five motors in the palm have been paralleled to control them with a single PWM. It has been considered that each finger can be used independently, while the palm is all interested when patients grasp an object. However, the Arduino does not have enough power to drive five motors parallel as they are limited in voltage and current. Therefore, to solve this problem, it was decided to make a switching circuit. The MOSFET chosen for this application has been the N-channel IRF530N. The circuit is outlined in Figure 7.16.

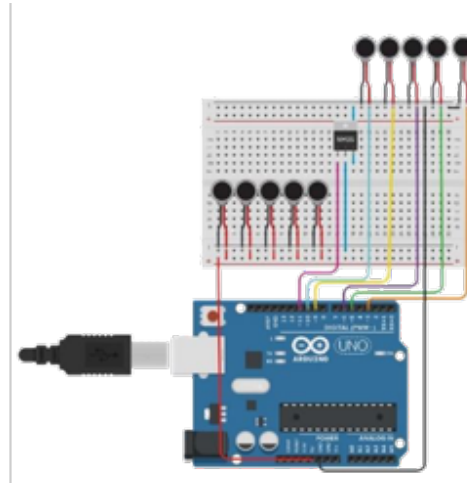


Figure 7.16 Vibrotactile glove electric circuits.

The SMA-haptic glove presents a more complex structure.

The initial concept was to wrap SMA threads around the fingertips as proposed in [426]. When threads are heated and contract, they touch the skin and provide a haptic perception. The SMA chosen was a 100 µm diameter Flexinol wire from the manufacturer Dynalloy. However, the first tests showed that the cable burned the user, making it impossible to continue with this design. On the other, the contraction was minimal and barely perceptible.

So, the design was changed. First of all, SMA was moved away from the fingers to avoid temperature problems. Therefore, the alternative proposed consists of thimbles with mobile platforms. Ropes would be attached to these mobile platforms, which in turn would be attached to SMA springs. The strings would pull these platforms up and into contact with the fingertips by contracting the springs, thus simulating touch sensation.

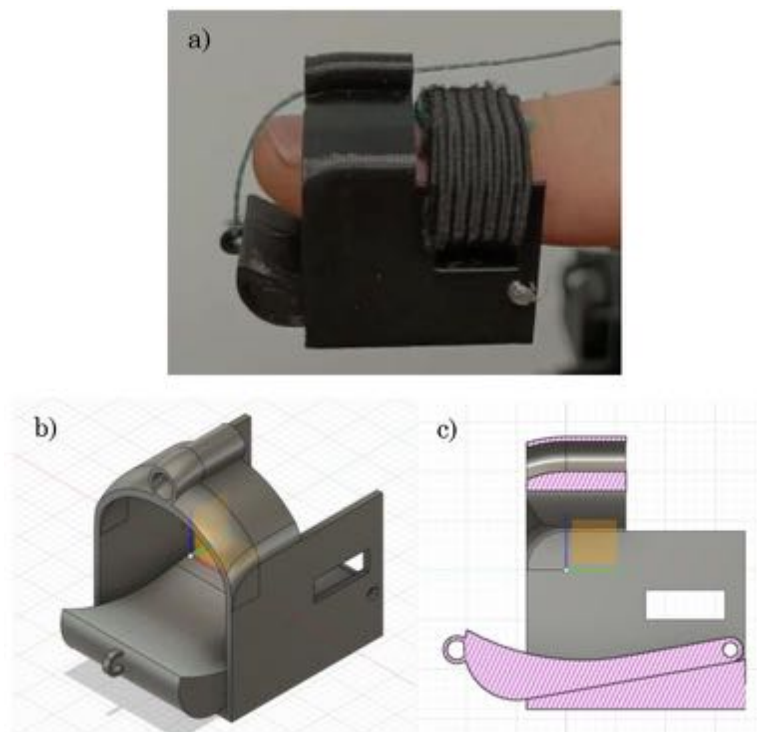


Figure 7.17 The thimble (a) The final version worn by a user (b) Cad model (c) Section view

The conduit to guide the string was placed on top of the finger. Elastic bands allow the wrapping of the finger, making the thimble adaptable for everyone. The mobile platform presents a curved shape to adapt better to the shape of the finger and touch the whole fingertip when lifting. The resulting thimble is shown in Figure 7.17.

A conventional work glove and plastic tubes were glued to guide the rope up to the SMA springs. Then all the thimble strings were joined in a metal hook at the wrist.

SMA springs are placed in an armband on the forearm. In this case, two SMA springs in series have been used to actuate the five thimbles. One SMA is the effective actuator, while the other works as a bias spring that forces the actuator to return to the rest position. A small fan accelerates the operation, cooling the actuator simultaneously the bias spring stretch it. The fan works with a supply voltage of 12V and a current of 0.1 A. One end of the SMA spring actuator is anchored to this structure, while the other is connected to the end of the bias spring through a mobile anchor. The other end of the bias spring is then connected to the thimbles threads. The actuation unit is shown in Figure 7.18. Results with

this assembly were satisfactory, giving a reasonably quick response both in the contraction and cooling phases.

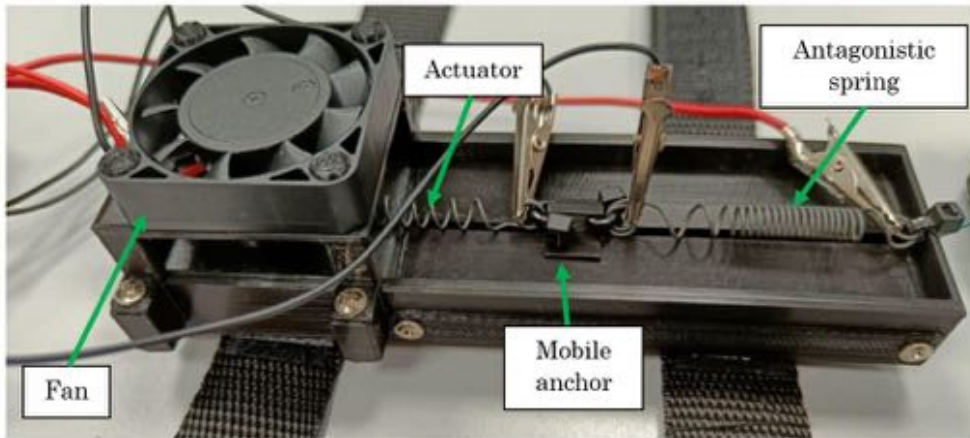


Figure 7.18 Actuation unit.

The SMA springs are the same as those used in the previous haptic glove in Section 7.2.1. The circuit (Figure 7.19) also was the same; the only difference was the addition of the fan, also controlled with a Mosfet.

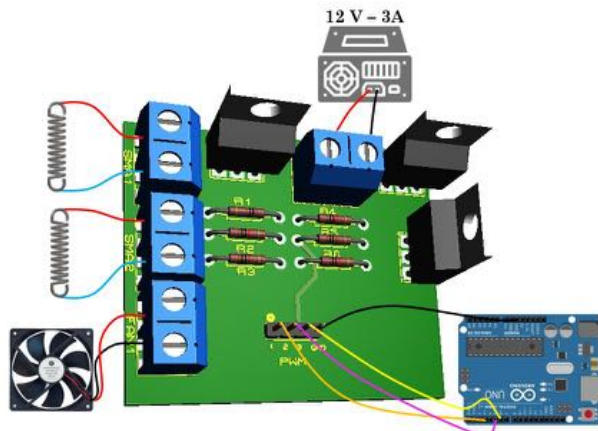


Figure 7.19 Electric circuit.

The final design is shown in Figure 7.20.

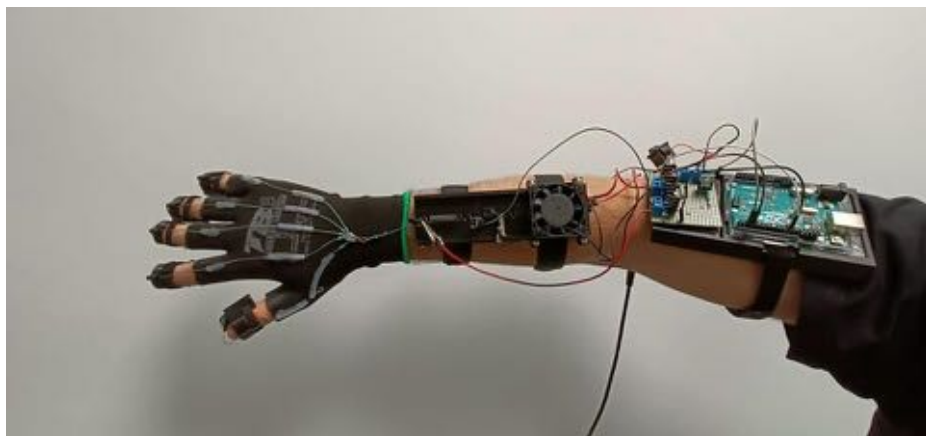


Figure 7.20 Final design of the SMA haptic glove.

7.2.2.2 Control

Controlling the vibrotactile glove is very simple. Through the Arduino serial port, the program allows to send two values by keyboard: the first is the value corresponding to the finger motors, and the second is the value corresponding to palm motors. Another program allows the fingers to be turned on and off separately.

Controlling the SMA-haptic glove is somewhat more complex since it is necessary to regulate the activation and deactivation of the SMA springs and the fan.

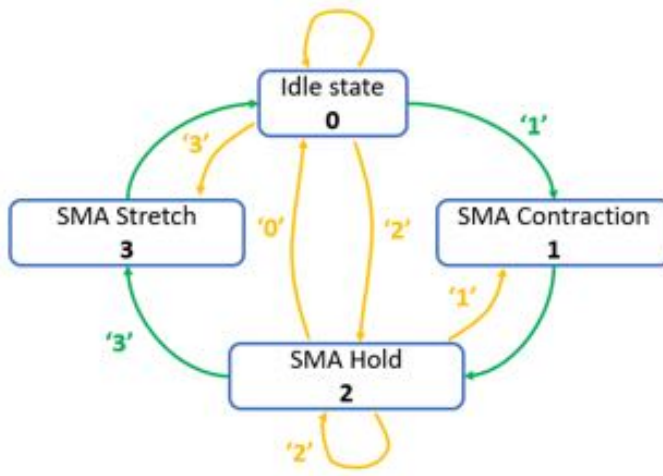


Figure 7.21 State diagram of SMA-haptic glove control.

The state diagram is shown in Figure 7.21. Green arrows reflect the normal flow of the program. On the other side, yellow arrows show other alternative routes. Within the states, there were the following functions:

- **SMA contraction(pin)**. This function receives as an argument the pin to which the signal is to be sent, the SMA actuator SMA pin, or the antagonistic SMA pin. A variable PWM signal is sent to perform the contraction. PWM values were chosen based on experimental tests, choosing the values that allow the fastest spring contraction but without giving an excessive current. Thus, a PWM is sent initially 100% for 5 seconds, then 80% for 4 seconds, and finally 50% for 4 seconds.
- **SMA hold ()**: This function sends an intermittent PWM signal to the pin connected to the SMA actuator. A 10% signal is sent for one second and then deactivated for another second. Thus the SMA actuator keeps warm once it has fully contracted.
- **SMA stretch ()**: This function houses the SMA contraction () function described above to contract the antagonistic SMA and thus stretch the SMA actuator. At the same time, it activates the fan signal.

In idle state (0), all signals are deactivated. In status 1, the collapse () function is associated with the SMA actuator pin. When this contraction ceases, it automatically goes to state 2, in which the SMA hold () function preserves the contracted conventional SMA. In status 3, the SMA stretch () function is encountered. When this process ceases, it automatically goes to idle state 0. The orders are sent through the Arduino serial port, so the corresponding state's number passes that state. Practically, a '1' is sent to give touch sensation, and a '3' is sent to stop this sensation.

A series of experiments will be carried out to evaluate the prototypes and compare them. They will be analyzed in Section 7.4.

7.3 Exoskeletons

The work on exoskeletons involved the development of two different types of devices. The first one presents a four-bar linkage structure for each finger, while the second is a glove actuated with tendons. The two solutions present similarities (actuators and sensors), but the designs are quite different, being in the second case more comfortable and easier to put on for patients.

7.3.1 Superficial Electromyography Sensors

Superficial electromyography (sEMG) is a non-invasive detection method used to measure myoelectric activity, the muscle response, or electrical activity in response to a nerve's stimulation of the muscle.

The electrical signals that are responsible for the contraction of the muscles to realize the different movements of our body (open or close the hand, lifting the arm, or moving fingers) are produced in the motor unit. The motor unit comprises a nerve cell, a branch called the axon, and a series of innervated fibers. This unit generates muscle contraction, reaching a 57% displacement concerning its relaxed position [450]. When the brain or spinal cord generates the movement signal, a movement of ions is generated, creating a potential difference between the outer and inner membranes of the muscle fibers. When these muscle fibers are activated, the EMG signal is generated.

The amplitude of this signal depends on the adipose tissue between the sensor and the fiber because the tissue behaves like a low-pass filter that attenuates high-frequency signals [451]. Thus, variations in the signal could appear depending on the placement of the sensor and depending on the user. Some muscle groups will contain more or less adipose tissue between the sensor and the muscle.

The non-invasive detection method uses three different surface electrodes attached to the skin. Two electrodes are placed along with the muscle from which the electromyographic signal has to be obtained. The third electrode serves as a reference and is located in a remote part without contact with the muscle. In this way, the potential difference between the two electrodes concerning the reference is measured, thus obtaining the signal. This electrode configuration is called a bipolar configuration.

By reading the muscular biopotential, it is possible to monitor the contraction of the muscle fibers, which makes this a valuable signal to control the hand exoskeleton. The EMG sensors can be positioned in different body parts, and different muscular signals can be withdrawn. Later, from the analysis of the sEMG signal, it is possible to estimate the forces exerted by the specific muscles.

In the case of a hand exoskeleton, the muscles that control the fingers' movements are located in the forearm. In particular, the muscular fascicles responsible for the finger flexure are located in the internal (palmar) side of the forearm, and the muscular fascicles responsible for the finger extension are located in the external (dorsal) side (see Figure 7.22). Since the exoskeletons studied are focused on the rehabilitation of the finger extension, only the muscle fascicles located on the dorsal side of the forearm are to be sensed.

Figure 7.23 shows the correct placement for the electrodes in the forearm. The sensor should be placed on the belly of the muscle. Furthermore, it must be correctly aligned with the muscle fiber to achieve an adequate signal possible.

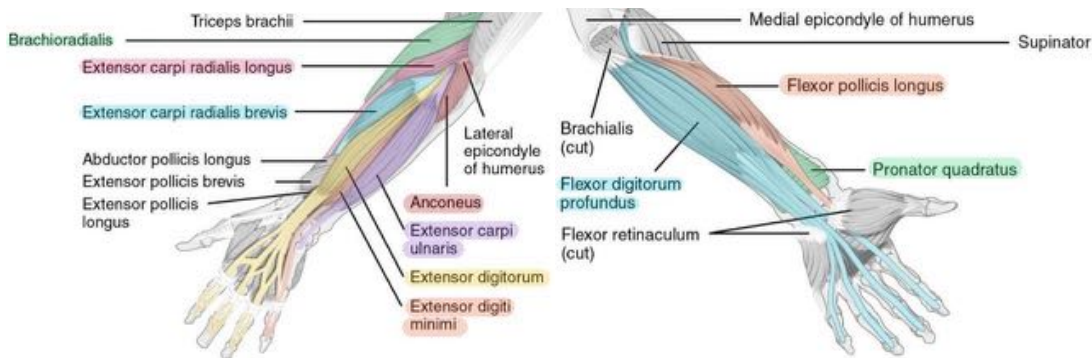


Figure 7.22 Scheme of the different muscles in the forearm.

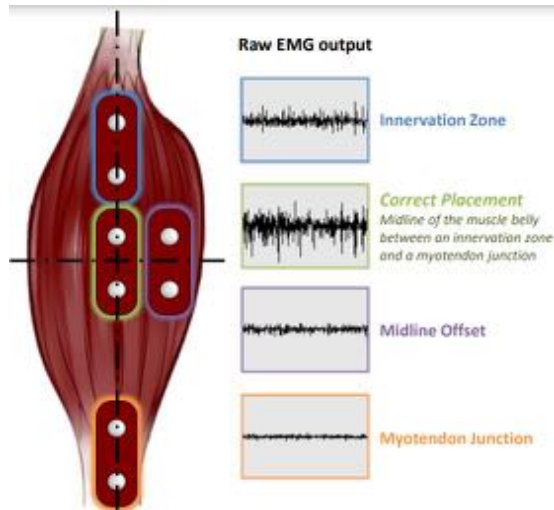


Figure 7.23 Correct placement of electrodes [450]

When the sensor placement is incorrect, the signal's intensity and quality are much lower than when the placement is correct. It is because a measurement taken in the central part of the muscle involves a greater number of motor units of the muscle. Another factor associated with the loss of signal quality is interference produced by crosstalk.

The electromyograph sensors selected utilize three sensors in order to measure two electric potential differences. In particular, two electrodes are positioned on the extensor muscle fascicle to sense the muscular biopotential. The third electrode is positioned as a reference for the EMG signal in a neutral, bony position where no specific muscular biopotentials exist, such as the elbow or the wrist.

The reference electrode is necessary because the superficial EMG collects the muscular signal on the skin above the muscular fascicles under exam, so the background muscular activity is also sensed. It also eliminates the common muscular electrical noise from the signal collected by the sensing electrodes.

The EMG signal withdrawn by the electrodes needs to be processed and analyzed. The sensor electronic filters and conditions the signal, removing the noise and amplifying the output according to the requirements.

After processing, the biopotential signals of the sensed muscle are translated into an output voltage, typically represented graphically as [mV] vs. time [sec].

The output signal depends on the filter and conditioning chain, and so it depends on the sensor board used; in this case, the output signal is a digital signal which ranges between 0 to 1023.

The EMG sensors used are the two versions of the same sensor Figure 7.24. The second is more compact and lightweight. There are no cables or batteries to connect. It is directly put on the arm.

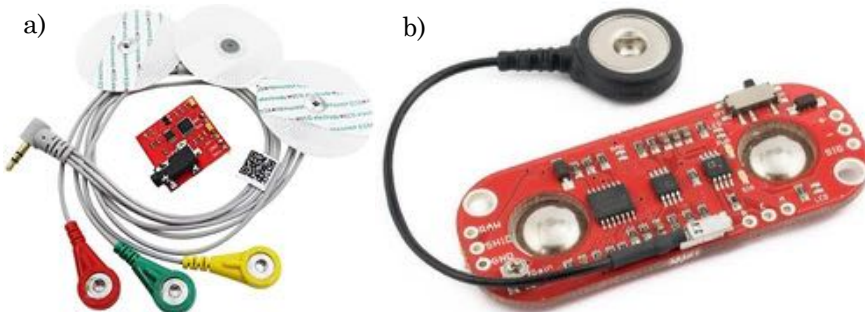


Figure 7.24 EMG sensors (a) the one used in the first exoskeleton and (b) the Myoware sensor used in the second prototype

Since most stroke patients have unilateral impaired muscular activity, the EMG sensor cannot be placed in the injured arm. Thus, the EMG signal can be sensed from the healthy arm: the exoskeleton replicates the movement of the healthy hand on the injured hand, thus working in a mirror way. This control method is the so-called self-motion control.

The signal obtained from the healthy hand is sent to the Arduino board and used to control the device. Actuators will be activated or deactivated to perform the movement that the user is requesting. Ultimately, the result is a master-slave system in which the healthy hand can control the damaged hand through the glove.

7.3.2 First exoskeleton prototype

The exoskeleton structure is a two 4-bar linkage structure and is tendon-driven by cables. The tendon-driven transmission is considered to work with displaced actuators, so the SMA unit is located on the dorsal side of the hand. The exoskeleton is underactuated, the two considered joints of each finger are coupled, and a single SMA unit moves the whole structure. The 4-bar mechanism has the advantage of being compatible with fingers of different lengths. Due to the reduced complexity of the SMA springs actuator, the device is compact and lightweight.

The exoskeleton has the same structure for each finger, and the SMA springs actuators are connected to the cable to actuate the two fingers together through a pulley system. The exoskeleton's aim is to the extended fingers. When the extended position is reached and the actuator is no longer active, the patients can flex the fingers and return to the original position with the hand closed. The patients must autonomously do this movement.

The starting point of hand exoskeleton design is hand anatomy comprehension. The human hand comprises 19 bones, 14 joints, and more than 20 degrees of freedom DOFs [452]. Index, middle, ring, and little fingers are composed of four phalanges. The thumb, instead, is composed of three phalanges, as shown in Figure 7.25.

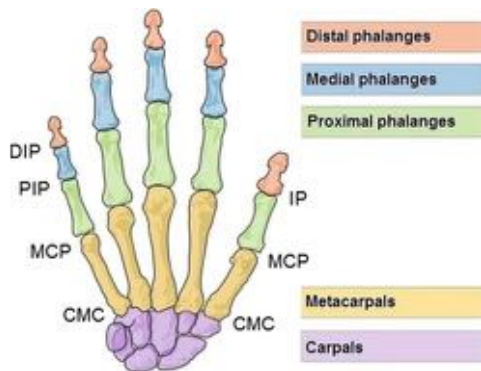


Figure 7.25 Hand structure and joints [435]

The MCP joints of the four fingers can be modeled by two DOFs joints each, allowing both flexion-extension and adduction-abduction motions (Figure 7.26). The same motions of flexion-extension and adduction-abduction are guaranteed for the CMC articulation of the thumb.

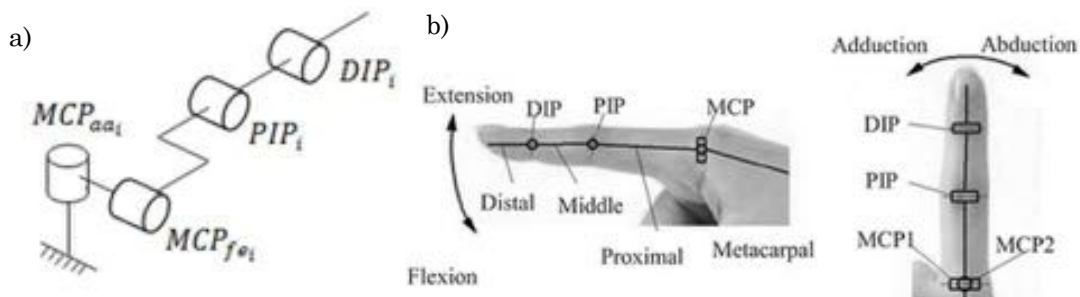


Figure 7.26 (a) Finger kinematics [453] (b) Physiological structure of finger [454]

Thus, each finger can be considered as a set of links connected by joints.

The second step consisted of looking for a normalized length of finger phalanges and the articulation static constraints which define the functional hand range of motion (ROM). ROMs are defined as the angular range to perform 90% of the hand activities. Articulation ROM can be considered a limitation of free movements. The following studies have been considered [455–457]

So, in the designed system, the first 4-bar linkage structure drives the MCP joint, while the second 4-bar linkage moves the PIP joint. The actuation of the DIP joint is not considered to reduce the complexity.

The mechanism is called 4-bar because of two external linkages R1 and R2, and two virtual linkages that connect the MCP joint with the rotational point on the fixed structures. The first virtual linkage of the first 4-bar mechanism, called P1 in the figure below, goes from the rotational point of the support S1, on the dorsal side of the hand, to the MCP joint. The second virtual linkage, P2, connects the MCP joint with the support S2 fixed on the first phalanx (see Figure 7.27). The same mechanism characterizes the second 4-bar linkage structure, and it works for the PIP joint in the same way as the previous structure worked for the MCP joint. The names of this second mechanism linkages are the same as the firsts but with lower case letters.

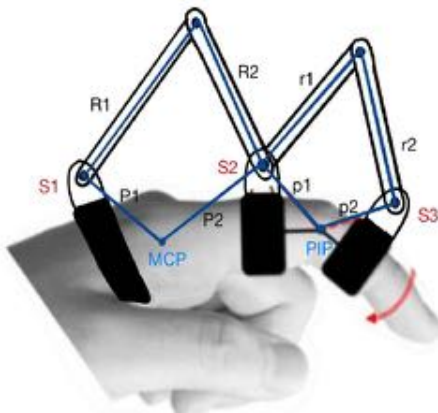


Figure 7.27 The four-bar linkage structure

The exoskeleton structure built involves two fingers: the index and middle finger.

Since stroke causes a continuous contraction of the hand muscles, that is acts as a resistance to the finger extension. To evaluate the design, these forces values $F_{prox}=10\text{ N}$, $F_{middle}=6\text{ N}$, $F_{dist}=3\text{ N}$ are applied to the center of mass of each phalanx respectively [458]. It is important to remember that the device wants to help and assist patients with the finger extension starting from the flexed position.

Dynamical simulations have been realized to verify actuators' force with different lengths of the linkage bars and minimize the required actuation force by selecting the optimal lengths of the exoskeleton links.

Simulations have been realized for the two fingers separately in Autodesk Inventor with a simplified model. A hand model is introduced to correctly simulate the interaction between the exoskeleton and the hand itself. In the simulation, the stroke rigidity on the MCP and PIP joints is considered opposing torques applied on the finger joints. The exoskeleton forces are inserted in the model as external forces applied to the exoskeleton structure.

The hand model dimensions are based on the previously cited studies.

The usage of rotational joints constrains the phalanges since PIP and DIP joints only allow flexion and extension. Spherical joints connect the hand-base and the first phalanx of the fingers because the MCP also admits abduction and adduction, and the spherical joint is necessary to carry out the simulations correctly.

The resistive force acting on the articulation joints due to stroke muscular rigidity is applied as an internal joint moment, with the direction opposing the extension of the finger.

The torques acting at each joint can be computed knowing the phalanges lengths and the force values due to stroke, which causes a muscular rigidity of the finger [458]. The values used in the simulations are reported in the following Table 7.3.

Table 7.3 Simulation values

	Index			Middle		
	Proximal	Middle	Distal	Proximal	Middle	Distal
Diameter [mm]	18	14	14	18	14	14
Phalanges Length [mm]	45	22.4	22.2	51	25.5	23.4
Forces at center of mass [N]	10	6	3	10	6	3
Resulting torques [Nm]	0.225	0.067	0.033	0.255	0.077	0.035

The forces imposed by the exoskeleton transmission cable on the exoskeleton are included in the simulations as external forces of the same value applied directly on the structure

supports. The forces directions are chosen according to the direction of the cable that runs over the pulleys.



Figure 7.28 Dynamical simulation of the index finger

The black arrows in Figure 7.28 represent the forces applied as external forces by the exoskeleton on the hand; the three values are kept equal to each other in every simulation. On the joints are applied the internal torques.

Different dispositions are simulated. By changing the linkage dimensions, the index articulation follows different motion trends. As a result of this analysis, it was possible to verify that, with the lengths of the linkages in [454], forces of about 5-7 N are sufficient to move the exoskeleton as requested and bring the fingers to a fully extended position.

Once the forces are set, the linkage relations are evaluated, changing the lengths of the single linkages one by one, thus modifying the ratios of the lengths. In conclusion, the linkage lengths are selected, and the measures of the two 4-bar linkage structures are reported in the following table (Table 7.4).

Table 7.4 Dimensions of index finger bars

4-bar linkage 1	Lengths [mm]	4-bar linkage 2	Lengths [mm]
R1	45.0	R1	35.0
R2	30.0	R2	30.0
P1	21.9	P1	19.1
P2	21.3	P2	24.7

With these final linkage lengths, the last simulation is done to verify the needed actuation force. As a result, the value of 5 N turns out to be sufficient to move the whole structure correctly.

Afterward, the middle finger is considered. The same simulation was realized using the values of the middle finger presented in Table 7.3.

The results in terms of lengths relations between linkages obtained in this case are presented in the following table (Table 7.5).

Table 7.5 Dimensions of middle finger bars

4-bar linkage 1	Lengths [mm]	4-bar linkage 2	Lengths [mm]
R1	50.0	R1	40.0
R2	35.0	R2	35.0
P1	22.7	P1	19.2
P2	21.9	P2	25.8

Also, in this case, the value of 5 N turns out to be sufficient to move the whole structure correctly. Therefore, the force of the actuator shall be 5N per finger, for a total of 10 N.

In addition, the simulation model has been used to perform some additional verifications. So, for example, it is verified that results are still coherent even if the structure is displaced by some millimeters. Thus, fixing the mechanical structure on the patient hand cannot be highly precise. It has also been verified that if the lengths of the phalanges change some millimeters, the simulation slope follows the same trend. Therefore, the exoskeleton can be worn by patients with different hand sizes.

The final prototype has been realized of aluminum and 3D printed PEGT parts.

The first support, called S1 and shown in Figure 7.29, is the element fixed on the dorsal side of the hand-base and is used as a reference for the movements of the other parts.



Figure 7.29 Support element S1

The two couples of rounded supports present a central hole that is the center of rotation of the first external links of the 4-bar mechanism, both for the index and middle finger.

On the other side, some holes are the anchored point for SMA springs.

The dimensions of support S1 allow the complete extension of the SMA springs.

The supports S2 and S3 (Figure 7.30) are four supports fixed on the first and second phalanx, respectively, of the index and middle finger. A hole is present on the top of the structure to connect the 4-bar linkage mechanism. A rectangular slot is present on the lower side to let a Velcro strap through to fix the structural element to the patient finger. The lower part is made with a cylindrical shape to fit the fingers. The supports S3 also presents two additional holes to anchor the tendons.

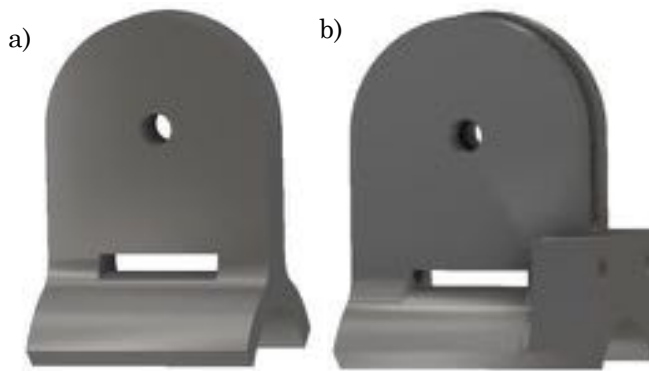


Figure 7.30 The supports (a) S2 and (b) S3

A single tendon (Figure 7.31) actuates both fingers since a single actuator is used. The cable begins in index finger S3, passes through the SMA actuator, and ends in middle finger S3. The actuator is equipped with a hook connected to a pulley to redistribute the cable forces when actuated. The cable is made of nylon since it is flexible to wrap around the pulleys, and it can slide with no significant friction.

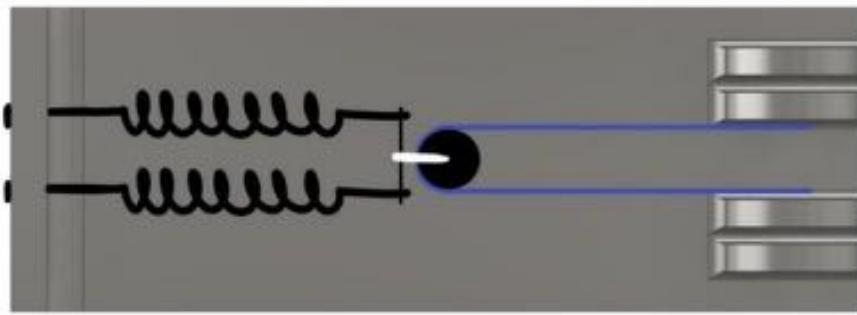


Figure 7.31 The tendon connection scheme

The final prototype is shown in Figure 7.32.

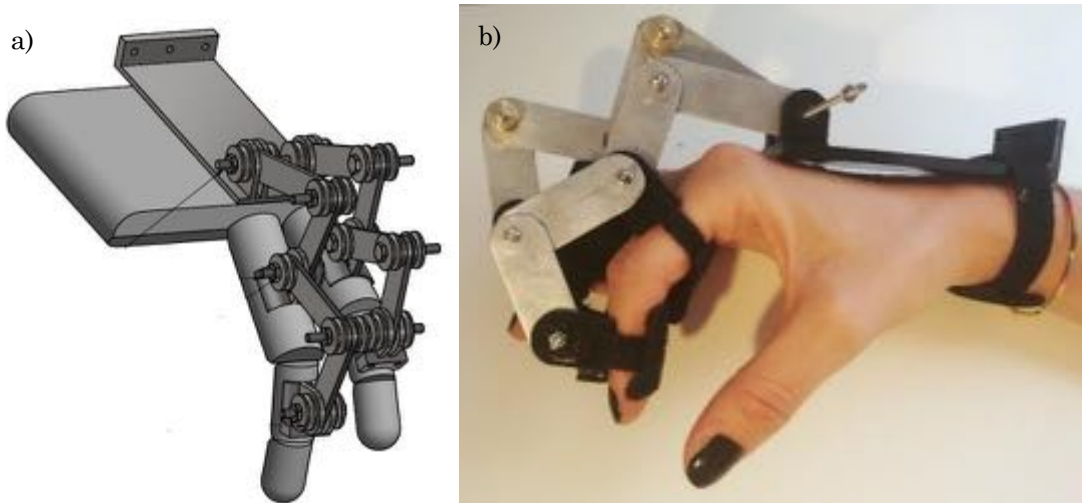


Figure 7.32 The final prototype (a) CAD model (b) the building model

The electronic system is composed of the microcontroller Arduino, the EMG sensor, and the same MOSFET circuit that integrates the SMA springs as a resistive load seen in the previous section. Also, the springs are the same type used in the haptic gloves.

It was possible to verify that each spring can generate approximately 5 N with deformation of around 25 mm through similar experiments carried out previously. Since to operate the exoskeleton, 10 N with a spring deformation of about 20 mm are required, two SMA springs are needed to actuate the two fingers properly (Figure 7.33).

The two SMA springs are placed paralleled under the mechanical point of view to generate a force up to 10 N and a contraction of about 20 mm. From the electrical point of view, the two springs are arranged in series to flow the same current in both springs.

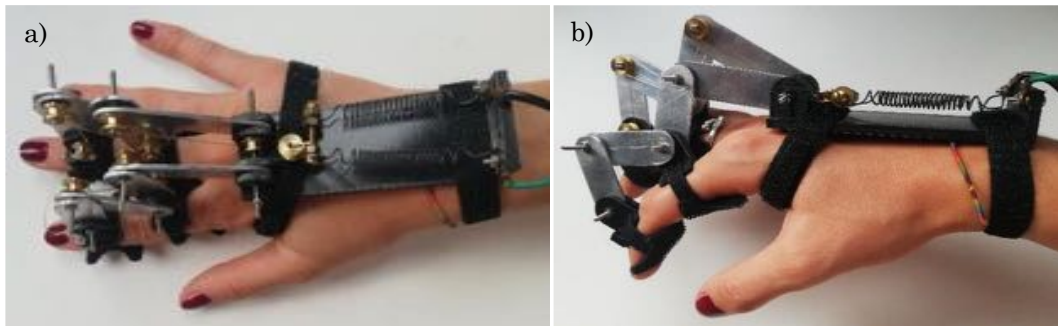


Figure 7.33 The final prototypes with the SMA springs connected (a) top view (b) lateral view

The exoskeleton is worn on a right hand and is actuated to verify its correct behavior (the set-up is reported in Figure 7.34). A PWM with an ON-time of 155 is applied to drive the actuation. The SMA springs heat up during the operation, and the exoskeleton extends the index and middle fingers.

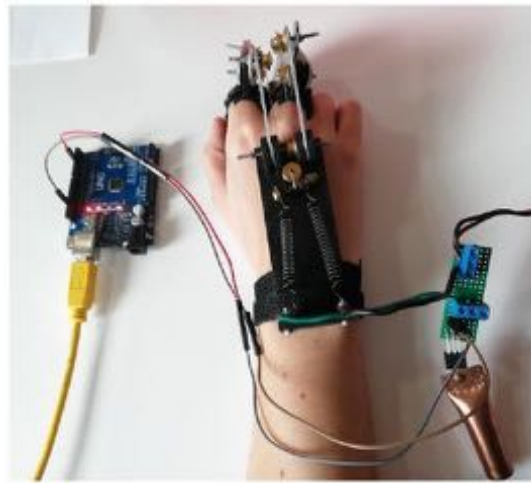


Figure 7.34 Integration set-up of the mechanical structure, actuators, and electronic circuit

The self-motion control and electromyographic sensor (EMG) are used to sense the patient's intention and drive the hand exoskeleton's actuation.

The activity of the extensor muscles is sensed as an electric signal which the EMG detects, and when the movement is sensed, the control algorithm implemented on the Arduino board evaluates the signal received and drives the actuation. The control algorithm is based on a threshold control which activates the extension of the patient's fingers of the injured hand when the patient activates the mirrored extensor muscles on the healthy forearm.

The mode of operation has been tested on a healthy volunteer to visualize the output range of the signal and verify the difference in range between the activation and rest muscle conditions. The three electrodes are positioned on the volunteer forearm and connected to the sensor board connected to the Arduino and the external power supplies. The set-up is shown in Figure 7.35.

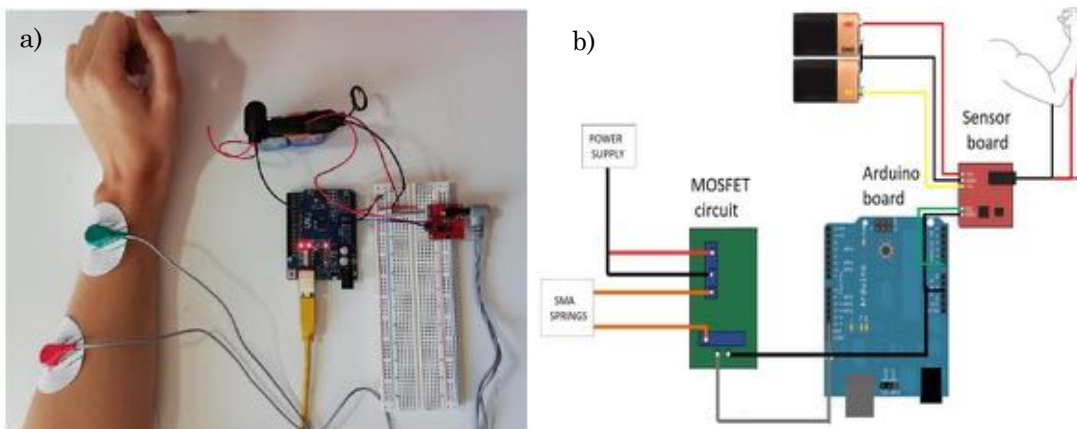


Figure 7.35 (a) EMG sensor placed on forearm volunteer **(b)** the electrical scheme

The volunteer is asked to activate the extensor muscles, the EMG signal is withdrawn, and the output range of the sEMG signal is visualized on the Arduino. Different signals have been withdrawn since the EMG signal varies according to the electrodes' position and muscular activities.

Results show that the EMG signal is around 500-600 (on a scale between 0 and 1023) when the hand is in rest condition (flexed fingers). In contrast, the EMG signal during fingers extension reaches peaks of 750-800 (Figure 7.36 shows one sensed signal).

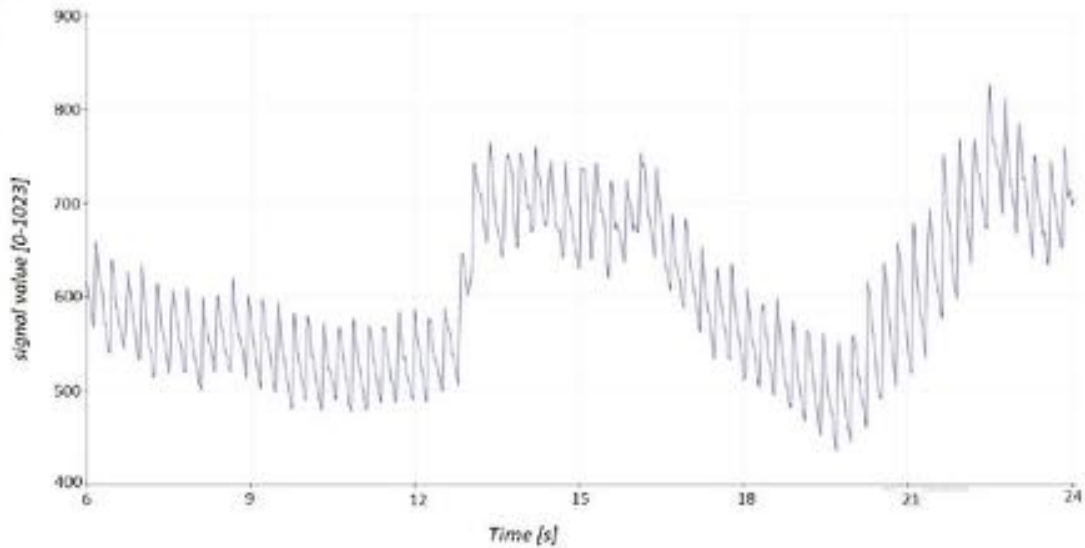


Figure 7.36 EMG signal from the extensor fascicle muscle on a healthy volunteer. Two muscular activations are withdrawn: at 13-17 seconds and 20-24 seconds.

Despite the filter and conditioning chain, the signal is quite noisy, but it shows a different range of values when the muscular fascicle is in rest condition and activated. Therefore, it is possible to use this signal to control the rehabilitative motion.

The exoskeleton control is based on a threshold on the EMG values. The EMG signal is sensed on the healthy forearm extensor muscles, and it is sent to the Arduino board that uses the input signal in the control algorithm. The Arduino generates a PWM signal as output which is responsible for enabling the actuators. This output changes the activation ON-time of the PWM according to the EMG read as input. If the muscular activity is sensed, the rehabilitation movement is activated, and for a predefined time interval, the Arduino stops reading the EMG input signal. This time interval is considered time to let the patient perform the extension of the finger and let him/her get back to the initial position of the flexed finger before performing another cycle of rehabilitation.

The control system is based on a switching control algorithm based on a predefined threshold on the EMG signal. Since the sEMG signal is patient-specific, the threshold must be chosen before the rehabilitation.

This kind of control system is suitable for hand rehabilitation since it allows the patient to perform repetitive exercises for the flexion-extension movements.

Patients can be aware and guide their rehabilitation; it is expected that the self-motion control facilitates the recovery of the injured functionalities [459].

A healthy volunteer wears the whole system to simulate the whole system's behavior and verify the correct rehabilitation movement. The three electrodes have been fixed on the left forearm to sense the fingers' extensor muscle fascicle, and the exoskeleton is mounted on the right hand. The complete set-up, which includes the exoskeleton mechanical structure, the electronic implementation, the control unit, and the sensors, is shown in Figure 7.37.

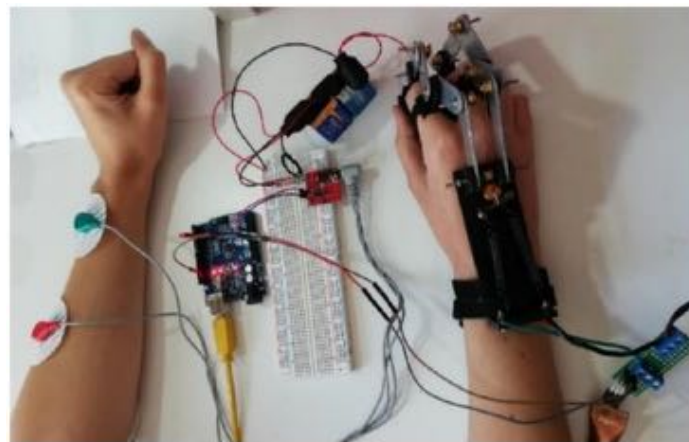


Figure 7.37 Complete set-up of the exoskeleton

As expected, when the patient activates the extensor muscle on the left healthy hand, the control algorithm recognizes the signal and activates the PWM output signal, so the SMA springs. In this way, the exoskeleton is activated, and the rehabilitative movement begins. The device works as expected.

Since this prototype is limited to only two fingers, another prototype is being studied (Figure 7.38).

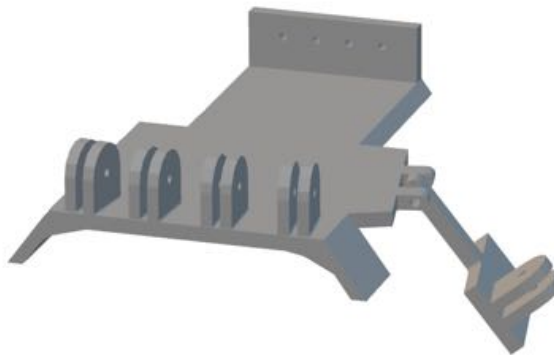


Figure 7.38 The following design of 4-bar linkage structure

7.3.3 Second exoskeleton prototype

The second device developed is a soft exoskeleton that helps patients to extend their hands properly. The flexion movement does not need to be assisted by considering the patient's hand stiffness sufficient to perform this movement. In this case, we used a glove as the principal structure. It is a tendon-driven structure actuated with SMA springs. Tendons transmit the force of the actuator to each of the fingers. Its distribution guarantees the correct transmission of efforts and ensures adequate movements of fingers. To maintain the device as soft as possible and avoid any discomfort to users, we discarded the possibility of using rigid elements to guide the cables.

For this reason, the cable was sewn to the glove. In this way, a highly cohesive joint between the cable and the glove was guaranteed. Thus, the forces transmitted from the actuators are applied at highly controlled points and directly on the finger. The way to sew it was chosen after carrying out different tests. A reinforced fishing line was used as a cable, as it is highly resistant with not too thick dimensions that allowed it to be sewn. How the cable was finally sewn is visible in Figure 7.39. Each phalanx of the finger has its

thread that later joins in the same actuator. Nevertheless, to achieve the correct union with the finger, the cable describes a ring shape around each phalanx, wrapping it in such a way that the cable well holds it. With this design, the extension movement of the fingers is carried out correctly.

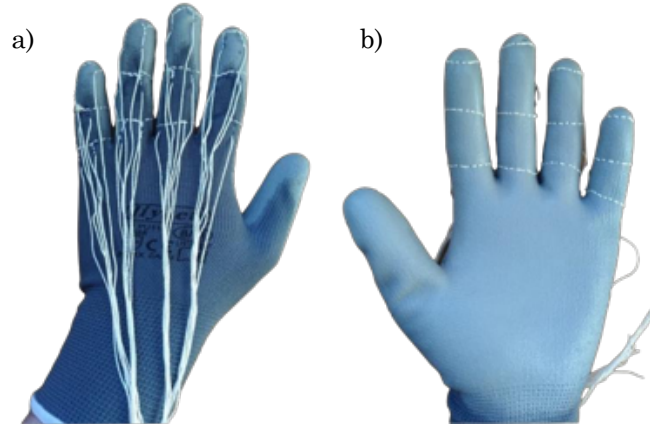


Figure 7.39 Detail of the sewn cable (a) dorsal view (b) palm view

However, the exoskeleton has to provide support to the hand's patient and avoid wrist torsion movement. So, an external structure 3D printed with PETG has been developed. It consists of three parts with laces that allow the union between them: upper, lower, and palm parts. The two first parts correspond to the armband (Figure 7.40). A strip of cloth with velcro strengthens the union between these two parts, allowing the bracelet to be opened and closed without difficulty and allowing a certain margin of adaptation for the different wrist sizes that different patients may have. The upper part includes hooks for the actuators and provides some protection from the heating of the actuators. The third part (the palm part) is fitted with the lower part through a trapezoidal male-female system, which allows a correct fixation between both pieces. Different types of palm can be made to fit better the user who will use the glove each time and allow modifications to be made without the need to re-print the part since it is an independent part. The design of the palm piece is designed not to hinder the movement of the thumb and has a curved shape so that the hand can rest comfortably on the piece.

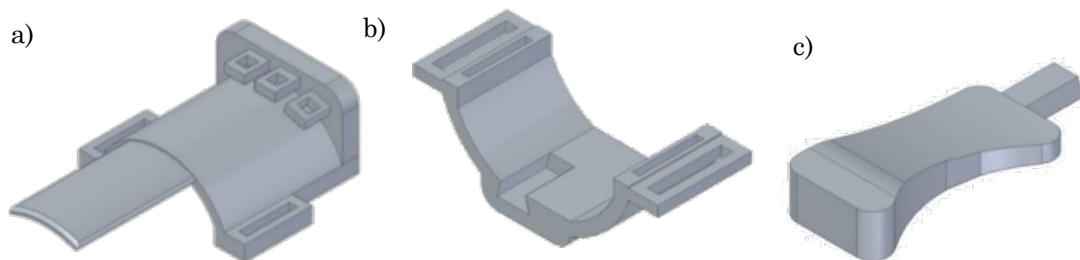


Figure 7.40 3D printed parts (a) the upper part, (b) the lower part, and (c) the palm part

We used three actuators to simplify the design: one spring for the thumb finger, one for index and medium fingers, and one spring for the ring and smaller fingers. An armband contains the Arduino and the electric circuit, the same as the haptic gloves.

The final prototype is shown in Figure 7.41.



Figure 7.41 Final prototype

The Myoware sensor (EMG sensor) was used to control the exoskeleton. In contrast to the previous sensor does not require an external supply with the two 9V batteries since power is provided directly with 5V from the Arduino board used to read the signal. Another advantage is that the electrodes are part of the same sensor, so no cables are needed to connect the sensor with electrodes. Consequently, it is possible to obtain a more compact and lightweight design.

The control software has been developed on Arduino. The sensor is placed on the healthy forearm as in the previous case. Sensor readings do not present high stability, so treatment of said values will have to be carried out to use these data correctly.

The code is divided into three main parts: data collection and management, control of the alternation of actuators, data displayed on the screen to allow the user to manage the activation or deactivation of the glove visually.

As previously mentioned, the signal is highly unstable, with significant variations and a strong dependence on the user and the muscle group where the sensor is placed. The measured signal varies between 0 to 1000, which correspond to 0 and 10mV.

The communication speed of this signal with the microcontroller is 115200 baud, that is, 115200 samples of the signal every second. This speed complicates the interpretation of the signal. Therefore, a 10 ms delay is introduced into the code so that the capture of said signal is carried out at a slower speed, facilitating the analysis and display of the signal on the screen, which will be interesting to facilitate use by the patient.

Once the signal has been captured, a signal calibration is carried out to establish an average of values to perform the control. This calibration is activated by a control flag called start. Said flag is initialized to zero so that when the system is started for the first time, a first calibration is carried out.

This flag will change to 1 when the data collection necessary for the calibration has been completed. It will change to 2 when the calibration has finished.

Calibration begins with collecting a data sample of the signal high enough for it to be valid. In this case, a sample of 60 data is considered. The collection is carried out in each cycle of

the loop function, thus requiring 60 cycles to perform the complete data collection. Said data is stored in a calibration vector, and when it is filled, the collection completion flag is activated.

Once the average is obtained, the calibration completion flag is activated, and the calibration vector index is reset for the next calibration cycle.

Since this average is the principal value used to manage the activation and disconnection of the actuators, this value needs to be as accurate as possible. Due to signal instability, recalibration is sometimes necessary. For this reason, it has been established a condition for carrying out the recalibration.

Once the signal has been correctly managed, with a value that offers sufficient stability to work with it, it is possible to actuate SMA springs.

It was observed that the crest amplitude to activate actuators was only adequate when a closing movement of the hand was performed with a significant force with the healthy hand. Thus, the control is based on activating or deactivating the actuators when closing hand movements that produce peaks in the signal representation.

For an activation signal to be valid, that is, for the crest to have a sufficient amplitude to be considered activation movement and not produced by the instability of the signal itself, a value is set that is equal to the mean calculated in a given moment plus 100 points, or what is the same, a variation of 0.1 mV concerning the value of the calculated mean. When this condition is fulfilled, the activation flag of the activated sensors is set to one, starting the passage of current through the actuators, initiating their heating phase.

Both activation and deactivation of the actuators are done by reading peaks in the EMG signal. Thus, an activation peak must end before deactivating. If this were not done, the flag would be activated and deactivated several times due to the effect of the same ridge, creating problems in operation.

The activation is accelerated if two consecutive peaks are received in a given period.

Therefore, using an auxiliary variable that allows us to count the number of cycles of the duration of a peak, we can establish a minimum duration time so that each peak is considered valid and allows us to avoid overlapping problems between activation and acceleration deactivation.

After several tests, a duration of 200 cycles has been established as the valid duration for a peak. Because a second peak can arrive, that implies the acceleration of warming, a duration count of 400 cycles is carried out, the equivalent of two peaks.

To facilitate the user's use and create a more understandable device, the led included in the Arduino board is used to signal the activation and deactivation of the actuators.

The activation of the springs can be carried out with greater or lesser power, modifying the value of the PWM (between 100 and 160). Said power can be adjusted depending on the force required for the user.

In the last part of the code, the variables useful when using the glove are graphically represented, as shown in Figure 7.42. With the signal value and the mean value, it can be seen if the peak produced by the movement has been high enough to generate the activation.

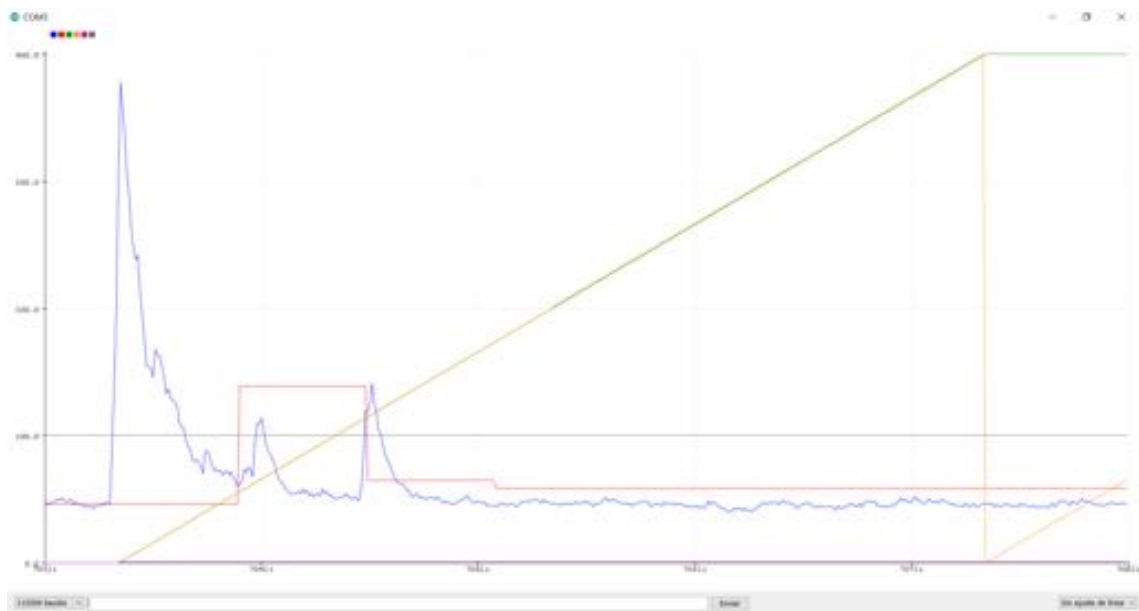


Figure 7.42 Graphic values seen for the user: the signal (in blue), the mean of the signal (in red), the cycle duration of the peak (in green), and the duty cycle (in yellow).

The cycle duration of the peak allows to know if a new activation or deactivation can be performed, which is observed when said graph remains constant at 400. With the duty cycle, it is observed which actuator is activated to detect possible malfunctions.

With the completion of the executive part of the project, testing began to verify the correct functioning of the built prototype.

7.4 Virtual Reality for wearable soft robots

Virtual reality is employed in this work as the natural complement of the prototypes explained below. As said before, it allows a more immersive experience and the possibility to realize home rehabilitation. In our study, all proposed games are thought to be realized with or without the glove or the exoskeleton. The two principal devices employed are an HDM-VR (in our case, an HTC VIVE Headset) and the Leap Motion controller connected to a PC. It is possible to realize games even with the Leap Motion and the PC. It represents a significant advantage because it reduces notably costs and does not need base stations. Therefore, it is possible to realize rehabilitation anywhere, and flexibility represents each day more an essential characteristic during the rehabilitation process. Given this, HDM-VR gives a more enjoyable experience and possibly increases patients' motivation.

Leap Motion (LM) is an optical hand tracking module that captures the hands' movements, and as explained before, the focus of this work is the rehabilitation of the hand, therefore selecting this type of sensor. Its price, usability, and dimensions represent other advantages. Through LM, it is possible to detect both the hand and the fingers' position and realize specific rehabilitation exercises.

All games are realized with Unity 3D, and an application has been finally developed, so installing the software is unnecessary, and it is possible to realize the rehabilitation with every PC.

A database connected directly with Unity has also been implemented to store patients' information and progress. The complete framework is shown in Figure 7.43.

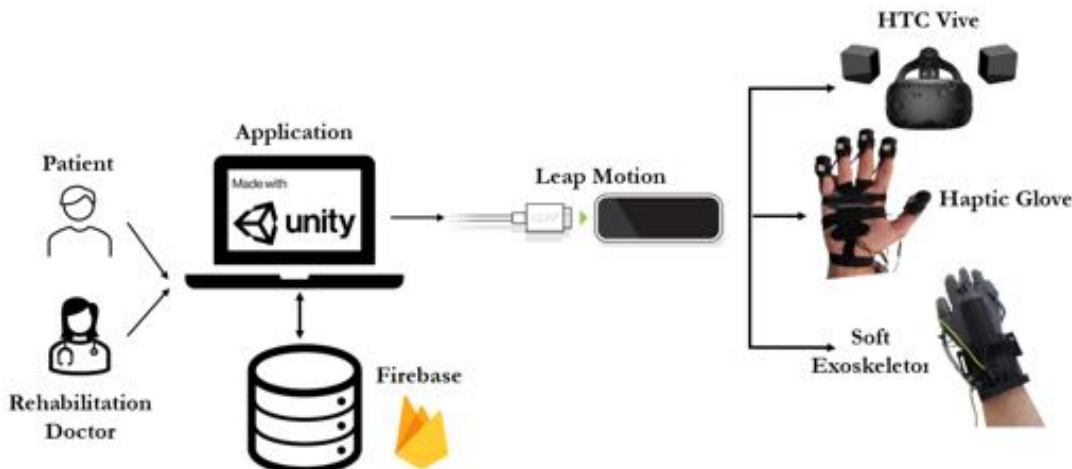


Figure 7.43 Framework of virtual reality for wearable soft robots

The database has been implemented with Google Firebase. It was chosen due to its simplicity and its high-level integration with Unity. Moreover, it provides many tools such as authentication, storage, hosting, functions, and analytics. We mainly used two of them: 1) authentication and 2) real-time database. Authentication allows users to register in the application with an email and a password and manage sign-in sessions (including password recovery). All data are saved safely in Google Cloud. The real-time database allows managing a database with all authenticated users. As before, all data are stored in Google Cloud in a JSON format.

First of all, patients can register themselves on the platform the first time they enter the application. They have to introduce a name, an actual email (an activation mail will be sent), and a password to create the account. Once the email has been verified, the next step

is to enter the application. Here, we can choose between a game or checking our progress and records. If we choose the first option, we then choose between the different games.

6.4.1 Games

Games are divided into two groups depending on the rehabilitation device, the haptic glove or the exoskeleton.

In the case of the soft haptic glove, three scenarios have been developed. These scenarios have been used to test the prototype and verify its proper functioning. However, they represent existent exercise realized by patients during occupational therapy. Each scenario is a little game that reproduces concrete objects. When the game starts, users can see the screen shown in Figure 7.44, where they can select the game with their fingers pressing the corresponding button. The "Donuts game" is shown in Figure 7.44b. In this scenario, it recreates the classical ring stacking toy. The exercise consists in stacking rings depending on their diameter. The "Keyboard game" is shown in Figure 7.44c. In this scenario, there is a keyboard, and patients can press different buttons to write words or phrases. The third game, called "First blocks," is shown in Figure 7.44a. In this case, there are a box and six geometric shapes that have to be inserted in the box matching the correct shape. At each moment, it is possible to return to the main menu and quit the application. All these commands are accessible using the hands. When patients grasp an object wearing the haptic glove, they perceive tactile feedback that depends on the type of touch. For example, in the keyboard game, the feedback is only perceived in the fingerprint, while the whole hand is interested in the donuts game. In this group of games, it has been considered irrelevant to sum points since it is not considered the speed of realization of the games, but on the correct execution.

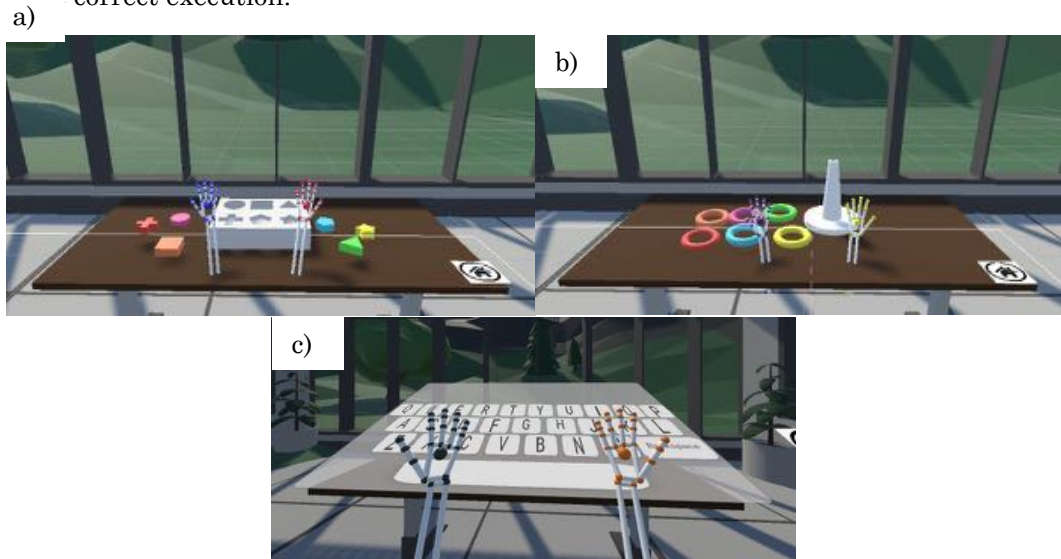


Figure 7.44 Tactile, haptic glove scenarios (a) Box game (b) Donuts game and (c) Keyboard

In the case of the exoskeleton, only one game has been developed because of the limitations of the prototype. In this case, the game is focused on three positions that can adopt the hand: a whole extended hand, a fist, and an intermediate position between them. The scenario is shown in Figure 7.45.



Figure 7.45 The airplane game

In this case, patients are an airplane that moves toward rings at a different height. To achieve pass through these rings, they have to open the hand to move up, close the hand to move down, and maintain the intermediate position not to move. Every time they realize correct the task sum points, they can see the total score at the end of the game. An arrow in the left of the screen helps patients know the next position of the hand. The speed of the game can be changed depending on the patient's conditions.

The last game focuses on fine motricity and works on pinch movement. In this scenario, shown in Figure 7.46, it is possible to see a piano and four spheres above it.



Figure 7.46 The piano game

Each sphere represents a pinching movement; the first is the thumb with the index, the second is the thumb with the middle finger, the third is the thumb with the ring finger, and the fourth is the thumb with the little finger. When the game starts, patients have to extend their hands. Then, one of the spheres turns green, and users realize the corresponding movement. If the movement is correct, one of the piano keys sounds, and they extend the hand again and wait for the next sphere to repeat the process. On the contrary, one of the piano keys turns red, and patients have to extend their hands before repeating the position. Also, in this case, users sum points every time they realize the correct position depending on the time they need to realize it correctly.

All data are stored in the database, so it is possible to view the scores relating to the last ten days in which the corresponding exercise has been realized to observe patient progression. It is worth mentioning that this time interval has been chosen because studies [460] affirm that a remarkable progression can be recorded in this period, following a constant routine. Even so, if necessary, it is possible to modify and adapt it. The rehabilitator can choose which results to exhibit, those corresponding to the piano game or the airplane game.

6.4.2 Experiments

Experiments have been realized separately for each application.

6.4.2.1 Experiments only with virtual reality

In the first phase, the last two games have been tested without any device (Figure 7.47) since they represent classical exercise realized by post-stroke patients. So the idea was to test if they worked correctly and if users could register and use the platform without problems.



Figure 7.47 Virtual Reality Experiments

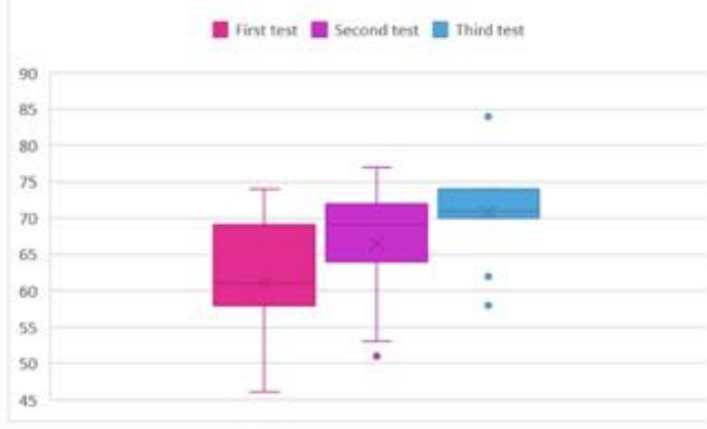
In order to standardize the experiments, each subject performs only ten actions and repeats the game three times to observe the progression that it presents as it becomes familiar with the application. As it was not possible to count on patients, health subjects carried out the tests with the non-dominant hand in order to reduce as much as possible the control they have over it when performing the exercises. All subjects have realized a previous training phase.

The tests have been carried out by 10 people of different genders (2 women and 8 men), ages (between 22 and 42 years). Each of the ten volunteers was subjected to two tests: the piano and the airplane. Information has been collected to calculate a score later and determine the performance and progress achieved.

In the piano test, the score obtained has been calculated considering the current time (the time it takes the patient to perform the movement correctly), the accumulated score, and the number of movements completed correctly. The results of the piano game are shown in the following Table 7.6

Table 7.6 Score Piano Game

Score Piano Game			
Vol. N°	1º test	2º test	3º test
1	60	53	71
2	46	64	62
3	64	51	58
4	61	71	73
5	74	77	74
6	58	72	74
7	72	69	84
8	58	71	70
9	69	72	70
10	49	64	72
Avg.	61,1	66,4	70,8
σ	9,13	8,51	7,02



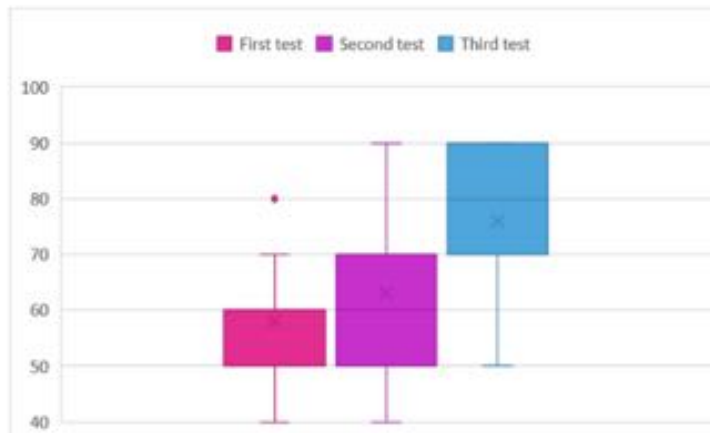
Results show a learning curve experienced by most of the volunteers. The average score of the last test is much higher than that of the first. It is also reflected in the standard deviation, which is very high in the first two tests, while in the last one, it decreases notably. Thus, the result obtained depends on the patient's skills, the fluency achieved in training prior, and the controller's effectiveness in recognizing gestures. These differences diminish as the user becomes more familiar with the game and with the sensor.

In the airplane test, the score obtained has been taken into account by the accumulated score, and the number of rings exceeded.

The results of the airplane game are shown in the following Table 7.7. Also, in this case, it is possible to appreciate the learning curve experienced by users. The scores are higher as the number of tests carried out increases.

Table 7.7 Score Airplane Game

Score Airplane Game			
Vol. Nº	1º test	2º test	3º test
1	60	50	70
2	50	60	90
3	60	80	80
4	70	70	80
5	80	90	90
6	60	60	70
7	50	40	50
8	40	70	50
9	60	50	90
10	50	60	90
Avg.	58	63	76
σ	11,35	14,94	15,78



At the end of the tests, each of the volunteers has filled out a form. They are asked to answer a series of questions about general aspects of the application, evaluation of the games, evaluation of the interface. Results are presented in the following Tables.

Table 7.8 Results concerning general aspects (1-Low, 10-High)

	Mental Demand	Physical Demand	Temporal Demand	Effort	Performance	Frustration
1	3	1	3	3	8	4
2	10	8	10	9	9	7
3	2	1	4	2	8	1
4	6	3	4	6	9	3
5	2	2	6	3	6	8
6	5	4	4	3	5	5
7	6	6	7	6	10	2
8	4	1	5	5	9	3
9	3	3	3	3	5	4
10	4	7	1	4	5	2
Avg.	4,5	3,6	4,7	4,4	7,4	3,9
σ	2,42	2,59	2,50	2,12	1,96	2,23

The standard deviations of most of the fields indicate that the results obtained in this section are very dispersed, from which it follows that it depends on the experience lived by each one. It can be attributed to the gesture recognition process prior to the tests, in which the time difference required between subjects was considerable.

Concerning games evaluation, opinions regarding both games are very positive (1 - Totally disagree, 2 - Strongly agree), as shown in Figure 7.48. The Airplane Game results easier and the most entertaining of the two games (Figure 7.49).

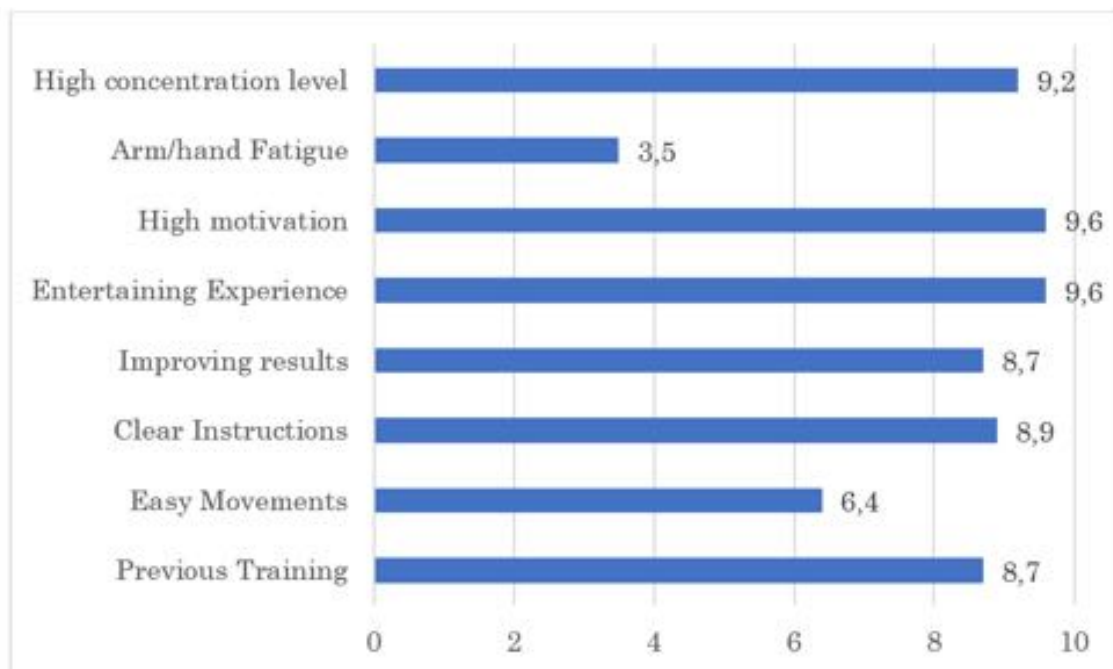


Figure 7.48 Games evaluation

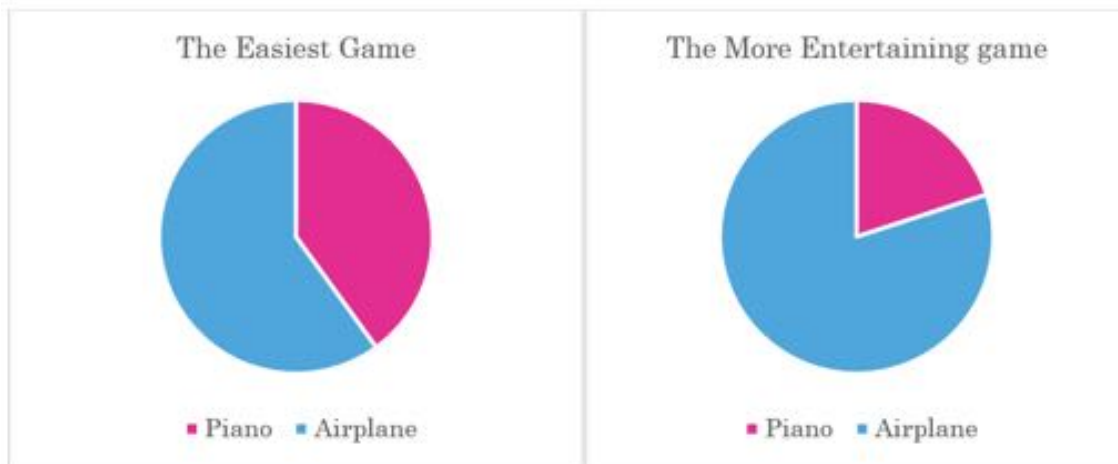


Figure 7.49 Comparison between the two games

Finally, concerning the interface, volunteers consider it user-friendly (Avg. 9.1).

6.4.2.2 Experiments with soft glove exoskeleton

As in the previous experiments, ten healthy volunteers have realized the tests. It implies that they do not present rigidity in hand. Thus, the participants in all the tests were instructed to start with the hand in a flexed position, closed, but leaving it quite relaxed to generate the opening movement and obtain valid tests.

The stiffness of the stroke survivors would perform the closing movement in patients. So, to simulate it, users were told that, once the opening movement of the hand had been carried out and the glove was deactivated, they could exert their force to make the grips or closures of the hand.

Only four of the ten volunteers could carry out the virtual reality tests; the other five only performed basic exercises.

The basic exercises consisted of glove-assisted grip exercises. The aim was to check the basic functionality of the glove, that is, to allow the user to carry out simple tasks that may appear on a day-to-day basis. Furthermore, it was desired to demonstrate the versatility of the grip achieved, proposing two different object morphologies: in the first case, the users had to grip a spherical shape (Figure 7.50), which requires a reasonably wide hand opening; and in a second case, the object used was in the shape of a torus (Figure 7.51), which required greater gripping precision.

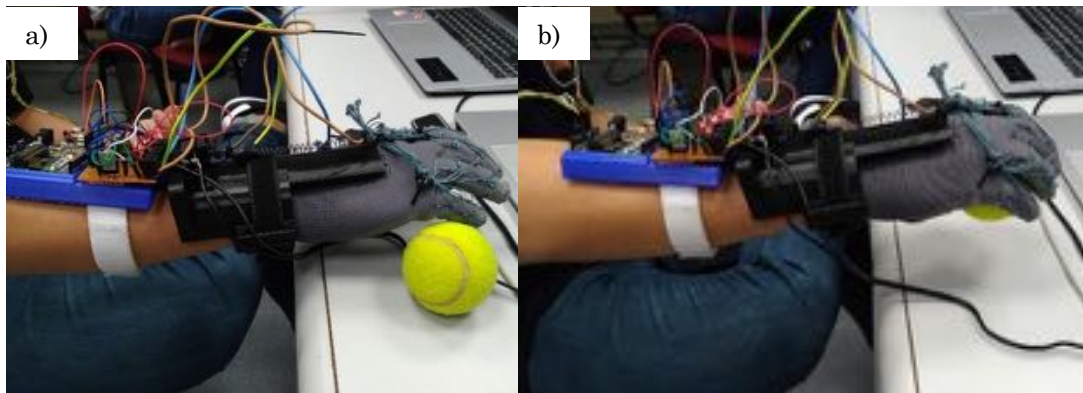


Figure 7.50 Basic exercise with soft exoskeleton (a) Extension of the fingers (b) Gripping task

The user begins with the hand closed, in a flexed position, recreating and possibly the initial position of the hand of stroke patients. The user sends an opening start signal using the EMG sensor placed in the healthy hand. When the compression of the springs begins, the opening movement of the hand occurs.

Once the proper opening for grasping the object has been achieved, the user deactivates the glove to close the hand around the object, making the grip. Upon completion of the grip, the user performs a movement of the object to another point. Thanks to the compact design of the prototype, the user has complete mobility and can change the object position without any impediment due to electronics.

Once the object is deposited at the final point, the user activates the glove again to perform the opening movement and release the object. Once this is done, the exercise is finished. This procedure is carried out similarly for both morphologies.

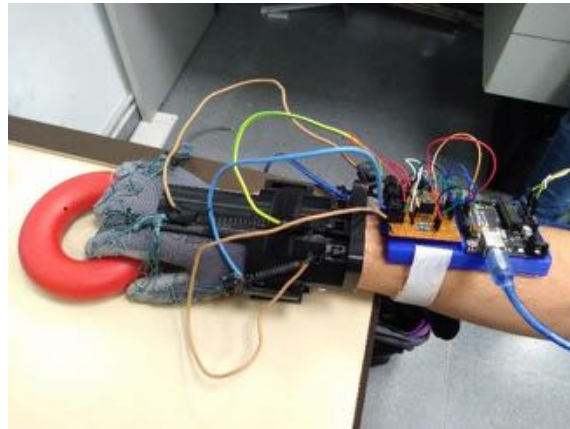


Figure 7.51 Basic exercise with the torus shape

Once the basic functionality of the prototype had been tested, a second experiment was carried out to evaluate the feasibility of using it in virtual reality experiences.

The proposed virtual reality game is the Airplane game previously explained (Figure 7.52). The game software was modified to slow its speed, adapting itself to the glove's actuation speed.

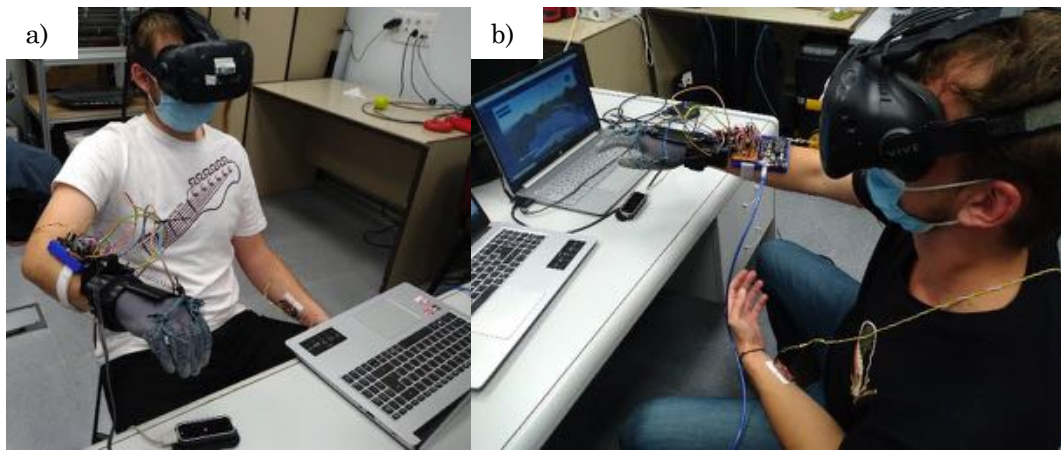


Figure 7.52 Soft glove exoskeleton tested with virtual reality

Users realize the movements required by the game with the help of the glove, activating the glove to climb and deactivating it to descend.

In Figure 7.53, the user's perspective on who performs the tests. The game that the user is watching in the HTC Vive while performing the tests is observed on the right screen, while on the left screen is the graphic representation of the signals received by the EMG sensor.

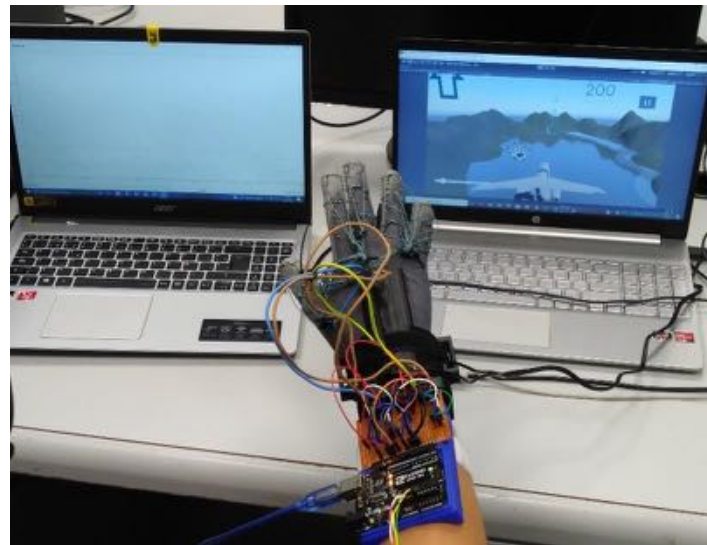


Figure 7.53 User's perspective. The screen on the left shows the EMG signal while the screen on the right the VR game.

At the end of each test, users were sent a survey to assess the experiments carried out and the glove's function. Volunteers are adults between the ages of 20 and 30 without previous experiences related to assisted robotics and virtual reality.

Principal questions and their results are shown in Figure 7.54.

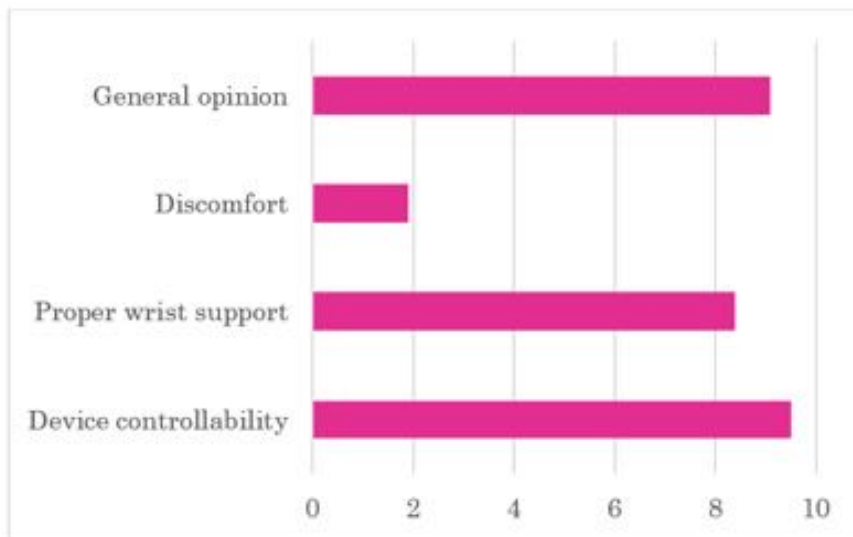


Figure 7.54 General aspects of the experience, as before (1 - Totally disagree, 2 - Strongly agree)

The first questions in the survey focused on the user's perspective on the correct functioning of the glove, the ease of carrying out the experiments' tasks, and the prototype's controllability. 100% of the participants rate the prototype with a score greater than or equal to 7 out of 10 points. Thus, it is possible to conclude that the prototype meets the desired specifications. Among these aspects, the ease control glove stands out, obtaining a score greater than 9 points out of 10 by all the participants. Regarding the glove's functionality, all respondents claim to have solved all the tasks set out in the experiments.

Regarding the support offered by the wristband, users consider that it is correctly holding the hand and is adjusted to it.

Another aspect analyzed was the comfort of the user. The main factors were the correct distribution of forces through the cable guidance system and the actuators' heating when activated. Only a participant complained about it.

In the questions referring to virtual reality, the aim was to analyze the results obtained by the users in the game and their general opinion about the experience. Most of the participants who performed this experimental part obtained good results in the game and valued the entertainment of said experience with high scores. In addition to this, the difficulty curve of these tests is considered adequate for novice users.

6.4.2.3 Experiments with tactile, haptic gloves

Two tests have been realized with 12 people: the first without VR and the second with VR. The tests without VR have been done with the Arduino codes described above.

In this case, the scenarios employed were the Box game, the Donuts game, and the keyboard.

The test without VR realized with the vibrotactile glove consisted of an initial phase of calibration in which the user adjusted the level of vibration between the palm and the fingers until it was as balanced as possible. In a second phase, the user would be given some objects (a tennis ball and a plastic torus) to hold with the other hand. Meanwhile, he would be instructed to slowly put the glove hand on in the same way while supplying vibration at the appropriate time.

Later, previous training with the virtual reality experience would be done without the glove to allow users to compare the two experiences and make the interface more familiar to them. Then, the same test would be done with VR but with the glove on (Figure 7.55).



Figure 7.55 Experiments with the vibrotactile glove and VR

After this, users repeat the same with the SMA-haptic glove. However, it was not possible to test this second device with virtual reality due to Leap Motion problems correctly detecting the hand with the glove. A failure of this type would significantly worsen the experience since the SMA would receive contradictory messages, and its slower response means that it cannot process all of them and would end up giving the wrong answer.

With some volunteers, an additional test in which they would have the palm platform of the vibrotactile glove placed together with the SMA-haptic glove.

Finally, a survey would be conducted to evaluate the experience.

Results of these last experiments are shown in the following Figure 7.56.

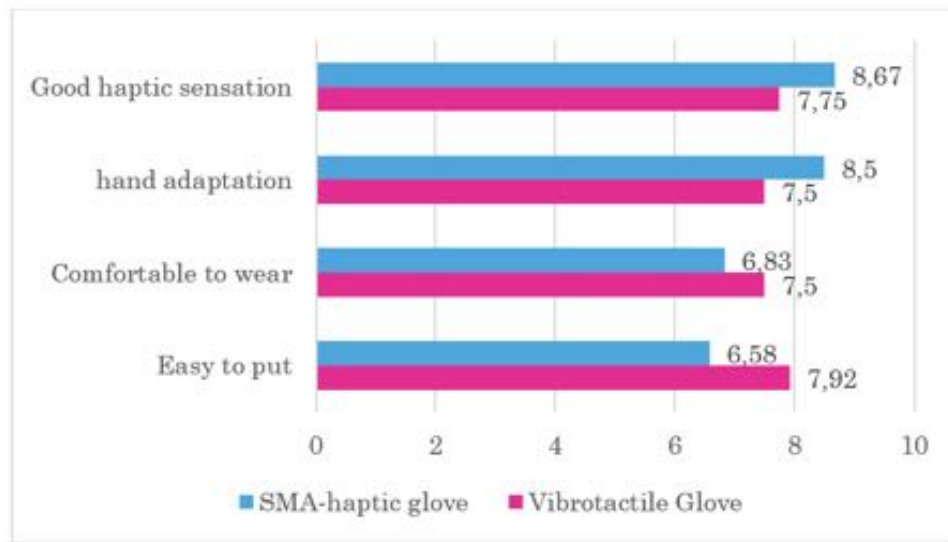


Figure 7.56 Comparison between the two haptic devices from the point of view of usability.

The vibrotactile prototype is the easiest to put and the most comfortable to wear. However, the SMA-haptic glove presents a better hand adaptation and provides a better haptic sensation with VR.

The global experience improves when the SMA-haptic glove is combined with the vibrotactile palm.

Concerning the experience with the vibrotactile glove and VR, the results have been significantly good. Volunteers believe that the glove improves the virtual reality experience (8.33 average score). Only one volunteer has not agreed with this, with a score of 2.

The game that, with the glove, gave the best haptic feedback was the Donuts game (Figure 7.57).

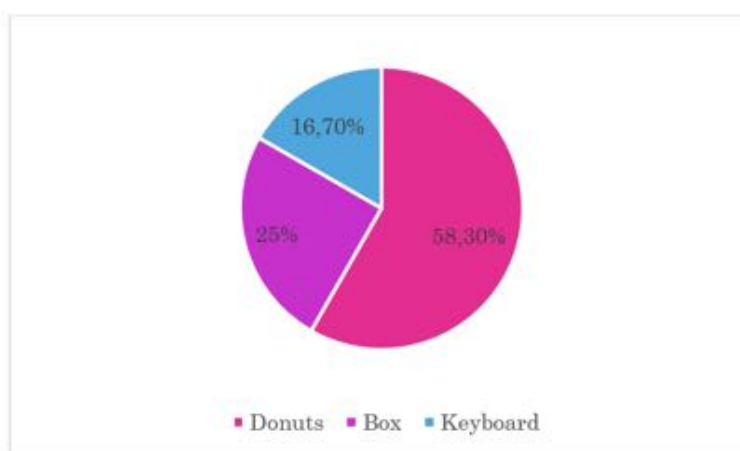


Figure 7.57 VR game that provides the best haptic sensation

6.5 Discussion

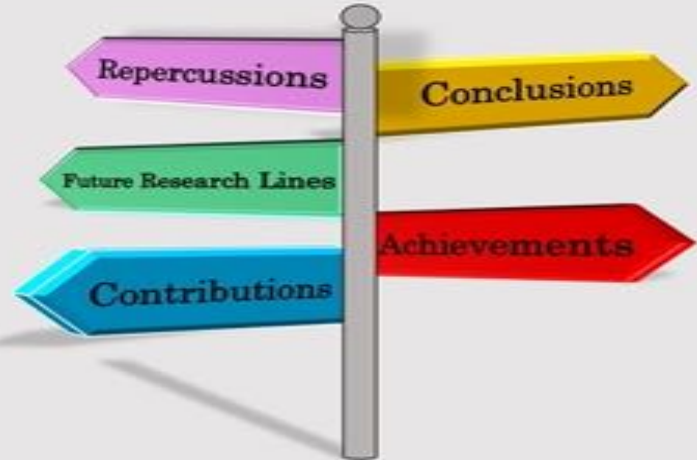
The wearable soft devices developed in this work show how soft solutions allow a more comfortable and natural experience than conventional devices. They are lightweight and adapt better to the hand. Both haptic devices and exoskeleton benefit from the use of soft materials and actuators. In the different tests realized, it has been possible to observe the positive attitude of volunteers towards the possibility of trying these devices since they were generally light and did not generate discomfort. For this reason, the older people to whom they can be mainly directed may even feel more comfortable in front of these devices that are not as bulky as the conventional ones.

The issue of weight then becomes critical in the case of exoskeletons since patients who have to use them may have muscle weakness that prevents them from carrying much weight. Desktop devices are used in many cases to avoid this problem, but these have the disadvantage of being fixed and not allowing the patient much freedom of movement. Furthermore, these devices can hardly be used by the patient at home.

The future of wearable devices is undoubtedly in soft robotics because more and more users need devices that are comfortable to wear and do not tire out the extremities that hold them. SMA actuators have proven to have potential in this field, and although they present some disadvantages, they significantly reduce weight and bulk.

The possibility of using these devices with virtual reality has become an almost essential feature of them since it allows to improve the overall experience. All the apparatus shown in this chapter can be enhanced by further lightening the structures at specific points, miniaturizing the electronics, and positioning it at the waist to reduce potential discomfort and allow users even more freedom of movement.

Finally, it is important to take into account the low cost of realization of these devices. It allows them to be accessible by many more people than can currently benefit from rehabilitation devices. According to a recent study, only 53% of post-stroke patients in Spain could access the recommended comprehensive rehabilitation. Two predictor variables significantly influenced this number: the residence in an urban environment and the possibility of complementing private rehabilitation [461]. It is due to a lack of structures that can accommodate and treat these people for months, which is why it is also very interesting that these devices can be taken home and used independently, while the therapist can remotely access data and check the patients' progress. Moreover, patients are more likely to use a device when it is easy to use, put on, does not generate discomfort, and is entertaining thanks to activities with virtual reality.



8. Conclusions

*" We judge ourselves by what we feel capable of doing,
while others judge us by what we have already done."*
Henry Wadsworth Longfellow

This section will summarize the present work's main contributions, conclusions, and future research lines.

8.1 Conclusions

This work started with an updated contextualization to better understand the challenges encountered in developing, modeling, and controlling the different prototypes presented. Moreover, soft robots have been divided into four groups: bio-inspired, manipulators, grippers, and wearables.

Different prototypes have been realized for each group, proposing new designs, modelings, or control depending on the prototypes. SMAs actuators have been employed in the majority of the case. Some SMA springs have been manufactured, while others have been directly acquired after FEM simulations.

For bio-inspired soft robots, a starfish and a jellyfish have been realized. Two different soft continuous manipulators have been designed and built: Kyma and Ruān. For soft grippers, four types of them have been developed. Finally, two types of exoskeletons and two types of haptic gloves have been manufactured for wearable soft robots. (Figure 8.1)

All these prototypes have been tested to verify their proper functioning. Different strategies have been applied to control and model them.

Moreover, virtual reality has been integrated into some of these devices: to realize teleoperation tasks, as in the case of Kyma, or to improve the user experience, as in the case of wearable devices.



Figure 8.1 The different prototypes of soft robots developed. Soft Manipulators: Aeruca Robot [462], Kyma, and Ruān. Wearable soft robots: haptic force glove [406], haptic tactile glove, and exoskeletons. Soft grippers [368] Bio-inspired soft robots: the starfish Asforb, JellyRobcib [16], and soft plant.

8.2 Contributions

The main contributions of this thesis to state of the art are the following:

	<i>Contributions</i>
<i>State-of-the-art</i>	<p>Proposal of a new division between soft robots and conventional robots</p> <p>Proposal of a new division of soft robots in four application groups</p>
<i>Bio-inspired soft robots</i>	<p>As far as we know, the development of the first soft robotic jellyfish actuated with SMAs springs able to move both vertically and laterally.</p> <p>Design and construction of a soft robotic starfish actuated with SMA.</p>
	<p>Concept and proposal design of a soft robotic climbing plant</p>
<i>Soft manipulators</i>	<p>Design and construction of Kyma, a tendon-driven soft robot with bending and prismatic capabilities.</p> <p>Design of Ruān, a three-module soft robot actuated with SMA</p> <p>Application of different modeling techniques for soft manipulators robots to achieve an efficient real-time model.</p>
<i>Soft grippers</i>	<p>As far as we know, the first comparison of soft grippers technologies.</p>
<i>Wearable soft robots</i>	<p>Design and re-design of different prototypes of soft exoskeletons and haptic gloves.</p> <p>The use of a stretchable sensor as a bias spring in a haptic glove. This strategy allows this sensor to measure the spring's displacement and help the SMA spring deform again, lightening the design.</p> <p>Comparison of conventional actuators and SMAs in a haptic tactile glove.</p> <p>Integration of VR into wearable devices to improve the user experience.</p>

8.3 Achievements

To this day, the thesis has produced 6 journal papers. Two other papers are currently under review. The already published papers are the following:

- ✓ Terrile, S., Migueláñez, J., & Barrientos, A. (2021). A Soft Haptic Glove Actuated with Shape Memory Alloy and Flexible Stretch Sensors. *Sensors*, 21(16), 5278. (Q1)
- ✓ Terrile, S., Argüelles, M., & Barrientos, A. (2021). Comparison of Different Technologies for Soft Robotics Grippers. *Sensors*, 21(9), 3253. (Q1)
- ✓ Cruz Ulloa, C., Terrile, S., & Barrientos, A. (2020). Soft underwater robot actuated by shape-memory alloys "JellyRobcib" for path tracking through fuzzy visual control. *Applied Sciences*, 10(20), 7160. (Q2)
- ✓ Martin-Barrio, A., Terrile, S., Diaz-Carrasco, M., del Cerro, J., & Barrientos, A. (2020, September). Modelling the Soft Robot Kyma Based on Real-Time Finite Element Method. In *Computer Graphics Forum* (Vol. 39, No. 6, pp. 289-302). (Q2)
- ✓ Martín Barrio, A., Terrile, S., Barrientos, A., & del Cerro, J. (2018). Hyper-Redundant Robots: Classification, State-of-the-Art and Issues. *Revista Iberoamericana de Automática e Informática industrial*, 15(4), 351-362. (Q3)

- ✓ Martín-Barrio, A., Roldán, J. J., Terrile, S., del Cerro, J., & Barrientos, A. (2020). Application of immersive technologies and natural language to hyper-redundant robot teleoperation. *Virtual Reality*, 24(3), 541-555. (Q1)
- ✓ Roldán Gómez, J. J., Garzón Oviedo, M. A., León Rivas, J. D., Garzón Ramos, D. A., Martín Barrio, A., Terrile, S., ... & Barrientos Cruz, A. (2017). Proyecto pric: protección robotizada de infraestructuras críticas.

Additionally, a total of 15 BSc (TFG) and MSc (TFM) theses were supervised with Professor Antonio Barrientos Cruz (Table 8.1).

Table 8.1 Co-supervised BSc and MSc projects during the execution of this thesis.

	Title	Author	Type	Year
1.	Desarrollo de un Robbot Manipulador Blando e Híper-Redundante	Cecilia Martínez Martín	TFG	2017
2.	Desarrollo de herramientas de agarre basadas en robótica blanda para robots manipuladores colaborativos	Miguel Argüelles Hortelano	TFG	2018
3.	Diseño e implementación de un robot blando bioinspirado actuado mediante materiales inteligentes con memoria de forma (SMA) para la adquisición y monitoreo de datos térmicos en entornos submarinos.	Christyan Mario Cruz Ulloa	TFM	2019
4.	Robot continuo actuado con SMA	Miguel Guzmán Merino	TFM	2020
5.	Development of a hand exoskeleton actuated with SMA	Matilde Brossa	TFM	2020
6.	Desarrollo de un guante haptico soft	Jesus Perez Migueláñez	TFG	2020
7.	Diseño y construcción de un robot blando	Diego Jeremías Efler Herranz	TFG	2020
8.	Modelado y control de un robot blando actuado con sma	Andrea Lopez Perez	TFM	2021
9.	Desarrollo de un robot blando bioinspirado en una estrella de mar actuado mediante materiales inteligentes con memoria de forma (SMA)	Alejandro Jimenez	TFG	2021
10.	Desarrollo de un guante haptico con feedback táctil	Manuel Repullo Menéndez	TFG	2021
11.	Desarrollo de un exoesqueleto para rehabilitación de la mano basado en materiales blandos	Jaime Gutiérrez Normand	TFG	2021
12.	Aplicación de realidad virtual para la rehabilitación de la mano post-ictus	Carlos Jiménez García	TFG	2021
13.	Exosqueleto de mano para rehabilitación post-ictus	David Sanchez Gonzalez	TFG	2022
14.	Redes neuronales aplicadas en la clasificación de señales neuronales EEG	Blanca Guillen Cebrian	TFM	2022
15.	Sensorización y control de un robot blando actuado con SMA	Celia Garijo del Río	TFM	2022

Spanish and European projects defined the funding resources to finish this work:

	Name of the project	Funding body	Code
1	Robotic Protection for Critical Infrastructures (PRIC)	Ministry of Economy and Competitiveness of the Governments	DPI2014-56985-R
2	GRob-UPM. RoboCity2030 Madrid Robotics Digital Innovation Hub	Community of Madrid	S2018/NMT-4331
3	ROBÓTICA. Robótica aplicada a la mejora de la calidad de vida de los ciudadanos (fase III)	Community of Madrid	S2013/MIT-2748

In addition, a research stay at IIT (Italian Institute of Technology) was realized during summer 2021 at Bioinspired Soft Robotics Laboratory under the supervision of Barbara Mazzolai. The author of this work was granted with a [scholarship](#) to research soft robotics climbing plants

8.4 Repercussions

Design, modeling, control, and application with VR of soft robots can generate uncountable benefits, as this work and previous works have already demonstrated.

Soft robots play a crucial role in medical applications. This work focuses mainly on soft wearable devices for post-stroke hand rehabilitation. The development of wearable devices that can help in the rehabilitation process is essential due to the increasing number of people who need them.

Also, soft manipulators, thanks to their high number of DOFs, have proven to be useful in many fields of applications, being able to be used in applications where a standard robotic arm could not. Not only in medical tasks but also agriculture, archeology, or inspection tasks. It is important to remember that it is not necessary to realize a soft prototype in many cases since also a hyper-redundant robot presents the advantage of many DOFs without employing soft materials to manufacture the body.

Nowadays, soft grippers represent the most advanced field of soft robots since they are already applied in industrial environments with many advantages. They can be employed in different sectors, like soft manipulators, since they can adapt their shape to the object to grasp without damaging it.

Finally, the study of bio-inspired soft robots can allow developing robots more similar to animals that, like these, can be soft enough so that it is safe to interact with them but that at the same time they can perform complex and heavier tasks than most soft robots can do today.

Therefore, the impact areas of this robotic field are extensive and can provide contributions in many others fields, providing robots with new capabilities.

8.5 Future Research Lines

Future research lines involve all the prototypes developed during this thesis. Each could generate many future developments since soft robotics is a continuously evolving field, so new materials, actuators, and fabrication technologies can improve their performance significantly.

Concerning bio-inspired soft robots, the starfish Asforb can be tested in an underwater environment to verify if it helps pattern realization, allowing it to advance more quickly. If so, it will be possible to collaborate with JellyRobCib to perform monitoring tasks.

Concerning soft manipulators, it will be interesting to verify the simulations results of Ruān and the proper functioning of the neural network experimentally. Thus, Ruān could be equipped with sensors to precisely measure each segment's inclination and flexion.

Concerning soft grippers, it will be interesting to equip the most versatile of them with sensors (for example, force sensors) and apply neural networks to realize an object recognition and grasp it successfully.

Finally, designs can be improved concerning wearable soft robots, especially regarding the electronics part. Circuits can be miniaturized and positioned in another area of the body. Moreover, SMA actuators need a cooling system to actuate faster.



9. References

- [1] K. Suzumori, S. Iikura, H. Tanaka, Applying a flexible microactuator to robotic mechanisms, *IEEE Control Syst. Mag.* 12 (1992) 21–27.
- [2] B. Tondu, P. Lopez, Modeling and control of McKibben artificial muscle robot actuators, *IEEE Control Syst. Mag.* 20 (2000) 15–38.
- [3] G. Bao, H. Fang, L. Chen, Y. Wan, F. Xu, Q. Yang, L. Zhang, Soft robotics: Academic insights and perspectives through bibliometric analysis, *Soft Robot.* 5 (2018) 229–241.
- [4] W. McMahan, V. Chitrakaran, M. Csencsits, D. Dawson, I.D. Walker, B.A. Jones, M. Pritts, D. Dienno, M. Grissom, C.D. Rahn, Field trials and testing of the OctArm continuum manipulator, in: Proc. 2006 IEEE Int. Conf. Robot. Autom. 2006. ICRA 2006, IEEE, 2006: pp. 2336–2341.
- [5] S. Seok, C.D. Onal, K.-J. Cho, R.J. Wood, D. Rus, S. Kim, Meshworm: a peristaltic soft robot with antagonistic nickel titanium coil actuators, *IEEE/ASME Trans. Mechatronics.* 18 (2012) 1485–1497.
- [6] D. Trivedi, C.D. Rahn, W.M. Kier, I.D. Walker, Soft robotics: Biological inspiration, state of the art, and future research, *Appl. Bionics Biomech.* 5 (2008) 99–117.
- [7] C. Majidi, Soft robotics: a perspective—current trends and prospects for the future, *Soft Robot.* 1 (2014) 5–11.
- [8] D. Rus, M.T. Tolley, Design, fabrication and control of soft robots, *Nature.* 521 (2015) 467–475.
- [9] N. Kastor, V. Vikas, E. Cohen, R.D. White, A definition of soft materials for use in the design of robots, *Soft Robot.* 4 (2017) 181–182.
- [10] A. Chen, R. Yin, L. Cao, C. Yuan, H.K. Ding, W.J. Zhang, Soft robotics: Definition and research issues, in: 2017 24th Int. Conf. Mechatronics Mach. Vis. Pract., IEEE, 2017: pp. 366–370.
- [11] K. Chubb, D. Berry, T. Burke, Towards an ontology for soft robots: what is soft?, *Bioinspir. Biomim.* 14 (2019) 63001.
- [12] F. Schmitt, O. Piccin, L. Barbé, B. Bayle, Soft robots manufacturing: a review, *Front. Robot. AI.* 5 (2018) 84.
- [13] M. Brandstötter, S. Mühlbacher-Karrer, D. Schett, H. Zangl, Virtual compliance control of a kinematically redundant serial manipulator with 9 dof, in: Int. Conf. Robot. Alpe-Adria Danube Reg., Springer, 2016: pp. 38–46.
- [14] A. Martín-Barrio, J.J. Roldán-Gómez, I. Rodríguez, J. Del Cerro, A. Barrientos, Design of a Hyper-Redundant Robot and Teleoperation Using Mixed Reality for Inspection Tasks, *Sensors.* 20 (2020) 2181.
- [15] H.D. Yang, A.T. Asbeck, A new manufacturing process for soft robots and soft/rigid hybrid robots, in: 2018 IEEE/RSJ Int. Conf. Intell. Robot. Syst., IEEE, 2018: pp. 8039–8046.
- [16] C. Cruz Ulloa, S. Terrile, A. Barrientos, Soft Underwater Robot Actuated by Shape-Memory Alloys “JellyRobcib” for Path Tracking through Fuzzy Visual Control, *Appl. Sci.* 10 (2020) 7160.
- [17] A.S. Curiel, Generacion de patrones de marcha para soft robot caminante, (2016). <http://oa.upm.es/44165/>.
- [18] C. Laschi, M. Cianchetti, B. Mazzolai, L. Margheri, M. Follador, P. Dario, Soft robot arm inspired by the octopus, *Adv. Robot.* 26 (2012) 709–727.
- [19] A. Martin, S. Terrile, A. Barrientos, J. del Cerro, Hyper-redundant robots: classification, state-of-the-art and issues, *Rev. Iberoam. Automática e Informática Ind.* 15 (2018) 351–362.
- [20] B. Zhang, Y. Fan, P. Yang, T. Cao, H. Liao, Worm-like soft robot for complicated tubular environments, *Soft Robot.* 6 (2019) 399–413.
- [21] S. Rozen-Levy, W. Messner, B.A. Trimmer,

- The design and development of branch bot: a branch-crawling, caterpillar-inspired, soft robot, *Int. J. Rob. Res.* (2019) 0278364919846358.
- [22] S. Mao, E. Dong, S. Zhang, M. Xu, J. Yang, A new soft bionic starfish robot with multi-gaits, in: 2013 IEEE/ASME Int. Conf. Adv. Intell. Mechatronics, IEEE, 2013: pp. 1312–1317.
- [23] H.-T. Lin, G.G. Leisk, B. Trimmer, GoQBot: a caterpillar-inspired soft-bodied rolling robot, *Bioinspir. Biomim.* 6 (2011) 26007.
- [24] A. Arienti, M. Calisti, F. Giorgio-Serchi, C. Laschi, PoseiDRONE: design of a soft-bodied ROV with crawling, swimming and manipulation ability, in: 2013 Ocean. Diego, IEEE, 2013: pp. 1–7.
- [25] F. Renda, F.G. Serchi, F. Boyer, C. Laschi, Structural dynamics of a pulsed-jet propulsion system for underwater soft robots, *Int. J. Adv. Robot. Syst.* 12 (2015) 68.
- [26] C. Laschi, B. Mazzolai, M. Cianchetti, Soft robotics: Technologies and systems pushing the boundaries of robot abilities, *Sci. Robot.* 1 (2016).
- [27] S. Kim, C. Laschi, B. Trimmer, Soft robotics: a bioinspired evolution in robotics, *Trends Biotechnol.* 31 (2013) 287–294.
- [28] H. Wang, M. Totaro, L. Beccai, Toward perceptive soft robots: Progress and challenges, *Adv. Sci.* 5 (2018) 1800541.
- [29] S. Coyle, C. Majidi, P. LeDuc, K.J. Hsia, Bio-inspired soft robotics: Material selection, actuation, and design, *Extrem. Mech. Lett.* 22 (2018) 51–59.
- [30] W. McMahan, B.A. Jones, I.D. Walker, Design and implementation of a multi-section continuum robot: Air-actor, in: 2005 IEEE/RSJ Int. Conf. Intell. Robot. Syst., IEEE, 2005: pp. 2578–2585.
- [31] M. Rolf, J.J. Steil, Constant curvature continuum kinematics as fast approximate model for the Bionic Handling Assistant, in: 2012 IEEE/RSJ Int. Conf. Intell. Robot. Syst., IEEE, 2012: pp. 3440–3446.
- [32] H. Yang, M. Xu, W. Li, S. Zhang, Design and implementation of a soft robotic arm driven by SMA coils, *IEEE Trans. Ind. Electron.* 66 (2018) 6108–6116.
- [33] M.W. Gifari, H. Naghibi, S. Stramigioli, M. Abayazid, A review on recent advances in soft surgical robots for endoscopic applications, *Int. J. Med. Robot. Comput. Assist. Surg.* 15 (2019) e2010.
- [34] W. Dou, G. Zhong, J. Cao, Z. Shi, B. Peng, L. Jiang, Soft Robotic Manipulators: Designs, Actuation, Stiffness Tuning, and Sensing, *Adv. Mater. Technol.* (2021) 2100018.
- [35] I. Hussain, M. Malvezzi, D. Gan, Z. Iqbal, L. Seneviratne, D. Prattichizzo, F. Renda, Compliant gripper design, prototyping, and modeling using screw theory formulation, *Int. J. Rob. Res.* (2020) 0278364920947818.
- [36] L.U. Odhner, L.P. Jentoft, M.R. Claffee, N. Corson, Y. Tenzer, R.R. Ma, M. Buehler, R. Kohout, R.D. Howe, A.M. Dollar, A compliant, underactuated hand for robust manipulation, *Int. J. Rob. Res.* 33 (2014) 736–752.
- [37] A. Thallemer, D. Diensthuber, Gripper device for gripping objects, 2012. <https://patents.google.com/patent/EP2735409A1/en>.
- [38] Soft Robotics Inc., Soft Robotics Inc., (n.d.). <https://www.softroboticsinc.com/> (accessed April 30, 2020).
- [39] J. Shintake, S. Rosset, B. Schubert, D. Floreano, H. Shea, Versatile soft grippers with intrinsic electroadhesion based on multifunctional polymer actuators, *Adv. Mater.* 28 (2016) 231–238.
- [40] J. Guo, C. Xiang, J. Rossiter, A soft and shape-adaptive electroadhesive composite gripper with proprioceptive and exteroceptive capabilities, *Mater. Des.* 156 (2018) 586–587.
- [41] E. Brown, N. Rodenberg, J. Amend, A. Mozeika, E. Steltz, M.R. Zakin, H. Lipson, H.M. Jaeger, Universal robotic gripper based on the jamming of granular material, *Proc. Natl. Acad. Sci.* 107 (2010) 18809–18814.
- [42] G. Kofod, W. Wirges, M. Paajanen, S. Bauer, Energy minimization for self-organized structure formation and actuation, *Appl. Phys. Lett.* 90 (2007) 81916.
- [43] J. Hughes, U. Culha, F. Giardina, F. Guenther, A. Rosendo, F. Iida, Soft manipulators and grippers: a review, *Front. Robot. AI*. 3 (2016) 69.
- [44] J. Shintake, V. Cacucciolo, D. Floreano, H. Shea, Soft Robotic Grippers, *Adv. Mater.* 30 (2018). <https://doi.org/10.1002/adma.201707035>.
- [45] B. Zhang, Y. Xie, J. Zhou, K. Wang, Z. Zhang, State-of-the-art robotic grippers, grasping and control strategies, as well as their applications in agricultural robots: A review, *Comput. Electron. Agric.* 177 (2020) 105694.
- [46] M. Cianchetti, C. Laschi, A. Menciassi, P. Dario, Biomedical applications of soft robotics, *Nat. Rev. Mater.* 3 (2018) 143–153.
- [47] M. Runciman, A. Darzi, G.P. Mylonas, Soft robotics in minimally invasive surgery, *Soft Robot.* 6 (2019) 423–443.
- [48] M. Sitti, Miniature soft robots—road to the clinic, *Nat. Rev. Mater.* 3 (2018) 74–75.
- [49] E.T. Roche, M.A. Horvath, I. Wamala, A.

- Alazmani, S.-E. Song, W. Whyte, Z. Machaidze, C.J. Payne, J.C. Weaver, G. Fishbein, Soft robotic sleeve supports heart function, *Sci. Transl. Med.* 9 (2017).
- [50] I. Baldoli, A. Cuttano, R.T. Scaramuzzo, S. Tognarelli, M. Ciantelli, F. Cecchi, M. Gentile, E. Sigali, C. Laschi, P. Ghirri, A novel simulator for mechanical ventilation in newborns: MEchatronic REspiratory System SImluator for Neonatal Applications, *Proc. Inst. Mech. Eng. Part H J. Eng. Med.* 229 (2015) 581–591.
- [51] C.Y. Chu, R.M. Patterson, Soft robotic devices for hand rehabilitation and assistance: A narrative review, *J. Neuroeng. Rehabil.* 15 (2018) 1–14. <https://doi.org/10.1186/s12984-018-0350-6>.
- [52] Y. Kim, S.S. Cheng, A. Ecins, C. Fermüller, K.P. Westlake, J.P. Desai, Towards a robotic hand rehabilitation exoskeleton for stroke therapy, in: *Dyn. Syst. Control Conf.*, American Society of Mechanical Engineers, 2014: p. V001T04A006.
- [53] A.J. Veale, S.Q. Xie, Towards compliant and wearable robotic orthoses: A review of current and emerging actuator technologies, *Med. Eng. Phys.* 38 (2016) 317–325. <https://doi.org/10.1016/j.medengphy.2016.01.010>.
- [54] T. Shahid, D. Gouwanda, S.G. Nurzaman, A.A. Gopalai, Moving toward soft robotics: A decade review of the design of hand exoskeletons, *Biomimetics*. 3 (2018). <https://doi.org/10.3390/biomimetics3030017>.
- [55] J. Ortiz, E. Rocon, V. Power, A. de Eyto, L. O'Sullivan, M. Wirz, C. Bauer, S. Schülein, K.S. Stadler, B. Mazzolai, Xosoft-a vision for a soft modular lower limb exoskeleton, in: *Wearable Robot. Challenges Trends*, Springer, 2017: pp. 83–88.
- [56] N. Agharese, T. Cloyd, L.H. Blumenschein, M. Raitor, E.W. Hawkes, H. Culbertson, A.M. Okamura, HapWRAP: Soft growing wearable haptic device, in: *2018 IEEE Int. Conf. Robot. Autom.*, IEEE, 2018: pp. 5466–5472.
- [57] S. Jadhav, V. Kannanda, B. Kang, M.T. Tolley, J.P. Schulze, Soft robotic glove for kinesthetic haptic feedback in virtual reality environments, *Electron. Imaging.* 2017 (2017) 19–24.
- [58] C. Rognon, M. Koehler, C. Duriez, D. Floreano, A.M. Okamura, Soft haptic device to render the sensation of flying like a drone, *IEEE Robot. Autom. Lett.* 4 (2019) 2524–2531.
- [59] E.H. Skorina, M. Luo, C.D. Onal, A soft robotic wearable wrist device for kinesthetic haptic feedback, *Front. Robot. AI.* 5 (2018) 83.
- [60] T. Ashuri, A. Armani, R. Jalilzadeh Hamidi, T. Reasnor, S. Ahmadi, K. Iqbal, Biomedical soft robots: current status and perspective, *Biomed. Eng. Lett.* 10 (2020) 369–385.
- [61] J.-H. Hsiao, J.-Y. Chang, C.-M. Cheng, Soft medical robotics: clinical and biomedical applications, challenges, and future directions, *Adv. Robot.* 33 (2019) 1099–1111.
- [62] Y. Zhang, M. Lu, A review of recent advancements in soft and flexible robots for medical applications, *Int. J. Med. Robot. Comput. Assist. Surg.* 16 (2020) e2096.
- [63] J. Yin, R. Hinche, H. Shea, C. Majidi, Wearable Soft Technologies for Haptic Sensing and Feedback, *Adv. Funct. Mater.* (2020) 2007428.
- [64] C. Thalman, P. Artemiadis, A review of soft wearable robots that provide active assistance: trends, common actuation methods, fabrication, and applications, *Wearable Technol.* 1 (2020).
- [65] F. Renda, M. Giorelli, M. Calisti, M. Cianchetti, C. Laschi, Dynamic model of a multibending soft robot arm driven by cables, *IEEE Trans. Robot.* 30 (2014) 1109–1122.
- [66] A. Al-Ibadi, S. Nefti-Meziani, S. Davis, T. Theodoridis, Novel design and position control strategy of a soft robot arm, *Robotics.* 7 (2018) 72.
- [67] P. Polygerinos, Z. Wang, K.C. Galloway, R.J. Wood, C.J. Walsh, Soft robotic glove for combined assistance and at-home rehabilitation, *Rob. Auton. Syst.* 73 (2015) 135–143.
- [68] T.E.T. Seah, T.N. Do, N. Takeshita, K.Y. Ho, S.J. Phee, Future of flexible robotic endoscopy systems, *ArXiv Prepr. ArXiv1703.05569.* (2017).
- [69] M. Wehner, R.L. Truby, D.J. Fitzgerald, B. Mosadegh, G.M. Whitesides, J.A. Lewis, R.J. Wood, An integrated design and fabrication strategy for entirely soft, autonomous robots, *Nature.* 536 (2016) 451–455.
- [70] Empire Robotics, Empire Robotics, (n.d.). <https://www.empirerobotics.com/products/> (accessed April 30, 2020).
- [71] OnRobot, OnRobot, (n.d.). <https://onrobot.com/en/products/soft-gripper> (accessed November 19, 2021).
- [72] S. Li, H. Bai, R.F. Shepherd, H. Zhao, Bio-inspired Design and Additive Manufacturing of Soft Materials, Machines, Robots, and Haptic Interfaces, *Angew. Chemie Int. Ed.* 58 (2019) 11182–11204.
- [73] J.T. Muth, D.M. Vogt, R.L. Truby, Y. Mengüç, D.B. Kolesky, R.J. Wood, J.A. Lewis, Embedded 3D printing of strain sensors within highly stretchable elastomers, *Adv. Mater.* 26 (2014) 6307–

- 6312.
- [74] J. Paek, I. Cho, J. Kim, Microrobotic tentacles with spiral bending capability based on shape-engineered elastomeric microtubes, *Sci. Rep.* 5 (2015) 1–11.
- [75] R.F. Shepherd, F. Ilievski, W. Choi, S.A. Morin, A.A. Stokes, A.D. Mazzeo, X. Chen, M. Wang, G.M. Whitesides, Multigait soft robot, *Proc. Natl. Acad. Sci.* 108 (2011) 20400–20403.
- [76] I.D. Rukhlenko, S. Farajikah, C. Lilley, A. Georgis, M. Large, S. Fleming, Performance optimization of polymer fibre actuators for soft robotics, *Polymers (Basel)*. 12 (2020) 454.
- [77] H. Koshima, Mechanically Responsive Materials for Soft Robotics, (2019).
- [78] C. Majidi, Soft-matter engineering for soft robotics, *Adv. Mater. Technol.* 4 (2019) 1800477.
- [79] J.A.-C. Liu, J.H. Gillen, S.R. Mishra, B.A. Evans, J.B. Tracy, Photothermally and magnetically controlled reconfiguration of polymer composites for soft robotics, *Sci. Adv.* 5 (2019) eaaw2897.
- [80] S.M. Mirvakili, A. Leroy, D. Sim, E.N. Wang, Solar-Driven Soft Robots, *Adv. Sci.* 8 (2021) 2004235.
- [81] S. Taccola, F. Greco, E. Sinibaldi, A. Mondini, B. Mazzolai, V. Mattoli, Toward a new generation of electrically controllable hygromorphic soft actuators, *Adv. Mater.* 27 (2015) 1668–1675.
- [82] F. Daerden, D. Lefever, Pneumatic artificial muscles: actuators for robotics and automation, *Eur. J. Mech. Environ. Eng.* 47 (2002) 11–21.
- [83] Y. Lee, W.J. Song, J.-Y. Sun, Hydrogel soft robotics, *Mater. Today Phys.* 15 (2020) 100258.
- [84] H. Yuk, S. Lin, C. Ma, M. Takaffoli, N.X. Fang, X. Zhao, Hydraulic hydrogel actuators and robots optically and sonically camouflaged in water, *Nat. Commun.* 8 (2017) 1–12.
- [85] Y. Takishima, K. Yoshida, A. Khosla, M. Kawakami, H. Furukawa, Fully 3D-Printed Hydrogel Actuator for Jellyfish Soft Robots, *ECS J. Solid State Sci. Technol.* 10 (2021) 37002.
- [86] R. Niyyama, D. Rus, S. Kim, Pouch motors: Printable/inflatable soft actuators for robotics, in: 2014 IEEE Int. Conf. Robot. Autom., IEEE, 2014: pp. 6332–6337.
- [87] J. Shintake, H. Sonar, E. Piskarev, J. Paik, D. Floreano, Soft pneumatic gelatin actuator for edible robotics, in: 2017 IEEE/RSJ Int. Conf. Intell. Robot. Syst., IEEE, 2017: pp. 6221–6226.
- [88] K. Takashima, K. Sugitani, N. Morimoto, S. Sakaguchi, T. Noritsugu, T. Mukai, Pneumatic artificial rubber muscle using shape-memory polymer sheet with embedded electrical heating wire, *Smart Mater. Struct.* 23 (2014) 125005.
- [89] N. Bira, P. Dhagat, J.R. Davidson, A Review of Magnetic Elastomers and Their Role in Soft Robotics, *Front. Robot. AI*. 7 (2020) 146.
- [90] W. Hu, W. Li, G. Alici, 3D printed helical soft pneumatic actuators, in: 2018 IEEE/ASME Int. Conf. Adv. Intell. Mechatronics, IEEE, 2018: pp. 950–955.
- [91] C. Tawk, G.M. Spinks, M. in het Panhuis, G. Alici, 3D Printable Linear Soft Vacuum Actuators: Their Modeling, Performance Quantification and Application in Soft Robotic Systems, *IEEE/ASME Trans. Mechatronics*. 24 (2019) 2118–2129.
- [92] S. Kim, S. Kim, H. Majditehran, D.K. Patel, C. Majidi, S. Bergbreiter, Electromechanical characterization of 3D printable conductive elastomer for soft robotics, in: 2020 3rd IEEE Int. Conf. Soft Robot., IEEE, 2020: pp. 318–324.
- [93] J.E. Slightam, V.R. Gervasi, Novel integrated fluid-power actuators for functional end-use components and systems via selective laser sintering nylon 12, in: 23rd Ann Int Solid Free. Fabr. Symp, 2012: pp. 197–211.
- [94] Q. Zhang, S. Weng, Z. Zhao, H.J. Qi, D. Fang, Soft pneumatic actuators by digital light processing combined with injection-assisted post-curing, *Appl. Math. Mech.* (2021) 1–14.
- [95] O.D. Yirmibesoglu, J. Morrow, S. Walker, W. Gosrich, R. Cañizares, H. Kim, U. Daalkhaijav, C. Fleming, C. Branyan, Y. Menguc, Direct 3D printing of silicone elastomer soft robots and their performance comparison with molded counterparts, in: 2018 IEEE Int. Conf. Soft Robot., IEEE, 2018: pp. 295–302.
- [96] E. Sachyani Keneth, A. Kamyshny, M. Totaro, L. Beccai, S. Magdassi, 3D Printing Materials for Soft Robotics, *Adv. Mater.* (2020) 2003387.
- [97] T. Nagai, J. Shintake, Characterization of Bio-Degradable Materials for Soft Robotics, in: 2019 Int. Symp. Micro-NanoMechatronics Hum. Sci., IEEE, 2019: pp. 1–3.
- [98] J. Rossiter, J. Winfield, I. Ieropoulos, Here today, gone tomorrow: biodegradable soft robots, in: Electroact. Polym. Actuators Devices 2016, International Society for Optics and Photonics, 2016: p. 97981S.
- [99] S. Walker, J. Rueben, T. Van Volkenburg, S. Hemleben, C. Grimm, J. Simonsen, Y. Mengüç, Using an environmentally benign and degradable elastomer in soft robotics, *Int. J. Intell. Robot. Appl.* 1 (2017) 124–142.

- [100] Z. Shen, F. Chen, X. Zhu, K.-T. Yong, G. Gu, Stimuli-responsive functional materials for soft robotics, *J. Mater. Chem. B*. 8 (2020) 8972–8991.
- [101] G. Stano, G. Percoco, Additive manufacturing aimed to soft robots fabrication: A review, *Extrem. Mech. Lett.* (2020) 101079.
- [102] J. Walker, T. Zidek, C. Harbel, S. Yoon, F.S. Strickland, S. Kumar, M. Shin, Soft robotics: a review of recent developments of pneumatic soft actuators, in: *Actuators, Multidisciplinary Digital Publishing Institute*, 2020: p. 3.
- [103] M. Calisti, M. Giorelli, G. Levy, B. Mazzolai, B. Hochner, C. Laschi, P. Dario, An octopus-bioinspired solution to movement and manipulation for soft robots, *Bioinspir. Biomim.* 6 (2011) 36002.
- [104] Y. Hu, S. Leigh, P. Maes, Hand development kit: Soft robotic fingers as prosthetic augmentation of the hand, in: *Adjunct. Publ. 30th Annu. ACM Symp. User Interface Softw. Technol.*, 2017: pp. 27–29.
- [105] M. Munadi, M. Ariyanto, J.D. Setiawan, M.F. Al Ayubi, Development of a low-cost quadrupedal starfish soft robot, in: *2018 5th Int. Conf. Inf. Technol. Comput. Electr. Eng.*, IEEE, 2018: pp. 225–229.
- [106] Y. Li, Y. Chen, T. Ren, Y. Li, S.H. Choi, Precharged pneumatic soft actuators and their applications to untethered soft robots, *Soft Robot.* 5 (2018) 567–575.
- [107] C. Cheng, J. Cheng, W. Huang, Design and development of a novel SMA actuated multi-DOF soft robot, *IEEE Access.* 7 (2019) 75073–75080.
- [108] S. Kim, E. Hawkes, K. Choy, M. Joldaz, J. Foleyz, R. Wood, Micro artificial muscle fiber using NiTi spring for soft robotics, in: *2009 IEEE/RSJ Int. Conf. Intell. Robot. Syst.*, IEEE, 2009: pp. 2228–2234.
- [109] H.-I. Kim, M.-W. Han, S.-H. Song, S.-H. Ahn, Soft morphing hand driven by SMA tendon wire, *Compos. Part B Eng.* 105 (2016) 138–148.
- [110] H. Jin, E. Dong, G. Aliche, S. Mao, X. Min, C. Liu, K.H. Low, J. Yang, A starfish robot based on soft and smart modular structure (SMS) actuated by SMA wires, *Bioinspir. Biomim.* 11 (2016) 56012.
- [111] A. Lendlein, S. Kelch, Shape-memory polymers, *Angew. Chemie Int. Ed.* 41 (2002) 2034–2057.
- [112] T. Xie, Recent advances in polymer shape memory, *Polymer (Guildf).* 52 (2011) 4985–5000.
- [113] M. Zarek, M. Layani, I. Cooperstein, E. Sachyani, D. Cohn, S. Magdassi, 3D printing of shape memory polymers for flexible electronic devices, *Adv. Mater.* 28 (2016) 4449–4454.
- [114] Y. Yang, Y. Chen, Y. Wei, Y. Li, 3D printing of shape memory polymer for functional part fabrication, *Int. J. Adv. Manuf. Technol.* 84 (2016) 2079–2095.
- [115] Y. Guo, Z. Lv, Y. Huo, L. Sun, S. Chen, Z. Liu, C. He, X. Bi, X. Fan, Z. You, A biodegradable functional water-responsive shape memory polymer for biomedical applications, *J. Mater. Chem. B*. 7 (2019) 123–132.
- [116] W. Sokolowski, A. Metcalfe, S. Hayashi, J. Raymond, Medical applications of shape memory polymers, *Biomed. Mater.* 2 (2007) S23.
- [117] J. Fan, G. Li, High performance and tunable artificial muscle based on two-way shape memory polymer, *RSC Adv.* 7 (2017) 1127–1136.
- [118] K. Takashima, J. Rossiter, T. Mukai, McKibben artificial muscle using shape-memory polymer, *Sensors Actuators A Phys.* 164 (2010) 116–124.
- [119] Y. Yang, Y. Chen, Novel design and 3D printing of variable stiffness robotic fingers based on shape memory polymer, in: *2016 6th IEEE Int. Conf. Biomed. Robot. Biomechatronics*, IEEE, 2016: pp. 195–200.
- [120] M. Barnes, R. Verduzco, Direct shape programming of liquid crystal elastomers, *Soft Matter.* 15 (2019) 870–879.
- [121] J.M. Boothby, J.C. Gagnon, E. McDowell, T. Van Volkenburg, L. Currano, Z. Xia, An Untethered Soft Robot Based on Liquid Crystal Elastomers, *Soft Robot.* (2021).
- [122] H. Shahsavani, L. Yu, A. Jákli, B. Zhao, Smart biomimetic micro/nanostructures based on liquid crystal elastomers and networks, *Soft Matter.* 13 (2017) 8006–8022.
- [123] C. Yuan, D.J. Roach, C.K. Dunn, Q. Mu, X. Kuang, C.M. Yakacki, T.J. Wang, K. Yu, H.J. Qi, 3D printed reversible shape changing soft actuators assisted by liquid crystal elastomers, *Soft Matter.* 13 (2017) 5558–5568.
- [124] C.P. Ambulo, S. Tasnim, S. Wang, M.K. Abdelrahman, P.E. Zimmern, T.H. Ware, Processing advances in liquid crystal elastomers provide a path to biomedical applications, *J. Appl. Phys.* 128 (2020) 140901.
- [125] H. Banerjee, H. Ren, Optimizing double-network hydrogel for biomedical soft robots, *Soft Robot.* 4 (2017) 191–201.
- [126] J. Li, D.J. Mooney, Designing hydrogels for controlled drug delivery, *Nat. Rev. Mater.* 1 (2016) 1–17.
- [127] X. Peng, H. Wang, Shape changing hydrogels and their applications as soft actuators, *J. Polym. Sci. Part B Polym.*

- Phys. 56 (2018) 1314–1324.
- [128] H. Al-Fahaam, S. Davis, S. Nefti-Meziani, Wrist rehabilitation exoskeleton robot based on pneumatic soft actuators, in: 2016 Int. Conf. Students Appl. Eng., IEEE, 2016: pp. 491–496.
- [129] L. Wang, G. Peng, W. Yao, S. Biggar, C. Hu, X. Yin, Y. Fan, Soft robotics for hand rehabilitation, in: Intell. Biomechatronics Neurorehabilitation, Elsevier, 2020: pp. 167–176.
- [130] A. Bartow, A. Kapadia, I. Walker, A novel continuum trunk robot based on contractor muscles, in: Proc. 12th WSEAS Int. Conf. Signal Process. Robot. Autom., 2013: pp. 181–186.
- [131] A.D. Marchese, R.K. Katzschmann, D. Rus, A recipe for soft fluidic elastomer robots, *Soft Robot.* 2 (2015) 7–25.
- [132] R. Deimel, O. Brock, Soft hands for reliable grasping strategies, in: *Soft Robot.*, Springer, 2015: pp. 211–221.
- [133] P. Polygerinos, S. Lyne, Z. Wang, L.F. Nicolini, B. Mosadegh, G.M. Whitesides, C.J. Walsh, Towards a soft pneumatic glove for hand rehabilitation, in: 2013 IEEE/RSJ Int. Conf. Intell. Robot. Syst., IEEE, 2013: pp. 1512–1517.
- [134] S.K. Talas, B.A. Baydere, T. Altinsoy, C. Tutcu, E. Samur, Design and Development of a Growing Pneumatic Soft Robot, *Soft Robot.* 7 (2020) 521–533.
- [135] R. Xie, M. Su, Y. Zhang, M. Li, H. Zhu, Y. Guan, PISRob: A pneumatic soft robot for locomoting like an inchworm, in: 2018 IEEE Int. Conf. Robot. Autom., IEEE, 2018: pp. 3448–3453.
- [136] P. Polygerinos, N. Correll, S.A. Morin, B. Mosadegh, C.D. Onal, K. Petersen, M. Cianchetti, M.T. Tolley, R.F. Shepherd, Soft robotics: Review of fluid-driven intrinsically soft devices; manufacturing, sensing, control, and applications in human-robot interaction, *Adv. Eng. Mater.* 19 (2017) 1700016.
- [137] K. Jung, J.C. Koo, Y.K. Lee, H.R. Choi, Artificial annelid robot driven by soft actuators, *Bioinspir. Biomim.* 2 (2007) S42.
- [138] Y. Guo, L. Liu, Y. Liu, J. Leng, Review of Dielectric Elastomer Actuators and Their Applications in Soft Robots, *Adv. Intell. Syst.* (2021) 2000282.
- [139] Z.J. Olsen, K.J. Kim, Design and modeling of a new biomimetic soft robotic jellyfish using IPMC-based electroactive polymers, *Front. Robot. AI.* 6 (2019) 112.
- [140] H. Wang, J. Chen, H.Y.K. Lau, H. Ren, Motion planning based on learning from demonstration for multiple-segment flexible soft robots actuated by electroactive polymers, *IEEE Robot. Autom. Lett.* 1 (2016) 391–398.
- [141] A. Sadeghi, L. Beccai, B. Mazzolai, Innovative soft robots based on electro-rheological fluids, in: 2012 IEEE/RSJ Int. Conf. Intell. Robot. Syst., IEEE, 2012: pp. 4237–4242.
- [142] S. Qi, H. Guo, J. Fu, Y. Xie, M. Zhu, M. Yu, 3D printed shape-programmable magneto-active soft matter for biomimetic applications, *Compos. Sci. Technol.* 188 (2020) 107973.
- [143] J.G. Kim, J.E. Park, S. Won, J. Jeon, J.J. Wie, Contactless manipulation of soft robots, *Materials (Basel).* 12 (2019) 3065.
- [144] K.Y. Ma, P. Chirarattananon, S.B. Fuller, R.J. Wood, Controlled flight of a biologically inspired, insect-scale robot, *Science (80-.).* 340 (2013) 603–607.
- [145] J.W. Sohn, S.B. Choi, Various Robots Made from Piezoelectric Materials and Electroactive Polymers: A Review, *Int J Mech Syst Eng.* 3 (2017) 2.
- [146] Y. Wu, J.K. Yim, J. Liang, Z. Shao, M. Qi, J. Zhong, Z. Luo, X. Yan, M. Zhang, X. Wang, Insect-scale fast moving and ultrarobust soft robot, *Sci. Robot.* 4 (2019) eaax1594.
- [147] F. Ercole, T.P. Davis, R.A. Evans, Photo-responsive systems and biomaterials: photochromic polymers, light-triggered self-assembly, surface modification, fluorescence modulation and beyond, *Polym. Chem.* 1 (2010) 37–54.
- [148] H.Y. Jiang, S. Kelch, A. Lendlein, Polymers move in response to light, *Adv. Mater.* 18 (2006) 1471–1475.
- [149] J. Wei, Y. Yu, Photodeformable polymer gels and crosslinked liquid-crystalline polymers, *Soft Matter.* 8 (2012) 8050–8059.
- [150] J.J. Wie, M.R. Shankar, T.J. White, Photomotility of polymers, *Nat. Commun.* 7 (2016) 1–8.
- [151] B. Wang, Y. Zhang, L. Zhang, Recent progress on micro-and nano-robots: Towards in vivo tracking and localization, *Quant. Imaging Med. Surg.* 8 (2018) 461.
- [152] N.W. Bartlett, M.T. Tolley, J.T.B. Overvelde, J.C. Weaver, B. Mosadegh, K. Bertoldi, G.M. Whitesides, R.J. Wood, A 3D-printed, functionally graded soft robot powered by combustion, *Science (80-.).* 349 (2015) 161–165.
- [153] R.F. Shepherd, A.A. Stokes, J. Freake, J. Barber, P.W. Snyder, A.D. Mazzeo, L. Cademartiri, S.A. Morin, G.M. Whitesides, Using explosions to power a soft robot, *Angew. Chemie Int. Ed.* 52 (2013) 2892–2896.
- [154] M.T. Tolley, R.F. Shepherd, M. Karpelson, N.W. Bartlett, K.C. Galloway, M. Wehner, R. Nunes, G.M. Whitesides, R.J. Wood, An

- untethered jumping soft robot, in: 2014 IEEE/RSJ Int. Conf. Intell. Robot. Syst., IEEE, 2014: pp. 561–566.
- [155] P. Boyraz, G. Runge, A. Raatz, An overview of novel actuators for soft robotics, in: Actuators, Multidisciplinary Digital Publishing Institute, 2018: p. 48.
- [156] N. El-Atab, R.B. Mishra, F. Al-Modaf, L. Joharji, A.A. Alsharif, H. Alamoudi, M. Diaz, N. Qaiser, M.M. Hussain, Soft Actuators for Soft Robotic Applications: A Review, *Adv. Intell. Syst.* 2 (2020) 2000128.
- [157] J. Kim, J.W. Kim, H.C. Kim, L. Zhai, H.-U. Ko, R.M. Muthoka, Review of soft actuator materials, *Int. J. Precis. Eng. Manuf.* 20 (2019) 2221–2241.
- [158] S. Mousavi, D. Howard, F. Zhang, J. Leng, C.H. Wang, Direct 3D printing of highly anisotropic, flexible, constriction-resistive sensors for multidirectional proprioception in soft robots, *ACS Appl. Mater. Interfaces*. 12 (2020) 15631–15643.
- [159] B. Shih, J. Mayeda, Z. Huo, C. Christianson, M.T. Tolley, 3D printed resistive soft sensors, in: 2018 IEEE Int. Conf. Soft Robot., IEEE, 2018: pp. 152–157.
- [160] B. Shih, C. Christianson, K. Gillespie, S. Lee, J. Mayeda, Z. Huo, M.T. Tolley, Design considerations for 3D printed, soft, multimaterial resistive sensors for soft robotics, *Front. Robot. AI*. 6 (2019) 30.
- [161] H. Khanbareh, K. de Boom, B. Schelen, R.B.N. Scharff, C.C.L. Wang, S. van der Zwaag, P. Groen, Large area and flexible micro-porous piezoelectric materials for soft robotic skin, *Sensors Actuators A Phys.* 263 (2017) 554–562.
- [162] J. Shintake, E. Piskarev, S.H. Jeong, D. Floreano, Ultrastretchable strain sensors using carbon black-filled elastomer composites and comparison of capacitive versus resistive sensors, *Adv. Mater. Technol.* 3 (2018) 1700284.
- [163] H.A. Sonar, J. Paik, Soft pneumatic actuator skin with piezoelectric sensors for vibrotactile feedback, *Front. Robot. AI*. 2 (2016) 38.
- [164] K. Song, S.H. Kim, S. Jin, S. Kim, S. Lee, J.-S. Kim, J.-M. Park, Y. Cha, Pneumatic actuator and flexible piezoelectric sensor for soft virtual reality glove system, *Sci. Rep.* 9 (2019) 1–8.
- [165] C.B. Cooper, K. Arutselvan, Y. Liu, D. Armstrong, Y. Lin, M.R. Khan, J. Genzer, M.D. Dickey, Stretchable capacitive sensors of torsion, strain, and touch using double helix liquid metal fibers, *Adv. Funct. Mater.* 27 (2017) 1605630.
- [166] S.E. Navarro, S. Nagels, H. Alagi, L.-M. Faller, O. Goury, T. Morales-Bieze, H. Zangl, B. Hein, R. Ramakers, W. Deferme, A model-based sensor fusion approach for force and shape estimation in soft robotics, *IEEE Robot. Autom. Lett.* 5 (2020) 5621–5628.
- [167] E.L. White, M.C. Yuen, J.C. Case, R.K. Kramer, Low-Cost, facile, and scalable manufacturing of capacitive sensors for soft systems, *Adv. Mater. Technol.* 2 (2017) 1700072.
- [168] D.P.J. Cotton, I.M. Graz, S.P. Lacour, A multifunctional capacitive sensor for stretchable electronic skins, *IEEE Sens. J.* 9 (2009) 2008–2009.
- [169] A.P. Gerratt, H.O. Michaud, S.P. Lacour, Elastomeric electronic skin for prosthetic tactile sensation, *Adv. Funct. Mater.* 25 (2015) 2287–2295.
- [170] H. Bai, S. Li, J. Barreiros, Y. Tu, C.R. Pollock, R.F. Shepherd, Stretchable distributed fiber-optic sensors, *Science* (80-.). 370 (2020) 848–852.
- [171] K.C. Galloway, Y. Chen, E. Templeton, B. Rife, I.S. Godage, E.J. Barth, Fiber optic shape sensing for soft robotics, *Soft Robot.* 6 (2019) 671–684.
- [172] M. Totaro, A. Mondini, A. Bellacicca, P. Milani, L. Beccai, Integrated simultaneous detection of tactile and bending cues for soft robotics, *Soft Robot.* 4 (2017) 400–410.
- [173] H. Zhao, K. O'Brien, S. Li, R.F. Shepherd, Optoelectronically innervated soft prosthetic hand via stretchable optical waveguides, *Sci. Robot.* 1 (2016) eaai7529.
- [174] S. Sareh, A. Jiang, A. Faragasso, Y. Noh, T. Nanayakkara, P. Dasgupta, L. Seneviratne, H. Wurdemann, K. Althoefer, Bio-inspired tactile sensor sleeve for soft surgical manipulators, in: IEEE Int. Conf. Robot. Autom. (ICRA), Hong Kong, China, 2014.
- [175] A. Alfadhel, J. Kosel, Magnetic nanocomposite cilia tactile sensor, *Adv. Mater.* 27 (2015) 7888–7892.
- [176] T. Hellebrekers, N. Chang, K. Chin, M.J. Ford, O. Kroemer, C. Majidi, Soft magnetic tactile skin for continuous force and location estimation using neural networks, *IEEE Robot. Autom. Lett.* 5 (2020) 3892–3898.
- [177] X. Wang, F. Gordanejad, M. Calgar, Y. Liu, J. Sutrisno, A. Fuchs, Sensing behavior of magnetorheological elastomers, *J. Mech. Des.* 131 (2009).
- [178] H. Wang, D. Jones, G. de Boer, J. Kow, L. Beccai, A. Alazmani, P. Culmer, Design and characterization of tri-axis soft inductive tactile sensors, *IEEE Sens. J.* 18 (2018) 7793–7801.
- [179] H. Wang, J. Kow, N. Raske, G. De Boer, M. Ghajari, R. Hewson, A. Alazmani, P. Culmer, Robust and high-performance soft inductive tactile sensors based on the Eddy-current effect, *Sensors Actuators A Phys.*

- 271 (2018) 44–52.
- [180] H. Wang, M. Totaro, A.A. Blandin, L. Beccai, A wireless inductive sensing technology for soft pneumatic actuators using magnetorheological elastomers, in: 2019 2nd IEEE Int. Conf. Soft Robot., IEEE, 2019: pp. 242–248.
- [181] R.K. Kramer, Soft electronics for soft robotics, in: Micro-and Nanotechnol. Sensors, Syst. Appl. VII, International Society for Optics and Photonics, 2015: p. 946707.
- [182] H. Jang, Y.J. Park, X. Chen, T. Das, M. Kim, J. Ahn, Graphene-based flexible and stretchable electronics, *Adv. Mater.* 28 (2016) 4184–4202.
- [183] Y. Liu, M. Pharr, G.A. Salvatore, Lab-on-skin: a review of flexible and stretchable electronics for wearable health monitoring, *ACS Nano.* 11 (2017) 9614–9635.
- [184] D.-H. Kim, R. Ghaffari, N. Lu, J.A. Rogers, Flexible and stretchable electronics for biointegrated devices, *Annu. Rev. Biomed. Eng.* 14 (2012) 113–128.
- [185] M.G. Mohammed, R. Kramer, All-printed flexible and stretchable electronics, *Adv. Mater.* 29 (2017) 1604965.
- [186] J. Yoon, S. Jo, I.S. Chun, I. Jung, H.-S. Kim, M. Meitl, E. Menard, X. Li, J.J. Coleman, U. Paik, GaAs photovoltaics and optoelectronics using releasable multilayer epitaxial assemblies, *Nature.* 465 (2010) 329–333.
- [187] K. Park, J.H. Son, G. Hwang, C.K. Jeong, J. Ryu, M. Koo, I. Choi, S.H. Lee, M. Byun, Z.L. Wang, Highly-efficient, flexible piezoelectric PZT thin film nanogenerator on plastic substrates, *Adv. Mater.* 26 (2014) 2514–2520.
- [188] S. Wang, L. Lin, Z.L. Wang, Nanoscale triboelectric-effect-enabled energy conversion for sustainably powering portable electronics, *Nano Lett.* 12 (2012) 6339–6346.
- [189] S. Xu, Y. Qin, C. Xu, Y. Wei, R. Yang, Z.L. Wang, Self-powered nanowire devices, *Nat. Nanotechnol.* 5 (2010) 366–373.
- [190] V.L. Pushparaj, M.M. Shaijumon, A. Kumar, S. Murugesan, L. Ci, R. Vajtai, R.J. Linhardt, O. Nalamasu, P.M. Ajayan, Flexible energy storage devices based on nanocomposite paper, *Proc. Natl. Acad. Sci.* 104 (2007) 13574–13577.
- [191] J.-S. Kim, D. Ko, D.-J. Yoo, D.S. Jung, C.T. Yavuz, N.-I. Kim, I.-S. Choi, J.Y. Song, J.W. Choi, A half millimeter thick coplanar flexible battery with wireless recharging capability, *Nano Lett.* 15 (2015) 2350–2357.
- [192] L. Hu, H. Wu, F. La Mantia, Y. Yang, Y. Cui, Thin, flexible secondary Li-ion paper batteries, *ACS Nano.* 4 (2010) 5843–5848.
- [193] A.M. Gaikwad, A.M. Zamarayeva, J. Rousseau, H. Chu, I. Derin, D.A. Steingart, Highly stretchable alkaline batteries based on an embedded conductive fabric, *Adv. Mater.* 24 (2012) 5071–5076.
- [194] J. Liu, M. Chen, L. Zhang, J. Jiang, J. Yan, Y. Huang, J. Lin, H.J. Fan, Z.X. Shen, A flexible alkaline rechargeable Ni/Fe battery based on graphene foam/carbon nanotubes hybrid film, *Nano Lett.* 14 (2014) 7180–7187.
- [195] N. Lu, D.-H. Kim, Flexible and stretchable electronics paving the way for soft robotics, *Soft Robot.* 1 (2014) 53–62.
- [196] Y. Qi, J. Kim, T.D. Nguyen, B. Lisko, P.K. Purohit, M.C. McAlpine, Enhanced piezoelectricity and stretchability in energy harvesting devices fabricated from buckled PZT ribbons, *Nano Lett.* 11 (2011) 1331–1336.
- [197] H. Bikas, P. Stavropoulos, G. Chryssolouris, Additive manufacturing methods and modelling approaches: a critical review, *Int. J. Adv. Manuf. Technol.* 83 (2016) 389–405.
- [198] B. Mosadegh, P. Polygerinos, C. Keplinger, S. Wennstedt, R.F. Shepherd, U. Gupta, J. Shim, K. Bertoldi, C.J. Walsh, G.M. Whitesides, Pneumatic networks for soft robotics that actuate rapidly, *Adv. Funct. Mater.* 24 (2014) 2163–2170.
- [199] R. Mutlu, S.K. Yildiz, G. Alici, M. in het Panhuis, G.M. Spinks, Mechanical stiffness augmentation of a 3D printed soft prosthetic finger, in: 2016 IEEE Int. Conf. Adv. Intell. Mechatronics, IEEE, 2016: pp. 7–12.
- [200] H.K. Yap, H.Y. Ng, C.-H. Yeow, High-force soft printable pneumatics for soft robotic applications, *Soft Robot.* 3 (2016) 144–158.
- [201] M. Schaffner, J.A. Faber, L. Pianegonda, P.A. Rühs, F. Coulter, A.R. Studart, 3D printing of robotic soft actuators with programmable bioinspired architectures, *Nat. Commun.* 9 (2018) 1–9.
- [202] V. Chan, J.H. Jeong, P. Bajaj, M. Collens, T. Saif, H. Kong, R. Bashir, Multi-material bio-fabrication of hydrogel cantilevers and actuators with stereolithography, *Lab Chip.* 12 (2012) 88–98.
- [203] L. Ge, L. Dong, D. Wang, Q. Ge, G. Gu, A digital light processing 3D printer for fast and high-precision fabrication of soft pneumatic actuators, *Sensors Actuators A Phys.* 273 (2018) 285–292.
- [204] D. Han, C. Farino, C. Yang, T. Scott, D. Browne, W. Choi, J.W. Freeman, H. Lee, Soft robotic manipulation and locomotion with a 3D printed electroactive hydrogel, *ACS Appl. Mater. Interfaces.* 10 (2018) 17512–17518.
- [205] D. Drotman, S. Jadhav, M. Karimi, P. de

- Zonia, M.T. Tolley, 3D printed soft actuators for a legged robot capable of navigating unstructured terrain, in: 2017 IEEE Int. Conf. Robot. Autom., IEEE, 2017: pp. 5532–5538.
- [206] A. Zatopa, S. Walker, Y. Menguc, Fully soft 3D-printed electroactive fluidic valve for soft hydraulic robots, *Soft Robot.* 5 (2018) 258–271.
- [207] A. Rost, S. Schädle, The sls-generated soft robotic hand—an integrated approach using additive manufacturing and reinforcement learning, in: 2013 12th Int. Conf. Mach. Learn. Appl., IEEE, 2013: pp. 215–220.
- [208] A.M. Dollar, R.D. Howe, A robust compliant grasper via shape deposition manufacturing, *IEEE/ASME Trans. Mechatronics.* 11 (2006) 154–161.
- [209] J. Rossiter, P. Walters, B. Stoimenov, Printing 3D dielectric elastomer actuators for soft robotics, in: Electroact. Polym. Actuators Devices 2009, International Society for Optics and Photonics, 2009: p. 72870H.
- [210] A. Zolfagharian, A.Z. Kouzani, S.Y. Khoo, I. Gibson, A. Kaynak, 3D printed hydrogel soft actuators, in: 2016 IEEE Reg. 10 Conf., IEEE, 2016: pp. 2272–2277.
- [211] S.S. Robinson, K.W. O'Brien, H. Zhao, B.N. Peele, C.M. Larson, B.C. Mac Murray, I.M. Van Meerbeek, S.N. Dunham, R.F. Shepherd, Integrated soft sensors and elastomeric actuators for tactile machines with kinesthetic sense, *Extrem. Mech. Lett.* 5 (2015) 47–53.
- [212] H.-J. Kim, S.-H. Song, S.-H. Ahn, A turtle-like swimming robot using a smart soft composite (SSC) structure, *Smart Mater. Struct.* 22 (2012) 14007.
- [213] P. Maeder-York, T. Clites, E. Boggs, R. Neff, P. Polygerinos, D. Holland, L. Stirling, K. Galloway, C. Wee, C. Walsh, Biologically inspired soft robot for thumb rehabilitation, *J. Med. Device.* 8 (2014).
- [214] C.M. Schumacher, M. Loepfe, R. Fuhrer, R.N. Grass, W.J. Stark, 3D printed lost-wax casted soft silicone monoblocks enable heart-inspired pumping by internal combustion, *RSC Adv.* 4 (2014) 16039–16042.
- [215] S. Russo, T. Ranzani, C.J. Walsh, R.J. Wood, An additive millimeter-scale fabrication method for soft biocompatible actuators and sensors, *Adv. Mater. Technol.* 2 (2017) 1700135.
- [216] B.K. Sharma, B. Jang, J.E. Lee, S. Bae, T.W. Kim, H. Lee, J. Kim, J. Ahn, Load-controlled roll transfer of oxide transistors for stretchable electronics, *Adv. Funct. Mater.* 23 (2013) 2024–2032.
- [217] R.J. Wood, S. Avadhanula, R. Sahai, E. Steltz, R.S. Fearing, Microrobot design using fiber reinforced composites, *J. Mech. Des.* 130 (2008).
- [218] F. Ilievski, A.D. Mazzeo, R.F. Shepherd, X. Chen, G.M. Whitesides, Soft robotics for chemists, *Angew. Chemie.* 123 (2011) 1930–1935.
- [219] J.Z. Gul, M. Sajid, M.M. Rehman, G.U. Siddiqui, I. Shah, K.-H. Kim, J.-W. Lee, K.H. Choi, 3D printing for soft robotics—a review, *Sci. Technol. Adv. Mater.* 19 (2018) 243–262.
- [220] Y.L. Yap, S.L. Sing, W.Y. Yeong, A review of 3D printing processes and materials for soft robotics, *Rapid Prototyp. J.* (2020).
- [221] J. Choi, O.-C. Kwon, W. Jo, H.J. Lee, M.-W. Moon, 4D printing technology: a review, *3D Print. Addit. Manuf.* 2 (2015) 159–167.
- [222] F. Momeni, X. Liu, J. Ni, A review of 4D printing, *Mater. Des.* 122 (2017) 42–79.
- [223] W. Shan, Y. Chen, M. Hu, S. Qin, P. Liu, 4D printing of shape memory polymer via liquid crystal display (LCD) stereolithographic 3D printing, *Mater. Res. Express.* 7 (2020) 105305.
- [224] H. Wei, Q. Zhang, Y. Yao, L. Liu, Y. Liu, J. Leng, Direct-write fabrication of 4D active shape-changing structures based on a shape memory polymer and its nanocomposite, *ACS Appl. Mater. Interfaces.* 9 (2017) 876–883.
- [225] F. Liravi, E. Toyserkani, Additive manufacturing of silicone structures: A review and prospective, *Addit. Manuf.* 24 (2018) 232–242.
- [226] E.B. Joyee, Y. Pan, Multi-material additive manufacturing of functional soft robot, *Procedia Manuf.* 34 (2019) 566–573.
- [227] S. Kee, M.A. Haque, D. Corzo, H.N. Alshareef, D. Baran, Self-healing and stretchable 3D-printed organic thermoelectrics, *Adv. Funct. Mater.* 29 (2019) 1905426.
- [228] H. Xiang, X. Wang, Z. Ou, G. Lin, J. Yin, Z. Liu, L. Zhang, X. Liu, UV-curable, 3D printable and biocompatible silicone elastomers, *Prog. Org. Coatings.* 137 (2019) 105372.
- [229] M. Manti, V. Cacucciolo, M. Cianchetti, Stiffening in soft robotics: A review of the state of the art, *IEEE Robot. Autom. Mag.* 23 (2016) 93–106.
- [230] N.G. Cheng, M.B. Lobovsky, S.J. Keating, A.M. Setapen, K.I. Gero, A.E. Hosoi, K.D. Iagnemma, Design and analysis of a robust, low-cost, highly articulated manipulator enabled by jamming of granular media, in: 2012 IEEE Int. Conf. Robot. Autom., IEEE, 2012: pp. 4328–4333.
- [231] F. Chen, M.Y. Wang, Design Optimization of Soft Robots: A Review of the State of the Art, *IEEE Robot. Autom. Mag.* (2020).

- [232] J. Rieffel, D. Knox, S. Smith, B. Trimmer, Growing and evolving soft robots, *Artif. Life.* 20 (2014) 143–162.
- [233] D.P. Holland, E.J. Park, P. Polygerinos, G.J. Bennett, C.J. Walsh, The soft robotics toolkit: Shared resources for research and design, *Soft Robot.* 1 (2014) 224–230.
- [234] A. Martin-Barrio, S. Terrile, M. Diaz-Carrasco, J. del Cerro, A. Barrientos, Modelling the Soft Robot Kyma Based on Real-Time Finite Element Method, in: *Comput. Graph. Forum*, Wiley Online Library, 2019.
- [235] T. Morales Bieze, Contribution to the kinematic modeling and control of soft manipulators using computational mechanics, (2017).
- [236] G.S. Chirikjian, J.W. Burdick, A modal approach to hyper-redundant manipulator kinematics, *IEEE Trans. Robot. Autom.* 10 (1994) 343–354.
- [237] M.W. Hannan, I.D. Walker, Novel kinematics for continuum robots, in: *Adv. Robot Kinemat.*, Springer, 2000: pp. 227–238.
- [238] M.W. Hannan, I.D. Walker, Analysis and experiments with an elephant's trunk robot, *Adv. Robot.* 15 (2001) 847–858.
- [239] V. Falkenhahn, A. Hildebrandt, R. Neumann, O. Sawodny, Model-based feedforward position control of constant curvature continuum robots using feedback linearization, in: 2015 IEEE Int. Conf. Robot. Autom., IEEE, 2015: pp. 762–767.
- [240] C. Della Santina, R.K. Katzschmann, A. Biechi, D. Rus, Dynamic control of soft robots interacting with the environment, in: 2018 IEEE Int. Conf. Soft Robot., IEEE, 2018: pp. 46–53.
- [241] A. Doroudchi, S. Berman, Configuration Tracking for Soft Continuum Robotic Arms Using Inverse Dynamic Control of a Cosserat Rod Model, in: 2021 IEEE Int. Conf. Soft Robot. RoboSoft, 2021.
- [242] F. Renda, V. Cacucciolo, J. Dias, L. Seneviratne, Discrete Cosserat approach for soft robot dynamics: A new piece-wise constant strain model with torsion and shears, in: 2016 IEEE/RSJ Int. Conf. Intell. Robot. Syst., IEEE, 2016: pp. 5495–5502.
- [243] J. Till, V. Alois, C. Rucker, Real-time dynamics of soft and continuum robots based on Cosserat rod models, *Int. J. Rob. Res.* 38 (2019) 723–746.
- [244] G. Olson, R.L. Hatton, J.A. Adams, Y. Mengüç, An Euler–Bernoulli beam model for soft robot arms bent through self-stress and external loads, *Int. J. Solids Struct.* 207 (2020) 113–131.
- [245] T. Zheng, D.T. Branson, R. Kang, M. Cianchetti, E. Guglielmino, M. Follador, G.A. Medrano-Cerda, I.S. Godage, D.G. Caldwell, Dynamic continuum arm model for use with underwater robotic manipulators inspired by octopus vulgaris, in: 2012 IEEE Int. Conf. Robot. Autom., IEEE, 2012: pp. 5289–5294.
- [246] K.-H. Lee, M.C.W. Leong, M.C.K. Chow, H.-C. Fu, W. Luk, K.-Y. Sze, C.-K. Yeung, K.-W. Kwok, FEM-based soft robotic control framework for intracavitary navigation, in: 2017 IEEE Int. Conf. Real-Time Comput. Robot., IEEE, 2017: pp. 11–16.
- [247] C. Duriez, Control of elastic soft robots based on real-time finite element method, in: 2013 IEEE Int. Conf. Robot. Autom., IEEE, 2013: pp. 3982–3987.
- [248] O. Goury, C. Duriez, Fast, generic, and reliable control and simulation of soft robots using model order reduction, *IEEE Trans. Robot.* 34 (2018) 1565–1576.
- [249] O. Goury, B. Carrez, C. Duriez, Real-Time Simulation For Control Of Soft Robots With Self-Collisions Using Model Order Reduction For Contact Forces, *IEEE Robot. Autom. Lett.* 6 (2021) 3752–3759.
- [250] J. Collins, S. Chand, A. Vanderkam, D. Howard, A Review of Physics Simulators for Robotic Applications, *IEEE Access*. (2021).
- [251] G. Runge, M. Wiese, L. Günther, A. Raatz, A framework for the kinematic modeling of soft material robots combining finite element analysis and piecewise constant curvature kinematics, in: 2017 3rd Int. Conf. Control. Autom. Robot., IEEE, 2017: pp. 7–14.
- [252] A.A. Amiri Moghadam, M. Moavenian, H.E. Toussi, Modelling and robust control of a soft robot based on conjugated polymer actuators, *Int. J. Model. Identif. Control.* 14 (2011) 216–226.
- [253] M. Giorelli, F. Renda, G. Ferri, C. Laschi, A feed-forward neural network learning the inverse kinetics of a soft cable-driven manipulator moving in three-dimensional space, in: 2013 IEEE/RSJ Int. Conf. Intell. Robot. Syst., IEEE, 2013: pp. 5033–5039.
- [254] J. Liang, M.C. Lin, Differentiable physics simulation, in: ICLR 2020 Work. Integr. Deep Neural Model. Differ. Equations, 2020.
- [255] Y. Hu, J. Liu, A. Spielberg, J.B. Tenenbaum, W.T. Freeman, J. Wu, D. Rus, W. Matusik, Chainqueen: A real-time differentiable physical simulator for soft robotics, in: 2019 Int. Conf. Robot. Autom., IEEE, 2019: pp. 6265–6271.
- [256] M. Bächer, E. Knoop, C. Schumacher, Design and Control of Soft Robots Using Differentiable Simulation, *Curr. Robot. Reports.* (2021) 1–11.
- [257] G.A. Naselli, B. Mazzolai, The softness

- distribution index: towards the creation of guidelines for the modeling of soft-bodied robots, *Int. J. Rob. Res.* **40** (2021) 197–223.
- [258] T. George Thuruthel, Y. Ansari, E. Falotico, C. Laschi, Control strategies for soft robotic manipulators: A survey, *Soft Robot.* **5** (2018) 149–163.
- [259] M. Thieffry, Model-Based Dynamic Control of Soft Robots, (2019).
- [260] T.G. Thuruthel, E. Falotico, M. Manti, C. Laschi, Stable open loop control of soft robotic manipulators, *IEEE Robot. Autom. Lett.* **3** (2018) 1292–1298.
- [261] C. Della Santina, R.K. Katzschmann, A. Bicchi, D. Rus, Model-based dynamic feedback control of a planar soft robot: trajectory tracking and interaction with the environment, *Int. J. Rob. Res.* **39** (2020) 490–513.
- [262] Z.Q. Tang, H.L. Heung, K.Y. Tong, Z. Li, Model-based online learning and adaptive control for a “human-wearable soft robot” integrated system, *Int. J. Rob. Res.* **40** (2021) 256–276.
- [263] K. Nakajima, H. Hauser, T. Li, R. Pfeifer, Exploiting the dynamics of soft materials for machine learning, *Soft Robot.* **5** (2018) 339–347.
- [264] Y. Zhou, M. Ju, G. Zheng, Closed-loop control of soft robot based on machine learning, in: 2019 Chinese Control Conf., IEEE, 2019: pp. 4543–4547.
- [265] H. Zhang, R. Cao, S. Zilberstein, F. Wu, X. Chen, Toward effective soft robot control via reinforcement learning, in: Int. Conf. Intell. Robot. Appl., Springer, 2017: pp. 173–184.
- [266] T.G. Thuruthel, E. Falotico, F. Renda, C. Laschi, Model-based reinforcement learning for closed-loop dynamic control of soft robotic manipulators, *IEEE Trans. Robot.* **35** (2018) 124–134.
- [267] D. Kim, S.-H. Kim, T. Kim, B.B. Kang, M. Lee, W. Park, S. Ku, D. Kim, J. Kwon, H. Lee, Review of machine learning methods in soft robotics, *PLoS One.* **16** (2021) e0246102.
- [268] A.A. Shabana, A.E. Eldeeb, Motion and shape control of soft robots and materials, *Nonlinear Dyn.* **104** (2021) 165–189.
- [269] A. Zolfagharian, A. Kaynak, A. Kouzani, Closed-loop 4D-printed soft robots, *Mater. Des.* **188** (2020) 108411.
- [270] C. Della Santina, M. Bianchi, G. Grioli, F. Angelini, M. Catalano, M. Garabini, A. Bicchi, Controlling soft robots: balancing feedback and feedforward elements, *IEEE Robot. Autom. Mag.* **24** (2017) 75–83.
- [271] J. Rossiter, H. Hauser, Soft robotics—the next industrial revolution, *IEEE Robot. Autom. Mag.* **23** (2016) 17–20.
- [272] F. Hartmann, M. Baumgartner, M. Kaltenbrunner, Becoming Sustainable, The New Frontier in Soft Robotics, *Adv. Mater.* (2020) 2004413.
- [273] B. Mazzolai, C. Laschi, A vision for future bioinspired and biohybrid robots, *Sci. Robot.* **5** (2020) eaba6893.
- [274] W. Coral, C. Rossi, J. Colorado, D. Lemus, A. Barrientos, SMA-based muscle-like actuation in biologically inspired robots: a state of the art review, *Smart Actuation Sens. Syst. Adv. Futur. Challenges.* (2012) 53–82.
- [275] M.A. Woodward, M. Sitti, Tailored Magnetic Springs for Shape-Memory Alloy Actuated Mechanisms in Miniature Robots, *IEEE Trans. Robot.* **35** (2019) 589–601.
- [276] S.J. Park, C.H. Park, Suit-type wearable robot powered by shape-memory-alloy-based fabric muscle, *Sci. Rep.* **9** (2019) 1–8.
- [277] L.M. Fonseca, G. V Rodrigues, M.A. Savi, A. Paiva, Nonlinear dynamics of an origami wheel with shape memory alloy actuators, *Chaos, Solitons & Fractals.* **122** (2019) 245–261.
- [278] P. Motzki, F. Khelfa, L. Zimmer, M. Schmidt, S. Seelecke, Design and validation of a reconfigurable robotic end-effector based on shape memory alloys, *IEEE/ASME Trans. Mechatronics.* **24** (2019) 293–303.
- [279] J.-H. Lee, Y.S. Chung, H. Rodrigue, Application of SMA spring tendons for improved grasping performance, *Smart Mater. Struct.* **28** (2019) 35006.
- [280] F. Ni, Y. Li, Y. Zhou, H. Liu, Y. Tang, Connectors Based on 2-Way SMA Actuator for Self-reconfigurable Chain Robots, in: 2018 IEEE Int. Conf. Mechatronics Autom., IEEE, 2018: pp. 1003–1008.
- [281] N.A. Mansour, A.M.R.F. El-Bab, S.F.M. Assal, O. Tabata, Design, characterization and control of SMA springs-based multi-modal tactile display device for biomedical applications, *Mechatronics.* **31** (2015) 255–263.
- [282] Y. She, C. Li, J. Cleary, H.-J. Su, Design and fabrication of a soft robotic hand with embedded actuators and sensors, *J. Mech. Robot.* **7** (2015).
- [283] J.M. Jani, M. Leary, A. Subic, M.A. Gibson, A review of shape memory alloy research, applications and opportunities, *Mater. Des.* **56** (2014) 1078–1113.
- [284] M. Cianchetti, Fundamentals on the use of shape memory alloys in soft robotics, *Interdiscip. Mechatronics.* (2013) 227–254.
- [285] J. Pons, Actuators in motion control systems: mechatronics, 2005. <https://doi.org/10.1002/0470091991.ch1>.
- [286] J.L. Pons, Emerging actuator technologies:

- a micromechatronic approach, John Wiley & Sons, 2005.
- [287] M. Follador, M. Cianchetti, A. Arienti, C. Laschi, A general method for the design and fabrication of shape memory alloy active spring actuators, *Smart Mater. Struct.* 21 (2012) 115029.
- [288] J.D. Harrison, Measurable changes concomitant with the shape memory effect transformation, Butterworth-Heinemann, Eng. Asp. Shape Mem. Alloy. 1990., (1990) 106–111.
- [289] S. Degeratu, N.G. Bizdoaca, G. Manolea, I. Diaconu, A. Petrisor, V. Degeratu, On the design of a shape memory alloy spring actuator using thermal analysis, *WSEAS Trans. Syst.* 7 (2008) 1006–1015.
- [290] G. Kulvietis, I. Tumasoniene, D. Mazeika, The design of the multicomponent ultrasonic actuators on the basis of mode-frequency analysis., *WSEAS Trans. Syst.* 5 (2006) 924–929.
- [291] SAES Group, SAES Group - Nitinol Brochure, 53 (2019).
- [292] A. Nespoli, S. Bessegini, S. Pittaccio, E. Villa, S. Viscuso, The high potential of shape memory alloys in developing miniature mechanical devices: A review on shape memory alloy mini-actuators, *Sensors Actuators A Phys.* 158 (2010) 149–160.
- [293] DYNALLOY inc., Technical Characteristics of FLEXINOL ® Actuator Wires Table of Contents Makers of Dynamic Alloys NICKEL - TITANIUM ALLOY PHYSICAL PROPERTIES, (2013) 1–12.
- [294] A. Czechowicz, S. Langbein, Shape memory alloy valves: Basics, potentials, design, Springer, 2015.
- [295] T. Ishii, Design of shape memory alloy (SMA) coil springs for actuator applications, in: *Shape Mem. Superelastic Alloy.*, Elsevier, 2011: pp. 63–76.
- [296] C. Naresh, P.S.C. Bose, C.S.P. Rao, Shape memory alloys: a state of art review, in: *IOP Conf. Ser. Mater. Sci. Eng.*, IOP Publishing, 2016: p. 12054.
- [297] J. Ma, H. Huang, J. Huang, Characteristics analysis and testing of SMA spring actuator, *Adv. Mater. Sci. Eng.* 2013 (2013).
- [298] J.E. Shigley, C.R. Mischke, Mechanical springs, in: *Mech. Eng. Des.*, McGraw-Hill, 2001: p. 590.
- [299] H.B. Gilbert, R.J. Webster, Rapid, reliable shape setting of superelastic nitinol for prototyping robots, *IEEE Robot. Autom. Lett.* 1 (2015) 98–105.
- [300] P. Chowdhury, Frontiers of theoretical research on shape memory alloys: a general overview, *Shape Mem. Superelasticity.* 4 (2018) 26–40.
- [301] T.D. Canonsburg, Technology Demonstration Guide, 15317 (2020) 724–746.
- [302] K.J. Quillin, Kinematic scaling of locomotion by hydrostatic animals: ontogeny of peristaltic crawling by the earthworm *lumbricus terrestris*, *J. Exp. Biol.* 202 (1999) 661–674.
- [303] A. Menciassi, S. Gorini, G. Pernorio, P. Dario, A SMA actuated artificial earthworm, in: *IEEE Int. Conf. Robot. Autom.* 2004. Proceedings. ICRA'04. 2004, IEEE, 2004: pp. 3282–3287.
- [304] S. Seok, C.D. Onal, R. Wood, D. Rus, S. Kim, Peristaltic locomotion with antagonistic actuators in soft robotics, in: *2010 IEEE Int. Conf. Robot. Autom.*, IEEE, 2010: pp. 1228–1233.
- [305] C.Y. Liu, W.-H. Liao, A snake robot using shape memory alloys, in: *2004 IEEE Int. Conf. Robot. Biomimetics*, IEEE, 2004: pp. 601–605.
- [306] R. Gasoto, M. Macklin, X. Liu, Y. Sun, K. Erleben, C. Onal, J. Fu, A Validated Physical Model For Real-Time Simulation of Soft Robotic Snakes, in: *2019 Int. Conf. Robot. Autom.*, IEEE, 2019: pp. 6272–6279.
- [307] J. Colorado, C. Rossi, A. Barrientos, A. Parra, C. Devia, D. Patiño, The Role of Massive Morphing Wings for Maneuvering a Bio-Inspired Bat-Like Robot, in: *2018 IEEE Int. Conf. Robot. Autom.*, IEEE, 2018: pp. 1–6.
- [308] J. Colorado, A. Barrientos, C. Rossi, K.S. Breuer, Biomechanics of smart wings in a bat robot: morphing wings using SMA actuators, *Bioinspir. Biomim.* 7 (2012) 36006.
- [309] R.K. Katzschmann, A.D. Marchese, D. Rus, Hydraulic autonomous soft robotic fish for 3D swimming, in: *Exp. Robot.*, Springer, 2016: pp. 405–420.
- [310] T. Li, G. Li, Y. Liang, T. Cheng, J. Dai, X. Yang, B. Liu, Z. Zeng, Z. Huang, Y. Luo, Fast-moving soft electronic fish, *Sci. Adv.* 3 (2017) e1602045.
- [311] R.K. Katzschmann, J. DelPreto, R. MacCurdy, D. Rus, Exploration of underwater life with an acoustically controlled soft robotic fish, *Sci. Robot.* 3 (2018) eaar3449.
- [312] A.D. Marchese, C.D. Onal, D. Rus, Autonomous soft robotic fish capable of escape maneuvers using fluidic elastomer actuators, *Soft Robot.* 1 (2014) 75–87.
- [313] Z. Wang, G. Hang, J. Li, Y. Wang, K. Xiao, A micro-robot fish with embedded SMA wire actuated flexible biomimetic fin, *Sensors Actuators A Phys.* 144 (2008) 354–360.
- [314] K. Nakajima, H. Hauser, R. Kang, E.

- Guglielmino, D.G. Caldwell, R. Pfeifer, A soft body as a reservoir: case studies in a dynamic model of octopus-inspired soft robotic arm, *Front. Comput. Neurosci.* 7 (2013) 91.
- [315] M. Cianchetti, M. Calisti, L. Margheri, M. Kuba, C. Laschi, Bioinspired locomotion and grasping in water: the soft eight-arm OCTOPUS robot, *Bioinspir. Biomim.* 10 (2015) 35003.
- [316] S.-W. Yeom, J. Jeon, H. Kim, B.-D. Youn, I.-K. Oh, Bio-inspired Jellyfish Robots based on Ionic-type Artificial Muscles, (n.d.).
- [317] H. Godaba, J. Li, Y. Wang, J. Zhu, A soft jellyfish robot driven by a dielectric elastomer actuator, *IEEE Robot. Autom. Lett.* 1 (2016) 624–631.
- [318] J.C. Nawroth, H. Lee, A.W. Feinberg, C.M. Ripplinger, M.L. McCain, A. Grosberg, J.O. Dabiri, K.K. Parker, A tissue-engineered jellyfish with biomimetic propulsion, *Nat. Biotechnol.* 30 (2012) 792.
- [319] Z. Ren, W. Hu, X. Dong, M. Sitti, Multi-functional soft-bodied jellyfish-like swimming, *Nat. Commun.* 10 (2019) 1–12.
- [320] M. Ishida, D. Drotman, B. Shih, M. Hermes, M. Luhar, M.T. Tolley, Morphing Structure for Changing Hydrodynamic Characteristics of a Soft Underwater Walking Robot, *IEEE Robot. Autom. Lett.* 4 (2019) 4163–4169.
- [321] K. Suzumori, S. Endo, T. Kanda, N. Kato, H. Suzuki, A bending pneumatic rubber actuator realizing soft-bodied manta swimming robot, in: Proc. 2007 IEEE Int. Conf. Robot. Autom., IEEE, 2007: pp. 4975–4980.
- [322] J. Shintake, H. Shea, D. Floreano, Biomimetic underwater robots based on dielectric elastomer actuators, in: 2016 IEEE/RSJ Int. Conf. Intell. Robot. Syst., Ieee, 2016: pp. 4957–4962.
- [323] K. Takagi, M. Yamamura, Z.-W. Luo, M. Onishi, S. Hirano, K. Asaka, Y. Hayakawa, Development of a rajiform swimming robot using ionic polymer artificial muscles, in: 2006 IEEE/RSJ Int. Conf. Intell. Robot. Syst., IEEE, 2006: pp. 1861–1866.
- [324] C. Lee, M. Kim, Y.J. Kim, N. Hong, S. Ryu, H.J. Kim, S. Kim, Soft robot review, *Int. J. Control. Autom. Syst.* 15 (2017) 3–15.
- [325] F. Renda, M. Cianchetti, M. Giorelli, A. Arienti, C. Laschi, A 3D steady-state model of a tendon-driven continuum soft manipulator inspired by the octopus arm, *Bioinspir. Biomim.* 7 (2012) 25006.
- [326] X. Huang, K. Kumar, M.K. Jawed, A.M. Nasab, Z. Ye, W. Shan, C. Majidi, Chasing biomimetic locomotion speeds: Creating untethered soft robots with shape memory alloy actuators, *Sci. Robot.* 3 (2018) 7557.
- [327] H. Jin, E. Dong, M. Xu, C. Liu, G. Alici, Y. Jie, Soft and smart modular structures actuated by shape memory alloy (SMA) wires as tentacles of soft robots, *Smart Mater. Struct.* 25 (2016) 85026.
- [328] S. Mao, E. Dong, H. Jin, M. Xu, K.H. Low, Locomotion and gait analysis of multi-limb soft robots driven by smart actuators, in: 2016 IEEE/RSJ Int. Conf. Intell. Robot. Syst., IEEE, 2016: pp. 2438–2443.
- [329] T. Mano, X. Guo, N. Fujii, N. Yoshie, E. Tsutsumi, R. Saito, Moon jellyfish aggregations observed by a scientific echo sounder and an underwater video camera and their relation to internal waves, *J. Oceanogr.* 75 (2019) 359–374.
- [330] J.M. Jani, S. Huang, M. Leary, A. Subic, Numerical modeling of shape memory alloy linear actuator, *Comput. Mech.* 56 (2015) 443–461.
- [331] P.B. Dehkordi, A. Azdarpour, E. Mohammadian, The hydrodynamic behavior of high viscous oil-water flow through horizontal pipe undergoing sudden expansion—CFD study and experimental validation, *Chem. Eng. Res. Des.* 139 (2018) 144–161.
- [332] S.P. Colin, J.H. Costello, Morphology, swimming performance and propulsive mode of six co-occurring hydromedusae, *J. Exp. Biol.* 205 (2002) 427–437.
- [333] F. Giorgio-Serchi, G.D. Weymouth, Underwater soft robotics, the benefit of body-shape variations in aquatic propulsion, in: *Soft Robot. Trends, Appl. Challenges*, Springer, 2017: pp. 37–46.
- [334] T.L. Daniel, Cost of locomotion: unsteady medusan swimming, *J. Exp. Biol.* 119 (1985) 149–164.
- [335] T.L. Daniel, Unsteady aspects of aquatic locomotion, *Am. Zool.* 24 (1984) 121–134.
- [336] C.K. Batchelor, G.K. Batchelor, An introduction to fluid dynamics, Cambridge university press, 2000.
- [337] J.H. Rife, S.M. Rock, Design and validation of a robotic control law for observation of deep-ocean jellyfish, *IEEE Trans. Robot.* 22 (2006) 282–291.
- [338] B. Mazzolai, L. Beccai, V. Mattoli, Plants as model in biomimetics and biorobotics: new perspectives, *Front. Bioeng. Biotechnol.* 2 (2014) 2.
- [339] S.A. Velero, Improvements in or relating to a method and a device for producing a velvet type fabric, Swiss Pat. (1955).
- [340] I. Must, E. Sinibaldi, B. Mazzolai, A variable-stiffness tendril-like soft robot based on reversible osmotic actuation, *Nat. Commun.* 10 (2019) 1–8.
- [341] A. Martín Barrio, S. Terrile, A. Barrientos, J. del Cerro, Robots Hiper-Redundantes:

- Clasificación, Estado del Arte y Problemática, Rev. Iberoam. Automática e Informática Ind. 15 (2018) 351–362.
- [342] A. Martín-Barrio, S. Terrile, M. Diaz-Carrasco, J. del Cerro, A. Barrientos, Modelling the Soft Robot Kyma Based on Real-Time Finite Element Method, in: Comput. Graph. Forum, Wiley Online Library, 2020: pp. 289–302.
- [343] A. Martín-Barrio, J.J. Roldán, S. Terrile, J. del Cerro, A. Barrientos, Application of immersive technologies and natural language to hyper-redundant robot teleoperation, Virtual Real. (2019) 1–15.
- [344] G.S. Chirikjian, J.W. Burdick, Design and Experiments with a 30 DOF Robot, in: [1993] Proc. IEEE Int. Conf. Robot. Autom., IEEE, 1993: pp. 113–119.
- [345] L.S. Cowan, I.D. Walker, The importance of continuous and discrete elements in continuum robots, Int. J. Adv. Robot. Syst. 10 (2013) 165.
- [346] T. Ranzani, G. Gerboni, M. Cianchetti, A. Menciassi, A bioinspired soft manipulator for minimally invasive surgery, Bioinspir. Biomim. 10 (2015) 35008.
- [347] B.L. Conrad, M.R. Zinn, Interleaved continuum-rigid manipulation: An approach to increase the capability of minimally invasive surgical systems, IEEE/ASME Trans. Mechatronics. 22 (2016) 29–40.
- [348] A. Eickhoff, J. Van Dam, R. Jakobs, V. Kudis, D. Hartmann, U. Damian, U. Weickert, D. Schilling, J.F. Riemann, Computer-assisted colonoscopy (the NeoGuide Endoscopy System): results of the first human clinical trial (“PACE study”), Off. J. Am. Coll. Gastroenterol. ACG. 102 (2007) 261–266.
- [349] J.S. Mehling, M.A. Diftler, M. Chu, M. Valvo, A minimally invasive tendril robot for in-space inspection, in: First IEEE/RAS-EMBS Int. Conf. Biomed. Robot. Biomechatronics, 2006. BioRob 2006., IEEE, 2006: pp. 690–695.
- [350] Y. Yang, W. Zhang, An elephant-trunk manipulator with twisting flexional rods, in: 2015 IEEE Int. Conf. Robot. Biomimetics, IEEE, 2015: pp. 13–18.
- [351] A.A. Stokes, R.F. Shepherd, S.A. Morin, F. Ilievski, G.M. Whitesides, A hybrid combining hard and soft robots, Soft Robot. 1 (2014) 70–74.
- [352] X. Dong, D. Axinte, D. Palmer, S. Cobos, M. Raffles, A. Rabani, J. Kell, Development of a slender continuum robotic system for on-wing inspection/repair of gas turbine engines, Robot. Comput. Integrat. Manuf. 44 (2017) 218–229.
- [353] G. Immega, K. Antonelli, The KSI tentacle manipulator, in: Proc. 1995 IEEE Int. Conf. Robot. Autom., IEEE, 1995: pp. 3149–3154.
- [354] I.A. Gravagne, I.D. Walker, Kinematic transformations for remotely-actuated planar continuum robots, in: Proc. 2000 ICRA. Millenn. Conf. IEEE Int. Conf. Robot. Autom. Symp. Proc. (Cat. No. 00CH37065), IEEE, 2000: pp. 19–26.
- [355] E. Coevoet, T. Morales-Bieze, F. Largilliere, Z. Zhang, M. Thieffry, M. Sanz-Lopez, B. Carrez, D. Marchal, O. Goury, J. Dequidt, Software toolkit for modeling, simulation, and control of soft robots, Adv. Robot. 31 (2017) 1208–1224.
- [356] K. Lu, K. Zhang, H. Zhang, X. Gu, Y. Jin, S. Zhao, C. Fu, Y. Yang, A Review of Model Order Reduction Methods for Large-Scale Structure Systems, Shock Vib. 2021 (2021).
- [357] J. Allard, S. Cotin, F. Faure, P.-J. Bensoussan, F. Poyer, C. Duriez, H. Delingette, L. Grisoni, Sofa—an open source framework for medical simulation, in: MMVR 15-Medicine Meets Virtual Real., IOP Press, 2007: pp. 13–18.
- [358] M.R. Endsley, Design and evaluation for situation awareness enhancement, in: Proc. Hum. Factors Soc. Annu. Meet., Sage Publications Sage CA: Los Angeles, CA, 1988: pp. 97–101.
- [359] J.J. Roldán, E. Peña-Tapia, A. Martín-Barrio, M.A. Olivares-Méndez, J. Del Cerro, A. Barrientos, Multi-robot interfaces and operator situational awareness: Study of the impact of immersion and prediction, Sensors. 17 (2017) 1720.
- [360] J. Raskin, The humane interface: new directions for designing interactive systems, Addison-Wesley Professional, 2000.
- [361] S.G. Hart, NASA-task load index (NASA-TLX); 20 years later, in: Proc. Hum. Factors Ergon. Soc. Annu. Meet., Sage publications Sage CA: Los Angeles, CA, 2006: pp. 904–908.
- [362] S.G. Hart, L.E. Staveland, Development of NASA-TLX (Task Load Index): Results of empirical and theoretical research, in: Adv. Psychol., Elsevier, 1988: pp. 139–183.
- [363] K. Sangpradit, H. Liu, P. Dasgupta, K. Althoefer, L.D. Seneviratne, Finite-element modeling of soft tissue rolling indentation, IEEE Trans. Biomed. Eng. 58 (2011) 3319–3327.
- [364] G. Runge, A. Raatz, A framework for the automated design and modelling of soft robotic systems, CIRP Ann. 66 (2017) 9–12.
- [365] R.J. Webster III, B.A. Jones, Design and kinematic modeling of constant curvature continuum robots: A review, Int. J. Rob. Res. 29 (2010) 1661–1683.
- [366] B.A. Jones, I.D. Walker, Kinematics for multisection continuum robots, IEEE

- Trans. Robot. 22 (2006) 43–55.
- [367] M. Kovandžić, V. Nikolić, M. Simonović, I. Ćirić, A. Al-Noori, Soft Robot Positioning using Artificial Neural Network, *Facta Univ. Ser. Autom. Control Robot.* 18 (2019) 19–30.
- [368] S. Terrile, M. Argüelles, A. Barrientos, Comparison of Different Technologies for Soft Robotics Grippers, *Sensors*. 21 (2021) 3253.
- [369] M. Foumani, I. Gunawan, K. Smith-Miles, M.Y. Ibrahim, Notes on feasibility and optimality conditions of small-scale multifunction robotic cell scheduling problems with pickup restrictions, *IEEE Trans. Ind. Informatics*. 11 (2014) 821–829.
- [370] K. Tai, A.R. El-Sayed, M. Shahriari, M. Biglarbegian, S. Mahmud, State of the art robotic grippers and applications, *Robotics*. 5 (2016) 1–20. <https://doi.org/10.3390/robotics5020011>.
- [371] C. Melchiorri, M. Kaneko, Springer Handbook of Robotics, Springer, Berlin/Heidelberg, Germany, 2008.
- [372] S. Hirose, Y. Umetani, The development of soft gripper for the versatile robot hand, *Mech. Mach. Theory*. 13 (1978) 351–359.
- [373] M. Manti, T. Hassan, G. Passetti, N. D'Elia, C. Laschi, M. Cianchetti, A Bioinspired Soft Robotic Gripper for Adaptable and Effective Grasping, *Soft Robot.* 2 (2015) 107–116. <https://doi.org/10.1089/soro.2015.0009>.
- [374] M. Liarokapis, A.M. Dollar, Post-contact, in-hand object motion compensation for compliant and underactuated hands, in: 2016 25th IEEE Int. Symp. Robot Hum. Interact. Commun., IEEE, 2016: pp. 986–993.
- [375] H.S. Stuart, S. Wang, M.R. Cutkosky, Tunable Contact Conditions and Grasp Hydrodynamics Using Gentle Fingertip Suction, *IEEE Trans. Robot.* 35 (2018) 295–306.
- [376] R. Mutlu, G. Alici, M. in het Panhuis, G.M. Spinks, 3D printed flexure hinges for soft monolithic prosthetic fingers, *Soft Robot.* 3 (2016) 120–133.
- [377] J. Gafford, Y. Ding, A. Harris, T. McKenna, P. Polygerinos, D. Holland, A. Moser, C. Walsh, Shape deposition manufacturing of a soft, atraumatic, deployable surgical grasper, *J. Med. Device.* 8 (2014).
- [378] C.-H. Liu, G.-F. Huang, C.-H. Chiu, T.-Y. Pai, Topology synthesis and optimal design of an adaptive compliant gripper to maximize output displacement, *J. Intell. Robot. Syst.* 90 (2018) 287–304.
- [379] G. Udupa, P. Sreedharan, P. Sai Dinesh, D. Kim, Asymmetric bellow flexible pneumatic actuator for miniature robotic soft gripper, *J. Robot.* 2014 (2014).
- [380] K.C. Galloway, K.P. Becker, B. Phillips, J. Kirby, S. Licht, D. Tchernov, R.J. Wood, D.F. Gruber, Soft Robotic Grippers for Biological Sampling on Deep Reefs, *Soft Robot.* 3 (2016) 23–33. <https://doi.org/10.1089/soro.2015.0019>.
- [381] Y. Hao, Z. Gong, Z. Xie, S. Guan, X. Yang, Z. Ren, T. Wang, L. Wen, Universal soft pneumatic robotic gripper with variable effective length, in: 2016 35th Chinese Control Conf., IEEE, 2016: pp. 6109–6114.
- [382] J. Guo, Y. Sun, X. Liang, J.-H. Low, Y.-R. Wong, V.S.-C. Tay, C.-H. Yeow, Design and fabrication of a pneumatic soft robotic gripper for delicate surgical manipulation, in: 2017 IEEE Int. Conf. Mechatronics Autom., IEEE, 2017: pp. 1069–1074.
- [383] J. Guo, K. Elgeneidy, C. Xiang, N. Lohse, L. Justham, J. Rossiter, Soft pneumatic grippers embedded with stretchable electroadhesion, *Smart Mater. Struct.* 27 (2018) 55006.
- [384] Y. Li, Y. Chen, Y. Li, Pre-charged pneumatic soft gripper with closed-loop control, *IEEE Robot. Autom. Lett.* 4 (2019) 1402–1408.
- [385] G. Mantriota, Optimal grasp of vacuum grippers with multiple suction cups, *Mech. Mach. Theory*. 42 (2007) 18–33.
- [386] J.M. Krahn, F. Fabbro, C. Menon, A soft-touch gripper for grasping delicate objects, *IEEE/ASME Trans. Mechatronics*. 22 (2017) 1276–1286.
- [387] J. Amend, N. Cheng, S. Fakhouri, B. Culley, Soft robotics commercialization: Jamming grippers from research to product, *Soft Robot.* 3 (2016) 213–222.
- [388] Z. Guo, Z. Sun, X. Li, Design and Fabrication of Pneumatic Soft Gripper, in: ASME 2018 Int. Mech. Eng. Congr. Expo., American Society of Mechanical Engineers Digital Collection, 2018.
- [389] K. Mizushima, T. Oku, Y. Suzuki, T. Tsuji, T. Watanabe, Multi-fingered robotic hand based on hybrid mechanism of tendon-driven and jamming transition, in: 2018 IEEE Int. Conf. Soft Robot., IEEE, 2018: pp. 376–381.
- [390] Y. Fei, J. Wang, W. Pang, A novel fabric-based versatile and stiffness-tunable soft gripper integrating soft pneumatic fingers and wrist, *Soft Robot.* 6 (2019) 1–20.
- [391] P.H. Nguyen, S. Sridar, S. Amatya, C.M. Thalman, P. Polygerinos, Fabric-based soft grippers capable of selective distributed bending for assistance of daily living tasks, in: 2019 2nd IEEE Int. Conf. Soft Robot., IEEE, 2019: pp. 404–409.
- [392] J. Nassour, F. Hamker, Enfolded textile actuator for soft wearable robots, in: 2019 IEEE Int. Conf. Cyborg Bionic Syst., IEEE, 2019: pp. 60–65.

- [393] G. Monkman, Electroadhesive microgrippers, *Ind. Robot An Int. J.* (2003).
- [394] H.R. Shea, S. Jun, F. Dario, Soft compliant gripper for safe manipulation of extremely fragile objects, 2016.
- [395] S. Song, C. Majidi, M. Sitti, Geckogripper: A soft, inflatable robotic gripper using gecko-inspired elastomer micro-fiber adhesives, in: 2014 IEEE/RSJ Int. Conf. Intell. Robot. Syst., IEEE, 2014: pp. 4624–4629.
- [396] P. Glick, S.A. Suresh, D. Ruffatto, M. Cutkosky, M.T. Tolley, A. Parness, A soft robotic gripper with gecko-inspired adhesive, *IEEE Robot. Autom. Lett.* 3 (2018) 903–910.
- [397] J. Shintake, B. Schubert, S. Rosset, H. Shea, D. Floreano, Variable stiffness actuator for soft robotics using dielectric elastomer and low-melting-point alloy, in: 2015 IEEE/RSJ Int. Conf. Intell. Robot. Syst., IEEE, 2015: pp. 1097–1102.
- [398] L. Xu, G. Gu, Bioinspired Venus flytrap: A dielectric elastomer actuated soft gripper, in: 2017 24th Int. Conf. Mechatronics Mach. Vis. Pract., IEEE, 2017: pp. 1–3.
- [399] S. Pourazadi, H. Bui, C. Menon, Investigation on a soft grasping gripper based on dielectric elastomer actuators, *Smart Mater. Struct.* 28 (2019) 35009.
- [400] Z. Wang, D.S. Chathuranga, S. Hirai, 3D printed soft gripper for automatic lunch box packing, in: 2016 IEEE Int. Conf. Robot. Biomimetics, IEEE, 2016: pp. 503–508.
- [401] A. Pettersson, S. Davis, J.O. Gray, T.J. Dodd, T. Ohlsson, Design of a magnetorheological robot gripper for handling of delicate food products with varying shapes, *J. Food Eng.* 98 (2010) 332–338.
- [402] A.M.B. Hamid, M.R. Makhdoomi, T. Saleh, M. Bhuiyan, Development of a Shape Memory Alloy (SMA) Based Assistive Hand, *Adv. Mater. Res.* 1115 (2015) 454–457.
<https://doi.org/10.4028/www.scientific.net/amr.1115.454>.
- [403] L. Kang, J.-T. Seo, S.-H. Kim, W.-J. Kim, B.-J. Yi, Design and Implementation of a Multi-Function Gripper for Grasping General Objects, *Appl. Sci.* 9 (2019) 5266.
- [404] Festo, MultiChoiceGripper, (n.d.).
<https://www.festo.com/group/en/cms/10221.htm> (accessed April 30, 2020).
- [405] Recreus, Recreus, (n.d.).
<https://recreus.com/en/> (accessed April 30, 2020).
- [406] S. Terrile, J. Miguelan  ez, A. Barrientos, A Soft Haptic Glove Actuated with Shape Memory Alloy and Flexible Stretch Sensors, *Sensors* . 21 (2021).
- [407] <https://doi.org/10.3390/s21165278>.
- [408] R. Boian, A. Sharma, C. Han, A. Merians, G. Burdea, S. Adamovich, M. Recce, M. Tremaine, H. Poizner, Virtual reality-based post-stroke hand rehabilitation, in: *Med. Meets Virtual Real. 02/10*, IOS Press, 2002: pp. 64–70.
- [409] A. Alamri, J. Cha, A. El Saddik, AR-REHAB: An augmented reality framework for poststroke-patient rehabilitation, *IEEE Trans. Instrum. Meas.* 59 (2010) 2554–2563.
- [410] L. Connolly, Y. Jia, M.L. Toro, M.E. Stoykov, R. V Kenyon, D.G. Kamper, A pneumatic glove and immersive virtual reality environment for hand rehabilitative training after stroke, *IEEE Trans. Neural Syst. Rehabil. Eng.* 18 (2010) 551–559.
- [411] A. Alamri, H.-N. Kim, J. Cha, A. El Saddik, Serious Games for Rehabilitation of stroke patients with Vibrotactile feedback., *Int. J. Comput. Sci. Sport (International Assoc. Comput. Sci. Sport)* 9 (2010).
- [412] H. Mousavi Hondori, M. Khademi, L. Dodakian, S.C. Cramer, C.V. Lopes, A spatial augmented reality rehab system for post-stroke hand rehabilitation, in: *Med. Meets Virtual Real.* 20, IOS Press, 2013: pp. 279–285.
- [413] D. Tsoupikova, N. Stoykov, R. Vick, Y. Li, D. Kamper, M. Listenberger, Use of virtual reality to promote hand therapy post-stroke, in: *Eng. Real. Virtual Real. 2013*, International Society for Optics and Photonics, 2013: p. 86490K.
- [414] M. Khademi, H. Mousavi Hondori, A. A. McKenzie, L. Dodakian, C.V. Lopes, S.C. Cramer, Free-hand interaction with leap motion controller for stroke rehabilitation, in: *CHI'14 Ext. Abstr. Hum. Factors Comput. Syst.*, 2014: pp. 1663–1668.
- [415] A. Karashanov, A. Manolova, N. Neshov, Application for hand rehabilitation using leap motion sensor based on a gamification approach, *Int. J. Adv. Res. Sci. Eng.* 5 (2016) 61–69.
- [416] C.-Y. Lin, C.-M. Tsai, P.-C. Shih, H.-C. Wu, Development of a novel haptic glove for improving finger dexterity in poststroke rehabilitation, *Technol. Heal. Care.* 24 (2016) S97–S103.
- [417] X. Yang, S.-C. Yeh, J. Niu, Y. Gong, G. Yang, Hand rehabilitation using virtual reality electromyography signals, in: 2017 5th Int. Conf. Enterp. Syst., IEEE, 2017: pp. 125–131.
- [418] T. Rose, C.S. Nam, K.B. Chen, Immersion of virtual reality for rehabilitation-Review, *Appl. Ergon.* 69 (2018) 153–161.
- [419] G. Tao, B. Garrett, T. Taverner, E. Cordingley, C. Sun, Immersive virtual reality health games: a narrative review of

- game design, *J. Neuroeng. Rehabil.* 18 (2021) 1–21.
- [419] H.-C. Wu, Y.-C. Liao, Y.-H. Cheng, P.-C. Shih, C.-M. Tsai, C.-Y. Lin, The potential effect of a vibrotactile glove rehabilitation system on motor recovery in chronic post-stroke hemiparesis, *Technol. Heal. Care.* 25 (2017) 1183–1187.
- [420] J.E. Deutsch, A.S. Merians, G.C. Burdea, R. Boian, S. V Adamovich, H. Poizner, Haptics and virtual reality used to increase strength and improve function in chronic individuals post-stroke: two case reports, *Pre.* 26 (2002) 79–86.
- [421] S. Adamovich, G.G. Fluet, A.S. Merians, A. Mathai, Q. Qiu, Recovery of hand function in virtual reality: training hemiparetic hand and arm together or separately, in: 2008 30th Annu. Int. Conf. IEEE Eng. Med. Biol. Soc., IEEE, 2008: pp. 3475–3478.
- [422] L. Connelly, M.E. Stoykov, Y. Jia, M.L. Toro, R. V Kenyon, D.G. Kamper, Use of a pneumatic glove for hand rehabilitation following stroke, in: 2009 Annu. Int. Conf. IEEE Eng. Med. Biol. Soc., IEEE, 2009: pp. 2434–2437.
- [423] X. Ji, X. Liu, V. Cacucciolo, Y. Civet, A. El Haitami, S. Cantin, Y. Perriard, H. Shea, Untethered feel-through haptics using 18- μm thick dielectric elastomer actuators, *Adv. Funct. Mater.* (2020) 2006639.
- [424] Y. Yoon, D. Moon, S. Chin, Fine tactile representation of materials for virtual reality, *J. Sensors.* 2020 (2020).
- [425] D. Leonardis, M. Solazzi, I. Bortone, A. Frisoli, A 3-RSR haptic wearable device for rendering fingertip contact forces, *IEEE Trans. Haptics.* 10 (2016) 305–316.
- [426] R. Scheibe, M. Moehring, B. Froehlich, Tactile feedback at the finger tips for improved direct interaction in immersive environments, in: 2007 IEEE Symp. 3D User Interfaces, IEEE, 2007.
- [427] G. Chernyshov, B. Tag, C. Caremel, F. Cao, G. Liu, K. Kunze, Shape memory alloy wire actuators for soft, wearable haptic devices, in: Proc. 2018 ACM Int. Symp. Wearable Comput., 2018: pp. 112–119.
- [428] K. Minamizawa, D. Prattichizzo, S. Tachi, Simplified design of haptic display by extending one-point kinesthetic feedback to multipoint tactile feedback, in: 2010 IEEE Haptics Symp., IEEE, 2010: pp. 257–260.
- [429] R. Hinche, V. Vechev, H. Shea, O. Hilliges, Dextres: Wearable haptic feedback for grasping in vr via a thin form-factor electrostatic brake, in: Proc. 31st Annu. ACM Symp. User Interface Softw. Technol., 2018: pp. 901–912.
- [430] Haptx, Haptx, (n.d.). <https://haptx.com/> (accessed October 8, 2021).
- [431] M. Caeiro-Rodríguez, I. Otero-González, F.A. Mikic-Fonte, M. Llamas-Nistal, A Systematic Review of Commercial Smart Gloves: Current Status and Applications, *Sensors.* 21 (2021) 2667.
- [432] I. Zubrycki, G. Granosik, Novel haptic glove-based interface using jamming principle, in: 2015 10th Int. Work. Robot Motion Control, IEEE, 2015: pp. 46–51.
- [433] I. Jo, J. Bae, Design and control of a wearable hand exoskeleton with force-controllable and compact actuator modules, in: 2015 IEEE Int. Conf. Robot. Autom., IEEE, 2015: pp. 5596–5601.
- [434] Teslasuit, (n.d.). <https://teslasuit.io/blog/vr-glove-by-teslasuit/> (accessed July 2, 2021).
- [435] S.H. Winter, M. Bouzit, Testing and usability evaluation of the MRAGES force feedback glove, in: 2006 Int. Work. Virtual Rehabil., IEEE, 2006: pp. 82–87.
- [436] F. Kobayashi, G. Ikai, W. Fukui, F. Kojima, Two-Fingered Haptic Device for Robot Hand Teleoperation, *J. Robot.* 2011 (2011) 1–8. <https://doi.org/10.1155/2011/419465>.
- [437] R. Zhang, A. Kunz, P. Lochmatter, G. Kovacs, Dielectric elastomer spring roll actuators for a portable force feedback device, in: 2006 14th Symp. Haptic Interfaces Virtual Environ. Teleoperator Syst., IEEE, 2006: pp. 347–353.
- [438] H. In, K.-J. Cho, K. Kim, B. Lee, Jointless structure and under-actuation mechanism for compact hand exoskeleton, in: 2011 IEEE Int. Conf. Rehabil. Robot., IEEE, 2011: pp. 1–6.
- [439] H. In, B.B. Kang, M.K. Sin, K.J. Cho, Exo-Glove: A wearable robot for the hand with a soft tendon routing system, *IEEE Robot. Autom. Mag.* 22 (2015) 97–105. <https://doi.org/10.1109/MRA.2014.2362863>.
- [440] S. Biggar, W. Yao, Design and evaluation of a soft and wearable robotic glove for hand rehabilitation, *IEEE Trans. Neural Syst. Rehabil. Eng.* 24 (2016) 1071–1080.
- [441] M. Xiloyannis, L. Cappello, D.B. Khanh, S.-C. Yen, L. Masia, Modelling and design of a synergy-based actuator for a tendon-driven soft robotic glove, in: 2016 6th IEEE Int. Conf. Biomed. Robot. Biomechatronics, IEEE, 2016: pp. 1213–1219.
- [442] M.M. Ullah, U. Hafeez, M.N. Shehzad, M.N. Awais, H. Elahi, A Soft Robotic Glove for Assistance and Rehabilitation of Stroke Affected Patients, in: 2019 Int. Conf. Front. Inf. Technol., IEEE, 2019: pp. 110–1105.
- [443] Z. Yao, C. Linnenberg, A. Argubi-Wollesen, R. Weidner, J.P. Wulfsberg, Biomimetic design of an ultra-compact and light-weight soft muscle glove, *Prod. Eng.* 11 (2017) 731–743.
- [444] A. Hadi, K. Alipour, S. Kazeminasab, M.

- Elahinia, ASR glove: A wearable glove for hand assistance and rehabilitation using shape memory alloys, *J. Intell. Mater. Syst. Struct.* 29 (2018) 1575–1585.
- [445] M. Li, T. Wang, Y. Zhuo, B. He, T. Tao, J. Xie, G. Xu, A soft robotic glove for hand rehabilitation training controlled by movements of the healthy hand, in: 2020 17th Int. Conf. Ubiquitous Robot., IEEE, 2020: pp. 62–67.
- [446] A. Mancisidor, A. Zubizarreta, I. Cabanes, P. Bengoa, J. Hyung Jung, Multifunctional Robotic Device for the Rehabilitation of the Upper Limbs, *Rev. Iberoam. Automática e Informática Ind.* Vol 15, No (2018). <https://doi.org/10.4995/riai.2017.8820>.
- [447] D. Purves, G.J. Augustine, D. Fitzpatrick, L.C. Katz, A.-S. LaMantia, J.O. McNamara, S.M. Williams, Mechanoreceptors specialized to receive tactile information, *Neuroscience*. (2001).
- [448] J. Cepriá-Bernal, A. Pérez-González, Dataset of Tactile Signatures of the Human Right Hand in Twenty-One Activities of Daily Living Using a High Spatial Resolution Pressure Sensor, *Sensors.* 21 (2021) 2594.
- [449] M.A. Cabrera, J. Heredia, D. Tsetserukou, Tactile Perception of Objects by the User's Palm for the Development of Multi-contact Wearable Tactile Displays, in: Int. Conf. Hum. Haptic Sens. Touch Enabled Comput. Appl., Springer, 2020: pp. 51–59.
- [450] L.A. Zabala Aguiar, Desarrollo de un sistema de adquisición y procesamiento de señales electromiográficas con Matlab para la identificación de los movimientos extensión, flexión, pronación y supinación de un brazo humano., (2017).
- [451] J.C. Montoya Cardona, Sistema de adquisición de biopotenciales para entornos académicos, (2013).
- [452] P. Heo, G.M. Gu, S. jin Lee, K. Rhee, J. Kim, Current hand exoskeleton technologies for rehabilitation and assistive engineering, *Int. J. Precis. Eng. Manuf.* 13 (2012) 807–824. <https://doi.org/10.1007/s12541-012-0107-2>.
- [453] A. Lince, N. Celadon, A. Battezzato, A. Favetto, S. Appendino, P. Ariano, M. Palleari, Design and testing of an underactuated surface EMG-driven hand exoskeleton, in: 2017 Int. Conf. Rehabil. Robot., IEEE, 2017: pp. 670–675.
- [454] T. Tang, D. Zhang, T. Xie, X. Zhu, An exoskeleton system for hand rehabilitation driven by shape memory alloy, in: 2013 IEEE Int. Conf. Robot. Biomimetics, IEEE, 2013: pp. 756–761.
- [455] J. Yang, J. Shi, H. Xie, Research on SMA actuated tendon driven hand exoskeleton with bidirectional finger joint motion coupling for rehabilitation usage, in: 2015 IEEE Int. Conf. Cyber Technol. Autom. Control. Intell. Syst., IEEE, 2015: pp. 336–340.
- [456] A. Lince, a portable assistive rehabilitation hand exoskeleton, (2016).
- [457] M.M. Kheirikhah, S. Rabiee, M.E. Edalat, A review of shape memory alloy actuators in robotics, in: Robot Soccer World Cup, Springer, 2010: pp. 206–217.
- [458] A. Chiri, F. Giovacchini, N. Vitiello, E. Cattin, S. Roccella, F. Vecchi, M.C. Carrozza, HANDEXOS: Towards an exoskeleton device for the rehabilitation of the hand, in: 2009 IEEE/RSJ Int. Conf. Intell. Robot. Syst., IEEE, 2009: pp. 1106–1111.
- [459] H. Kawasaki, S. Ito, Y. Ishigure, Y. Nishimoto, T. Aoki, T. Mouri, H. Sakaeda, M. Abe, Development of a hand motion assist robot for rehabilitation therapy by patient self-motion control, in: 2007 IEEE 10th Int. Conf. Rehabil. Robot., IEEE, 2007: pp. 234–240.
- [460] A.S. Merians, D. Jack, R. Boian, M. Tremaine, G.C. Burdea, S. V Adamovich, M. Recce, H. Poizner, Virtual reality-augmented rehabilitation for patients following stroke, *Phys. Ther.* 82 (2002) 898–915.
- [461] V. Olmedo-Vega, M.J. Aguilar-Idáñez, J.F. Arenillas-Lara, Comprehensive post-stroke rehabilitation: its long-term effects and the socio-environmental factors conditioning access to it, *Rev. Neurol.* 73 (2021) 1–9.
- [462] D.J.E. Herranz, DISEÑO Y CONSTRUCCIÓN DE UN ROBOT BLANDO., (2020).